Sustainable Preparation of Cellulose Nanofibrils and Their Applications for Multifunctional Nanocomposites

by

Haishun Du

A dissertation submitted to Graduate Faculty of
Auburn University
in partial fulfillment of the
requirements for the Degree of
Doctor of Philosophy

Auburn, Alabama
August 7, 2021

Keywords: Cellulose nanofibrils, Conducting polymers, Nanocomposites, Antimicrobility, EMI shielding, Supercapacitors

Approved by

Dr. Xinyu Zhang, Chair, Professor, Department of Chemical Engineering
Dr. Zhihua Jiang, Assistant Professor, Department of Chemical Engineering
Dr. Allan David, Associate Professor, Department of Chemical Engineering
Dr. Siyuan Dai, Assistant Professor, Department of Mechanical Engineering

Abstract

Cellulose nanofibrils (CNFs), which are commonly produced from lignocellulosic biomass, have received increasing attention in recent years due to their unique properties, such as high specific surface area (up to 600 m^2/g), high elastic modulus (29-36 GPa), high thermal stability (being stable against temperatures up to 200-300 °C), as well as renewability and biodegradability. These unique properties make CNFs as promising building blocks for the manufacture of many sustainable nanomaterials. However, sustainable and low-cost production of CNFs is still challenging, which limits their large-scale applications.

As a kind of agro-industrial wastes, paper mill sludge (PMS) has posed serious environmental and economic challenges for disposal due to the more stringent regulations and diminishing land availability recently. Instead of the traditional landfill or burning treatment strategies, PMS, usually with negative cost, could be used as a cheap and sustainable feedstock for producing CNFs. Thus, the main objectives of this research are to valorize PMS into value-added CNFs through a sustainable approach and to develop multifunctional nanocomposites based on the PMS-derived CNFs.

In the first project (Chapter 2), a sustainable approach was demonstrated to efficiently convert PMS to CNFs by formic acid (FA) hydrolysis pretreatment and the followed microfluidization. It was found that the mild FA hydrolysis (at 95 ºC for 3-6 h) pretreatment could hydrolyze most of hemicellulose, swell and break down the cellulose fibers, and the collected cellulosic solid residue with a high yield (over 75%) could be further converted to CNFs with relatively low-intensity microfluidization (only two passes). Notably, more than 90% FA in the collected supernatant can

be recovered through a simple vacuum distillation process. Moreover, cellulose nanopaper (CNP) was prepared from the CNFs suspension via a simple vacuum filtration approach. The obtained CNP exhibited good mechanical properties with the maximum tensile strength and toughness of 106.4 MPa and 6.62 MJ/m^3, respectively.

In light of the advantages of superior mechanical properties, high thermal stability, low thermal expansion coefficient, tunable optical properties, etc., CNP has been considered as a promising material with great application potential in diverse fields. However, the hydrophilic nature of CNP significantly limits its practical application. In the second project (Chapter 3), a facile and sustainable approach was demonstrated to functionalize the CNP obtained in Chapter 2 by impregnation of chitosan (CS) and the followed halogenation. The mechanical strength of the functionalized CNP was improved at both dry and wet conditions, especially the wet tensile strength was increased by 512.6%. Meanwhile, both the transparency and barrier properties were significantly enhanced. Importantly, part of the amino groups on CS can be transformed into N-halamines during the halogenation process, which endowed the chlorinated CNP/CS with excellent antibacterial performance against both *S. aureus* and *E. coli*. The functionalized CNP with water resistance, high transparency, excellent antibacterial and barrier properties shows great application potential in the field of advanced packaging materials.

Polypyrrole (PPy) with hydrophobic and conductive nature has been investigated as a promising conducting polymer with numerous potential applications. In order to further improve the water resistance of the PMS-derived CNP and introduce new features to expand its potential applications, in the third project (Chapter 4), PPy was further introduced into the CNP/CS through a facile *in situ* polymerization process. Results indicate that the obtained CNP/CS/PPy showed excellent

water resistance with the wet tensile strength up to 80 MPa, which doubled the value of CNP/CS and was more than 10 times higher than that of the pure CNP. Intriguingly, the functionalized CNP/CS/PPy exhibited a high conductivity of 6.5 S cm^{-1} and good antibacterial activity towards *S. aureus* and *E. coli*. In addition, the EMI shielding application of the CNP/CS/PPy was further examined which showed a high shielding performance around 18 dB. Considering the multifunctional properties, the CNP/CS/PPy may find applications in a variety of high-tech fields such as medical packaging, electronic packaging, EMI shielding, and so forth.

As another promising conducting polymer, PEDOT:PSS has been widely used as the electrode materials for supercapacitors. However, processing PEDOT:PSS bulk films with good flexibility and mechanical stability is still challenging. In the fourth project (Chapter 5), we investigated the feasibility of using the PMS-derived CNFs as building blocks for the fabrication of PEDOT:PSS based flexible electrodes. Instead of using the costly commercial PEDOT:PSS, we developed a facile and low-cost strategy for the fabrication of mechanically strong and conductive PEDOT:PSS/CNF nanopaper (denoted as PEDOT:PSS/CNP). Firstly, well-dispersed PEDOT:PSS/CNF aqueous suspension was prepared through an in situ polymerization process, in which the CNFs were coated with conductive PEDOT:PSS. Afterwards, flexible PEDOT:PSS/CNP was fabricated from the PEDOT:PSS/CNF suspension by a vacuum filtration approach and the followed DMSO treatment. Results indicated that the as-prepared PEDOT:PSS/CNP showed high tensile strength (70 MPa) and electrical conductivity (66.67 S/cm), which can be directly used as the electrodes for flexible supercapacitors. It was found that the assembled supercapacitor exhibited high areal specific capacitance of 888.7 mF cm^{-2}, high areal energy density of 30.86 μWh cm^{-2}, and remarkable cycling stability (95.8% capacitance

retention after 10,000 charge/discharge cycles), which was among the best electrical performance reported for PEDOT:PSS based supercapacitors.

In summary, this research established sustainable and economically feasible approaches to valorize the PMS into CNFs and their functional nanocomposites. To the best of our knowledge, this work is among the very few pioneering studies that explore the sustainable production of CNFs from agro-industrial wastes. Also, the findings in the development and application of the CNFs based nanocomposites will provide many sustainable alternatives for the traditional packaging materials, EMI shielding materials, and energy storage electrode materials. It is expected that this research will contribute to the revival of the pulp and paper industry in the United States by enabling various biomass-derived products on the market in the near future.

Acknowledgments

Firstly, I would like to give special thanks to my advisor Dr. Xinyu Zhang for his constant encouragement and guidance throughout my Ph.D. career. I am also grateful to my committee members, Dr. Zhihua Jiang, Dr. Allan David, Dr. Siyuan Dai, and my university reader, Dr. Russell Mailen for providing their precious time and insightful comments in my research projects and the dissertation.

I would like to express my sincere gratitude to Dr. Zhihua Jiang for generously sharing his lab facilities and resources with me to support my research. The achievements in this dissertation would not have been realized without this precious collaboration.

I would like to thank Dr. Mahesh Parit and Dr. Burak Aksoy at the Alabama Centre for Paper and Bioresource Engineering; Dr. Maria Auad, Dr. Ramsis Farag, Dr. Nima Alizadeh, and Ms. Archana Bansode at the Center for Polymers and Advanced Composites; Dr. Tung-Shi Huang in the College of Agriculture; Dr. Ruigang Wang and Dr. Zhongqi Liu in the University of Alabama; Dr. Chuanling Si and Mr. Kun Liu in Tianjin University of Science and Technology; Dr. Bin Li and Dr. Meiyan Wu in Qingdao Institute of Bioenergy and Bioprocess Technology, Chinese Academy of Sciences; for their numerous support and discussions for my research projects.

Additionally, I would like to extend my gratitude to my labmates, Miaomiao Zhang, Mao-Chia Lin, Hung-En Wang, Shatila Sarwar, and Dr. Amit Nautiyal for their help and support in lab.

Lastly, I am very grateful to my parents for their endless love, constant moral support and encouragement throughout the years.

Table of contents

List of Figures

List of Tables

List of Abbreviations

CNC	Cellulose nanocrystals
CNF	Cellulose nanofibrils
CNP	Cellulose nanopaper
CNS	Cellulose nanosheets
CS	Chitosan
CV	Cyclic voltammetry
DMF	Dimethylformamide
DMSO	Dimethyl sulfoxide
EIS	Electrochemical impedance spectroscopy
GCD	Galvanostatic charge-discharge
LbL	Layer-by-Layer
OP	Oxygen permeability
OTR	Oxygen transmission rate
PANI	Polyaniline
PDMS	polydimethylsiloxane
PEDOT:PSS	Poly(3,4-ethylenedioxythiophene) polystyrene sulfonate
PMS	Paper mill sludge
PPy	Polypyrrole
TEMPO	(2,2,6,6-Tetramethylpiperidin-1-yl)oxyl
WVP	Water vapor permeability
WVPR	Water vapor transmission rate

Chapter 1 Introduction

1.1 Lignocellulosic biomass and chemical composition

In recent years, along with the increasing concerns about environmental issues, fossil fuel depletion, and global warming, lignocellulosic biomass, the most abundant sustainable carbon source on the planet, has been considered as alternative sources to fossil resources because of their large amount of stock and renewability.[1] The world production of lignocellulosic biomass is estimated more than 200 billion tons a year.[2] As shown in **Fig. 1-1**, the lignocellulosic biomass (e.g. wood, bagasse, grass and agricultural wastes) mainly contains three constituents (cellulose, hemicellulose and lignin) with different mass ratio. **Table 1-1** summarizes the main composition of different lignocellulosic biomass.

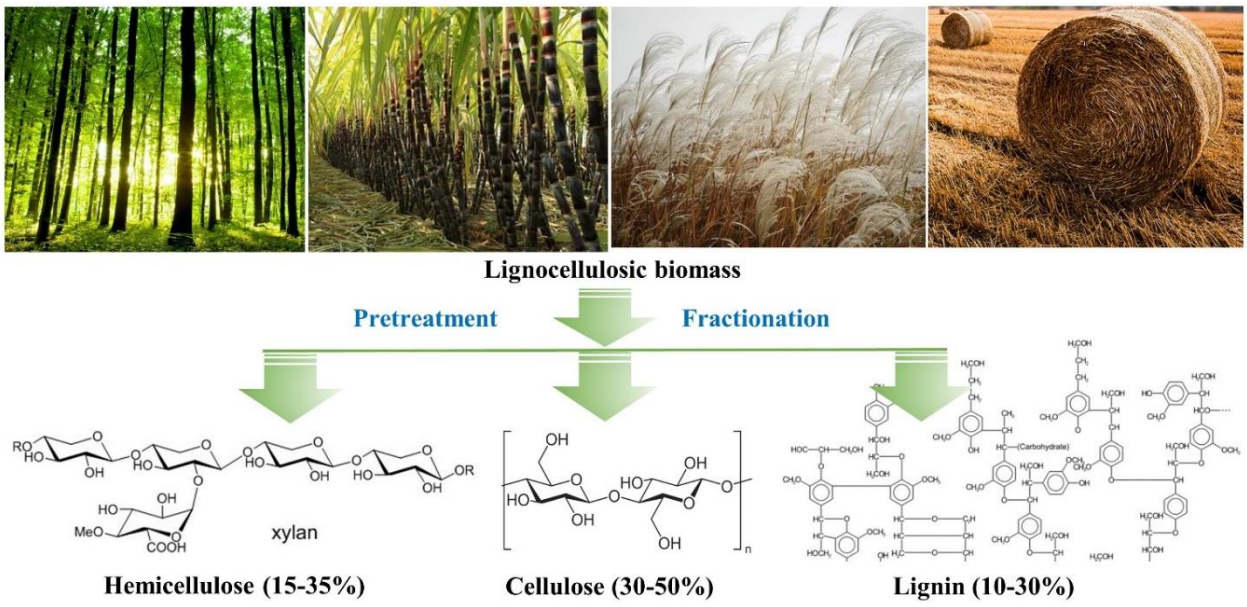

Figure 1-1. Various lignocellulosic biomass and the main constituents.

1.1.1 Cellulose

Cellulose is the major skeletal component with a proportion of 30-50% of dry weight in lignocellulosic biomass and it is the most abundant natural polymer on earth. The global annual production of cellulose is estimated at 150 billion tons.[3, 4] Especially in some special plant species such as cotton, hemp, and jute, the cellulose content is significantly high with the percentage of 60-95%.[5] Since Anselme Payen first discovered and isolated cellulose in 1838, extensive efforts have been made to the biosynthetic process, physical and chemical properties, as well as the structural characteristics of cellulose, which have greatly promoted the development of related disciplines.[6] In recent years, modern technologies such as information technology, biotechnology and nanotechnology have contributed to the rapid development of our society in all different fields, and future technologies are expected to concern more about the development of a greener and more sustainable society.[7] As a kind of renewable and sustainable materials, cellulose has attracted a great deal of attention from a wide variety of fields recently.[8] The fascination of cellulose is a result of its specific structure, which will be described in more detail in sections 3.

1.1.2 Hemicellulose

Hemicellulose is a group of heteropolysaccharides present in the plant cell walls. Generally, they constitute 15-35% of cell walls and mainly locate in the primary and secondary cell walls of various plants.[9] As the second most abundant polysaccharide in nature, an estimated annual production of hemicelluloses in nature is in the range of 60-70 billion tons.[10, 11] Depending on the plant species, hemicellulose is made up of various sugars include pentoses (D-xylose, L-arabinose), hexoses (D-glucose, D-galactose, D-mannose) and sugar acids such as D-glucuronic and D-galacturonic acids.[12, 13] In general, the main chain of hemicelluloses can consist of only one

sugar unit like xylan (homopolymers), or two or more sugar units, i.e., heteropolymers such as glucomannans, and some of the units (e.g. 4-O-methylglucuronic acid, galactose) are usually served as the side groups of a backbone of hemicellulose.[5] Thus, hemicellulose normally consists of 50-3000 sugar units and has a branched, random and amorphous structure with little strength, and it can be easily hydrolyzed by dilute acid or base and various of hemicellulase enzymes.[14] Therefore, the hydrolysis of hemicelluloses for sugars production has been extensively investigated to valorize hemicellulose. These sugars have already commercial applications or are potential intermediates for synthesis of pharmaceuticals and health-promoting agents.[15] In addition, the hemicellulosic sugars could be further converted to fuel ethanol and other high value-added chemicals (e.g. xylitol, lactic acid, furfural, levulinic acid) by bioconversion and chemical transformation.[16]

1.1.3 Lignin

Lignin is the generic term for a large group of aromatic polymers which is made up of predominantly C-O-C and C-C linkages.[17] More specifically, lignin is formed by radical coupling reactions of three main monolignols namely *p*-coumaryl (4-hydroxycinnamyl), coniferyl (4-hydroxy-3-methoxycinnamyl) and sinapyl (4-hydroxy-3,5-dimethoxycinnamyl) alcohols.[18] Correspondingly, these monolignols are widely called as hydroxyl-phenyl lignin (H-lignin), guaiacyl lignin (G-lignin) and syringyl lignin (S-lignin), respectively.[5] Lignin is the second most abundant organic polymers in nature after cellulose, constituting 30% of non-fossil organic carbon.[19] The lignin content in wood species ranges from 20-40% while aquatic and herbaceous angiosperms as well as many monocotyledons content less lignin.[20] Lignin mainly locates in the secondary cell walls as an embedding material for the cellulosic polymers, and it is also the major

polymer in the middle lamellae between adjacent cell walls.[21] Importantly, lignin provides the hydrophobic surface that allows plants to transport water to heights over 100 m and contributes to the mechanical strength that can support trees weighing more than 2,000 tons.[22] Moreover, its unique physical and chemical properties provide a barrier against the invasion of pests and pathogens.[23] However, lignin is the major barrier for the efficient extraction of cellulose fibers in the pulp and paper industry and is the main hurdle to saccharification for production of liquid biofuel in the bioenergy industry.[24, 25] Thus, lignin is usually generated as a waste product from the paper and biofuel production. The worldwide production of lignin is approximately 100 million tons per year and 50-70% of the production comes from pulp and paper industry.[26] Traditionally, lignin is considered as low-value waste product and burned for process heat because its inherent heterogeneity and recalcitrance.[27] With the intensive studies of lignocellulosic biorefinery in recent years, various promising approaches have been developed to valorize lignin to produce high-value products such as carbon fiber, multifunctional hydrocarbons, syngas and various platform chemicals (e.g. aromatic aldehydes, vanillic acid, syringic acid).[28-30]

1.1.4 Extractives and ash

In addition to cellulose, hemicellulose and lignin, lignocellulosic biomass contains a small portion of other constituents such as extractives and ash. Extractives are nonstructured components of biomass, including fats, fatty acids, fatty alcohols, phenolics, waxes, proteins, essential oils, pectins, rosin and other organic compounds, which can be extracted by solvents (e.g. water, ethanol, acetone, and toluene).[31] Note that each of these extractives has specific functions for the plant. The content and properties of the extractives vary from biomass to biomass, and even vary between different parts of the same plant.[32] The ash in lignocellulosic biomass typically comprises of

calcium, potassium, magnesium, manganese, sodium oxides, and less amount of other oxides of iron, aluminum, etc.[33]

Table 1-1. The main composition of lignocellulosic biomass.[5, 34]

Feedstock	Cellulose (%)	Hemicellulose (%)	Lignin (%)
Hardwood	43-47	25-35	16-24
Softwood	40-44	25-29	25-31
Bagasse	42-45	25-28	14-21
Coir	32-43	10-20	43-49
Cotton	95	2	1
Flax	63-71	12-21	2-3
Hemp	70	22	6
Jute	71	14	13
Sisal	73	14	11
Rice straw	32-47	19-27	5-24
Wheat straw	35-45	20-30	8-15
Corn stover	21-37	22-31	14-20
Switchgrass	35-40	25-30	15-20

1.2 Wood category and its hierarchical structure

Wood is a mixture of dead and living cells of many different cell types, and the cell wall as the supportive framework is the main component of wood cell.[35] Wood can be broadly classified into

two categories: hardwoods (e.g. birch, aspen, eucalyptus and oak) and softwoods (e.g. pine, spruce, cedar, and redwood). The distinction between these two types mainly comes from the way that the tree reproduces: Hardwoods are scientifically known as angiosperms, which are flowering plants that produce seeds with enclosures; softwoods are known as gymnosperms, which are also called coniferous trees, producing seeds without enclosures.[36] In general, hardwoods are denser than softwoods since they grow slowly, but with a few exceptions: balsa tree is classed as hardwood but is softer than most of softwoods, yew tree is classed as softwood but is denser than most of hardwoods. Softwoods are famous for faster growing and around 80% of all timber used in the world comes from softwoods.[37]

1.2.1 Wood cell structure

From a microstructural point of view, cellular structures of softwoods differ in appearance from that of hardwoods. As shown in **Fig. 1-2a**, hardwoods contain three main types of cells: fibers (50%), vessels (30%) and parenchyma (20%).[38] Among them, fiber cells provide structural support and have a honeycomb-like structure. Vessels appear much larger in diameter and shorter than fibers and they are used for the transport of fluids and nutrients. Parenchyma normally appears as box-like cells within the rays and longer tubular cells associated with the vessels.[39] In addition, a small number of tracheids with much thinner cell walls than fibers may be found, but they may be completely missing in some hardwood species. As shown in **Fig. 1-2b**, softwoods consist mainly of longitudinal tracheids (90-95 %) and a small number of parenchyma and ray cells (5-10 %), in which the tracheids with roughly honeycomb-like structure make up the bulk of the cells.[37] In addition, some softwoods (e.g. white pine) may have resin canals lined with epithelial cells, and most of softwoods lack of fibers or vessel elements. Among all the above cells in both hardwoods

and softwoods, fibers and tracheids are the best cells for papermaking, and other cells cause mainly problems. Thus, softwoods are the best feedstocks and widely used in the pulp and paper industry. Generally, the cellulose fibers can be produced in two different pulping approaches: mechanical pulping and chemical pulping. In mechanical pulping process, the fibers are softened and separated from each other using mechanical grinding or refining at elevated temperature.[40] Since there is almost no loss of material in mechanical pulping, the mechanical pulp usually has a high yield up to 90% based on the wood. However, the mechanical process is highly energy intensive and the resulting fiber and paper usually show inferior strength.[41] Chemical pulping on the other hand gives the pulp of lower yield (40-50%) but with better mechanical strength. There are two main purposes in chemical pulping process: i) chemicals attack on the lignin in the middle lamella in order to separate the individual fibers; ii) removing lignin from the cell wall to make the fibers sufficiently flexible for higher paper strength.[42] Delignification of wood during chemical pulping is carried out by two main types of processes: sulfate (kraft) process and sulfite process, and the kraft pulping is the most popular and predominant pulping method so far. Normally, about 90% of lignin can be removed in kraft pulping.[41] The residual lignin can be further removed by bleaching process, resulting in the bleached pulp with less than 0.1% lignin.[43]

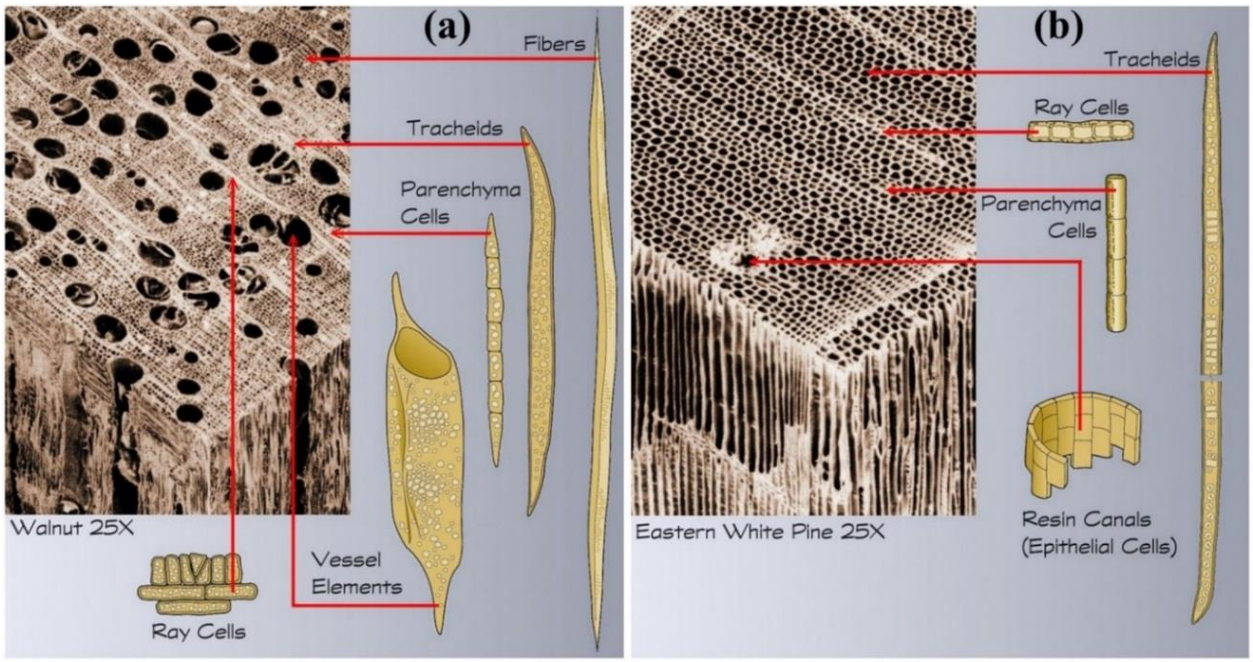

Figure 1-2. The cells that make up hardwood (a) and softwood (b), respectively, adapted from http://workshopcompanion.com.

1.2.2 Cell wall structure

As shown in the top-right inset in **Fig. 1-3**, the cell wall is comprised of multilayers include primary cell wall, secondary cell wall and middle lamella, in which the secondary cell wall could be further divided into three layers namely S1, S2, and S3.[44] The primary cell wall is very thin which contains randomly oriented cellulose microfibrils surrounded by a lignin-rich materials include lignin, pectic substances, and hemicelluloses.[45] Surrounding the primary cell wall is a thin lignin-rich layer (0.5 to 1.5 μm) named the middle lamella, which functions as the cellular glue to provide compressive strength to the plant tissue and stiffness to the cell wall.[46] The secondary cell wall layers are the most important for the wood cell in terms of mechanical strength. Among these layers, S1 layer is the thinnest layer, being only 0.1 to 0.35 μm thick, which is considered as an intermediate between the primary cell wall and the S2 and S3 layers. The cellulose microfibrils

angle with regard to the cell axis in the S1 layer is in the range of 60° to 80°. The S2 layer is the thickest layer (1-10 μm) in the secondary cell wall, which contributes to 75% to 85% of the total cell wall thickness and contains majority of the total cellulose. The cellulose microfibrils angle in this layer is 5° to 30° relative to the cell axis. Note that the cellulose microfibrils angle in the S2 layer can significantly influence the physical and mechanical properties of the cell and even stem wood as a whole. With regard to the cell axis, an increase in the cellulose microfibrils angle will result in a decrease in the stiffness and longitudinal modulus of elasticity of the wood. The S3 layer is relatively thin, being 0.5 to 1.1 μm thick, and the cellulose microfibrils angle is 60° to 90° relative to the cell axis.[47]

1.2.3 Spatial arrangement of cellulose, hemicellulose and lignin

The center-right inset in **Fig. 1-3** illustrates a spatial arrangement of cellulose microfibrils, hemicellulose and lignin in the cell wall. The arrangement of these components allows cellulose microfibrils to be embedded in hemicellulose-lignin network, much as steel bars are embedded in concrete to form reinforced concrete.[11] Among them, cellulose microfibrils serve as the reinforcing steel bars, hemicellulose-lignin matrices act as the concrete.[48] Hemicellulose is thought to bind non-covalently to the cellulose microfibrils and covalently cross-link with lignin, forming a complex network of bonds that provides structural strength.[49] It has been suggested that hemicellulose could also act as an amorphous matrix material which holds the stiff cellulose microfibrils in place.[50] Lignin acts as a waterproof mechanical reinforcement element, which is covalently linked to hemicellulose. For decades, lignin has been considered as the glue that binds cellulose microfibrils with hemicellulose.[51] However, one recent study suggested that lignin and cellulose are spaced and joined by hemicellulose (e.g. xylan).[52] It is reported that in contrast to

cellulose, the substitution with some hydrophobic groups such as acetyl and methyl groups could enhance the affinity of hemicellulose to lignin.[50] Although several attempts to describe the specific locations of the different cell wall components and their mutual interactions have been made, the detailed structure of the lignin-carbohydrate complexes surrounding the cellulose microfibrils in the plant cell wall is still not well understood.[53]

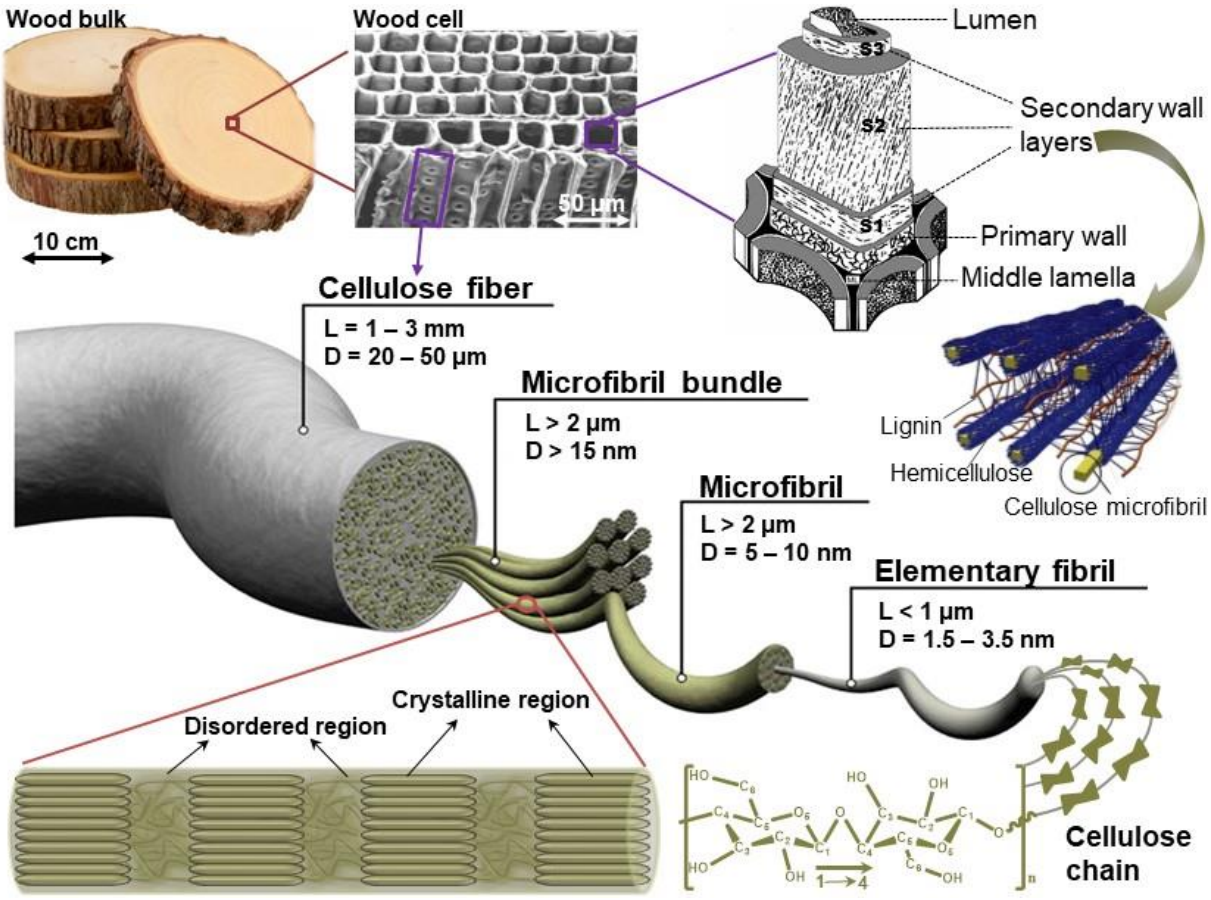

Figure 1-3. Schematic illustration of the hierarchical structure of wood, from macroscopic to molecular scale. Wood cell image is adapted from ref [10]. The cell wall comprised of multilayers is adapted from ref [54]. Spatial arrangement of cellulose, hemicellulose and lignin in the cell wall of lignocellulosic biomass is adapted from ref [55]. Hierarchical structure of cellulose fiber is adapted from ref [56].

1.3 Structure of cellulose

1.3.1 Molecular structure

From a definition point of view, cellulose is a linear chain of ringed glucose molecules with a flat ribbon-like conformation.[57] As shown in the molecular structure represented in the right-bottom inset of **Fig. 1-3**, the repeated unit is comprised of two anhydroglucose rings linked together through an oxygen covalently bonded to the C1 of one glucose ring and the C4 of the adjoining ring (1→4 linkage) namely β-1,4-glycosidic bond.[58] The degree of polymerization (DP) of cellulose is defined by the number of repeated unit, and the DP is in the range of 10,000 to 15,000 depending on the cellulose source material.[59] The hydroxyl groups of β-1,4-glucan cellulose are placed at positions C2 (secondary), C3 (equatorial) and C6 (primary), and the CH_2OH side group is arranged in a *trans-gauche* position relative to the O5-C5 and C4-C5 bonds.[6] These abundant hydroxyl groups have high ability to form strong intrachain and interchain hydrogen bonds which are conductive to the physical properties of cellulose. As a consequence, multiple cellulose chains form elementary fibrils of 1.5-3.5 nm in diameter. These elementary fibrils further aggregate into larger microfibrils with the diameter of 5-10 nm and several microns in length. Finally, the microfibrils and their bundles (typically 10-20 nm across)[60] along with hemicellulose and lignin form the secondary cell wall.

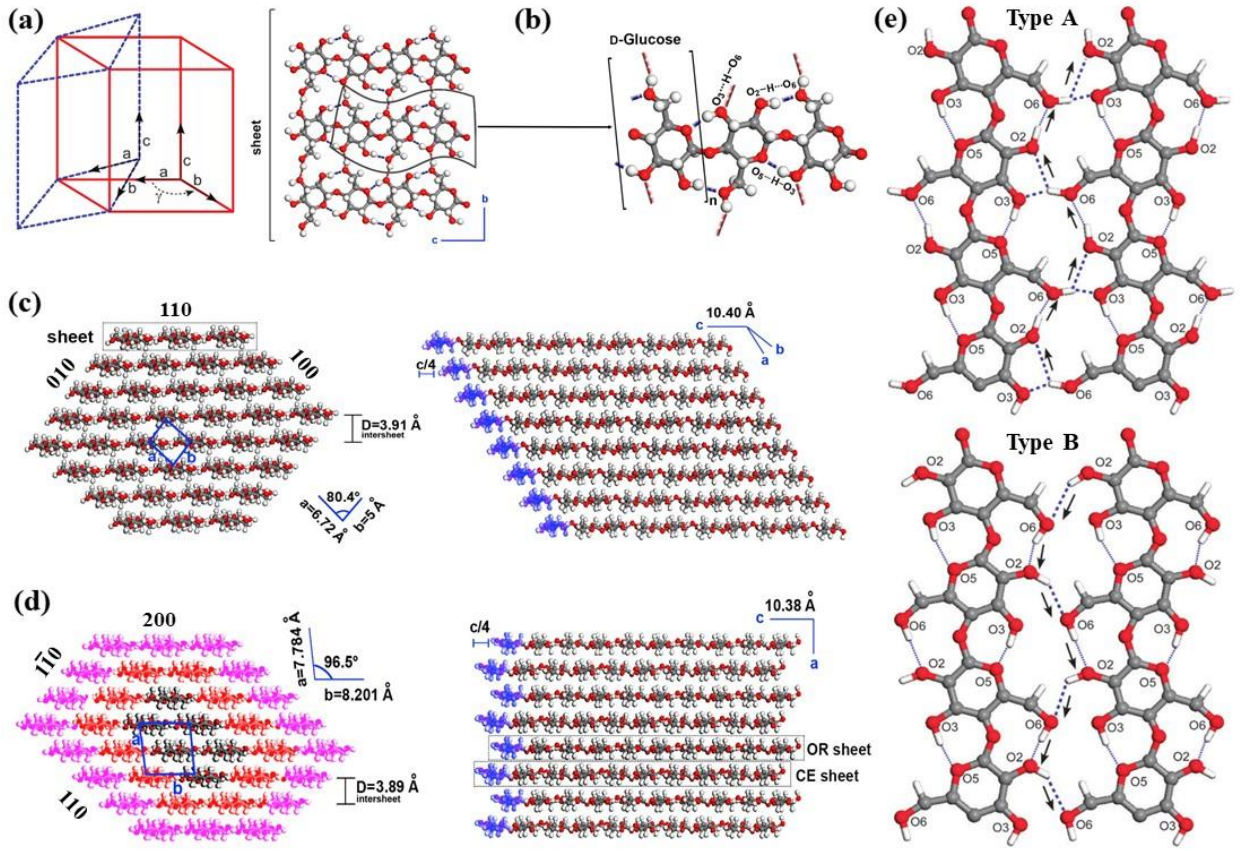

Figure 1-4. (a) Schematic configuration of the unit cells for cellulose Iα (dashed line) and Iβ (solid line).[57] (b) Illustration of a cellulose elementary fibril sheet which contains an arrangement of cellulose chains interconnected by hydrogen bonds (left) and one cellulose chain contains three D-glucose repeated units with hydrogen bonds. (c) Illustrations of a perpendicular view to the c-axis of a 36-chain elementary fibril of cellulose Iα, where Axes a, b and c (in blue color) define the triclinic unit cell formed by one chain (left) and a longitudinal view of parallel sheets packing in cellulose Iα, where each sheet is shifted along the c-axis by +c/4 (right). (d) Illustrations of a perpendicular view (left) and a longitudinal view (right) of a 36-chain elementary fibril of cellulose Iβ. Axes a, b and c define the monoclinic unit cell made up of two chains namely origin (OR) chain and center (CE) chain of cellulose Iβ. In the perpendicular view, the 36 cellulose chains are hexagonally arranged in the transverse section of the elementary fibril, where 18 chains (in pink color) represent the outer chains that sheath other sub-crystalline 12 chains (in orange color), and inner 6 chains form the crystalline core. In the longitudinal view, there is an alternated displacement between OR and CE sheets by c/4 in the parallel sheets of cellulose Iβ.[61] (e) Schematic illustration of two suggested hydrogen bond patterns within the hydrogen-bonded plane ((110) plane for cellulose Iα and (200) plane for cellulose Iβ). Note: thin dotted lines refer to intrachain hydrogen bonds, thick dotted lines refer the interchain hydrogen bonds, arrows show the donor-acceptor-donor directions.[57]

1.3.2 Crystalline structure

As a result of the supramolecular structure of cellulose, cellulose microfibrils consist of both high order (crystalline) and disordered (amorphous-like) regions, as illustrated in the bottom-left inset in **Fig. 1-3**. Depending on the different crystal packings, there are four different polymorphs of cellulose: Cellulose I, II, III, and IV. Among them, cellulose I is naturally produced by various organisms, and it is sometimes called "natural" cellulose.[57] Cellulose I has two crystal forms namely Iα and Iβ, which coexist in different proportions depending on the organisms. Cellulose in higher plants (e.g. cotton, trees) cell walls and in tunicates are rich in Iβ, whereas some algae and bacteria are predominantly composed of Iα.[62] As illustrated in **Fig.1-4a**, cellulose Iα appears a one-chain triclinic unit cell (P_1 symmetry) while cellulose Iβ displays a two-chain monoclinic unit cell (P_{21} symmetry). For cellulose Iα unit cell, the unit-cell parameters are a = 0.672 nm, b = 0.596 nm, c = 1.040 nm, α = 118.08º, β = 114.80º, γ = 80.375º. For cellulose Iβ unit cell, the unit-cell parameters are a = 0.778 nm, b = 0.820 nm, c = 1.038 nm, α = 90º, β = 90º, γ = 96.5º.[57] For both cellulose Iα and Iβ, the cellulose chains making up the sheets are parallel and aligned along the crystallographic c-axis, as displayed in **Fig. 1-4b**. **Figs. 1-4c** and **4d** illustrate a perpendicular view to the c-axis of a 36-chain elementary fibril of cellulose Iα and cellulose Iβ, respectively. At the molecular level, cellulose Iα and Iβ share similar conformation and chain packing in the a-b planes.[63] The main difference between these two polymorphs is the relative displacement of hydrogen-bonded planes, i.e. (110) plane for cellulose Iα and (200) plane for cellulose Iβ, in the c-axis direction. More specifically, hydrogen-bonded planes in cellulose Iα always displace along the molecular axis by +c/4, whereas for cellulose Iβ the displacement between hydrogen-bonded planes alternates between +c/4 and -c/4.[57]

1.3.3 Hydrogen bonding

For both cellulose Iα and cellulose Iβ, a remarkable feature is that cellulose chains are well-stabilized within the sheets (hydrogen-bonded planes) by intrachain and interchain (O─H···O) hydrogen bonds interaction, as illustrated in **Fig. 1-4b**.[61] As shown in **Fig.1-4e**, two coexisting hydrogen bond patterns have been proposed, which are well described in the previous work.[62] It is reported that cellulose Iβ has a higher percentage (70-80%) of Type A hydrogen bonds configuration in the hydrogen-bonded planes than cellulose Iα, resulting in a better bonding geometry. Moreover, within other planes ((100) and (010) plane for cellulose Iα and (110) and (1-10) plane for cellulose Iβ) the number of hydrogen bonds in cellulose Iβ is believed to be higher than that in the cellulose Iα.[64] Thus, cellulose Iβ shows higher stability than cellulose Iα. This inference has been supported by the fact that heating of the cellulose Iα causes irreversible conversion to cellulose Iβ.[63] From the Type A hydrogen bonds pattern (**Fig. 1-4e**), it is clear to see that the intrachain hydrogen bonds include O3─H···O5 and O2─H···O6 bonds while the interchain hydrogen bonds are dominated by O6─H···O3 bonds. As show in **Fig. 1-5a**, the intrachain hydrogen bonds limit the rotation of glucose units in the linear chains around the glycosidic linkages and contribute to the linear configuration of cellulose chain, whereas the interchain hydrogen bonds are beneficial to the sheet stability.[65] Further, the intersheet interactions involved both C─H···O pseudo hydrogen bonds and van der Waals interactions ensure the sheets stack on top of each other to form a 3D crystal structure.[61] Gross and Chu[66] investigated and compared the interaction network of cellulose Iα and cellulose Iβ by using all-atom molecular dynamics simulations.

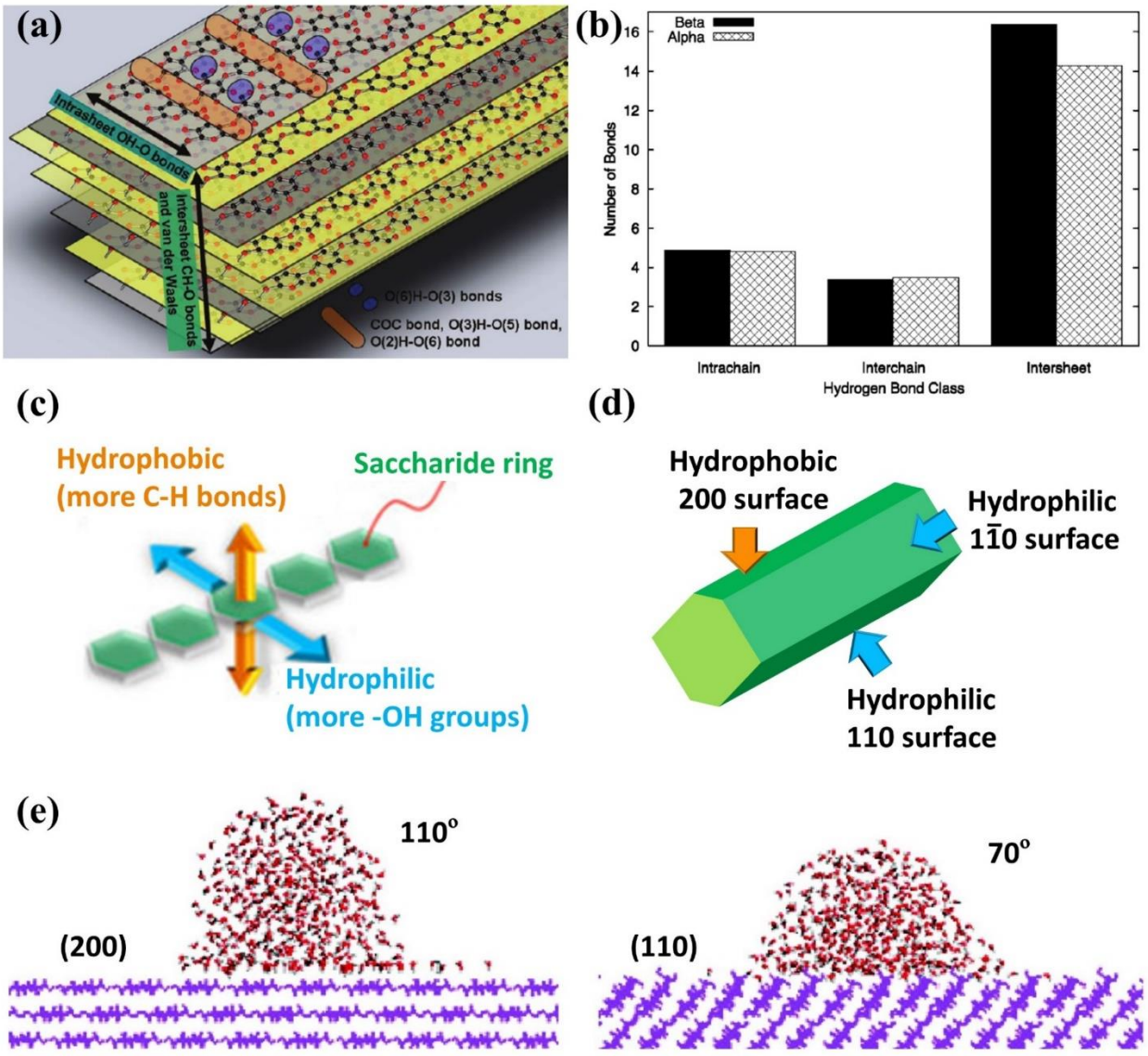

Figure 1-5. (a) Schematic diagram of hydrogen-bond network and layer structure for cellulose Iβ.[65] (b) Average number of hydrogen bonds per glucose of cellulose Iα and cellulose Iβ.[66] Schematic illustrations of cellulose molecular chain (c) and crystal planes (d) of cellulose Iβ showing amphipathicity.[67] (e) Water wetting of the (200) and (110) surfaces of cellulose Iβ.[68]

As indicated in **Fig. 1-5b**, while both cellulose Iα and Iβ possess almost the same amount of intrachain and interchain hydrogen bonds, cellulose Iβ has two more intersheet pseudo hydrogen bonds per glucose than cellulose Iα. This finding again proved the fact that cellulose Iβ is the more stable form. In addition, the number of C—H---O pseudo hydrogen bonds per glucose is much

higher than the sum of intrachain and interchain hydrogen bonds. Although individual C—H···O pseudo hydrogen bond shows a much lower interaction energy of 2 kcal/mol than O—H···O hydrogen bond (6 kcal/mol), the large amount of these pseudo hydrogen bonds plus van der Waals interactions make intersheet interactions stronger than interchain interactions.

1.3.4 Wetting behavior and amphiphilic character

In general, natural cellulose is considered as highly hydrophilic due to the existence of abundant hydroxyl groups. However, several studies have proven that cellulose also exhibits a hydrophobic character due to its anisotropic supramolecular structure. As illustrated in Figs. 1-5c and 5d, the surfaces of cellulose Iβ are topographically and chemically heterogeneous, i.e. plenty of -OH groups appear on the (110) and (1-10) surfaces while the (200) surface has the most -CH groups exposure with buried -OH groups, thus leading to the amphipathicity of cellulose.[69] **Fig. 1-5e** displays the water wetting behavior of the (200) and (110) surfaces of cellulose Iβ by using atomistic molecular dynamics simulations.[68] It can be clearly seen that (200) surface exhibits a much higher contact angle than (110) surface, indicating higher hydrophobicity.

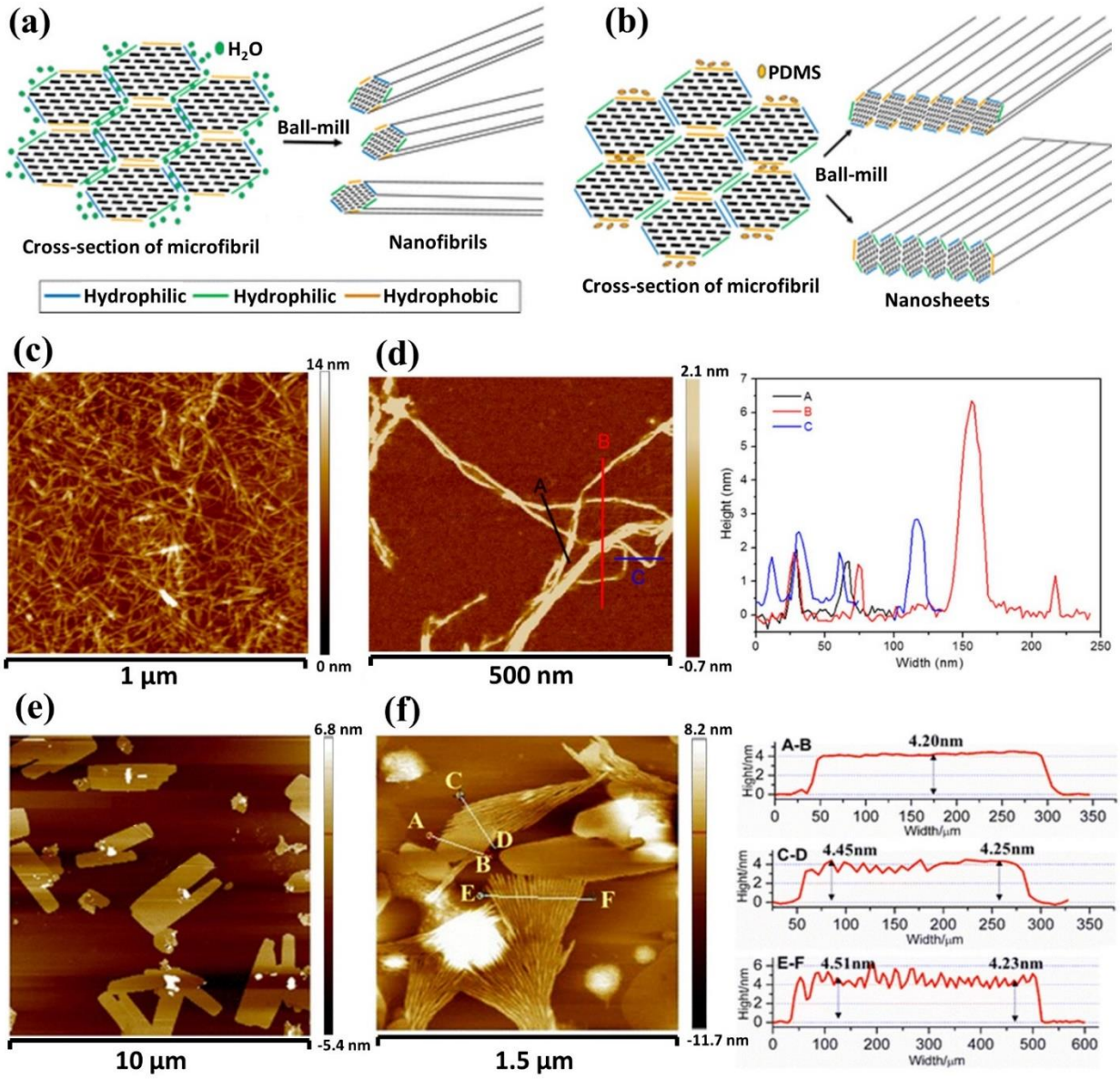

Figure 1-6. Schematic illustration of disintegration of cellulose in water (a) and polydimethylsiloxane (PDMS) (b) media.[70] (c) AFM image of esterified cellulose nanofibrils (CNFs) produced through one-step mechanochemical esterification by ball milling in DMF; (d) magnified AFM image of the CNFs and the corresponding height profile.[71] (e) AFM image of cellulose nanosheets (CNS) prepared by ball milling in PDMS; (f) AFM image of the CNS after sonication in ethanol for 60 min and the corresponding height profile.[70]

Based on the amphiphilic nature of cellulose, Zhao et al.[70] proposed a theory of cellulose disintegration along the crystallographic planes induced by mechanical force and

microenvironmental polarity. As illustrated in the cross-section of cellulose microfibrils (**Fig. 1-6a**), elementary fibrils in the microfibrils are associated with each other through close contacts. As described above, different crystallographic planes exhibit different supramolecular structures. As a consequence, the interactions of these planes with different solvents vary from each other.[72] Therefore, it is expected that both disintegration and reorganization of the cellulose microfibrils will be affected by changing the type of medium during mechanical shearing.[73] For instance, when mill cellulose in polar solvents such as water, dimethylformamide (DMF) and dimethyl sulfoxide (DMSO), cellulose nanofibrils (CNFs) can be obtained, as illustrated in Figure 6a. This result is probably attributed to polar solvents have great affinity to hydrophilic (110) and (1-10) surfaces, thus can penetrate into the interstitial space between these hydrophilic planes of the tightly bound elementary fibrils. During the ball milling process, the strong impact and frictional shear accompanying with the solvent swelling effect cause the big microfibril bundles disintegrated into CNFs. Intriguingly, the fibrillation efficiency could be remarkably enhanced by simultaneously applying esterification during ball milling. More importantly, the functionality of the as-prepared CNFs could be tuned by changing esterifying agents.[74] For example, by milling corncob cellulose in DMF with hexanoyl chloride as esterifying agent, thin and hydrophobic CNFs with the diameter approx. 1.5-2.8 nm could be obtained, as shown in the AFM images (Figs. 1-6c and 6d). In another case, hydrophilic CNFs could be prepared by milling cellulose in DMSO with succinic anhydride. It was found that the succinylated CNFs exhibited great dispersibility in aqueous media with a Zeta potential around -34 mV.[75]

As shown in **Fig. 1-6b**, nonpolar solvents such as polydimethylsiloxane (PDMS), toluene and stearic acid exhibit strong affinity to hydrophobic (200) surfaces. When mill cellulose in these nonpolar solvents, breaking interfaces mainly take place at the interstitial space between these

hydrophobic planes while the hydrophilic (110) and (1-10) planes still keep connected, resulting in the formation of cellulose nanosheets (CNS). As displayed in **Fig. 1-6e**, thin CNS with the thickness around 4.2 nm (which is consistent with the thickness (3-5 nm) of elementary fibrils) and varied lateral size and shape were successfully produced by milling cellulose in PDMS for 12 h (5 min pause after every 20 min). In addition, **Fig. 1-6f** shows the AFM image of the CNS after sonicating in ethanol for 60 min. It is clear to see that some CNS can be spread into 4.2-4.5 nm wide elementary fibrils with fan-like shapes, indicating that the CNS can be further disintegrated into nanofibrils.

According to the above discussion, it can be concluded that the solvent polarity plays an important role on the hydrogen bonds or van der Waals force among cellulose molecular chains and crystallographic planes during mechanical disintegration.[76] This fundamental knowledge provides the evidence for the fact that most of the cellulose nanomaterials produced from lignocellulosic biomass exhibit fibrous morphology, since the processing media for the production of cellulose nanomaterials is mainly in aqueous solution.

1.4 Cellulose nanomaterials

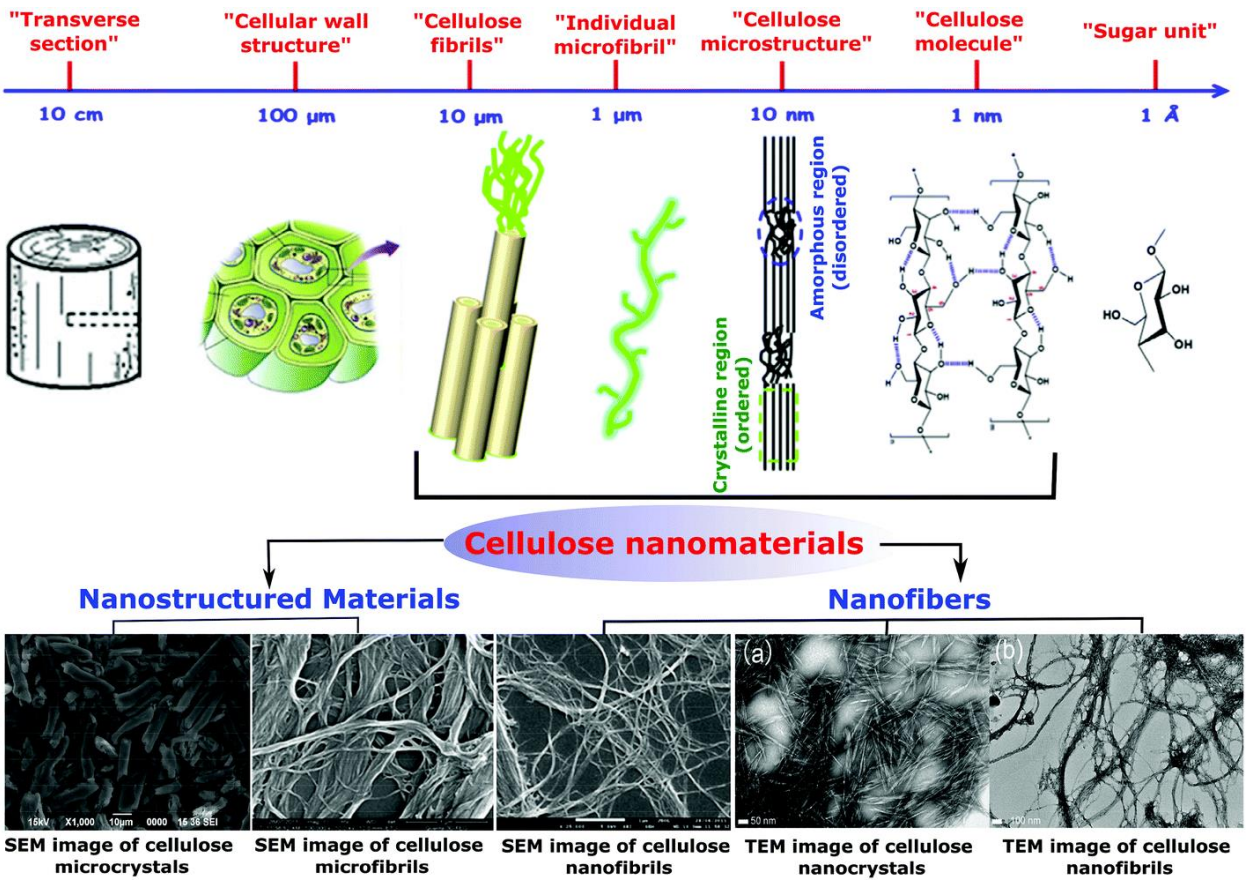

Figure 1-7. Hierarchical structure of cellulose and its nanomaterials types.[77]

Over the past two decades, cellulose nanomaterials, also known as nanocellulose, have attracted rapidly growing scientific and technological interest from both academic and industrial researchers due to their unique nanostructure and impressive physicochemical properties such as high tensile strength (2-6 GPa) and elastic modulus (130-150 GPa), high specific surface area (up to several hundreds of m^2/g), low density (1.6 g/cm^3), reactive surfaces combined with biodegradability and renewability. [78, 79] Therefore, cellulose nanomaterials have been widely used in diverse fields such as reinforcing agents, coatings, rheology modifiers, optical materials, electroconductive materials,

sensors, and biomedical materials.[80, 81] Based on the size, morphology and preparation techniques, cellulose nanomaterials are mainly divided into cellulose nanostructure materials (e.g. cellulose microcrystals, cellulose microfibrils) and cellulose nano-objects or nanofibers (e.g. cellulose nanocrystals (CNCs), CNFs), as summarized in **Fig. 1-7**.[77]

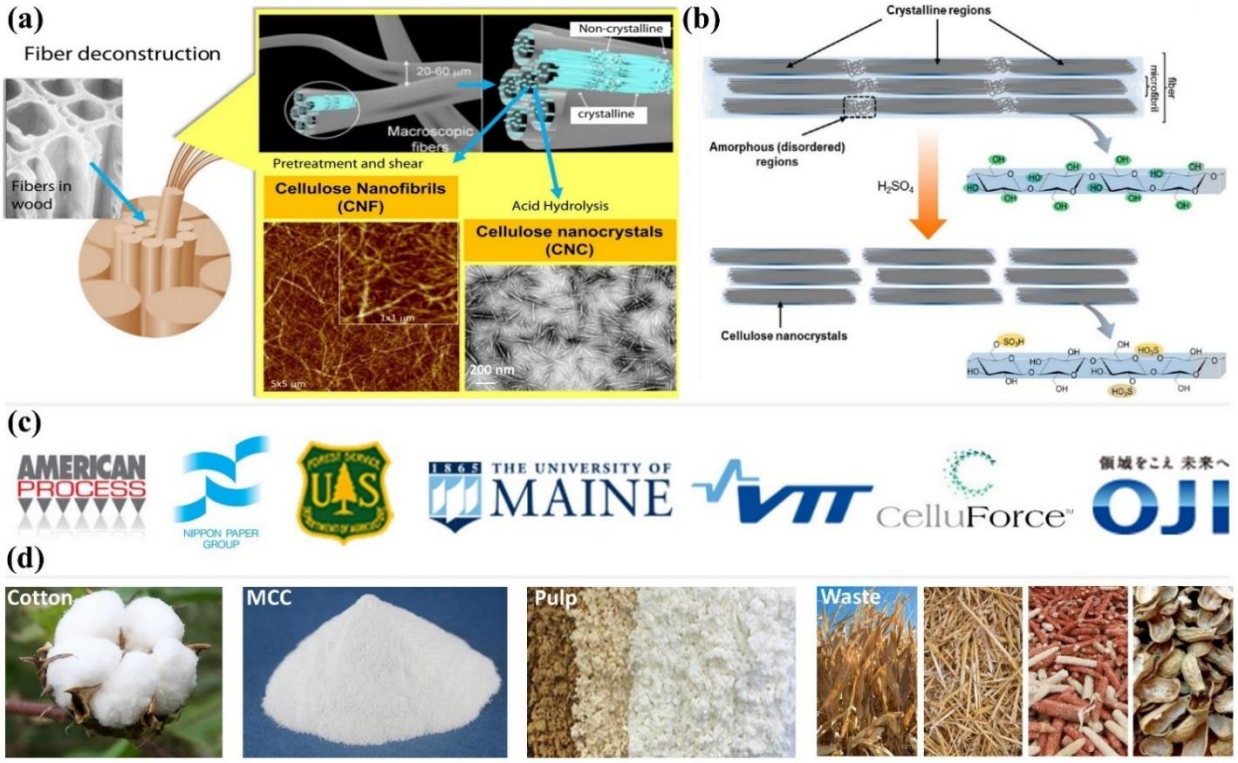

Figure 1-8. (a) Schematic illustration of CNFs and CNCs production from fiber cell walls by mechanical and chemical treatments, respectively.[82] (b) Schematics of idealized cellulose fibers showing one of the suggested configurations of the crystalline and amorphous regions, and CNCs after sulfuric acid hydrolysis of the amorphous regions, exhibiting the characteristic sulfate half ester surface groups formed as a side reaction.[83] (c) Representatives of institutions and enterprises of the industrialization of CNCs and CNFs.[84] (d) Representatives of feedstocks used for the production of CNCs and CNFs (the photographs were adapted from www.google.com).

Compared to cellulose nanostructure materials, CNCs and CNFs possess higher specific surface area and more uniform particle size distribution thus have been widely investigated in recent years. As shown in **Fig. 1-8a**, CNCs and CNFs are the two main categories of cellulose nano-objects

produced from lignocellulosic biomass. To date, a variety of lignocellulosic biomass such as cotton, microcrystalline cellulose (MCC), wood pulp, and different kinds of agricultural wastes have been used as the feedstocks for the production of CNCs and CNFs (**Fig. 1-8d**). Also, the industrialization of CNCs and CNFs has been realized by some companies (e.g. CelluForce, Nippon Paper Group) on the tons-per-day scale, as listed in **Fig. 1-8c**. According to a recent report by Zion Market Research, global nanocellulose market was valued at approx. 232 million USD in 2017 and the number is anticipated to reach around 784 million USD by the end of 2024. Notably, CNFs accounted for the major market share in 2017 and is expected to continue its dominance during the forecast period.

1.4.1 Preparation of cellulose nanocrystals

In general, CNCs, sometimes termed as nanocrystalline cellulose (NCC) or cellulose nanowhiskers (CNW), are rigid rod-like particles of 10-30 nm in diameter and several hundred nanometers in length, and they are mostly crystalline in nature.[85] The typical method for the preparation of CNCs is inorganic strong acid hydrolysis, sulfuric acid is the most commonly used acid for producing sulfonated CNCs with good dispersibility in water.[86] Some other inorganic acid such as hydrochloric acid,[87, 88] phosphoric acid,[89, 90] hydrobromic acid [91] and nitric acid [92, 93] have been invented for the preparation of CNCs as well. As shown in **Fig. 1-8b**, during sulfuric acid hydrolysis process, the amorphous regions of cellulose are more easily degraded while the crystalline regions of cellulose are remained as CNCs because of their inherent structure stability.[57, 94] Also, the introduction of sulfate half ester surface groups would endow the CNCs with good dispersibility in aqueous media.[83] Strong acid hydrolysis is indeed a simple and time-saving method for the preparation of CNCs [93]. However, certain issues such as harsh corrosion of

equipment, severe environmental pollution, large water usage, and low production yield need to be well addressed.[79] Thus, some sustainable and environmentally friendly methods based on the replacement by recyclable chemicals have been invented recently to address the above drawbacks, such as solid acid (e.g. phosphotungstic acid) hydrolysis,[95, 96] organic acid (e.g. formic acid, oxalic acid) hydrolysis [85, 97-99] and ionic liquid [100, 101] or deep eutectic solvents treatment.[102, 103]

1.4.2 Preparation of cellulose nanofibrils

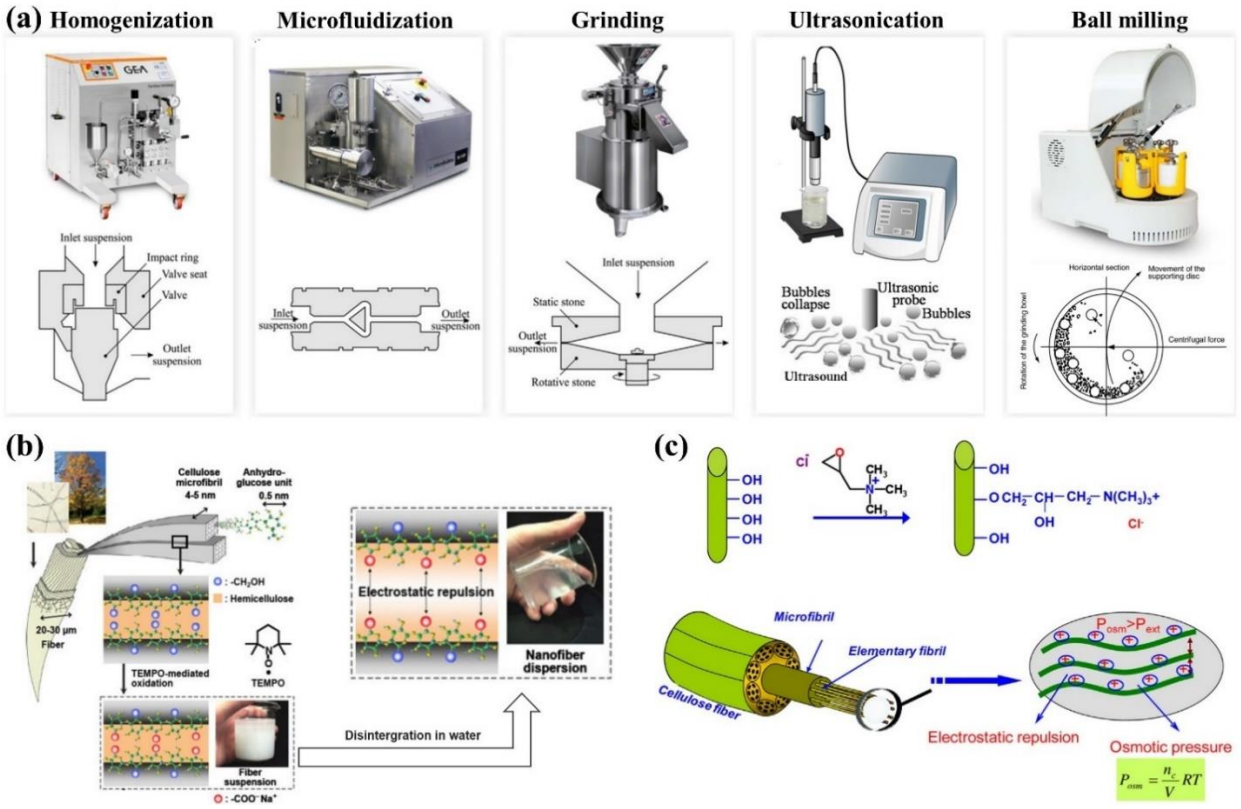

Figure 1-9. (a) Representatives of mechanical fibrillation approaches and the corresponding instruments and their schematic diagrams.[104-106] (c) Systematic diagram of preparation of CNFs by surface carboxylation using TEMPO oxidation.[107] (d) Schematic illustration of how the fibers quaternization enhanced the fibrillation process.[108]

CNFs, sometimes termed as nanofibrillated cellulose (NFC), are flexible fiber-like with a diameter less than 100 nm and the length of 500 nm or even longer, which are composed of both amorphous and crystalline domains.[109] Different from CNCs, CNFs are mainly obtained by mechanical treatment of cellulosic fibers, such as high-pressure homogenization, microfluidization, grinding, ball milling and ultrasonication.[104, 110, 111]

Fig. 1-9a illustrates the corresponding instruments and their schematic diagrams. Among them, high-pressure homogenization and microfluidization are the most widely used methods for the preparation of high-quality CNFs.[112] Basically, both homogenization and microfluidization follow similar working mechanism just with different configurations. In general, the homogenizer works at a pressure below 150 MPa while the microfluidizer can provide a pressure over 250 MPa. During the mechanical fibrillation process, the homogenizer or microfluidizer can generate various forces such as high pressure, high shear, high speed and turbulence through the rapid change of pressure, which are able to break down the cellulose fibers and finally release aggregated nanofibrils.[113] However, mechanical fibrillation by high-pressure homogenization or microfluidization for CNFs production is very energy intensive. It is estimated that the energy consumption is in the range of 12-70 MWh/t.[114] Another issue with homogenization and microfluidization is clogging when processing cellulose fibers, which is mainly attributed to the fact that long cellulose fibers tend to form entanglements.[112]

In order to reduce energy consumption and avoid clogging issue, some pretreatment methods have been proposed in recent years, including enzymatic hydrolysis,[115-117] mineral acid hydrolysis,[118, 119] TEMPO-mediated oxidation,[120, 121] carboxymethylation,[122, 123] quaternization,[124, 125] among others. Among them, enzymatic or acid hydrolysis is intended to break down the big fibers into

small pieces, meanwhile swelling the cellulose fibers. The other pretreatment approaches are designed to introduce surface charges onto the cellulose fibers. The negative or positive charges on the surface of cellulose fibers could reduce energy input needed for fibrillation by electrostatic repulsion and to enhance colloidal stability of the final CNFs [104]. For example, a large amount of negative carboxyl groups could be introduced on the cellulose pulp by TEMPO oxidation, which can selectively oxidize the cellulose C6 hydroxyls to carboxylates [126-128], the mechanism of oxidation reaction is as shown in **Fig. 1-9b**. After mild mechanical disintegration, transparent and gel-like CNF suspension could be obtained. Also, the mechanical energy consumption after TEMPO oxidation was significantly reduced from 70 MWh/t (without pretreatment) to 1-10 MWh/t. Chaker and Boufi [108] demonstrated another strategy by introducing positive quaternary trimethylammonium groups on the surface of cellulose fiber to increase the electrostatic repulsion and finally enhanced the fibrillation efficiency, as shown in **Fig. 1-9c**. Saini et al.[125] evaluated that the energy consumption at fibrillation stage could be reduced by five times by using this cationic modification pretreatment. More interestingly, the introduced cationic groups endowed the final CNFs with antibacterial properties, which could be applied into food packaging and biomedical applications. Nevertheless, the above conventional pretreatment methods still face several deficiencies such as high cost of enzymes and chemicals, time-consuming process, difficulty to recover chemicals and environmental issues.[112] Thus, it is of critical importance to develop more cost effective, sustainable and environmental benign pretreatment methodology for the preparation of high-quality CNFs.

1.4.3 Application of cellulose nanofibrils

When compared to CNFs, the self-assembled nanostructure (e.g., film, aerogel) of CNCs is very brittle due to the lack of an energy-dissipating amorphous phase and its inability to form entangled networks.[129] Also, the large-scale production for CNCs is still limited to the method by sulfuric acid hydrolysis which involves serious environmental challenge and high production cost.[130] Thus, considering mechanical performance, environmental aspects and economics, the focus of this work is on high-performance nanomaterials derived from CNFs for multifunctional applications. It is reported that the Young's modulus and tensile strength of individual CNFs is in the range of 29-36 GPa and 2-6 GPa, respectively, which is comparable to those of commercial multiwalled carbon nanotubes, yet with much lower price.[131] More importantly, the density of CNFs is in the range of 1.32-1.58 g/cm^3, far lower than traditional engineering materials (e.g., mass density of steel ~7.78 g/cm^3).[129] This puts CNFs in a highly attractive place in an Ashby plot (**Fig. 1-10a**), surpassing traditional materials like metals, concrete, glasses and ceramics. Such outstanding properties of CNFs make them an attractive building block for strong and light structural materials.

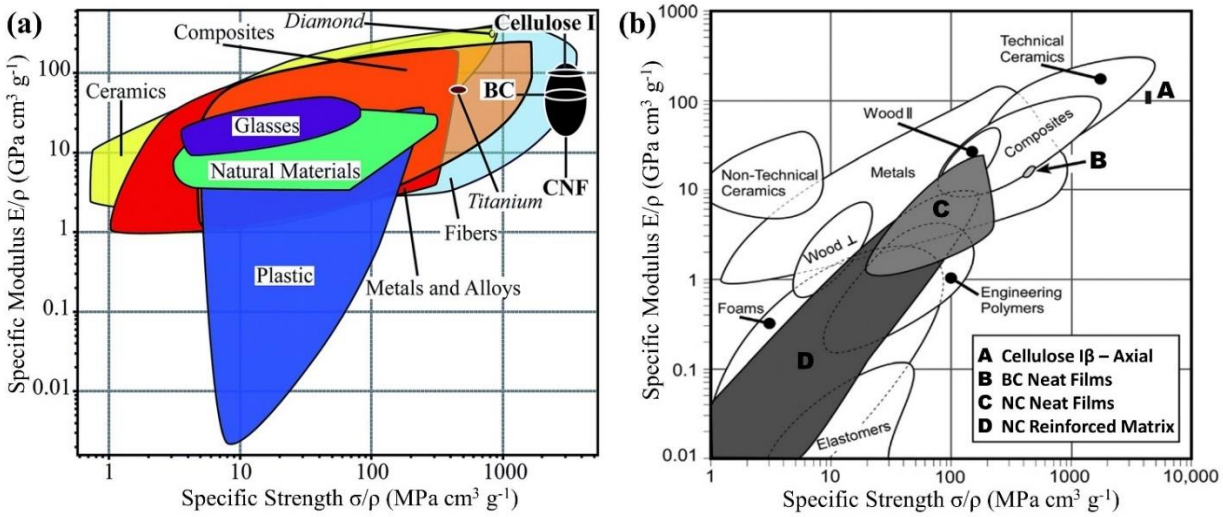

Figure 1-10. (a) Comparison of the specific modulus and specific strength of CNFs, bacterial cellulose (BC) and Cellulose I against a wide range of materials.[129] (b) Comparison of the specific stiffness and specific strength of nanocellulose (NC) neat films, BC neat films and NC reinforced matrix against other traditional materials.[57]

As summarized in **Fig.1-11**, CNFs exhibit remarkable tendency to form three-dimensionally entangled networks suitable to fabricate high-performance nanomaterials such as cellulose nanopaper (CNP), hydrogel, and aerogel, due to the high aspect ratio and semi-crystalline structure.[80]

Figure 1-11. Examples of the self-assembled structures of CNFs and their potential applications. The images of nanopapers are adapted from refs.[132, 133] The image of 3D-printed hydrogel is adapted from ref.[134] The images of aerogel are adapted from refs.[135, 136] The other images are adapted from www.google.com.

1.4.3.1 Cellulose nanopaper

CNP is usually prepared from CNF suspension by a self-assembly process in which the solvent is removed and the CNFs finally form the CNP.[129] As illustrated in **Fig. 1-12**, casting and filtration are two popular approaches for CNP production.[137] Among them, casting is a simple but time-consuming process, by which CNF suspension is usually kept in an open Petri dish, and the solvent is allowed to evaporate, finally leaving the self-assembled CNP.[138] Normally, a slow drying rate is necessary to reduce wrinkling problem and make flat, and uniform CNP.[139] This process usually takes several days to obtain final CNP. Filtration, which is similar to a papermaking process, is a relatively fast method to prepare CNP. Typically, filtration process involves two separate

operations: (a) filtration of CNF suspension under vacuum or pressure and (b) drying (e.g. air-drying, oven-drying, hot-pressing) of thus obtained CNF gels.[140, 141] The total time of filtration process is reported to be a few hours instead of days, which is much faster than the casting method. As shown in **Fig. 1-10b**, when compared to single CNFs, both specific modulus and strength of self-assembled CNP are lower, but it still surpasses most engineering polymers, and comparable to some metals.[57] Recent works have shown that CNP is a promising material for use in photovoltaic cells,[142] as visual display substrate,[143] energy storage electrode material,[144] etc., in light of its good thermal stability, low coefficient of thermal expansion (<10 ppm/K) and tunable optical properties besides renewability and superior mechanical properties.[145, 146]

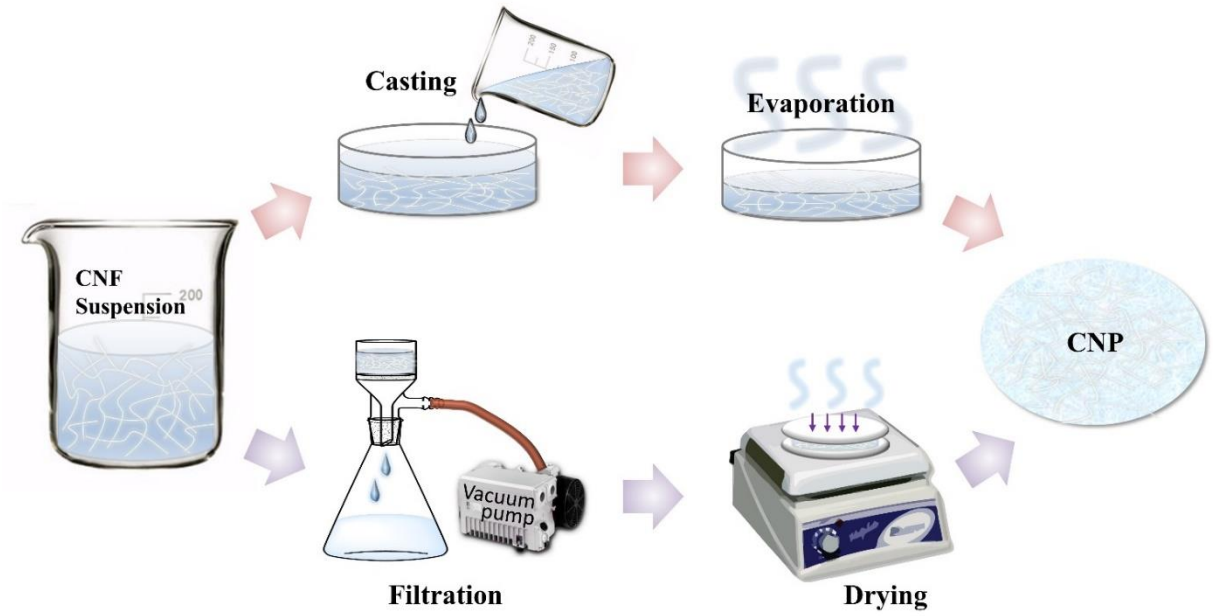

Figure 1-12. Schematic of casting and filtration methods for the preparation of cellulose nanopaper (CNP).

1.4.3.2 Hydrogel and aerogel

Other than CNP, CNFs could form mechanically stable self-assembled hydrogels via specific cross-linking strategy (e.g., metal cation cross-linking). For instance, Dong and co-workers[147] reported the hydrogelation of TEMPO oxidized CNFs with different kinds of metal cations (e.g. Ca^{2+}, Zn^{2+}, Cu^{2+}, Al^{3+} and Fe^{3+}). They found that the storage moduli of the fabricated hydrogels were strongly related to valency of the metal cations and their binding strength with carboxylate groups on the CNFs. The driving force of crosslinking was proposed to be a screening effect of the repulsive potentials on the CNFs surfaces by strong metal-carboxylate bonding. Moreover, CNFs can be used as reinforcing agents for polymeric hydrogel networks by physical or chemical strategies to prepare composite hydrogels with enhanced mechanical property. Up to now, different kinds of methods include straightforward mixing, cyclic freeze-thaw processing, free radical polymerization, UV/ion mediated cross-linking, and 3D printing have been exploited for incorporating CNFs into various types of network polymers such as poly(vinyl alcohol) (PVA), polyacrylamides, poly(ethylene glycol), as well as some kinds of natural polymers (e.g. alginate, gelatin).[80] In general, aerogels are porous materials with low density and large specific surface area which usually prepared by replacing the solvent of the hydrogels with gas with very moderate shrinkage of the hydrogel solid network. Thus, CNFs based hydrogels can be further converted to CNFs based aerogels by replacing water with air through freeze-drying or supercritical drying. Due to the high surface area, controllable porosity and good biocompatibility, CNFs based hydrogels and aerogels can be used for a variety of applications such as sensors,[148] energy storage devices,[149] biomedical implants,[83] etc.

1.4.3.3 Rheology modifier and reinforcing agent

In addition, CNFs can bind water strongly and their suspensions in aqueous medium usually exhibit high viscosity at a low solid content (e.g., 0.5-3.0%). In general, CNFs suspensions exhibit shear-thinning behavior, i.e., breakdown or change of the viscoelastic structure of the suspensions induced by shear force.[150] Due to this unique thixotropic behavior, CNFs have been widely used as the rheology modifier in the fields of cosmetics, food additives, drilling fluids, and paper coatings. Moreover, CNFs have been proven as promising reinforcing agent (i.e. nanofillers) for a variety of polymers such as polyethylene, polypropylene, polyamides, poly(lactic acid), and polycaprolactone.[151] For example, a Nano Cellulose Vehicle (NCV) was developed by a consortium headed by Kyoto University in 2019. The NCV was designed towards better sustainability and lightweight manufacturing by using CNFs reinforced resins or plastics to replace traditional metals. The CNFs reinforced nanocomposites are up to 5 times stronger yet 1/5 of the weight of conventional steel panels. It is reported that most of the bodywork and a significant part of the tub can be crafted from the CNFs reinforced nanocomposites. Eventually, the NCV can achieve 10% total weight savings and significant reduction of CO_2 emissions when compared to the conventional vehicle. However, due to the high hydrophilicity of CNFs and the hydrophobicity of most aforementioned polymers, compatibility between CNFs and polymer matrices is the main challenge so far.[152] In order to solve this problem, different standalone surface treatments, such as grafting with monomers, silylation, surfactants, acetylation, and esterification have been applied to CNFs to decrease its hydrophilicity to facilitate better dispersion in polymer matrices.[153] Such modifications are, however, tedious and often involve hazardous chemicals and impractical solvent-exchange protocols.[145] In this regard, developing one-pot synthesis approach to produce hydrophobicity CNFs or green and facile modification methodology is highly desirable.

1.5 Conducting polymers

For a long time, synthetic polymers such as plastics, rubber, and resins have been considered to be non-conductive and have been widely used as insulating materials in our daily life. However, the fact that polymers do not conduct electricity was changed by scientists in the late 1970s. In 1974, a visiting scientist in Hideki Shirakawa's laboratory at University of Tsukuba (Japan) mistakenly added too much Ziegler-Natta catalyst (1,000 times the conventional amount) when he or she synthesized polyacetylene (PA). Eventually, a glittering and silvery PA film was obtained rather than the anticipated black powder. By chance, the shining PA film caught the eyes of Alan G. MacDiarmid in the tea break after a lecture at Tokyo Institute of Technology. Later on, Hideki Shirakawa was invited by Alan G. MacDiarmid to the University of Pennsylvania to study this fascinating PA film, where Alan J. Heeger, an expert in physics, joined this project as well.[154] In 1977, it was reported for the first time that the conductivity of the AsF_5-doped PA film can reach as high as 560 S/cm. In addition, the conductivity of the PA film can be tuned over the full range from insulator to semiconductor to metal by changing the types and amounts of dopants (e.g., chlorine, bromine, iodine, and AsF_5).[155, 156]

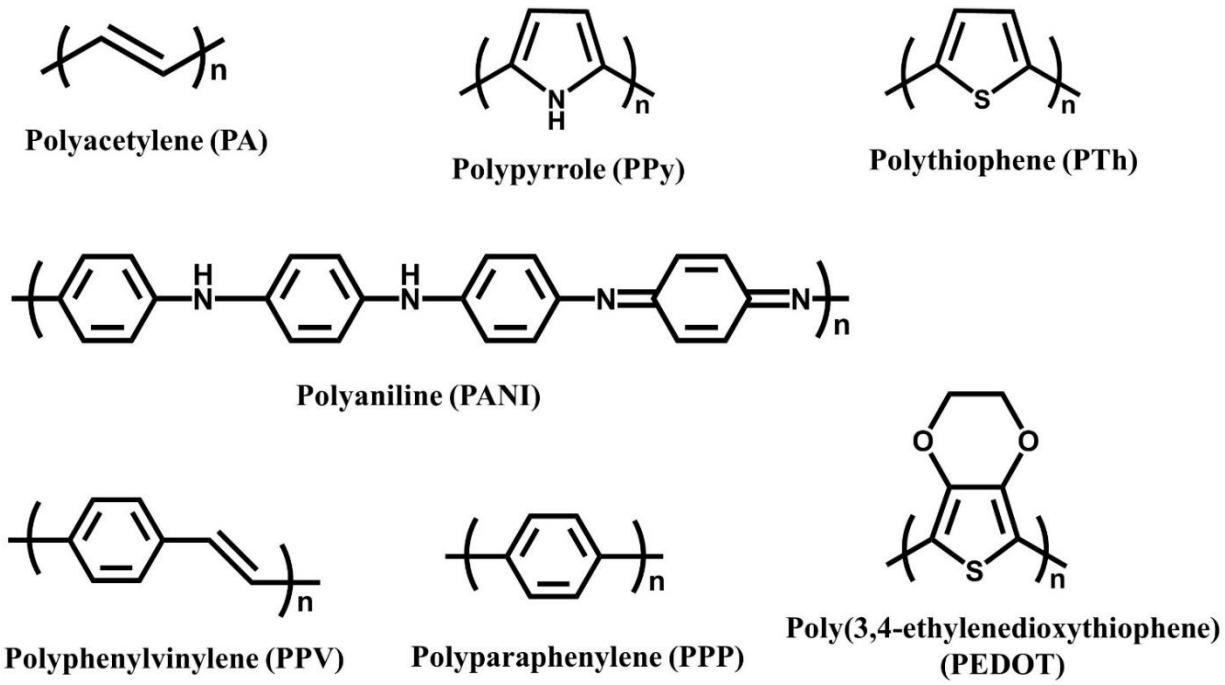

Figure 1-13. Chemical structures of repeat unit in various conducting polymers.

Since then, as shown in Figure 1-13, a variety of intrinsically conducting polymers (ICPs), also called electrically conducting polymers or synthetic metals, such as polyaniline (PANI), polypyrrole (PPy), polythiophene (PTh), poly(3,4-ethylenedioxythiophene):poly(styrene sulfonate) (PEDOT:PSS) have been developed, which initiated an interesting field of research.[157] In 2000, Alan G. MacDiarmid, Alan J. Heeger, and Hideki Shirakawa received the Nobel Prize in Chemistry for the discovery and development of ICPs.

In addition to ICPs, there are two other types of conducting polymers including conductive filler composites and ionically conducting polymers. Basically, conductive filler composites are consisted of conductive fillers such as metal or carbon and insulating polymer matrix, in which the conductive fillers form a connected network throughout the polymer matrix.[158] In order to achieve electrical conductivity, the conductive fillers must be present at a certain concentration, known as

percolation threshold. Normally, high aspect ratio fillers such as nanofibers are prone to achieve higher conductivity at a lower threshold, as they are able to span larger distances through the polymer matrix at the same weight when compared to their granular counterparts.[159] The conductive filler composites have been widely used in diverse fields such as conducting adhesives, printed circuit boards, aircrafts and spacecrafts, and so forth. In general, ionically conducting polymers, often named as polymer electrolytes, are composed of polymer matrix (e.g. polyethylene glycol), high-dielectric solvent or plasticizer, and inorganic salts, forming a mechanically stable polymer network with the electrolytes entrapped in the polymer matrix.[160] The conductivity is derived from the transport of ions along and between the polymer chains and can be adjusted by varying the relative proportions of each component.[161] Due to the advantages of flexibility, shape versatility, and easy processability, ionically conducting polymers exhibit great potential for applications such as fuel cells, supercapacitors, batteries, actuators, sensors, and flexible electronics.[160] In this thesis, we mainly focus on the design and application of ICPs. The structure, conduction mechanism, synthesis, and application of ICPs will be discussed in detail in the following sections.

1.5.1 Conduction mechanism of ICPs

1.5.1.1 Molecular structure

The electrical and electrochemical properties of ICPs are mainly attributed to their unique molecular structure. In order to understand the phenomenon of electrical conductivity in ICPs, fundamental insights into the electronic configuration of molecules are necessary. Carbon is the most important element in ICPs. As illustrated in Figs 1-14a and 1-14b, a carbon atom contains six electrons which occupy in the ground state following the electronic configuration:

$(1s)^2(2s)^2(2p_x)^1(2p_y)^1$.[162] In this ground state configuration, there are two unpaired electrons in the outer shell which are expected to establish two covalent bonds to other atoms in a molecule. However, this is not going to occur in nature. In fact, experimental results proved that carbon atom has a binding ability for four electrons through hybridization, i.e., carbon atom forms hybrid orbitals. As depicted in **Fig. 1-14c**, one of the electrons in 2s orbital can be easily excited into the third empty 2p orbital because of the small energy difference between 2s and the 2p orbitals. For example, the energy difference can be overcome in the presence of an external perturbation, such as a nearby hydrogen atom.[163] Therefore, a mixed state consisted of one 2s orbital and three 2p orbitals can be produced. Further, three possible hybrid orbitals can be formed, they are sp^3, sp^2, and sp hybrid orbitals. In the case of sp^3 hybrid orbitals, the 2s and all the three 2p orbitals participate in hybridization, resulting in four equivalent sp^3 hybrid orbitals. The sp^3 hybrid orbitals look somehow like asymmetric dumbbells and arrange in a tetrahedral geometry, as illustrated in **Fig. 1-14d**. Each of the four hybrid orbitals occupied with one electron is able to establish one covalent bond to the neighboring atoms, forming one σ bond. For example, methane (CH_4) is the simplest hydrocarbons following sp^3 hybridization. In addition to methane, the carbon atoms in all the alkanes have sp^3 hybridization. Moving on to sp^2 hybridization, the 2s and two of the three 2p orbitals participate in hybridization, leading to three sp^2 hybrid orbitals which also look like asymmetric dumbbells. As shown in **Fig. 1-14e**, the resulting three sp^2 hybrid orbitals arrange in a trigonal planar geometry which is in the same plane. The unhybridized 2p orbital (usually denoted as $2p_z$) is perpendicular to the hybridized plane. Ethylene is a typical example to illustrate the sp^2 hybridization of carbon in a molecule.

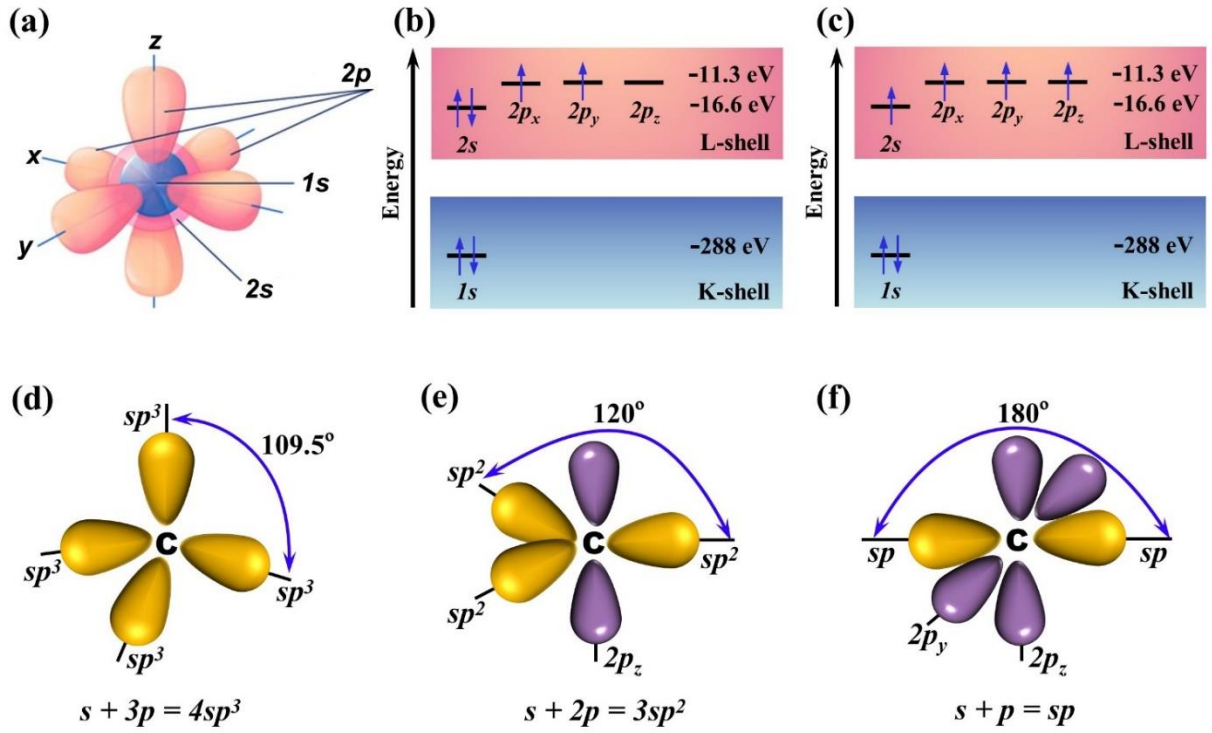

Figure 1-14. Schematic illustrations of electronic structure of carbon atom showing the electronic density distribution of s and p orbitals (a), electronic configuration of carbon atom in the ground state (b) and in the excited state (c). Note: the energy levels show inverted values of the electron binding energies, the images are adapted from ref.[162] Schematic representation of three types of hybridization of carbon, including sp^3 (d), sp^2 (e), and sp (f) hybridization.

As displayed in **Fig. 1-15a**, two sp^2 hybridized carbon atoms can form a C-C σ bond by overlapping one of the three sp^2 orbitals. Each of the remaining four sp^2 hybrid orbitals can make sigma bonds with hydrogen by sp^2-s overlap. The left-out two unhybridized and side-by-side $2p_z$ orbitals are perpendicular to the plane of the hybrid orbitals. Since each of the $2p_z$ orbitals contains one valence electron and both of which are in the bonding molecular orbital, an additional bond called π bond can be formed between the two carbon atoms. As a consequence, a double bond formed between the carbon atoms in ethylene molecule. Besides of ethylene, all the alkenes are double-bonded. In each double bond, there is one σ bond formed by overlapping sp^2 hybrid orbitals and one π bond resulting from the overlap of the $2p_z$ orbitals. As for the sp hybridization, only one out of the three

2p orbitals mixes with the 2s orbital, resulting in two sp hybrid orbitals. Acetylene can be a typical example, in which two sp hybridized carbon atoms arrange in a linear geometry and the four unhybridized 2p orbitals are placed at 90º. Similar to the 2p orbitals in sp^2 configuration, these four unhybridized 2p orbitals can form two π bonds between the two carbon atoms. Thus, a triple bond can be formed between the two carbon atoms in acetylene molecule.

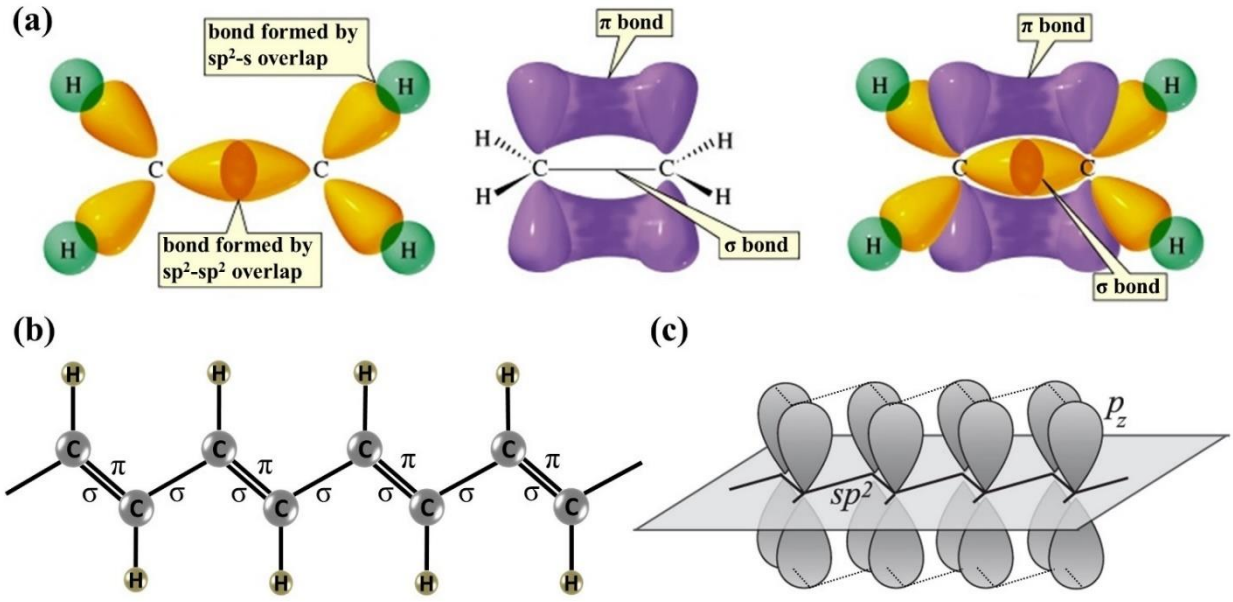

Figure 1-15. (a) Schematic illustration of sigma and pi bond hybridization for ethylene showing de-localized pi-electrons. The images are adapted from ref.[164] (b) The chemical structure of trans-polyacetylene showing alternating single and double bonds, and the corresponding 3D configuration showing hybrid sp^2 and $2p_z$ orbitals and conjugated π bonds (c). The images are adapted from ref.[165]

1.5.1.2 Conjugated Double Bonds

Based on the hybridization phenomenon in molecular structure discussed above, all the electrons are localized in the bonds between two atoms. However, the charge carriers like electrons or holes can be delocalized and mobile in the molecules under certain conditions in the case of sp^2

hybridization. Take 1,3-butadiene (CH_2=CH–CH=CH_2) as an example, there four sp^2 hybridized carbon atoms in the molecule, showing an alternation of single and double bond namely conjugated double bond. From the chemical structure of 1,3-butadiene, we can see that there is a double bond formed between the first (C1) and second (C2) carbon atoms due to the overlapping of the $2p_z$ orbitals. Likewise, a double bond can be formed between the third (C3) and fourth (C4) carbon atoms following the same rule. By contrast, there is only a single bond formed between C2 and C3, which is because that there is supposed to be no interaction between the $2p_z$ orbitals of the C2 and C3. However, all these four $2p_z$ orbitals interact with each other in reality. The experiments have proved that the bond length between C1 and C2, C3 and C4 is around 134 pm, which is similar to that of the normal C=C double bond. Interestingly, the bond length between C2 and C3 is approximately 147 pm, which is much longer than the normal double bond and obviously shorter than a normal C-C single bond (154 pm).[166] This phenomenon is mainly due to the delocalization of the π-electrons along the carbon chain. The delocalization of the π-electrons is the foundation of electrical conductivity of ICPs.

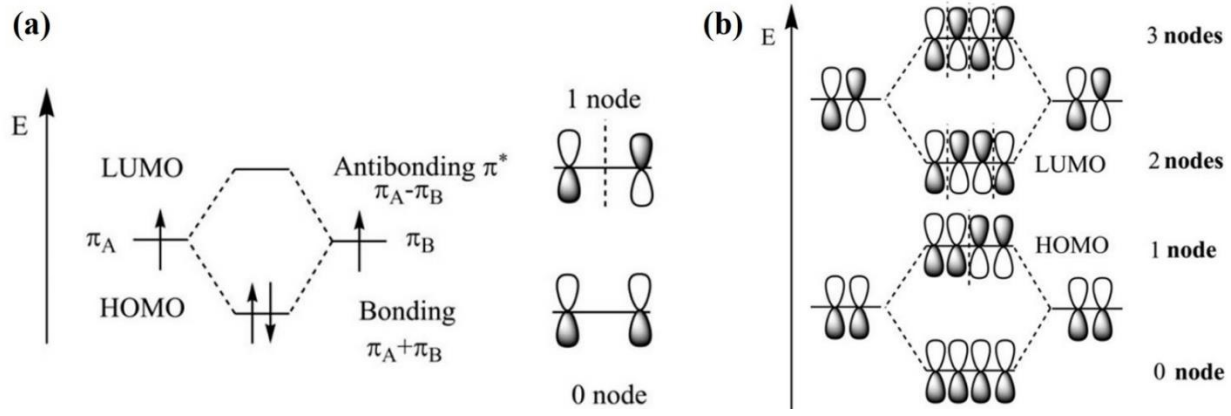

Figure 1-16. (a) HOMO/LUMO diagram and wave functions of π-electrons for ethylene. (b) Wave functions of π-electrons for 1,3-butadiene. (the diagrams are adapted from http://cleanenergywiki.org/index.php?title=The_Polyene_Series)

Basically, the overlap of two atomic orbitals will lead to the formation of two molecular orbitals. As illustrated in **Fig. 1-16a**, when the $2p_z$ orbital overlaps with the other in the ethylene molecule, two molecular orbitals including a bonding orbital and an antibonding orbital can be formed. Considering the wave function of π-electrons, the positive combination (0 nodes) results in the formation of a bonding molecular orbital with the highest occupied molecular orbital (HOMO). In contrast, the negative combination (1 nodes) leads to an antibonding orbital corresponds to the lowest unoccupied molecular orbital (LUMO). As shown in **Fig. 1-17**, the energy difference between π_{HOMO} and π^*_{LUMO} of ethylene is 6.7 eV. In the case of 1,3-butadiene molecule, which can be considered as the combination of two ethylene sub-units, four molecular orbitals including two bonding and two antibonding can be formed. Based on the wave functions illustrated in **Fig. 1-16b**, the positive combination leads to the formation of two bonding orbitals, in which one is more stable (0 node) and the other one is less stable (1 node) when compared with the π_{HOMO} in ethylene. Similarly, the antibonding orbitals include a relatively lower energy level (2 nodes) and a higher energy level (3 nodes), compared to the π^*_{LUMO} of ethylene. As a consequence, the energy difference between π_{HOMO} and π^*_{LUMO} of 1,3-butadiene decreased to 5.4 eV. As the number of carbon atoms increase, the energy difference between π_{HOMO} and π^*_{LUMO} becomes smaller and smaller. Eventually, an energy difference of around 1.5 eV can be achieved, which brings the trans-polyacetylene in the semiconducting range (bandgap from 0.25 to 2.5 eV). As illustrated in **Figs. 1-15b** and **1-15c**, the $2p_z$ orbitals of the π-bonds within the trans-PA molecule overlap continuously and the π-electrons are able to move along the carbon skeleton. Thus, the unique conjugated double bonds of trans-PA allow electric flow.[167]

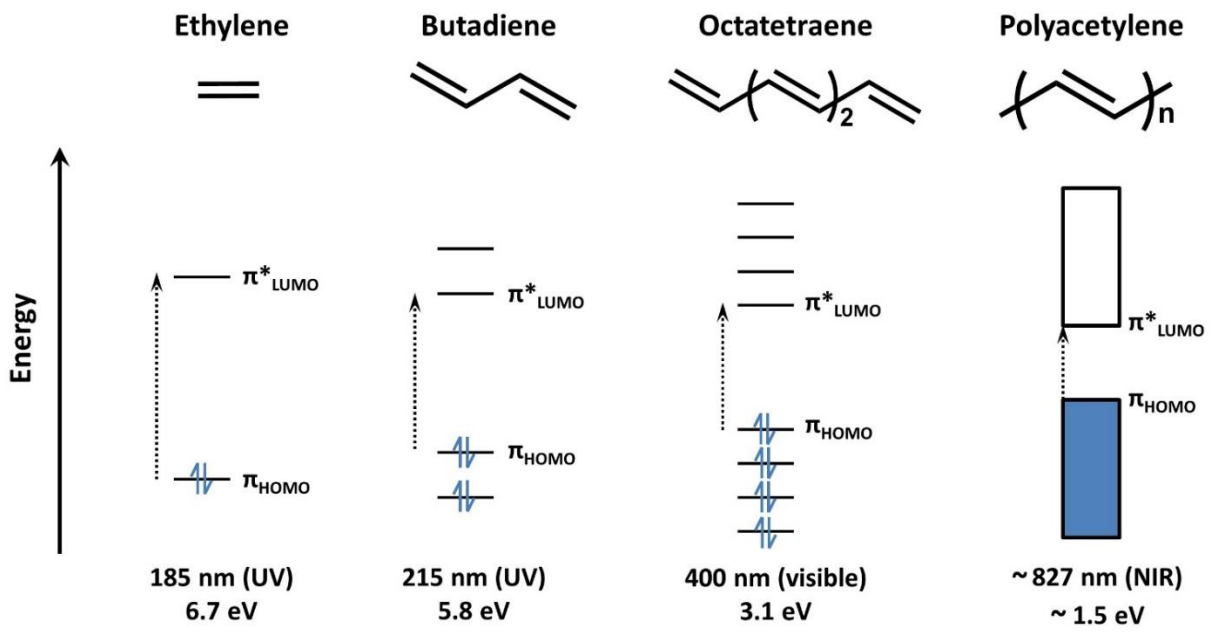

Figure 1-17. Schematic of energy-level splitting and absorption in alkenes with increasing conjugation length. Note: the bandgap of polyacetylene depends on both the degree of polymerization and the effective conjugation length. https://www.oe.phy.cam.ac.uk/research/materials/osemiconductors

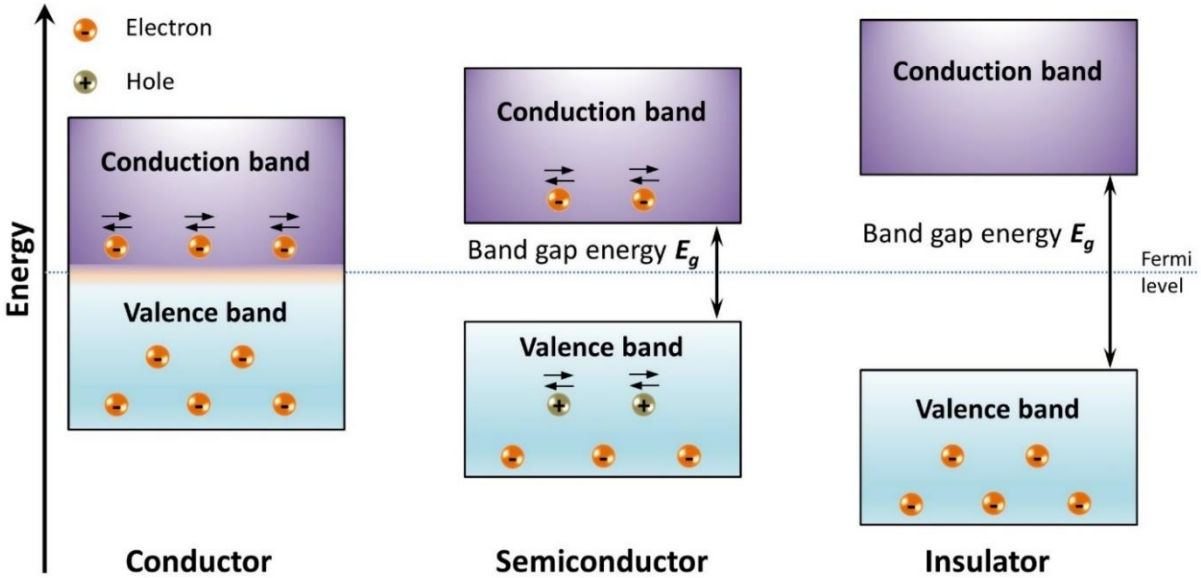

Figure 1-18. Energy bands of electrons in conductor, semiconductor and insulator. The images are adapted from ref.[168]

In solid state physics, the concept of energy bands has been widely used to explain the electrical conductivity of solids. The HOMO levels constitute the valence band (VB), and the LUMO levels refer to the conduction band (CB). The width of the forbidden band, also called band gap energy, between the VB and CB determines the intrinsic electrical properties of the solids.[168] As shown in **Fig. 1-18**, materials can be classified as conductor, semiconductor, and insulator based on the band gap energy. It is reported that the energy bands can be appropriately used for conjugated polymers with sufficiently large number of carbon atoms, including most of the ICPs such as PA, PPy, PANI, PEDOT, etc.[169]

Table 1-2. Summary of the band gap energy and the maximum conductivity of different ICPs at the doped states.[170, 171]

ICPs	Band gap energy (eV)	Type of doping	Maximum conductivity (S/cm)
PA	1.5	n, p	200-100000
PTh	2.1	p	10-100
PANI	3.2	p	10-1000
PPy	3.1	p	10-75000
PEDOT	1.1	p	10-10000
PPV	2.5	p	3000-5000

Note: the maximum conductivity is for the doped forms of the ICPs.

Table 1-2 summarizes the band gap of different kinds of ICPs, as well as the maximum conductivity of their doped forms. As mentioned earlier, the trans-PA behaves like a semiconductor at the undoped state. Depending on the band gap energy, some ICPs such as PPy

and PANI with higher band gap energy are insulating at the undoped state. Intriguingly, the conductivity of ICPs can be significantly regulated by a doping process through chemical or electrochemical oxidation or reduction.

1.5.1.3 Doping process

In solid-state physics terminology, replacing part of atoms in a host lattice with dopant atoms with less valence electrons will introduce additional holes (excess charges), this process is called p-type doping. Conversely, if the dopant atoms with more valence electrons are introduced to the host lattice, additional electrons are provided, leading to the n-type doping.[172] Similarly, doping process for ICPs also includes p-type doping and n-type doping, yet following a different mechanism from the inorganic semiconductors. More specifically, the doping process of ICPs can be viewed as a redox reaction, i.e., the neutral polymer can be converted into an ionic complex which is consisted of a polymeric cation or anion and a counterion that originated from the reduced form of the oxidizing agent or the oxidized form of the reducing agent.[171] The charge carriers can be created during the redox reaction in the form of polarons, bipolarons, or solitons in the polymers. These charge carriers can be delocalized along the polymer chains with good mobility, which significantly facilities the electrical conductivity. Chemical doping has been widely used to alter the electrical conductivity of ICPs. For the p-type doping, also known as oxidative doping, the polymer is chemically treated with an oxidizing agent which possesses electron withdrawing groups, and the electricity is conducted predominantly through hole transport. While for the n-type doping, also known as reductive doping, the polymer is treated by a reducing agent with electron donating groups, leading to electron conductors. Take polyacetylene $(C_2H_2)_n$ as an example, p-type doping and n-type doing can be written as:

p-doping (oxidation with iodine) $(C_2H_2)_n + \frac{3}{2} I_2 \rightarrow (C_2H_2)_n^+ + I_3^-$

n-doping (reduction with alkali metal) $(C_2H_2)_n + Na \rightarrow (C_2H_2)_n^- + Na^+$

In addition, the doping can be achieved by applying positive or negative potential to the polymers in some specific electrolytes, which called electrochemical doping. Compared to the chemical doping, electrochemical doping is more cost-effective with less safety issues, since most of oxidizing or reducing agents are not only costly but also harmful to human body.[173] Moreover, the doping levels can be readily regulated by controlling the electrochemical parameters such as potential or current density. As indicated in **Fig. 1-19**, the electrical conductivity of ICPs can be controlled by orders of magnitude ranging from 10^{-10} (insulator) to 10^5 S.cm^{-1} (metal) by tuning the density and mobility of charge carriers in the doping process. In the following sections, the mechanism of doping process for enhancing the electrical conductivity of ICPs will be illustrated from the point of view of band gap theory.

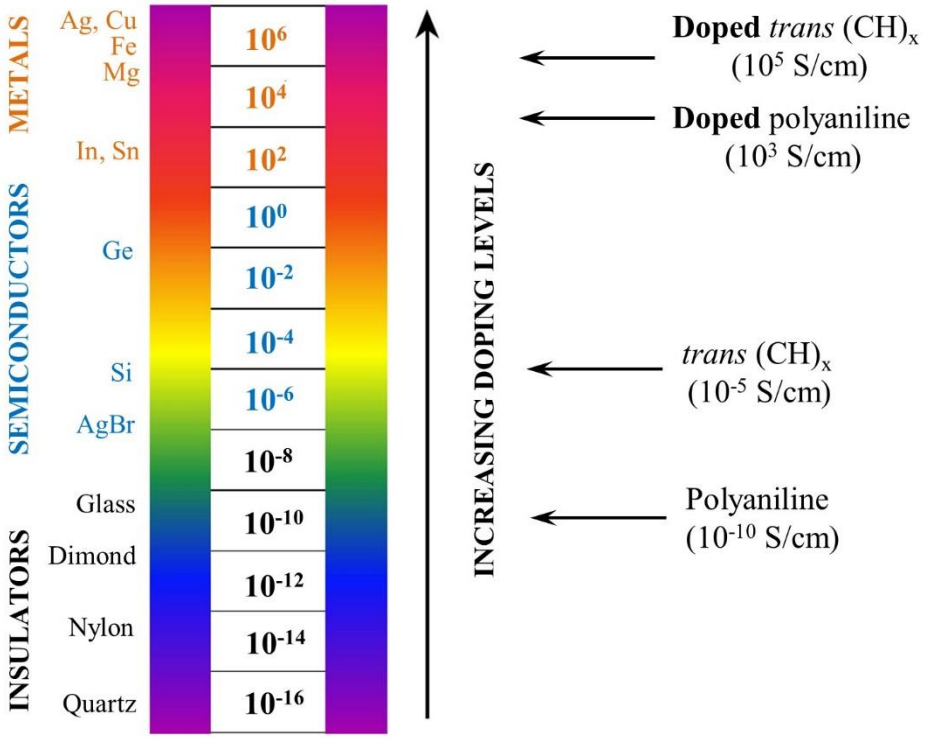

Figure 1-19. Chart showing the conductivity (S/cm) of metal, semiconductor and insulator, as well as polyaniline and *trans* polyacetylene $(CH)_x$ before and after doping. The image is adapted from ref.[174]

Depending on the bond structures in the ground state, ICPs can be divided into two categories: degenerate and non-degenerate systems, in which the degenerate ICP has two identical geometric structures in the ground state while the non-degenerate ICPs possess two different ground state with different energies. As shown in **Fig. 1-20a**, trans-PA is a unique ICP due to its degenerate ground state, i.e. two geometric structures (phase A and phase B) have the same energy. When the trans-PA contains an odd number of carbons, there will be an unpaired π electron (a radical) between A and B phases, which refers to a neutral soliton (**Fig. 1-20a**). Normally, the neutral solitons are not stable since they can move along the polymer chain and can be destroyed by forming a double bond when meet with one another. Also, there are very limited number of neutral

solitons in the ground state, this accounts for the low conductivity (10^{-5} S/cm) of undoped trans-PA. Importantly, the neutral solitons (**Fig. 1-20b**) can be oxidized or reduced to form positive solitons (**Fig. 1-20c**) or negative solitons (**Fig. 1-20d**) upon doping. **Fig. 1-20e** illustrates the formation of two positively charged solitons on the trans-PA chain. From **Figs. 1-20b** to **1-20d**, we can see that compared to the neutral solitons, both the positive and negative solitons have no unpaired spin, which make them more stable as they can be delocalized along the polymer chain without any possibility of being destroyed by forming a chemical bond. Since the π-electrons in the trans-PA are able to travel over a long distance, the regions of individual charged solitons can overlap. Eventually, the interaction between charged solitons results in a band-like feature called the soliton band.[167] As shown in **Figs. 1-20f** and **1-20g**, a soliton band can be formed between the HUMO and LUMO levels and a higher doping level will lead to a wider soliton band.

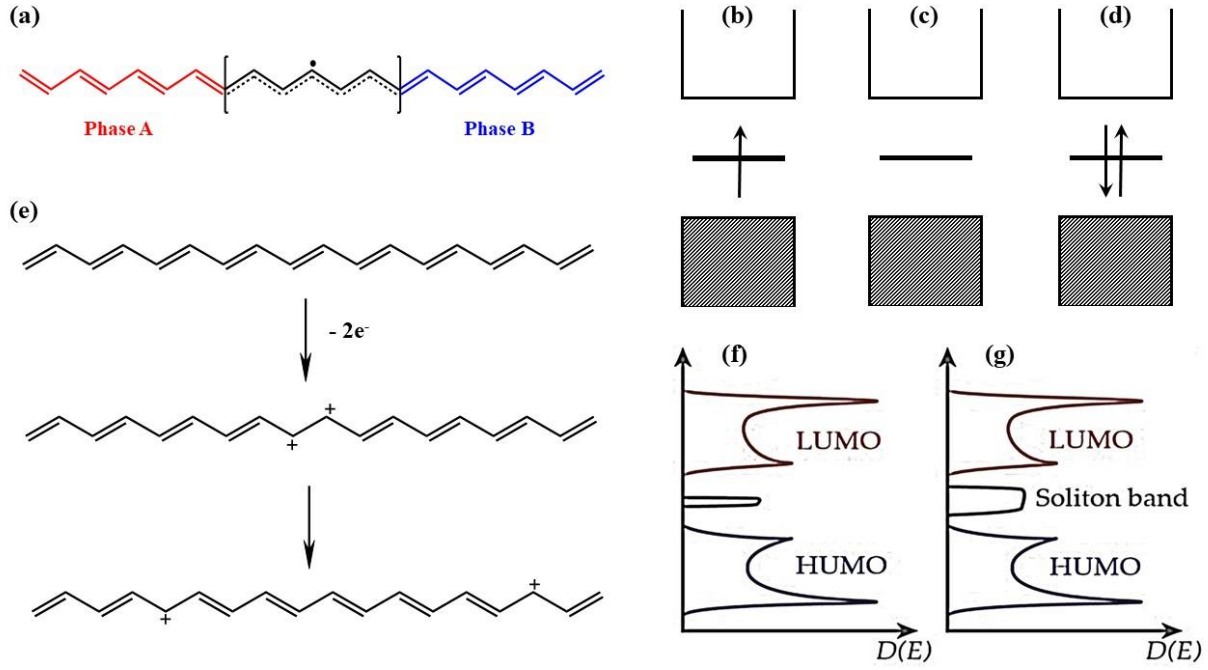

Figure 1-20. (a) Schematic illustration of the geometric structure of a neutral soliton on a trans-PA chain. Band structure of trans-PA containing a neutral soliton (b), a positively charged soliton (c), and a negatively charged soliton (c). Schematic illustration of the formation of two positively charged solitons on a trans-PA chain (e). Illustration of the formation of a soliton band with high doping level (f) and high doping level (g). The images are adapted from ref.[167, 171]

To summary, there are two prerequisites need to be satisfied to make sure a polymer can efficiently conduct electricity: 1) the polymer backbone has conjugated double bonds which enable the π-electrons to be delocalized along the polymer chain. 2) the charge carriers in the form of holes or electrons need to be created by the doping process which are able to travel along the polymer backbone. Briefly, the charge carriers are able to move along the conjugated polymer backbone with uninterrupted path, thus electrical conductivity can be achieved. In addition, the charge carriers not only travel along the polymer chains but also jump from one chain to another. The later phenomenon has been descripted as interchain hopping. Obviously, the hopping process is the rate-limiting step which determines the macroscopic electrical conductivity.[171] Therefore, in

order to achieve high electrical conductivity, tightly packed polymer chains are desired to avoid any obstacle in charge transport in the interchain hopping process.

1.5.2 Synthesis of ICPs

Generally, ICPs can be synthesized by two main approaches: chemical polymerization and electrochemical polymerization. In the chemical polymerization process, ICPs are synthesized by oxidizing the monomer by some specific oxidizing agents (e.g., ammonium persulfate, ferric chloride) in the presence of suitable counterions (as dopants). For the electrochemical polymerization, the ICPs can be directly polymerized on the conductive substrate by applying a suitable potential or current in the electrolytes (as dopants). In general, chemical polymerization is used to produce large quantity of ICPs. However, the as-prepared ICPs is always contaminated with the oxidants which need further purification. Compared with chemical polymerization, the properties of ICPs can be easily controlled by the changing the potential or current density, and polymerization time. Also, the polymer synthesized by electrochemical polymerization is free from oxidant impurity. For both the chemical and electrochemical polymerization, there are two main steps: 1) oxidation of monomer and 2) polymer chain growth.

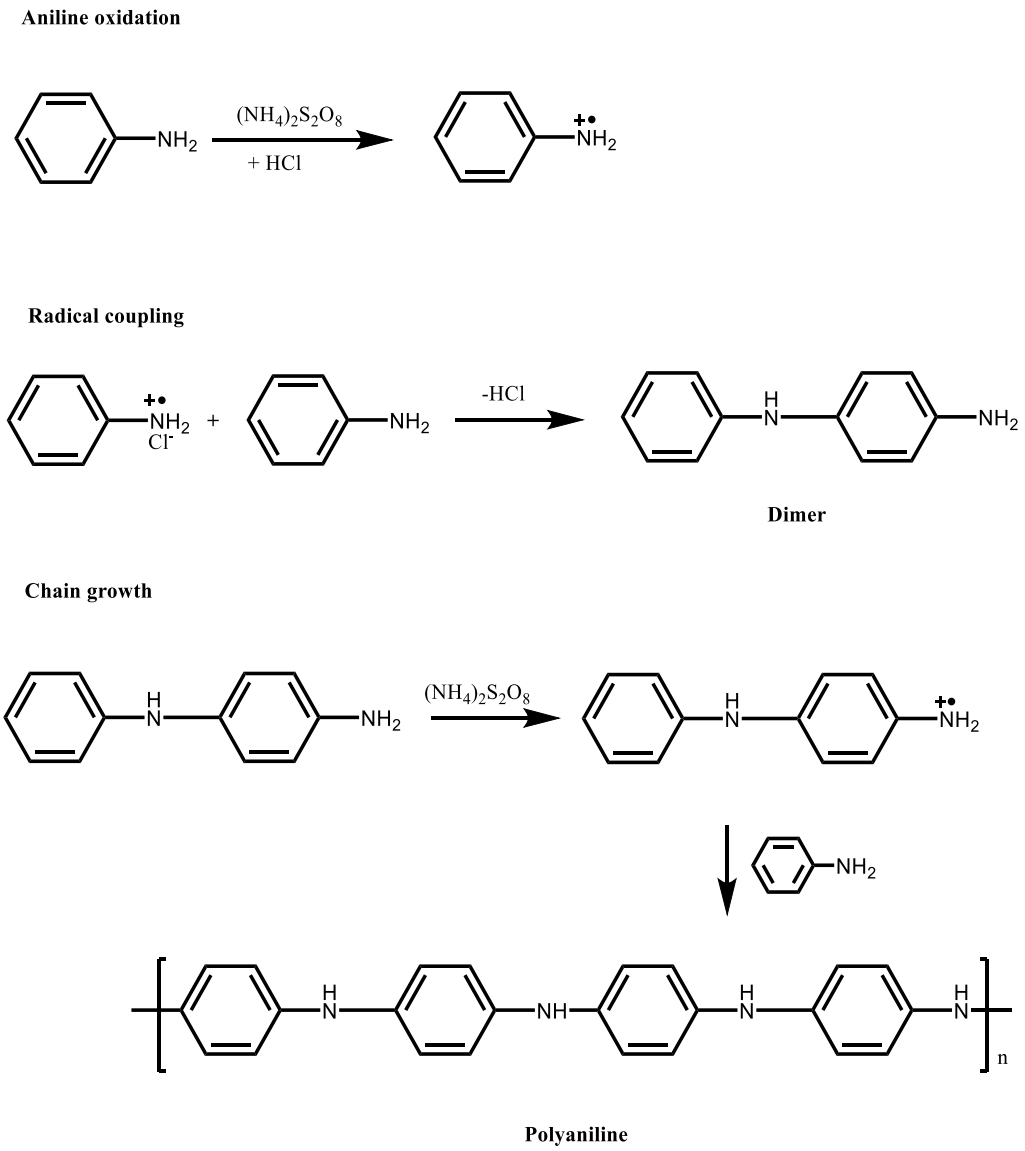

Figure 1-21. Scheme of the chemical oxidative polymerization of aniline.

As shown in **Fig. 1-21**, the chemical polymerization of aniline is taken as an example. Firstly, the oxidant (ammonium persulfate) takes an electron from monomer and forms a monomer cation radical. Then, the monomer cation radical couples with another monomer unit to form a dimer. This process will continue and finally lead to polymer chain growth until all the reagents are consumed or reached equilibrium.

1.5.3 Application of ICPs

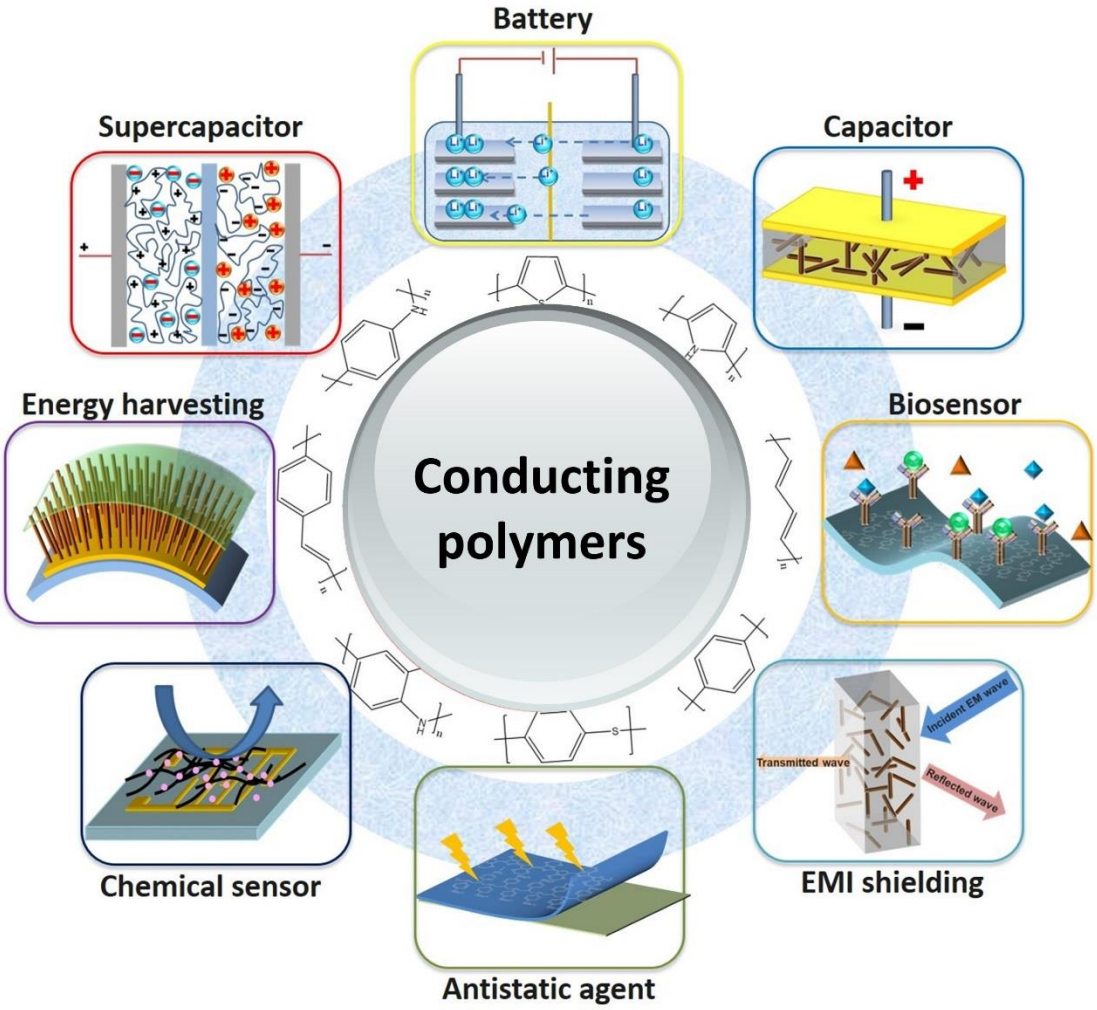

Figure 1-22. Potential applications of conducting polymers. The images are adapted from ref.[175]

During the past few decades, ICPs have been under intensive research and development in both academia and industry worldwide. As summarized in **Fig. 1-22**, ICPs have been widely used in variety of applications including energy harvesting and storage (e.g. solar cells, fuel cells, batteries, supercapacitors, dielectric capacitors), antistatic agents, electromagnetic interference (EMI)

shielding, chemical sensors, biosensors, anticorrosion, optical devices, biomedical devices, among others.[175]

1.6 Research objectives

As discussed above, CNFs exhibit outstanding physiochemical properties and have a variety of applications. However, the main hurdles for large-scale application of CNFs are the inability to recover chemicals, high cost, and environmental issues. In order to overcome these drawbacks, the first objective of this work is to provide a green and sustainable approach to convert a waste material namely paper mill sludge (PMS) to functionalized CNFs.

As shown in **Fig. 1-23**, PMS will be directly treated with formic acid (FA). After FA treatment, the solid part from PMS will go to microfluidization to produce CNFs. On the other hand, the liquid part (supernatant) will go to distillation to recover FA, and the solid residues will be collected as by products (e.g., glucose, xylose). Moreover, the as-prepared CNFs can be used to produce transparent CNP by a simple filtration process. Since FA is the only used chemical in the whole process and it can be easily recycled with a high recycle rate over 90%, as well as the fact that PMS is abundant and renewable agro-industrial waste, the whole process proposed in this work can be considered as a sustainable and promising method to valorize PMS into valuable products such as CNFs, CNP, and carbohydrates.

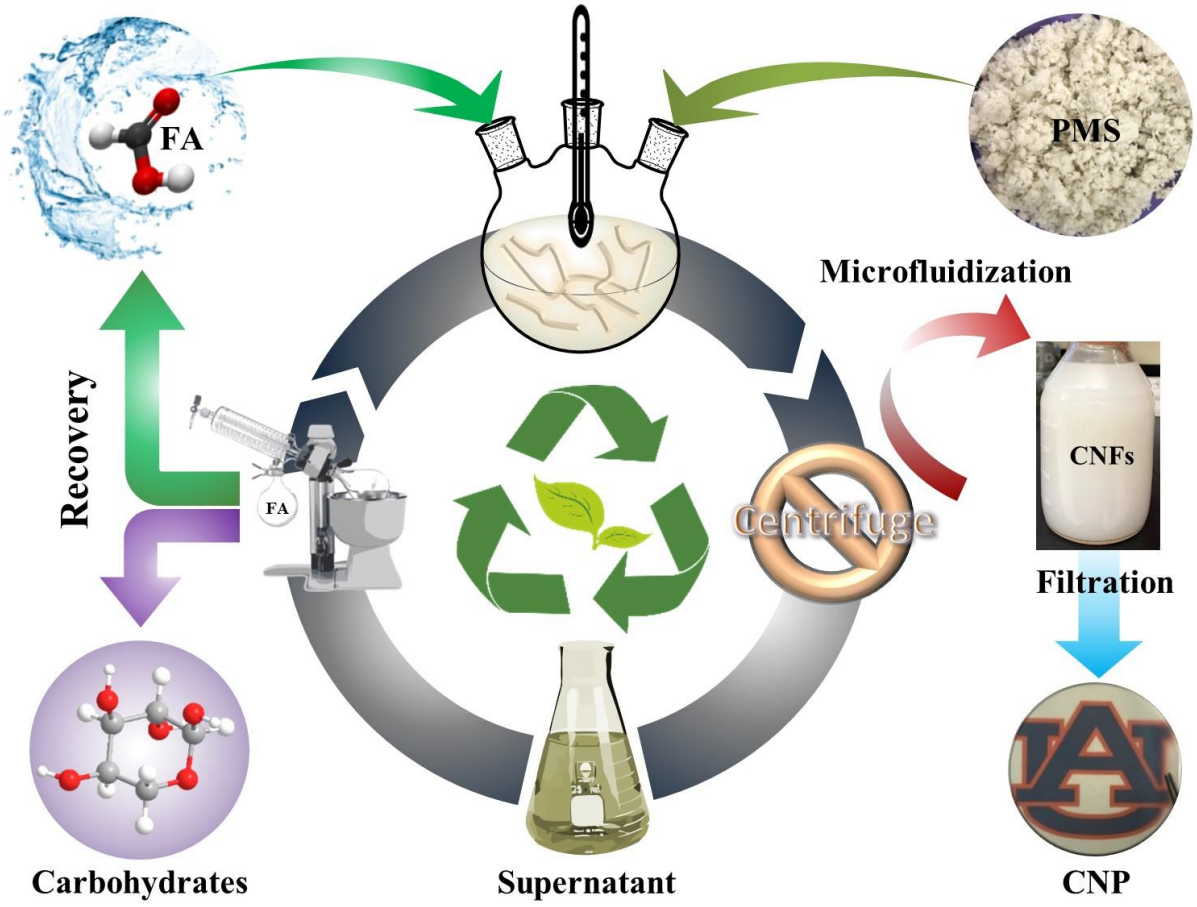

Figure 1-23. Schematic process flow diagram for the valorization of PMS by FA hydrolysis and the followed microfluidization.

As displayed in **Fig. 1-24**, the most widely used ICPs such as PPy, PANI and PEDOT lack the ability to form structural materials due to their rigid structure and poor processability, which significantly limited their practical applications. On the contrary, CNFs show great tendency to form stable structures such as CNP, aerogels and hydrogels. Therefore, the second objective of this work is to design and fabricate CNFs/ICPs nanocomposite structures (e.g., CNP) by compounding CNFs with ICPs through different strategies. In the CNFs/ICPs nanocomposites, CNFs serve as the building blocks and provide the structural stability, and the ICPs act as conductive or active materials. The as-prepared multifunctional CNFs/ICPs nanocomposites show

great potential for various applications such as flexible supercapacitors, strain sensors, chemical sensors, antistatic packaging materials, etc.

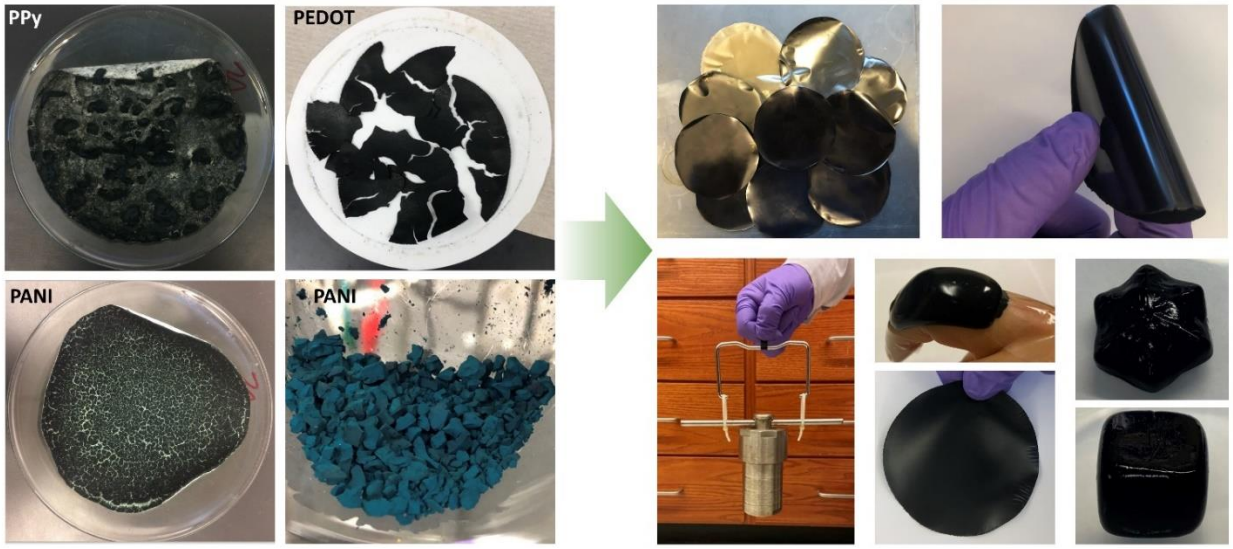

Figure 1-24. Photographs showing the failure in making pure ICPs bulk films (left) and the success on the preparation of mechanically stable CNFs/ICPs nanocomposites.

Chapter 2 Sustainable valorization of paper mill sludge into cellulose nanofibrils and cellulose nanopaper

2.1 Introduction

Cellulose nanofibrils (CNFs), as a kind of renewable and biodegradable nanomaterials have attracted rapidly growing interests from both academia and industry in recent years.[79, 176] Due to its unique nanostructure and physicochemical properties such as high aspect ratio, high specific surface area, excellent mechanical properties, tunable surface chemistry, great biocompatibility and biodegradability,[84, 177] CNFs have great application potential in the fields of reinforcing nanofillers,[151, 178] biomedicine,[80, 179] optoelectronic devices,[3, 180] sensors,[181, 182] and energy storage devices.[183-185] In general, CNFs are mostly produced from raw cellulose materials via different kinds of mechanical approaches such as high-pressure homogenization, microfluidization, grinding, ultrasonication, among others.[104] During the mechanical fibrillation, the generated mechanical shear could break down cellulose fiber into aggregated nanofibrils with the diameter below 100 nm and the length of 500 nm to several microns.[186] However, the mechanical fibrillation process is very energy intensive due to the intense inter- and intramolecular hydrogen bonds among cellulose chains.[187] It is reported that the energy consumption is in the range of 3-24 MWh/t and 12-70 MWh/t for grinding and homogenization, respectively.[114] At present, the high cost derived from high energy consumption is the main obstacle for the larger-scale production and application of CNFs.

In order to reduce the energy consumption, various pretreatment methods have been developed in recent years, such as enzymatic hydrolysis,[188, 189] TEMPO oxidation,[121, 190] carboxymethylation,[123] quaternization.[124] For example, it is reported that the mechanical energy consumption could be

significantly reduced from 70 MWh/t for unmodified CNFs preparation to 1-10 MWh/t after TEMPO oxidation depending on the carboxyl content.[79, 191] However, the above enzymatic or chemical pretreatments do have several drawbacks like high cost of enzymes and chemicals, time-consuming process, inability to recover chemicals and environmental issues.[112, 192] More recently, organic acid hydrolysis has been considered as a sustainable and promising pretreatment method due to the fact that organic acids are mild, recyclable, reusable, low corrosive and environmentally benign. To date, two types of organic acids: solid organic acids and liquid organic acid have been used in the pretreatment process for CNFs production. Solid organic acids such as oxalic acid, maleic acid and *p*-toluenesulfonic acid were firstly used to hydrolyze wood pulp for the cellulose nanomaterials production.[98] It is demonstrated that these concentrated dicarboxylic acids (50-70 wt.%) at elevated temperatures (80-120 ºC) were able to hydrolyze hemicellulose and depolymerize cellulose, leading to the resultant solid part consisted of a small proportion of CNCs and majority of cellulosic solid residue (CSR).[193, 194] The CSR could be further converted to CNFs with low-intensity mechanical fibrillation.[195, 196] It was found that both the as-prepared CNCs and CNFs exhibited high thermal stability and surface functionality with hydrophilic carboxyl groups.[197] Notably, over 90% of the solid organic acids in the liquid part could be recovered by a conventional crystallization method.[198] For the first time, recyclable liquid organic acid (FA) hydrolysis was developed for the preparation of cellulose nanomaterials.[199] It was demonstrated that FA as the simplest liquid carboxylic acid with high acidity could simultaneously hydrolyze the disordered regions of cellulose and hemicellulose, swell and shorten cellulose fiber, functionalize the surface by esterification, which have been proven as an effective pretreatment for CNFs production.[112, 200] After hydrolysis, the FA could be easily recovered by a simple distillation process with a high recovery rate over 90%. In addition, the FA hydrolysis efficiency

could be significantly enhanced by adding specific catalyst (e.g. HCl, $FeCl_3$), which enabled the integrated production of CNCs and CNFs.[97, 109, 201] Intriguingly, the FA could be directly used to fractionate biomass feedstocks such as tobacco stalks and corn husk to produce valuable products like xylose, lignin-containing CNFs and functional cellulose nanopapers (CNP).[145, 202]

In order to further reduce the cost of CNFs, different kinds of agro-industrial wastes such as corncob residue,[150] sugarcane bagasse,[203] coconut husk[204] have been investigated as the feedstocks for CNFs production, instead of using the commercial bleached pulp, microcrystalline cellulose or cotton. However, prior to the preparation of CNFs, purification of these feedstocks is usually indispensable in which the lignin and other components should be removed.[78] In general, alkali treatment (e.g. NaOH, KOH) and the followed bleaching (like $NaClO_2$, H_2O_2) are widely used for the purification. Nevertheless, the purification process will definitely increase the production cost and cause environmental issues to some extent due to the alkali and bleaching agents are normally unrecyclable.[145] Generally, paper mill sludge (PMS) which contains cellulose fibers and other materials is produced during papermaking or paper recycling in large volumes.[205] Traditional landfill is the common approach for PMS treatment. However, it is becoming increasingly difficult and costly to construct and operate because of more stringent regulations, diminishing land availability, and public opposition in recent years.[206] Being a waste material, PMS carries zero or, in most cases, negative cost of $20-50/ton for the disposal.[207] Unlike other agro-industrial wastes, PMS has high carbohydrate content and low or no lignin content, as well as well-dispersed structure, the purification process is normally not necessary prior to the production of CNFs. Thus, PMS could be used as a cheap and sustainable feedstock for the production of CNFs without the concerns derived from purification.

In this project, we aim to convert PMS to CNFs and CNP via a sustainable approach, as shown in **Fig. 2-1**. Firstly, PMS was directly pretreated with FA at fixed acid concentration, solid-to-liquid ratio and temperature for different hydrolysis time (1-6 h). After centrifugation, the liquid part was subjected to distillation for the recycle of FA and the solid part (CSR) was washed and diluted for subsequent microfluidization to produce CNFs. Secondly, the obtained CNFs suspension was used to make CNP by a simple vacuum filtration process. To the best of our knowledge, there is no report about producing CNFs from PMS using FA hydrolysis pretreatment combined with microfluidization. This study will provide a sustainable and economically feasible approach to convert PMS into valuable nanomaterials.

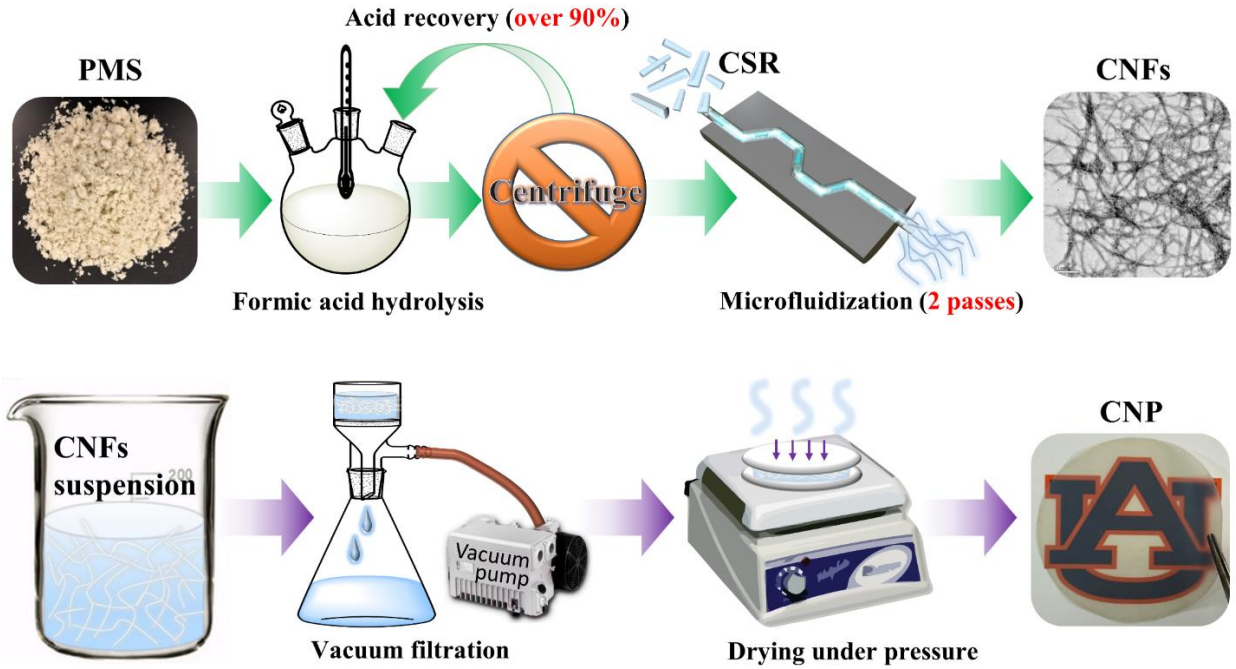

Figure 2-1. Schematic process flow diagram for the FA hydrolysis of PMS combined with microfluidization to produce CNFs, along with the preparation of CNP.

2.2 Experimental section

2.2.1 Materials

The never-dried PMS with the moisture content of 75.65 ± 0.5% was provided by a paper mill in USA. The PMS mainly contains 68.1 ± 0.9% cellulose, 13.5 ± 0.1% hemicellulose, 9.1 ± 0.6% extractives, 5.8 ± 0.1% ash, and less than 0.1% lignin. The formic acid (95 wt.%) was purchased from Eastman Chemical Co. Dimethylformamide (DMF) was purchased from Alfa Aesar, USA. All the chemicals were used as received without further purification.

2.2.2 FA hydrolysis pretreatment

First, 41 g never-dried PMS (10 g in oven dry weight) and 259 mL 95 wt.% FA were added into a 500 mL spherical flask, the final concentration of FA was calculated to be 82.02 wt.%. Then, the flask was heated up to 95 ºC in an oil bath with magnetic stirring at 500 rpm for different hydrolysis times (1-6 h) with an interval of 1 hour, in which the FA concentration, solid-to-liquid ratio and temperature were fixed at 82.02 wt.%, 1/30 and 95 ºC, respectively, for all the hydrolysis reactions. Upon completion, the flask was immediately cooled down to room temperature with tap water, and the mixture was centrifuged at 6000 rpm for 3 min to separate the supernatant and cellulosic solid residual (CSR). Subsequently, the separated CSR was washed by successive centrifugation at 6000 rpm with deionized (DI) water until the pH near to 6.0. After washing, the CSR was diluted with deionized water to a concentration of 1.0 wt.%, which can be directly used for CNFs production by microfluidization. The yield of CSR was calculated based on the weight percentage of the obtained CSR to the starting PMS. In order to facilitate discussion, the obtained CSR was noted as CSR-x (where x stand for FA hydrolysis time). In addition, the separated supernatant was

collected for recovery of FA and sugars by vacuum distillation. The recovery rate of FA was found to be over 90%. Afterwards, the residual sugars were dissolved with the same volume of deionized water, and the obtained solution was used to detect and quantify the hydrolyzed sugars by HPLC.

2.2.3 Microfluidization

The above diluted CSR suspensions were directly fed into a microfluidizer (M-110EH, Microfluidics Corp., USA) to mechanically fibrillate the CSR at 160 MPa for 2 passes through two Z-shaped orifices in series with the diameters of 200 μm and 87 μm, respectively. The photograph and schematic illustration of the microfluidizer is shown in **Fig. 2-2**. The microfluidization parameters were kept same for all the CSR samples. Correspondingly, the obtained CNFs were named as CNF-x (where x represents FA hydrolysis time). We assume that all the collected sample after microfluidization are CNFs, thus the yield of CNF-x is equal to the CSR-x yield. The energy consumption for CNFs production by microfluidization (with the same model of microfluidizer to the one used in this work) was estimated to be 2221 kWh/t for one-time microfluidization at 1600 bar of a 2 wt.% fibrous system. Based on the following equation (1) proposed by Naderi et al.,[208] the energy consumption for microfluidization in the current work could be calculated to be 8884 kWh/t, which is much lower than the reported value.

$$EC\ (kWh/t) = \frac{2221*2*p*n}{1600*c} \qquad \text{Eq (1)}$$

where p is the applied pressure; n is the number of passes through the microfluidizer; c is the concentration of the fiber suspension.

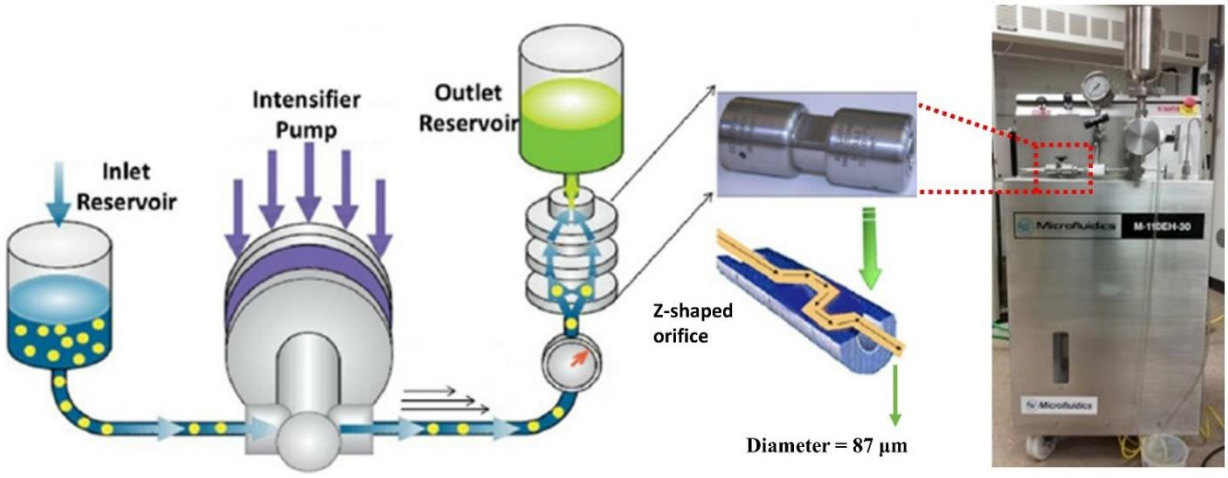

Figure 2-2. Photograph and the schematic illustration of the microfluidizer used in this work.

2.2.4 Preparation of CNP

The as-prepared CNFs suspension was diluted with DI water to a concentration of 0.2 wt.%. 150 mL of the diluted CNF suspension was used to fabricate CNP by vacuum filtration using a polypropylene filter membrane (diameter of 10 cm, pore size of 0.45 µm). Then, the obtained wet CNP was placed between two filter membranes and dried at 105 °C for 2 h by using a hot plate with 10 N force upon the membranes. For comparison, paper sheet was prepared from PMS suspension using the same procedure, and the resultant paper sheet was named as PMS-PS.

2.2.5 Characterizations

2.2.5.1 Quantitative analysis of sugars in the supernatants

The sugars in the supernatant from FA hydrolysis were quantitated by HPLC equipped with a refractive index detector (Showa Denko K.K., Japan) and a BioRad-HPX-87P column (Bio-Rad

Laboratories, Hercules, CA). Ultrapure water was used as the mobile phase at a flow rate of 0.55 mL/min and the column temperature was set to 85 °C.

2.2.5.2 Micrographs

The morphologies of PMS and the obtained CSR samples after FA hydrolysis pretreatment were observed by using a microscope (Micromaster Model CK, Fisher Scientific).

2.2.5.3 Transmission electron microscope (TEM)

The morphologies of CNFs samples were observed by using a transmission electron microscope (TEM, Hitachi H-7600, Japan) with an accelerating voltage of 100 kV. The procedure for the sample preparation for TEM observation was identical to our previous work.[202] Briefly, CNFs suspensions with a concentration of 0.01 wt.% were sonicated for 10 min. Then, one drop of the CNFs suspension was dropped onto a carbon-supported copper grid. Afterwards, the samples were placed in a vacuum oven for 24 h to remove moisture. Finally, the dried samples were dyed with 2 wt.% uranyl acetate (20 μL) for 1 h to enhance the contrast of TEM images. The diameter distribution of the CNFs was determined by ImageJ analysis software.

2.2.5.4 Attenuated total reflection-Fourier transform infrared spectroscopy (ATR-FTIR)

FTIR spectra of PMS and CNFs samples were obtained on a Thermo Nicolet 6700 FTIR spectrometer equipped with diamond ATR accessory and OMNIC 7.3 software. Prior to measurement, air-dried PMS and freeze-dried CNFs samples were conditioned at 50% RH and 23 °C for 24 h. For each measurement, around 10 mg dried sample was directly placed upon the

crystal stage of the instrument. The spectra were recorded in the wavenumber range from 4000 to 400 cm^{-1} at a resolution of 4 cm^{-1}.

2.2.5.5 X-ray diffraction (XRD) analysis

X-ray diffraction patterns of the sludge and CNFs samples were characterized on an X-ray diffractometer (Philips X'Pert MPD) with a Cu Kα radiation source (λ = 1.5405 Å) operating at 45 kV and 40 mA. The range of scattering angle (2θ) was from 5° to 40° with a scan rate of 0.01°/s. Prior to measurement, air-dried PMS, freeze-dried CSR and CNFs samples were individually placed on a sample holder and leveled to get uniform X-ray exposure. The crystallinity index (CrI) was calculated using the empirical equation shown as follows:

$$CrI\ (\%) = (I_{200}\text{-}I_{am})/I_{200} * 100 \qquad \text{Eq (2)}$$

where I_{200} is the maximum peak intensity at lattice diffraction (200), I_{am} is the minimum intensity between planar reflections (200) and (110).

2.2.5.6 Thermal gravimetric analyses

The thermal stability of PMS and CNFs samples were examined by a thermogravimetric analyzer (TA instruments T650, USA). Each sample was heated from room temperature to 600 °C at a heating rate of 10 °C/min under nitrogen (25 mL/ min) to record the thermogravimetric (TG) and differential thermogravimetric analysis (DTG) curves.

2.2.5.7 Dispersibility

The dispersibility of CNFs in aqueous and organic (DMF) phases was examined at a concentration of 5 mg/mL. In order to get CNFs suspension in DMF, the CNFs aqueous suspension was exchanged with DMF by centrifugation twice. Afterwards, the CNFs suspensions in aqueous and DMF were dispersed by magnetic stirring for 1 hour, respectively. Around 20 mL of the CNFs suspensions were poured into a vial to check the suspension stability. The pictures of samples were taken after standing for 1 day and 30 days, respectively.

2.2.5.8 Degree of substitution

The degree of substitution (DS) of formylation was determined according to the usual back-titration method, as descripted in our previous work.[112] Firstly, 0.3g of the freeze-dried CNFs and 30 mL 0.2 N KOH in 50% aqueous alcohol were transferred into a 100 mL Erlenmeyer flask. The flasks were tightly covered and placed onto a magnetic stirrer at 200 rpm. The reaction was maintained at room temperature for 24 h. Afterwards, 30 mL 0.2 N HCl was added into the flask. After another one hour, the mixture was titrated with 0.1 N NaOH solution, and one drop of phenolphthalein was used as the indicator. PMS as the control sample was performed using the same procedure.

The formyl content was calculated by equation (3), as follows:

$$\text{Formyl (\%)} = (V_S - V_B) \times N_{NaOH} \times M_{formyl} \times 10^{-3} / W \times 100\% \qquad \text{Eq (3)}$$

where V_B (mL) is the volume of NaOH required for titration of the blank, V_S (mL) is the volume of NaOH required to titrate the sample, N_{NaOH} is the normality of the NaOH solution, M_{formyl} is the molecular weight of the formyl group (29 g/mol), and W (g) is the mass of sample used.

The DS of formylation was calculated by equation (4), as follows:

$$DS = (162 \times Formyl) / [M_{formyl} \times 100 - ((M_{formyl} - 1) \times Formyl)] \quad \text{Eq (4)}$$

where 162 is the molecular weight of the anhydroglucose units.

2.2.5.9 Tensile test

Tensile strength of the CNP samples was examined by an Instron 4465 universal testing machine following the TAPPI standard method (TAPPI T497 and TAPPI T456). The tensile test experiment was carried out under a temperature of 23 ºC with a relative humidity of 50%. The initial distance between the two clamps was set to 20 mm and the crosshead speed was maintained at 5 mm/min. The CNP specimens were cut into 1 cm × 5 cm segments. Before testing, the specimens were placed at the conditions of 50% RH and 23 °C for 24 h. Five measurements were made for each CNP sample and the data averaged to obtain a mean value.

2.3 Results and discussion

2.3.1 Preparation of CNFs from PMS

In order to investigate and evaluate the FA hydrolysis pretreatment, CSR samples were collected at different FA hydrolysis time intervals. **Fig. 2-3** displays the microscopy images of CSR fibers at different FA hydrolysis time (1-6 h). Obviously, the length of the CSR fibers significantly decreased with the increasing hydrolysis time. Compared to the morphology of raw PMS fibers (**Fig. 2-5**), the morphology of CSR-1 changed inconspicuously while part of long fibers in the CSR-2 sample were broke up into fragments. It should be noted that clogging is of frequent occurrence during microfluidization if the fibers are too long due to the narrow microfluidic

channels, which results in many production stops for cleaning.[209] In the current study, we found that less than 3 h FA hydrolysis pretreatment was not sufficient to get short enough CSR fibers for smooth microfluidization. Thus, we mainly discuss the production and characterization of CNFs and CNP samples obtained from 3-6 h FA hydrolyzed CSR samples in the following sections. From the magnified images (**Fig. 2-4**), we can clearly see the morphology change from CSR-1 to CSR-6 with the increasing FA hydrolysis time. Although the fiber length in CSR-1 and CSR -2 samples is not significantly reduced, we do distinctly see a number of small holes on the fiber surface. This is because FA could swell the fibers and part of hemicellulose and disordered region of cellulose are hydrolyzed to sugars.[112] With the further extension of hydrolysis time, the fibers structure is gradually changed to fragments and fiber fines, which would benefit to the subsequent fibrillation for CNFs production. Based on the above discussions, the schematic representation (**Fig. 2-6)** of FA hydrolysis pretreatment was proposed to illustrate the triple purposes including hydrolysis of the disordered regions of cellulose and hemicellulose, swell and shorten cellulose fiber, functionalize the surface by esterification between cellulose and FA.

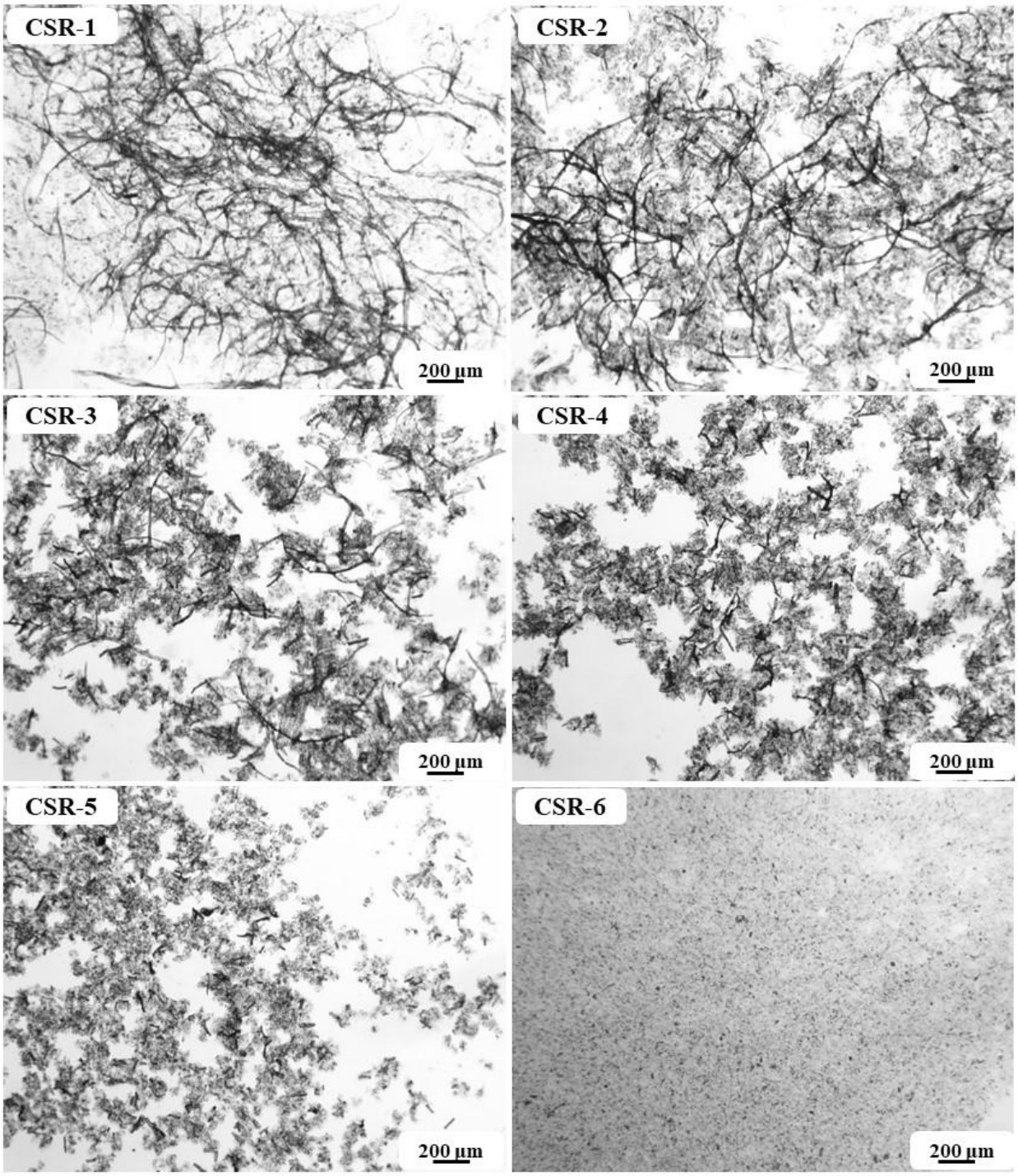

Figure 2-3. Microscopy images of CSR fibers at FA hydrolysis time intervals (1, 2, 3, 4, 5 and 6 h) sowing a reduction in fiber lengths.

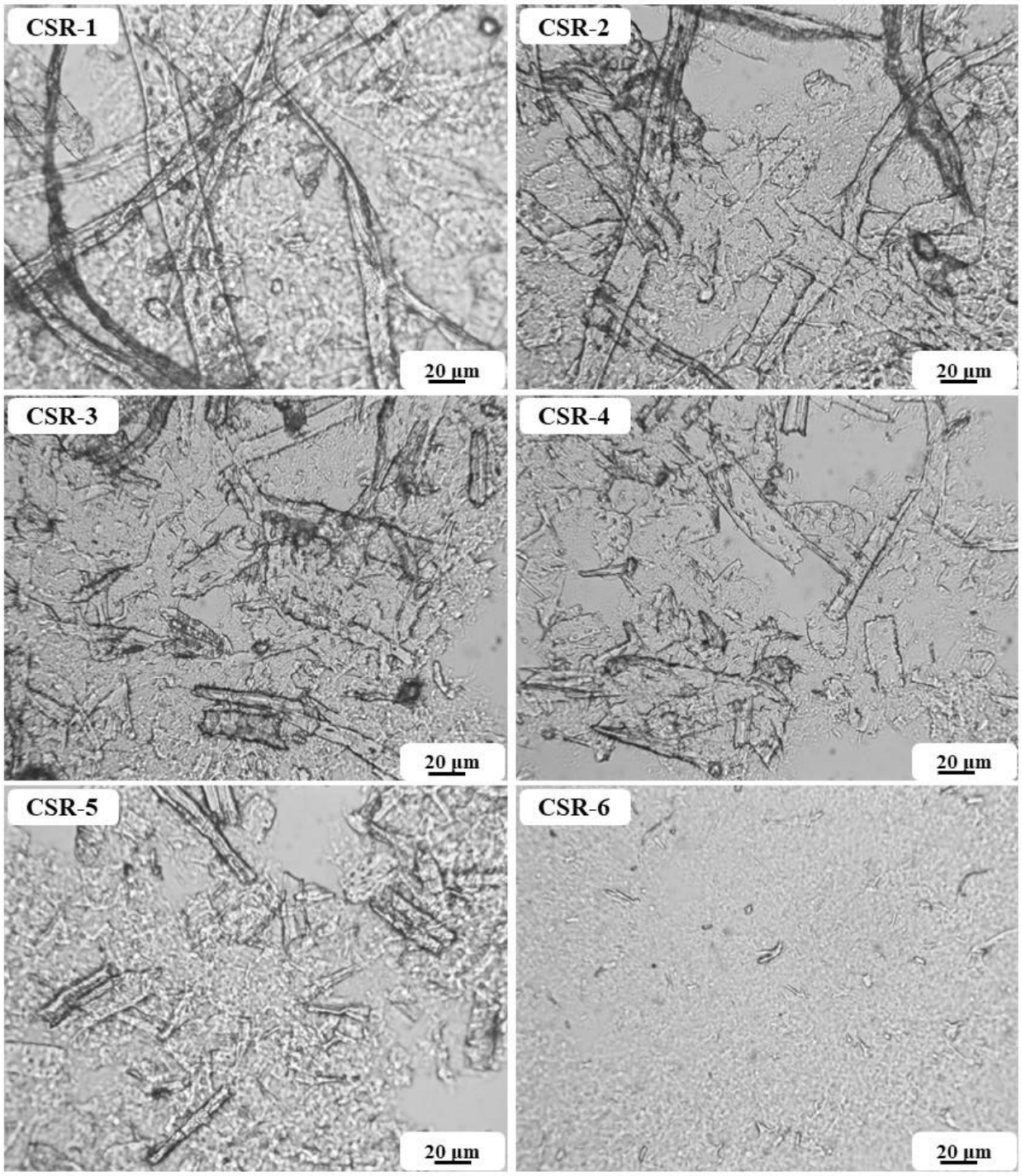

Figure 2-4. Magnified microscopy images of CSR fibers at different FA hydrolysis time (1, 2, 3, 4, 5 and 6 h).

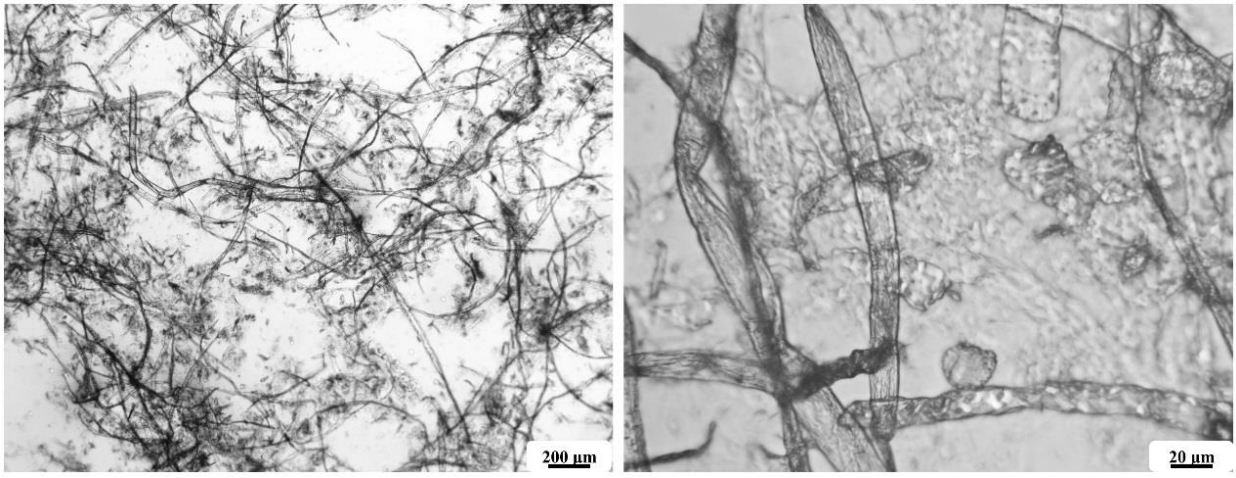

Figure 2-5. Microscopy images of raw PMS fibers at different magnification.

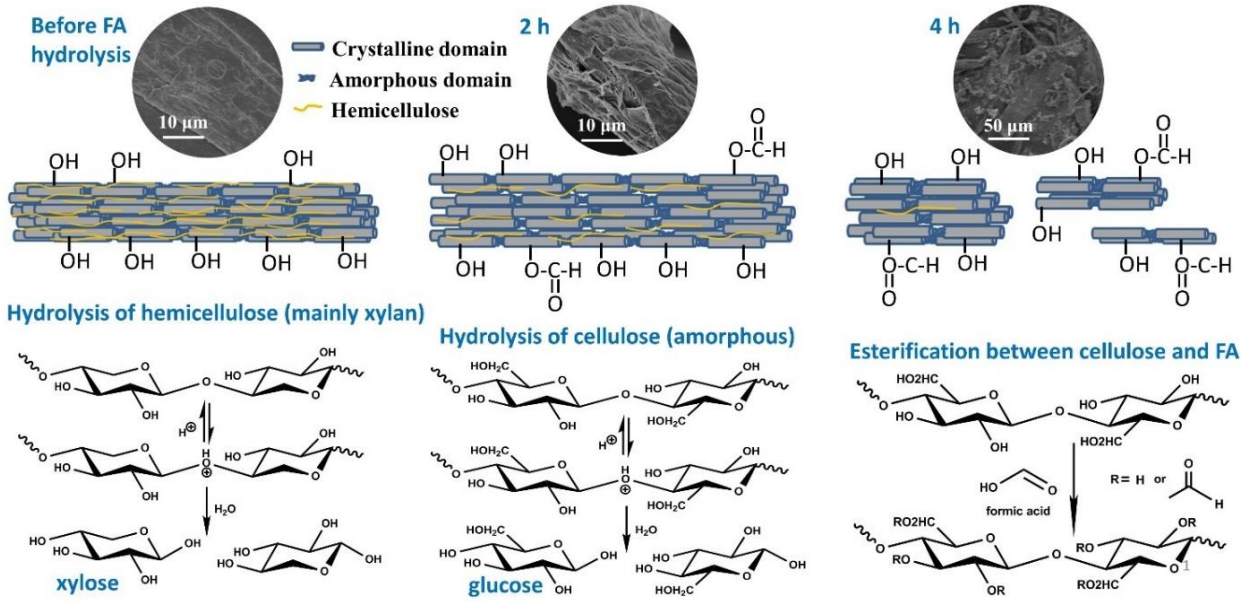

Figure 2-6. Schematic representation of FA hydrolysis pretreatment showing the triple purposes: hydrolysis of the disordered regions of cellulose and hemicellulose, swell and shorten cellulose fiber, functionalize the surface by esterification between cellulose and FA.

Fig. 2-7 shows the morphology of CNFs and the corresponding diameter distribution. Since we used the same energy input and parameters in the microfluidization process for all CNFs samples, the effect of FA hydrolysis pretreatment could be indirectly evaluated by observing the fibrillation

degree of CNFs. As shown in **Fig. 2-7**, large microfibril bundles with the diameter larger than 100 nm could be distinctly observed. The low extent of fibrillation in CNF-3 sample could be evidently attributed to the insufficient hydrolysis of CSR-3, as we can clearly see some of big fibers (length > 500 μm) in **Fig. 2-3**. With the increasing hydrolysis time, more uniform CNFs could be obtained, and the uniformity of CNF-x in **Fig. 2-7** is consistent with that of the CSR-x in **Fig. 2-3**. Finally, the CNF-6 sample shows the most homogeneous diameter distribution with majority of nanofibers showing a diameter below 20 nm. It should be noted that we only implemented 2-pass microfluidization with relatively low energy input (e.g. 8884 kWh/t), which could be comparable with or even lower than that for the widely used TEMPO oxidation.[191, 210] As summarized in **Table 2-1**, the chemical cost for TEMPO oxidation was estimated to be around 224 USD/kg CNFs, the extremely high chemical cost does not compensate for the energy savings.[211] Notably, the chemical cost for FA hydrolysis is only 2.6 USD/kg CNFs, which is about 86 times lower than that for TEMPO oxidation. Moreover, the production cost of FA hydrolysis method is much lower than sulfuric acid hydrolysis and enzymatic hydrolysis pretreatment approaches, even though without considering the raw material cost. It is worth noting that the price of bleached wood pulp is in the range of 0.8-1.2 USD/kg, while the PMS carries zero or negative cost. In addition, the separated supernatant after FA hydrolysis can be directly reused for 1-3 times, as reported in our previous study.[112] Also, the hydrolyzed sugars can be recovered as valuable by-products. Thus, the production cost of the current method could be further reduced to some extent. Based on the above discussion, FA hydrolysis could be considered as a high-efficient and cost-effective pretreatment approach for conversion of PMS to CNFs.

Table 2-1. Comparison of production cost (USD/kg CNFs), including pretreatment cost and mechanical fibrillation cost, FA hydrolysis pretreatment vs. traditional pretreatment methods[a].

Pretreatment methods	Pretreatment cost			Mechanical fibrillation cost	Production cost
	Chemical	Enzyme	Energy		
TEMPO oxidation	224.02	-	0.60	1.69	226.31
Sulfuric acid hydrolysis	1.01	-	5.36	1.69	8.06
Enzymatic hydrolysis	12.22	0.70	0.40	1.69	15.01
FA hydrolysis[b]	2.60	-	0.02[c]	1.17	3.79

[a] the production cost of traditional pretreatment methods was adapted from the work by Delgado-Aguilar et al. (2015).

[b] the pretreatment cost of FA hydrolysis was estimated on the basis of 79% CNFs yield, 10% FA loss, 600 USD/t 85% FA and energy cost of 0.132 USD/kWh.

[c] the energy cost includes 0.007 USD/kg CNFs consumed during FA hydrolysis pretreatment and 0.015 USD/kg CNFs consumed in the FA recycling process (See **Table 2-2** for detailed calculation).

Table 2-2. Theoretical calculation of energy consumption and cost during FA hydrolysis pretreatment and FA recycling process.[a]

Processing section	Energy consumption (MJ/kg CNFs)	Amount of steam needed (kg)[d]	Cost (USD/kg CNFs)
FA hydrolysis pretreatment[b]	8.06	3.66	0.007
FA recycling process[c]	17.00	7.72	0.015

[a] the energy consumption was calculated on the basis of 79% CNFs yield and 10% FA loss, under the reaction condition at 95 ºC, solid-to-liquid ratio of 1/30, and 82.0 wt.% FA.

[b] assume that the room temperature is 25 ºC, the density and specific heat capacity of 82.0 wt.% FA are 1.19 g/cm^3 and 2560 J/(kg ºC), respectively.

[c] assume that the heating and cooling process consume the same amount of energy, the boiling point of 82.0 wt.% FA is 107 ºC.

[d] low pressure steam of 200 kPa with 2201.56 kJ/kg heating value was used to evaluate the energy cost, as previously reported by Novo et al.[212] The unit cost of the low-pressure steam is assumed to be 0.002 USD/kg.

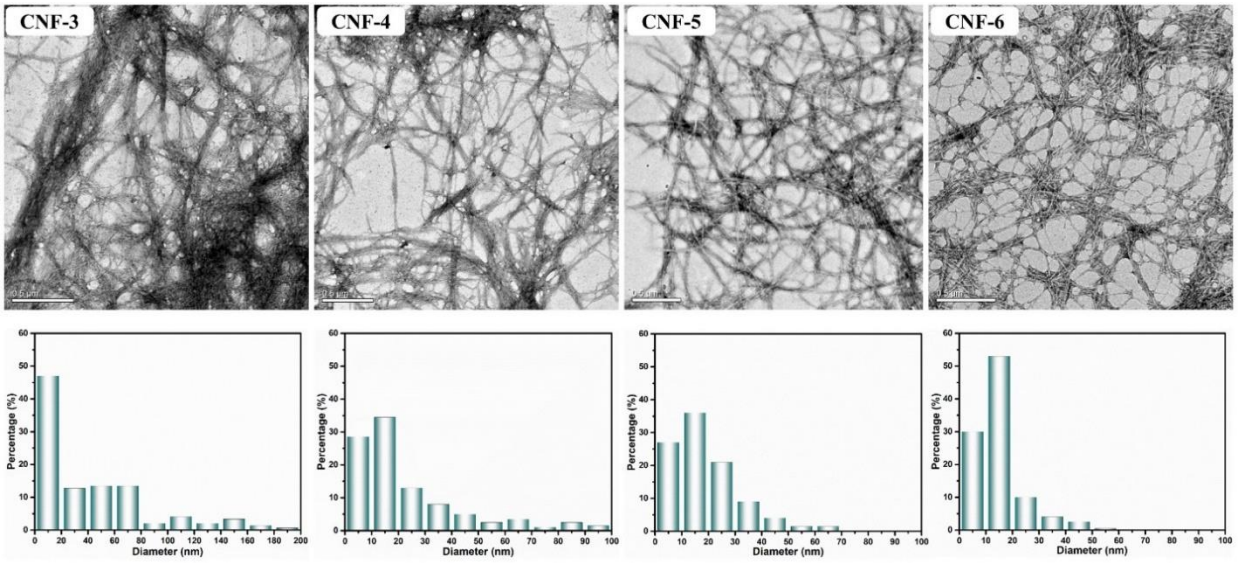

Figure 2-7. TEM images of CNFs (the scale bar in all images is 500 nm) and the corresponding diameter distribution.

As shown in **Fig. 2-8**, the yield of CNFs (equal to CSR) drops gradually with the increasing hydrolysis time, which is attributed to the fact that more sugars could be hydrolyzed from the PMS, as displayed in **Fig. 2-8b**. As we previously reported, the FA hydrolysis is relatively mild compared to traditional inorganic acid hydrolysis. Thus, a high yield (e.g. 79 wt.% after 4 h FA hydrolysis) of CNFs could be achieved, which is much higher than that of 25-45 wt.% by H_2SO_4 hydrolysis.[213] In addition, glucose and xylose in a yield range of 0.85-4.5 wt.% and 5.9-7.43 wt.%, respectively could be obtained during the FA hydrolysis pretreatment process. These sugars could be potentially used to produce platform chemicals (e.g. lactic acid, furfural) by fermentation or catalytic reaction.[49] Therefore, the whole pretreatment process is green and sustainable, in which the PMS could be almost fully converted to valuable products.

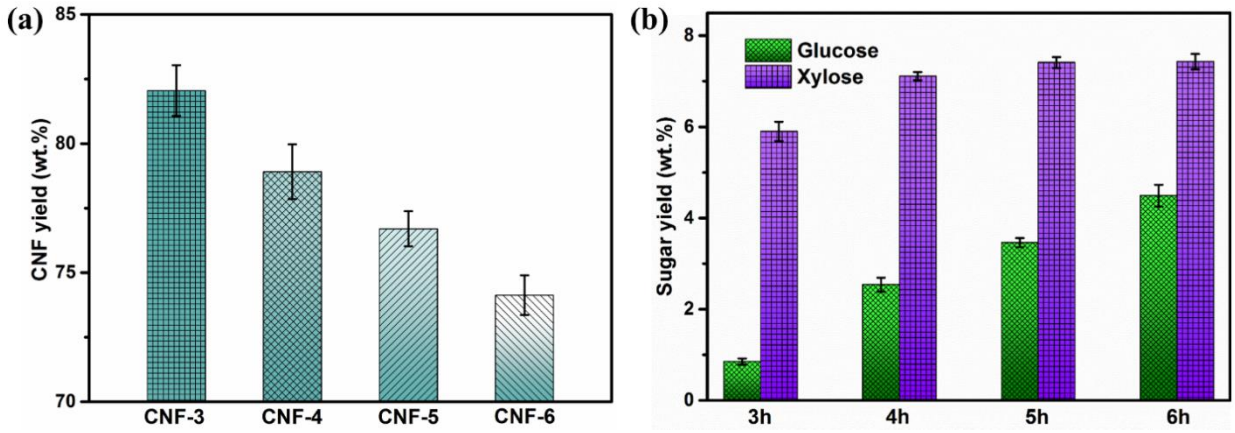

Figure 2-8. Yields of CNFs (a), glucose and xylose (b) based on dry PMS.

2.3.2 FTIR and XRD analyses of PMS and CNFs

To investigate the surface chemistry and crystalline structure, FTIR and XRD analyses of the raw PMS and the as-prepared CNFs were further conducted. As shown in **Fig. 2-9a**, a new strong band at 1717 cm^{-1} appears in the FTIR spectra of all the CNFs samples, which is attributed to C=O stretching from ester groups. Our previous studies have proven that the esterification between FA and cellulose occurred during the FA hydrolysis pretreatment.[112, 202] In order to quantify the degree of esterification, titration analysis was carried out and the DS values of the obtained CNFs was summarized in **Fig. 2-9b**. The results demonstrate that the content of ester groups on the surface of CNFs shows an upward trend with the increasing FA pretreatment time. In addition, other bands at 3335, 2918, 1645, 1429, 1161, 1105, and 897 cm^{-1} in the spectra of CNFs and raw PMS are nearly parallel, indicating the main cellulose I_β crystalline structure remains unchanged after FA hydrolysis pretreatment and the followed microfluidization.

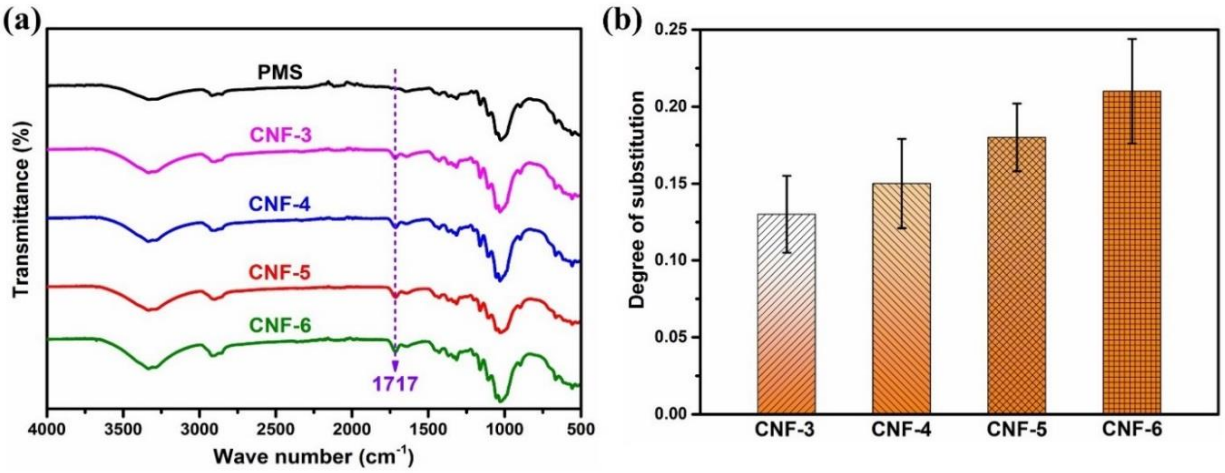

Figure 2-9. FTIR spectra of PMS and CNFs (a), DS of CNFs (b)

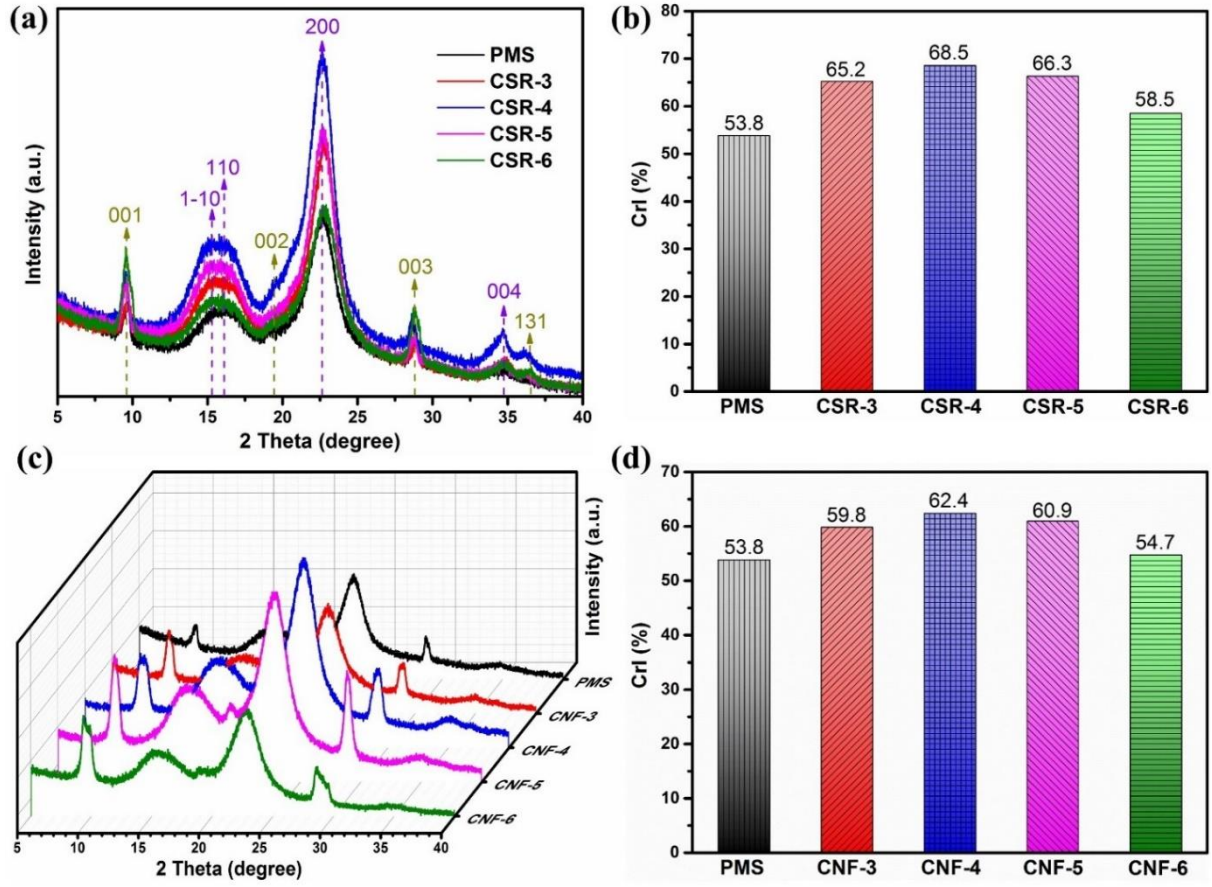

Figure 2-10. XRD patterns of PMS and CSR (a) and the corresponding CrI (b); XRD patterns of PMS and CNFs (c) and the corresponding CrI (d).

As shown in **Fig. 2-10**, XRD patterns of raw PMS and the obtained CSR and CNFs samples display diffraction peaks at 2θ = 15.6°, 16.7°, 22.7° and 34.6°, corresponding to the (1-10), (110), (200) and (004) crystallographic planes of cellulose I_β,[85] which again proves the unchanged cellulose I_β crystalline structure. Notably, several extra small diffraction peaks at 2θ = 9.7°, 19.3°, 28.8° and 36.3° can be clearly observed in all the CSR, CNFs and raw PMS samples. Based on the previous studies, these diffraction peaks should be ascribed to the (001), (002), (003) and (131) crystallographic planes of crystalline talc ($MgSi_4O_{10}(OH)_2$), since talc is widely used as fillers in the paper industry.[214] Similar XRD patterns of PMS and CNFs have been reported by Adu et al.[215] As shown in **Fig. 2-10b**, the CrI for the raw PMS is only 53.8%, while the CrI for the CSR-3 dramatically increases to 65.2% after 3h FA hydrolysis pretreatment. The 11.4% increasement in CrI is mainly attributed to the removal of hemicellulose and disordered regions of cellulose in PMS, and the hydrolyzed sugars (**Fig. 2-8b**) could be the evidence for this inference. When the hydrolysis pretreatment was prolonged 4 h, the CrI kept increasing to 68.5 for CSR-4. This is due to more hemicellulose and disordered regions of cellulose could be hydrolyzed to sugars, as indicated in **Fig. 2-8b**. However, with the pretreatment time continue to increase, a slightly declined CrI of 66.3% and an obviously decreased CrI of 58.5% can be observed for CSR-5 and CSR-6, respectively. This is probably because that part of crystalline regions of cellulose could be degraded with longer hydrolysis time.[112] In addition, **Fig. 2-10d** summarizes the CrI values of the obtained CNFs after microfluidization. Compared to CSR-x samples, all the corresponding CNF-x samples exhibit a lower CrI value. This is probably due to the damage of the crystalline domains of cellulose during the mechanical fibrillation process, as we reported previously.[97] It is worth noting that the CrI values for all the CNFs samples are still higher than that of the raw PMS, and

4 h FA hydrolysis could be the optimal pretreatment for PMS, leading to the resultant CNFs with the highest CrI (62.4%).

2.3.3 Dispersibility of CNFs

Fig. 2-11 displays the dispersibility of the as-prepared CNFs in water and DMF. With the concentration of 5 mg/mL, all the CNFs samples exhibit very stable colloidal suspensions in aqueous media for over 3 months, even though with the functionality of kind of hydrophobic ester groups. This is probably due to the fact that a huge amount of hydrophilic hydroxyl groups exposed on the CNFs surfaces during mechanical fibrillation process, which could improve their ability to bind water molecules and thus facilitate the colloidal stability.[216] Importantly, all the CNFs samples show a much clearer dispersion in DMF at the same concentration (5 mg/mL), indicating a better dispersibility in DMF. This is because the introduced ester groups on the CNFs surfaces improved their compatibility with organic solvents.[201] Thus, it can be expected that the as-prepared surface functionalized CNFs could be used as nanofillers for polymeric matrix materials (e.g. PLA) due to the improved compatibility.[217] Additionally, it should be noted that the CNFs dispersions in DMF become more transparent with the increase of FA pretreatment time. This result is consistent with the fact that more uniform CNFs with smaller average diameter (**Fig. 2-7**) and higher DS (**Fig. 2-9b**) were obtained with the increase in pretreatment time. Smaller CNFs can reduce the scattering of light improving the transparency of the suspension, and higher DS of CNFs can increase the compatibility to the solvent.

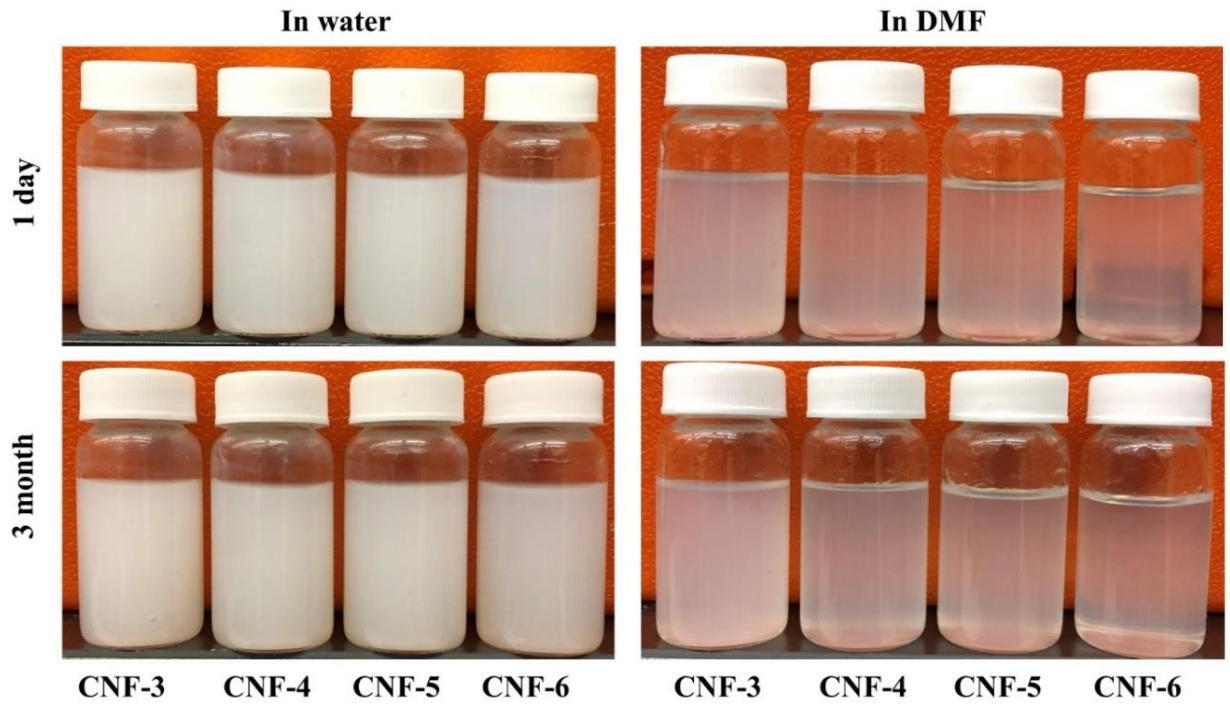

Figure 2-11. Dispersibility of CNFs in water and DMF (Note: the concentration of CNFs in both media is 5 mg/mL).

2.3.4 Thermal Stability of PMS and CNFs

Fig. 2-12 shows the thermogravimetric (TG) and derivative thermogravimetric (DTG) curves of the raw PMS and as-prepared CNFs. Correspondingly, the start decomposition temperature (T_0), the decomposition temperature at 10% weight loss ($T_{10\%}$) and maximum decomposition temperature (T_{max}) are summarized in **Table 2-3**. As shown in **Fig. 2-12a**, thermogravimetric curves indicate that raw PMS shows the lowest T_0 and $T_{10\%}$, while there is a notable increase in both T_0 and $T_{10\%}$ for CNF-3. This is mainly due to the efficient removal of hemicellulose and disordered regions of cellulose in PMS during FA hydrolysis pretreatment. Similar to the trend of CrI results, CNF-4 shows the highest T_0 and $T_{10\%}$, and the followed decrease of T_0 and $T_{10\%}$ for both CNF-5 and CNF-6 due to the over-degradation of crystalline regions in cellulose.

Interestingly, as shown in **Fig. 2-12b**, the raw PMS shows the highest T_{max}, and the T_{max} values of CNF-3, CNF-4, CNF-5 and CNF-6 could be sorted in a descending order. There are two possible reasons causing this decrease in T_{max}: 1) As we discussed in the XRD results section, the mechanical fibrillation could cause damage of part of crystalline domains of cellulose. Although the raw PMS shows a relatively lower CrI, the crystalline regions in the raw PMS are not damaged; 2) With the increasing degree of fibrillation from CNF-3 to CNF-6, more uniform CNFs would definitely have higher specific surface area. It is reported that the increase in the surface area of cellulose nanomaterials could accelerate their degradation, resulting in a reduced T_{max} value.[218] In addition, it should be noted that the optimized sample (CNF-4) exhibited relatively higher thermal stability than that of the CNFs produced by TEMPO oxidation,[219] sulfuric acid hydrolysis[118] and carboxymethylation[220] pretreatment combined with mechanical fibrillation. The presence of carboxyl or sulfonic groups could promote the thermal degradation of cellulose,[199, 221] while the presence of ester groups and talc is beneficial for the increase of thermal stability of the CNFs obtained in this work.[112, 215] Therefore, the obtained CNFs in the current work possess surface functionality and high thermal stability showing great potential in reinforcing polymer matrix.

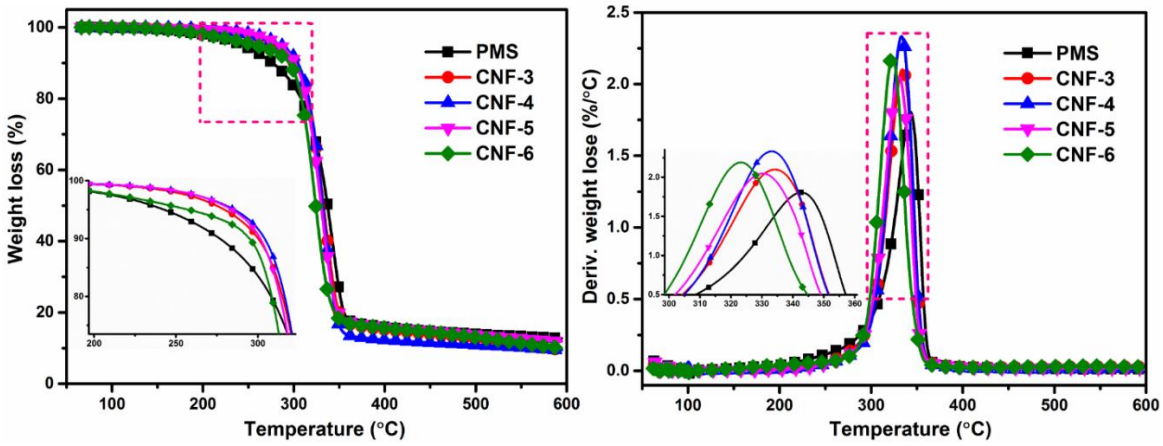

Figure 2-12. TG (a) and DTG (b) curves of PMS and CNFs.

Table 2-3. Summary of thermal decomposition parameters of PMS and CNFs samples.

Samples	T_0 (ºC)	$T_{10\%}$ (ºC)	T_{max} (ºC)
PMS	171.1	276.7	342.7
CNF-3	222.8	300.2	335.0
CNF-4	228.2	304.1	333.3
CNF-5	227.5	301.5	330.8
CNF-6	176.5	295.0	323.1

Note: T_0, $T_{10\%}$, T_{max} represent the start decomposition temperature, the decomposition temperature at 10% weight loss, and maximum decomposition temperature, respectively.

2.3.5 Mechanical Properties of CNP

Fig. 2-13a shows the strain-stress curves of CNP samples and the control paper sheet (PMS-PS) that directly made from PMS fibers. Correspondingly, tensile strength, Young's modulus and toughness are summarized in **Figs. 2-13b, 2-13c and 2-13d,** respectively. Compared with the PMS-PS, the tensile strength of CNP-3 dramatically increases from 13.6 MPa to 72.4 MPa. Moreover, CNP-4 shows the highest tensile strength of 106.4 MPa, which is around 8 times higher than that of the PMS-PS. The main reason for the remarkable increase in tensile strength is due to the much larger specific surface area offered by CNFs than that of PMS fibers. It is reported that the larger surface area directly affects the number of hydrogen bonding and thus the final mechanical properties.[222] Another reason is due to the more compact structure of CNP than that of PMS-PS which is attributed to the significantly reduced size of CNFs compared to PMS fibers. This inference can be verified by the fact that CNP-4 shows a higher density of 1287 ± 23 kg/m^3

than that of PMS-PS (788 ± 17 kg/m^3). For better comparison with other reported works, the tensile strength of the optimal CNP-4 could be converted to tensile index (also called specific strength) of 82.7 Nm/g, which is higher than the value (71.9 Nm/g) of PMS-derived CNP reported by a previous study,[215] and similar to that of the CNP made from commercial CNFs.[139, 223]

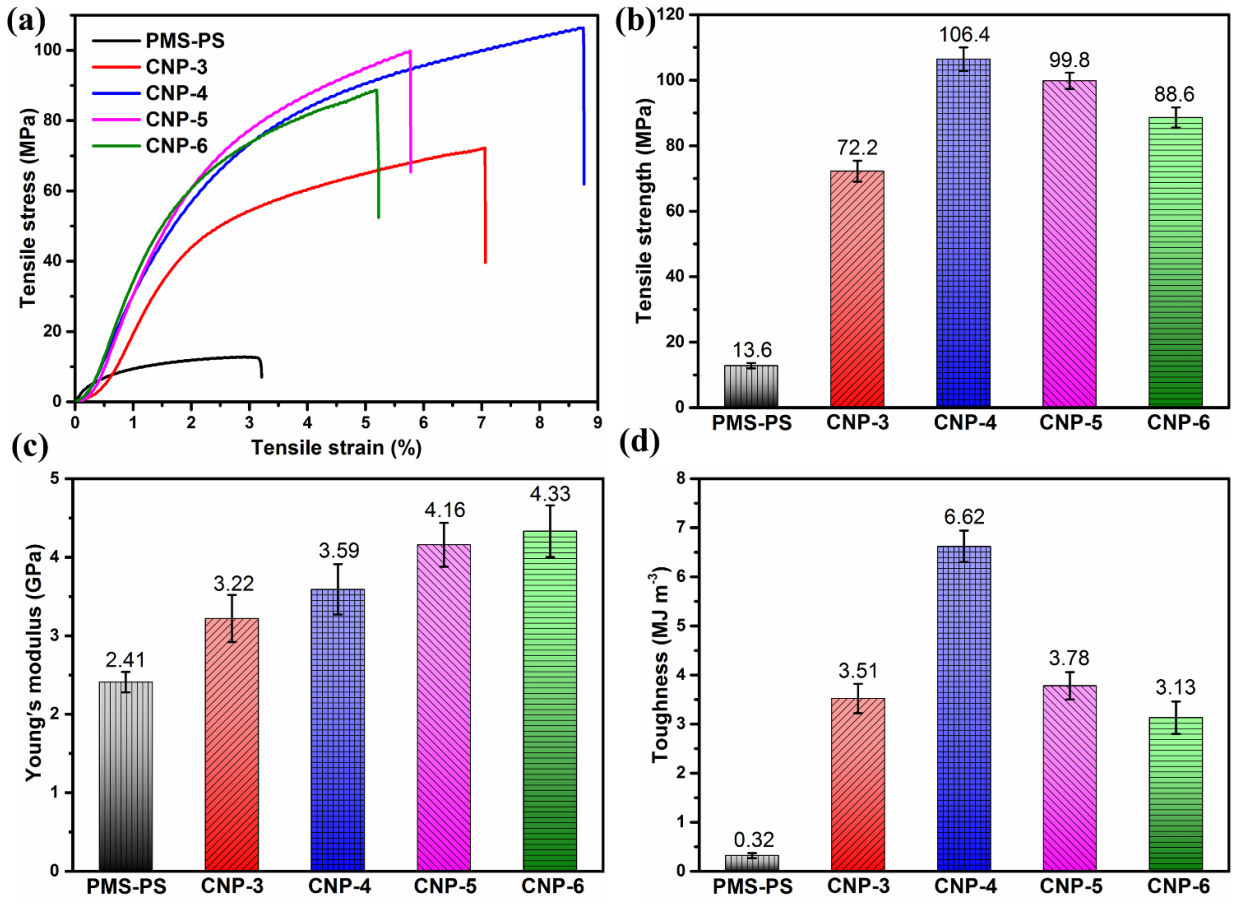

Figure 2-13. Strain-stress curves of PMS-PS and CNP samples (a), and the corresponding tensile strength (b), Young's modulus (c) and toughness (d).

In addition, although CNF-5 and CNF-6 show higher degree of fibrillation and more uniform diameter distribution than CNF-4 (see **Fig. 2-7**), they exhibit lower tensile strength. This result is probably attributed to the lower CrI and poor stress transfer between the shorter nanofibrils of

CNF-5 and CNF-6. It is reported that the degree of crystallinity has a strong positive correlation with the mechanical properties of CNFs, thus affecting the mechanical strength of the self-assembled CNP.[224] Moreover, CNP-5 and CNP-6 exhibit higher modulus and lower strain, indicating more rigid structure than CNP-4. Finally, **Fig. 2-13d** illustrates that CNP-4 shows the highest toughness of 6.62 MJ/m^3 which is 20.7 times higher than that of PMS-PS, indicating great mechanical strength and ductility. Considering the high mechanical strength, good transparency, flexibility and high thermal stability, the as-prepared CNP could be potentially used in the fields of packaging materials and flexible electronic devices.

2.4 Conclusion

In conclusion, a facile and sustainable approach by FA hydrolysis pretreatment and the followed microfluidization was established to prepare thermally stable and surface functionalized CNFs from PMS. Results demonstrated that FA hydrolysis could achieve a threefold purpose of swelling and shortening PMS fibers, hydrolyzing the disordered regions of cellulose and hemicellulose, and surface esterification simultaneously. It was found that FA hydrolysis pretreatment for longer than 3 h was necessary to get short enough fibers to avoid clogging issues during microfluidization. Afterwards, CNFs could be efficiently produced by relatively low-intensity mechanical fibrillation (only two-pass microfluidization). The energy consumption during mechanical fibrillation process was estimated to be 8884 kWh/t which is comparable with or even lower than that by implementing TEMPO oxidation pretreatment. Notably, the chemical cost for FA hydrolysis is only 2.6 USD/kg CNFs, about 86 times lower than that for TEMPO oxidation. Moreover, the resultant CNFs showed high thermal stability and good dispersibility in organic solvents (e.g., DMF), indicating their potential application as reinforce agent for polymers. Finally, the as-prepared CNFs were used to fabricate CNP by a simple filtration process. The obtained CNP showed high mechanical strength

and good optical transparency which could be potentially used as the substrate for flexible electronics. More importantly, the only used chemical (FA) could be easily recovered by distillation with a high recovery rate over 90%, and the hydrolyzed sugars could be potentially used to produce platform chemicals. Thus, the current study demonstrated a clean and sustainable approach for efficient valorization of PMS into valuable materials, and this strategy would be applicable to other agro-industrial wastes.

Chapter 3 Engineering cellulose nanopaper with water resistant, antibacterial, and improved barrier properties by impregnation of chitosan and the followed halogenation

3.1 Introduction

Over the past two decades, cellulose nanofibrils (CNFs) have received a great deal of attention due to their outstanding physiochemical properties such as high mechanical strength, large specific surface area, high aspect ratio, low density, tunable surface chemistry, as well as good biodegradability and biocompatibility.[112, 201] In light of these fascinating properties, CNFs have broad application prospect as reinforcing fillers,[97, 151] rheology modifiers,[150, 225] biomedical materials,[80, 226] and flexible electronics,[81, 227] among others. Recently, cellulose nanopaper (CNP), which is made from CNFs by a self-assembly process such as vacuum filtration or casting,[228] has attracted extensive interest from researchers because of its advantages such as high thermal stability, low thermal expansion coefficient (< 10 ppm/K), tunable optical properties and superior mechanical properties.[229] Recent studies have demonstrated that CNP has great potential for applications in many interdisciplinary fields such as energy storage electrodes and separators,[44, 185] EMI shielding materials,[230, 231] electronic and photonic devices,[232, 233] etc.

It should be pointed out that the mechanical properties of CNP are sensitive to moisture due to the hydrophilic nature of cellulose, which significantly limits the practical application of CNP in high-moisture environments. To address this issue, several hydrophobic modification approaches such as physical adsorption, esterification, and polymer grafting have been developed in recent years.[234] However, most of these modification processes are time-consuming, low efficient and involved in hazardous substances, which show less possibility for commercial application.[145] Therefore,

developing facile and environmentally friendly methodologies to improve the water resistance of CNP is highly desired.

In recent years, chitosan (CS) has emerged a renewable and sustainable polysaccharide with diverse potential applications such as food packaging materials, adsorbents for wastewater treatment, biomedical materials due to its low cost, nontoxicity, biocompatibility, as well as good film-forming and gelling properties.[235] It is worth noting that CS shows good water resistance in neutral and alkaline environments, and it can form strong hydrogen bonding with cellulose due to the presence of abundant surface hydroxyl and amino groups.[236] Therefore, some attempts have been made to improve the wet strength of cellulose paper or CNP by introducing CS as coatings or additives.[237] Blending and Layer-by-Layer (LbL) assembly have been considered as two prevalent methods for this purpose. For example, Toivonen et al.[238] reported the preparation of CNF/CS film by blending CNF suspension and CS solution, followed by a casting process. It was found that the CNF/CS (80/20 w/w) film showed an ultimate wet strength up to 100 MPa. Zhao et al.[239] systematically compared the mechanical, optical, and barrier properties of CNF/CS films produced by two different methods (blending vs. LbL). Results indicated that visible agglomeration occurred in the blending process, resulting in decreased mechanical strength, increased opacity, and inferior barrier property. While the agglomeration can be efficiently avoided in the LbL assembly process, which enabled the formation of compacted structure of CNF/CS films with higher mechanical strength and better barrier property. Although LbL assembly technique shows many advantages and has been used for development of various functional materials,[240] large-scale processing of CNF and CS by LbL assembly seems to be challenging. Thus, developing simple and effective method for the preparation of CNF/CS films is highly desired.

In addition to wet strength, antimicrobial activity can be imparted to CNP by introducing CS, due to the presence of positively charged amino groups in the CS molecule backbone. Nevertheless, the moderate antibacterial activity of CS cannot meet the requirement of most practical applications.[241] It is worth mentioning that the antimicrobial activity of CS could be significantly enhanced upon chlorine bleach treatment, in which the amino groups can be transformed into N-halamines, resulting in CS based N-halamines (usually denoted as CS-Cl).[242] Note that the N-halamines are compounds containing one or more nitrogen-halogen covalent bonds which is generated by halogenation of imide, amide, or amine groups.[243] The antimicrobial activity is attributed to the fact that positive halogens in the N-halamine structure can be transferred to appropriate receptors in the cells, eventually causing the bacteria killed.[244] More importantly, after the halide atoms are consumed, the antimicrobial activity of N-halamines can be easily recovered by recharging them with halogenation agents.[243]

Motivated by the above discussions, this project is aimed to functionalize CNP with CS and the followed halogenation to achieve water resistance and antibacterial property. As illustrated in **Fig. 3-1**, CNP is firstly immersed in CS solution and the CS functionalized CNP (CNP/CS) could be obtained after drying. Afterwards, halogenation of CS is performed by immersing the CNP/CS into NaClO solution, resulting in the CNP/CS-Cl. To the best of our knowledge, this is the first report on the functionalization of CNP with CS-Cl. This study could supply a facile and sustainable strategy to functionalize CNP and expand its potential applications.

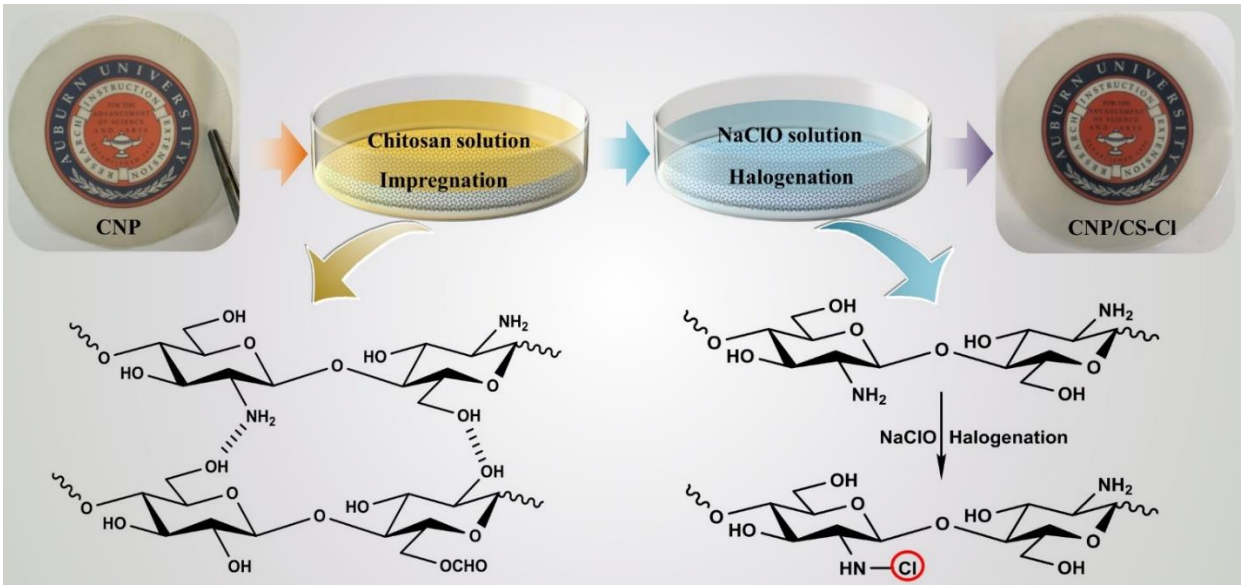

Figure 3-1. Schematic process flow diagram for the functionalization of CNP including the CS impregnation and halogenation of CS. The corresponding reaction schemes show the hydrogen bonding between CNFs and CS, and halogenation of CS.

3.2 Experimental section

3.2.1 Materials

CNFs aqueous suspension (1.0 wt.%) was produced from paper mill sludge according to the procedure reported in Chapter 2. Acetate acid, sodium hydroxide, sodium hypochlorite aqueous solution (14.0%), potassium iodide, and sodium thiosulfate (99%) were purchased from VWR, USA. Chitosan with deacetylation degree of 85% and molecular weight of 310-375 kDa was purchased from Sigma-Aldrich, USA. *Staphylococcus aureus* (*S. aureus* ATCC 6538, gram-positive) and *Escherichia coli* (*E. coli* O157:H7 ATCC 43895, gram-negative) were provided by American Type Culture Collection, Rockville, MD. Trypticase soy agar was purchased from Difco Laboratories, Detroit, MI. All reagents were used as received without further purification.

3.2.2 Preparation of CNP

CNP samples were prepared from the optimized CNF (with FA hydrolysis of 4 h) in Chapter 2. Briefly, 40 mL of the CNFs suspension (1.0 wt.%) were diluted with 160 mL deionized (DI) water. The diluted CNFs suspension was further mixed uniformly using magnetic stirring for 2 h. Afterwards, the mixed CNFs suspension was poured into a filtration setup with a polypropylene filter membrane with the diameter of 100 mm and pore size of 0.45 μm. After filtration, the obtained wet CNP was covered with another filter membrane and dried at 105 ºC for 2 h.

3.2.3 Impregnation of CS into CNP

Firstly, CNP was soaked into 1.5 wt.% CS solution (acetic acid, 2% v/v aqueous solution) at room temperature for 1 h. Then, the CS impregnated CNP (denoted as CNP/CS) was dried on a glass plate under room temperature for 12 h. The dried CNP/CS samples were further immersed in 0.1 mol/L NaOH aqueous solution at room temperature for 1 h to neutralize the residual acetic acid. Finally, the CNP/CS samples were thoroughly washed with DI water and air dried. This procedure was repeated for 1-3 times, and the obtained CNP/CS samples were referred as CNP/CS-1, CNP/CS-2, and CNP/CS-3, respectively.

3.2.4 Halogenation of CNP/CS

In order to transfer part of the amino groups of CS into N-halamine structure. The CNP/CS samples were submerged into 0.6 wt.% NaClO aqueous solution at room temperature for 30 min. Then, the samples were washed thoroughly with DI water and air dried. The chlorinated CNP/CS samples were denoted as CNP/CS-Cl.

3.2.5 Characterizations

3.2.5.1 Quantification of active chlorine content

The active chlorine content of CNP/CS-Cl samples was determined using an iodometric/thiosulfate titration method reported previously. Briefly, the CNP/CS-Cl was cut into small pieces and 0.1 g of the sample was put into a flask containing 20 mL DI water, 10 µL of 0.1 N acetic acid, and 0.2 g of potassium iodine. The mixture was stirred at 200 rpm at room temperature for 20 minutes. Then, 5 drops of 1 wt.% starch aqueous solution was added into the flask and the mixture was stirred for another 5 minutes. Finally, the formed iodine was titrated by 0.001 N sodium thiosulfate aqueous solution. In addition, 0.1 g of the un-chlorinated CNP/CS as control sample was treated under the same conditions. The active chlorine content was calculated by the Equation (1), as follows:

$$Cl\ \% = \frac{35.45\times(V_{Cl}-V_0)\times10^{-3}\times0.001}{2\times W}\times 100 \qquad (1)$$

where V_{Cl} and V_0 are the volumes (mL) of 0.001 N sodium thiosulfate consumed in the titration of the CNP/CS-Cl and CNP/CS samples, respectively. W is the dry weight of CNP/CS-Cl sample.

The active chlorine content of the CNP/CS-Cl sample was calculated to be 0.45 ± 0.05%. Based on the dry weight of CS, the active chlorine content will be around 2.85%.

3.2.5.2 Antimicrobial efficacy test

The antimicrobial efficacy of pure CNP and functionalized CNP samples against gram-positive *S. aureus* ATCC 6538 and gram-negative *E. coli* O157:H7 ATCC 43895 strains was evaluated

following the AATCC Test Method100-2400 with a slight modification. A single colony of each bacterium was transferred into 15 mL of Trypticase soy broth and incubated at 37 °C for 16 h. The culture was washed twice with Butterfield's phosphate buffer by centrifugation and was re-suspended in the same buffer. Bacterial population was estimated by the absorbance at O.D. $_{640\ nm}$ and the inoculum with the designated population was prepared. Prior to the antibacterial test, the samples were cut into 1 inch × 1 inch specimens. Firstly, a pair of the specimens were placed on a sterile plate. Then, an aliquot of 25 µL of the inoculum was added onto the center of one of the specimens, and the other specimen was overlaid on the previous specimen to ensure complete contact with the inoculated bacteria. After contacting for 5, 10, and 30 min, the specimens were immediately immersed in 5 mL of sterile 0.01 N sodium thiosulfate solution to quench the residual chlorine. Afterwards, the mixture was vortexed vigorously for 2 min to detach survived bacteria from the specimens. After vortexing, the liquid part for each sample was tenfold serial diluted and each dilution was plated on a Trypticase soy agar plate, respectively. Finally, all the plates were incubated at 37 ºC for 48 h and bacterial colonies were enumerated and recorded for antimicrobial efficacy analysis.

3.2.5.3 Fourier transform infrared spectroscopy (FTIR)

FTIR spectra of samples were collected on a Thermo Nicolet 6700 FTIR spectrometer equipped with diamond ATR accessory and OMNIC 7.3 software. The spectra were recorded in the wavenumber range from 4000 to 500 cm^{-1} at a resolution of 4 cm^{-1}.

3.2.5.4 X-ray photoelectron spectroscopy (XPS)

XPS spectra of samples were collected on a photoelectron spectrometer (EscaLab Xi+, Thermo Fisher Scientific) using non-monochromatized Al Kα radiation (1486.6 eV) under the vacuum pressure of 8×10^{-10} Pa. The C1s spectrum (284.8 eV) was used to calibrate the binding energy scale for all the samples.

3.2.5.5 Scanning electron microscopy (SEM) and energy dispersive X-ray spectroscopy (EDS)

The surface and cross-section morphology and elemental compositions of samples were examined by using a field emission scanning electron microscope (FESEM, Apreo FE) at 1.0 kV.

3.2.5.6 Optical transmittance

The optical transmittance and haze of samples were measured from 400 to 800 nm using an UV/VIS/NIR spectrophotometer (Lambda 950, PerkinElmer, USA). The haze was measured according to ASTM D1003 standard method, and the haze was calculated by Equation (2),[245] as follows:

$$Haze = \frac{T_d}{T_t} = \left(\frac{T_4}{T_2} - \frac{T_3}{T_1}\right) \times 100\% \qquad (2)$$

where T_d is the transmittance of diffused light, T_t is the total transmittance, T_1 is the reference transmittance, T_2 is the light transmitted by the sample, T_3 is the light scattered by the instrument, and T_4 is the light scattered by both the sample and instrument.

3.2.5.7 Water contact angle

Static water contact angle of samples was measured on a contact angle goniometer (Rame-Hart model 200) at room temperature. The contact angle was determined immediately after the water

droplets placed on the film surface. Three measurements were performed for each sample and the averaged value was reported.

3.2.5.8 Water uptake ratio

Water uptake ratio was measured by calculating the weight change of samples before and after immersion in DI water at room temperature. Briefly, the samples were cut into strips and the strips were transferred to a vacuum oven at 60 ºC for 24 h to eliminate any moisture. Afterwards, the strips were immediately weighted separately, and the weight of each of strips was noted as M_0. Then, the strips were immersed in DI water for 30 min. After that, the strips were weighted after removing any free water by using a blotting paper, and the weight of each of strips was noted as M_1. Finally, the water uptake ratio was calculated by the Equation (3), as follows:

$$Water\ uptake\ ratio = \frac{M_1 - M_0}{M_0} \times 100\% \qquad (3)$$

3.2.5.9 Tensile test

Dry and wet mechanical properties of the samples was evaluated by an Instron 4465 universal testing machine following the TAPPI standard method (TAPPI T497 and TAPPI T456). The samples were cut into 1 cm × 5 cm strips and placed at the conditions of 50% RH and 23 °C for at least 24 h before testing. Crosshead speed was set at 5 mm/min and the initial distance between the two clamps was set to 20 mm. The results were reported as a mean value averaged from five measurements for each sample.

3.2.5.10 Density and porosity measurement

The CNP and CNP/CS samples were cut into 3 cm × 3 cm square specimens and placed into an oven at 105 °C for 24 h for completely drying. The density of samples was calculated based on the dry weight and volume of the specimens. For each sample, the measurements were conducted in triplicate. The corresponding porosity was calculated according to the Equation (4), as follows:

$$Porosity = \left(1 - \frac{\rho_1}{\rho_2}\right) \times 100\% \qquad (4)$$

where ρ_1 is the density of the sample, ρ_2 is the density of cellulose (1.5 g/cm^3).

3.2.5.11 Barrier property test

Water vapor transmission rate (WVPR) and water vapor permeability (WVP) of the samples were examined using a desiccant method according to the ASTM Standard E96. Briefly, the samples were cut into round specimens with the diameter of 75 mm. Prior to testing, the specimens were placed at the conditions of 50% RH and 23 °C for at least 24 h. Then, the specimens were sealed on test cups containing anhydrous calcium chloride as desiccants. The test cups were placed at the conditions of 50% RH and 23 °C. Each of the test cups was periodically weighed at 24-hour intervals for at least five times. The slope of weight gain vs. time was calculated by linear regression. WVPR can be further calculated as the slope (g/day) divided by the cup mouth area (m^2). The WVP was calculated based on the Equation (5), as follows:

$$WVP = \frac{WVPR \times t}{S \times \Delta\%\, RH} \qquad (5)$$

where *t* is the thickness of the specimen, *S* is the saturation vapor pressure of water at the test temperature (*S* at 23 °C is 2.812 kPa), the RH gradient is 50% in this study.

The oxygen transmission rate (OTR) and oxygen permeability (OP) were measured using a Labthink OX2/230 Oxygen Transmission Rate Tester following the ASTM Standard D 3985. Before testing, the samples were placed at the conditions of 50% RH and 23 ℃ for at least 24 h. The sample was exposed to 100% O_2 on one side and to oxygen-free N_2 on the other side. The measurement was carried out under the conditions of 50% RH, 23 ℃ and normal atmospheric pressure. The OP was calculated based on the formula as Equation (6), as follows:

$$OP = \frac{OTR \times t}{\Delta P} \qquad (6)$$

where t is the thickness of the specimen, ΔP is the O_2 partial pressure difference between the two sides. For both the WVPR and OTR test, each of the samples was determined in duplicate and the averaged value with standard deviation was reported.

3.3 Results and discussion

3.3.1 Optimization of CS impregnation

Firstly, we optimized the influence of CS amount on the mechanical properties of the obtained CNP/CS samples by repeating the impregnation process for 1-3 times. As summarized in **Table 3-1**, the CS weight gain significantly increased from 9.17% to 31.12% as the impregnation process repeated for 1 to 3 times. **Fig. 3-2** shows the strain-stress curves of pure CNP and CNP/CS samples and the corresponding tensile strength, Young's modulus, and toughness. Compared with pure CNP, the tensile strength remarkably increased by 18% and 42% after impregnating with CS for 1 and 2 times, respectively. This result is mainly attributed to two reasons: 1) As illustrated in **Fig. 3-4**, the CNP was swelled in the CS solution during the impregnation process. Thus, CS could penetrate into the small voids among CNFs and eventually filled up the voids upon drying, which

would fix the interstitial defects of CNP.[246] This speculation can be verified by the obvious increment in density after impregnation, as indicated in **Table 3-1**; 2) As shown in the reaction scheme of CNFs and CS in **Fig. 3-1**, the introduction of CS within the CNP could interact with CNFs through hydrogen bonding, covalent bonding, and electrostatic interaction.[200] These extra and abundant bonds or interactions are beneficial to more mechanically stable structure of the obtained CNP/CS under tension. However, as the impregnation process was further increased to 3 times, an obvious decrease in tensile strength (CNP/CS-3) was observed when compared to that of CNP/CS-2. The possible reason for this result is mainly due to the fact that 2-time repeated impregnation was sufficient to ensure excellent filling of the defects of CNP and efficient interaction with CNFs, while excess CS only results in increased thickness of the CNP/CS-3. It should be noted that the pure CS film exhibits inferior tensile strength (only 75.5 MPa) when compared to CNP. Thus, excess CS coating would definitely lower the tensile strength of CNP/CS-3. As shown in **Fig. 3-3**, compared to the pure CNP, the pure CS film shows a much higher tensile strain of around 42.5% with a much lower Young's modulus (0.8 GPa), indicating excellent flexibility and ductility. Thus, the introduction of CS leads to enhanced flexibility and ductility of the CNP-CS samples, which can be proved by the increment in tensile strain and the diminution of Young's modulus with the increasing impregnation times. As indicated in **Fig. 3-2d**, the CNP/CS-2 sample exhibits the highest toughness of 13.01 MJ/m^3, which almost doubled that of the pure CNP. It is worth noting that this simple impregnation process enabled a notable enhancement in mechanical strength of CNP, while the traditional blending method led to significantly reduced mechanical strength.[247] As pointed by Zhao et al.,[239] the declined mechanical strength was mainly attributed to the agglomeration through electrostatic interaction between CNF and CS. While the current impregnation process can be somehow considered as a modified LbL

process with only two layers, in which the agglomeration could be avoided. Although the pure CNP shows a much larger thickness (50 μm) than the bilayer (mostly below 1 μm) in the conventional LbL assembly process, two repeating impregnation processes are sufficient for CS to penetrate into the interior of CNP, as verified by the SEM and EDS results. Considering the tensile strength, flexibility, and toughness, CNP/CS-2 can be regarded as the optimized sample. Without further specification, CNP/CS-2 (simplified as CNP/CS) was used to make CNP/CS-Cl in the following sections.

Table 3-1. Summary of the weight, thickness, density, and CS weight gain of CNP/CS samples with different coating times.

Samples	**Weight (g)**	**Thickness (μm)**	**Density (g/cm^3)**	**Porosity (%)**	**CS weight gain (%)**
Pure CNP	0.400 ± 0.008	50 ± 1	1.257 ± 0.023	16.20 ± 0.28	-
CNP/CS-1	0.437 ± 0.012	53 ± 1	1.296 ± 0.026	13.60 ± 0.32	9.17 ± 0.75
CNP/CS-2	0.475 ± 0.010	55 ± 1	1.357 ± 0.036	9.53 ± 0.25	18.75 ± 1.47
CNP/CS-3	0.514 ± 0.015	58 ± 1	1.393 ± 0.046	7.13 ± 0.31	31.12 ± 2.63

Note: the diameter of CNP and CNP/CS samples is 9 cm; the density of pure CS film is 1.412 ± 0.051 g/cm^3.

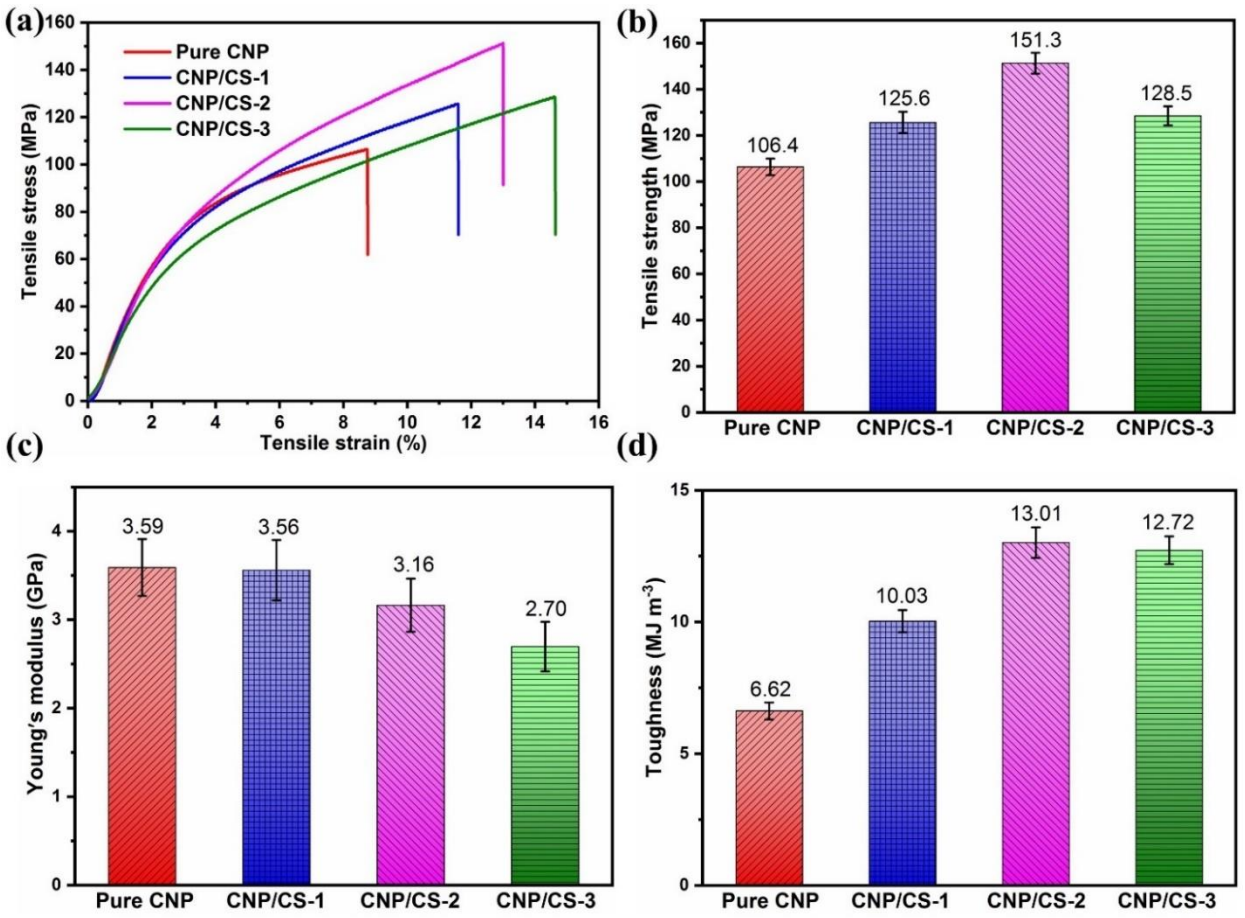

Figure 3-2. Strain-stress curves of CNP/CS with different coating times and pure CNP samples (a), and the corresponding tensile strength, Young's modulus, and toughness (b-d).

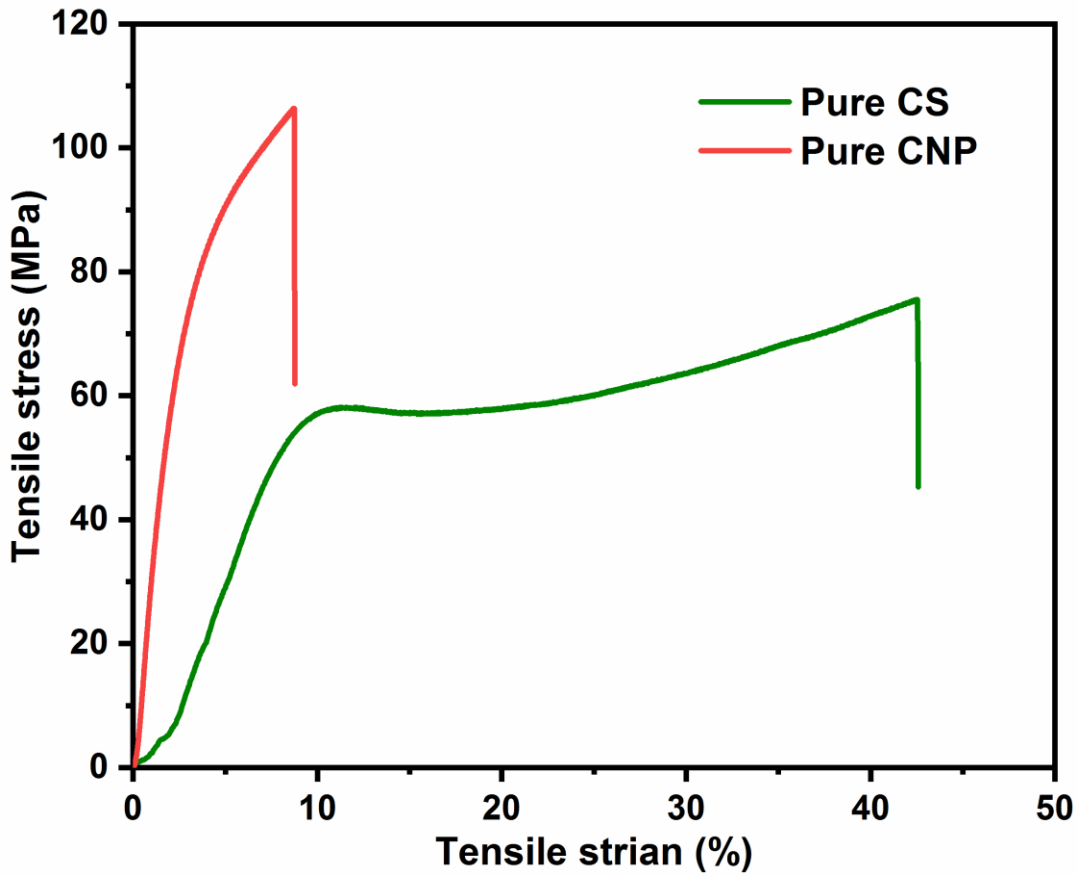

Figure 3-3. Strain-stress curves of pure CS and pure CNP samples.

3.3.2. Optical property

The light transmittance of pure CNP and CS functionalized CNP was further evaluated, and the obtained UV-Vis transmittance spectra are shown in **Fig. 3-5a**. It is reported that the optical properties of CNP are mainly affected by its surface roughness and porosity.[248] More specifically, the surface roughness plays an important role on the back scattering while the porosity of the specimen affects the forward scattering very much.[245] According to the definition of total transmittance and haze described in the experimental section, smaller back scattering will result in a higher total transmittance, whereas smaller forward scattering will lead to a lower haze. As

shown in **Fig. 3-7a**, entangled nanofiber network can be clearly seen in the SEM image of pure CNP, indicating a rough and porous surface. By contrast, compact and smooth surface is observed for the CNP/CS sample due to the introduction of CS coating. As verified in the SEM images and **Table 3-1**, both the surface roughness and porosity of pure CNP are reduced after introducing CS. Thus, the CNP/CS sample exhibits both smaller back scattering and forward scattering when compared to pure CNP, as illustrated in **Fig. 3-4**. As a result, CNP/CS shows a higher transmittance and a lower haze than pure CNP, as presented in **Fig. 3-5**. Specifically, the light transmittance increased from 75% to 83% at 550 nm, and the optical haze significantly decreased from 78% to 42% at 550 nm after introducing CS.

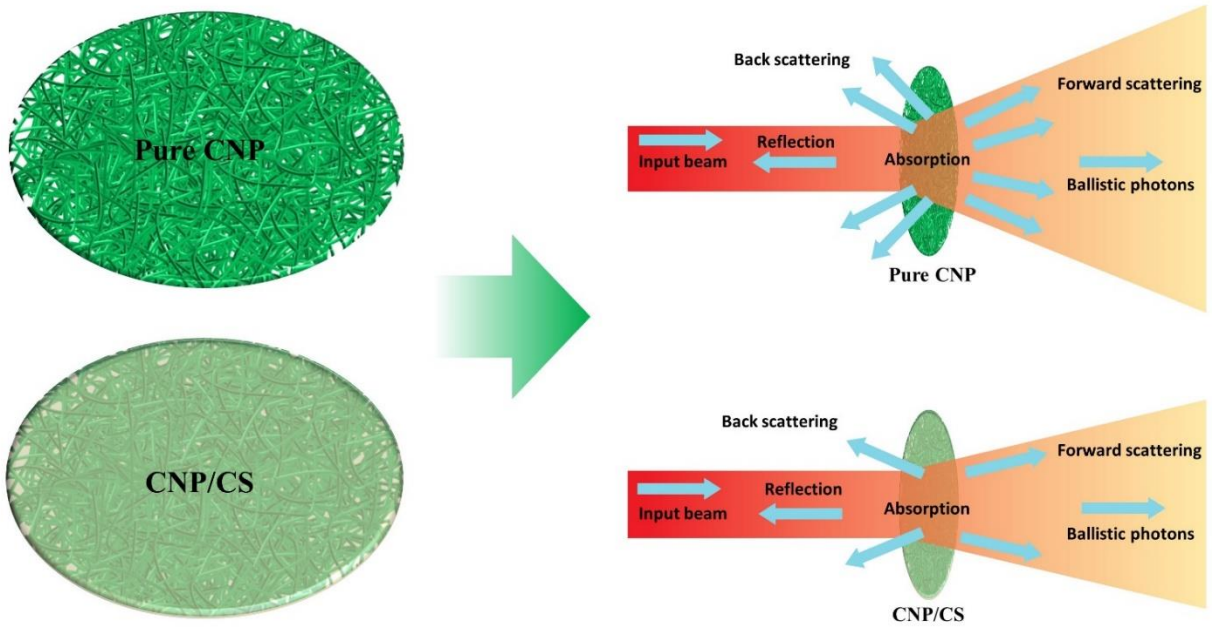

Figure 3-4. Schematic illustration of the structures of pure CNP and CNP/CS samples, and the schematic sketch showing light propagation through the corresponding samples.

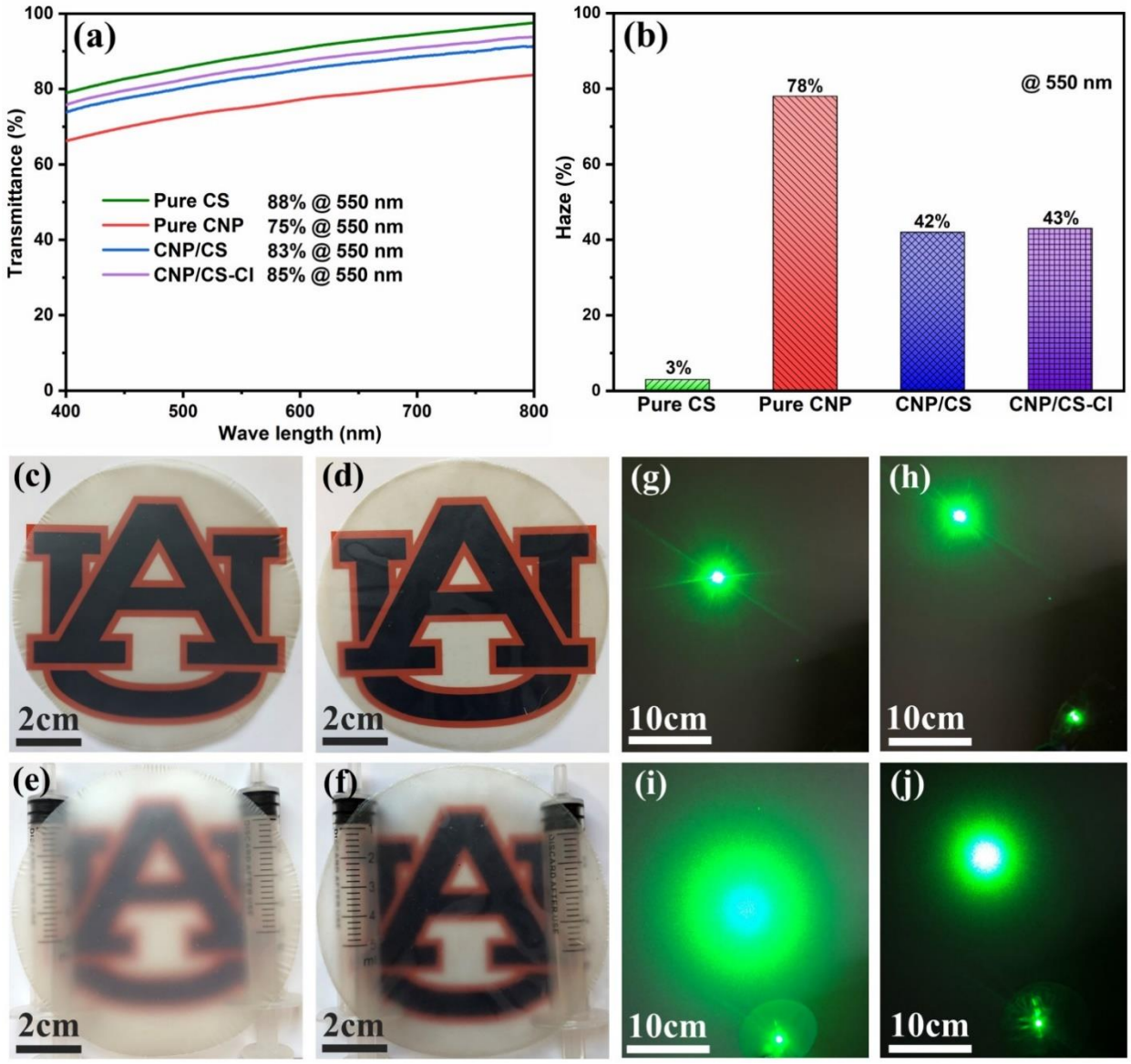

Figure 3-5. UV-Vis transmittance spectra (a) of pure CS, pure CNP, CNP/CS and CNP/CS-Cl samples and the corresponding optical haze at 550 nm (b). Digital photographs of pure CNP (c) and CNP/CS (d) closely contact underneath the patterned paper. Digital photographs of pure CNP (e) and CNP/CS (f) when they were lifted up with a certain distance (1.5 cm) from the patterned paper. Digital photographs showing the illuminated circular area from the bare laser (g), the laser passed through pure CS film (h), the laser passed through pure CNP (i), and the laser passed through CNP/CS (j).

Figs. 3-5 (c-j) vividly display the difference in light transmittance and haze of the CNP before and after impregnating CS. For example, as indicated in **Figs. 3-5 (c-f),** when the samples were placed

on a patterned paper, the image under the CNP/CS was much clearer than that under the pure CNP, indicating enhanced transmittance. When the samples were lifted with a certain height from the patterned paper, it can be clearly seen that the pattern under the CNP/CS was much clearer than that under the pure CNP, implying the decreased optical haze. Moreover, as shown in **Figs. 3-5 (g-j)**, when a laser with a wavelength of 532 nm passed through the pure CS film, the illuminated circular area is very closed to that illuminated from bare laser, which is due to the fact that pure CS film has a compact structure with high transparency and low haze. Notably, a much larger illuminated circular area can be observed when the laser pass through the pure CNP. This result is mainly attributed to the light scattering effect that is derived from the big difference between the refractive indexes of air (1.0) and cellulose film (1.51-1.55).[249] In contrast, the illuminated circular area remarkably decreased when the laser passed through the CNP/CS, indicating the optical haze significantly reduced. This phenomenon is due to the fact that most of the voids inside the CNP were filled up with CS, and CS has a similar refractive index (1.51-1.55) to cellulose film.[250] In addition, the CNP/CS-Cl exhibits a slightly increased total transmittance than CNP/CS after chlorination, which is probably due to some of impurities containing chromophoric groups were bleached during the chlorination process. As indicated in **Fig. 3-5b**, the chlorination seems not to affect the optical haze of CNP/CS.

3.3.3 Chemical and structural characterization

The chemical structure of pure CNP and functionalized CNP samples was investigated by FTIR and XPS. As shown in **Fig. 3-6a**, the characteristic peaks of cellulose Iβ at 3335, 2918, 1645, 1429, 1161, 1105, and 897 cm^{-1} can be observed in the spectrum of pure CNP.[112, 251] It should be pointed out that the band at 1717 cm^{-1} is attributed to the C=O stretching from ester groups, which has

been reported in our previous study.[252] After impregnating CS, the typical bands of CS can be observed in the FTIR spectrum of CNP/CS. For example, the strong band in the range of 3286 and 3353 cm^{-1} is attributed to the O-H and N-H stretching, and the peaks at 2920 and 2854 cm^{-1} correspond to the C-H symmetric and asymmetric stretching, respectively.[253] The band at 1647 cm^{-1} is assigned to the C=O stretching of amide I, and the band at 1316 cm^{-1} corresponds to C-N stretching of amide III, both of which confirm the presence of residual N-acetyl groups. The peak at 1574 cm^{-1} is attributed to the N-H bending of the primary amine. The peaks at 1420 and 1376 cm^{-1} are caused by CH2 bending and CH3 symmetrical deformations, respectively. The band at 1152 cm^{-1} corresponds to the asymmetric stretching of C-O-C bridge.[254, 255] It can be seen that the bands in the spectrum of CNP/CS-Cl are nearly parallel with the bands in the spectrum of CNP/CS, indicating that the main CS structure remains unchanged after halogenation. It is worth noting that the intensity of the band at 1574 cm^{-1} becomes weaker after chlorination treatment, which is probably due to the fact that part of the N-H bonds in the primary amine are converted to N−Cl bonds. As shown in **Fig. 3-6b**, a stronger C 1s peak and a new N 1s peak appear in the XPS spectrum of CNP/CS when compared to that of the pure CNP, which is due to the formation of CS coating on the CNP surface. In addition, compared with the XPS spectrum of CNP/CS, two new Cl 2s and Cl 2p core level peaks appear in the XPS spectrum of CNP/CS-Cl, indicating the N−Cl bonds were formed in the CS after chlorination.[242]

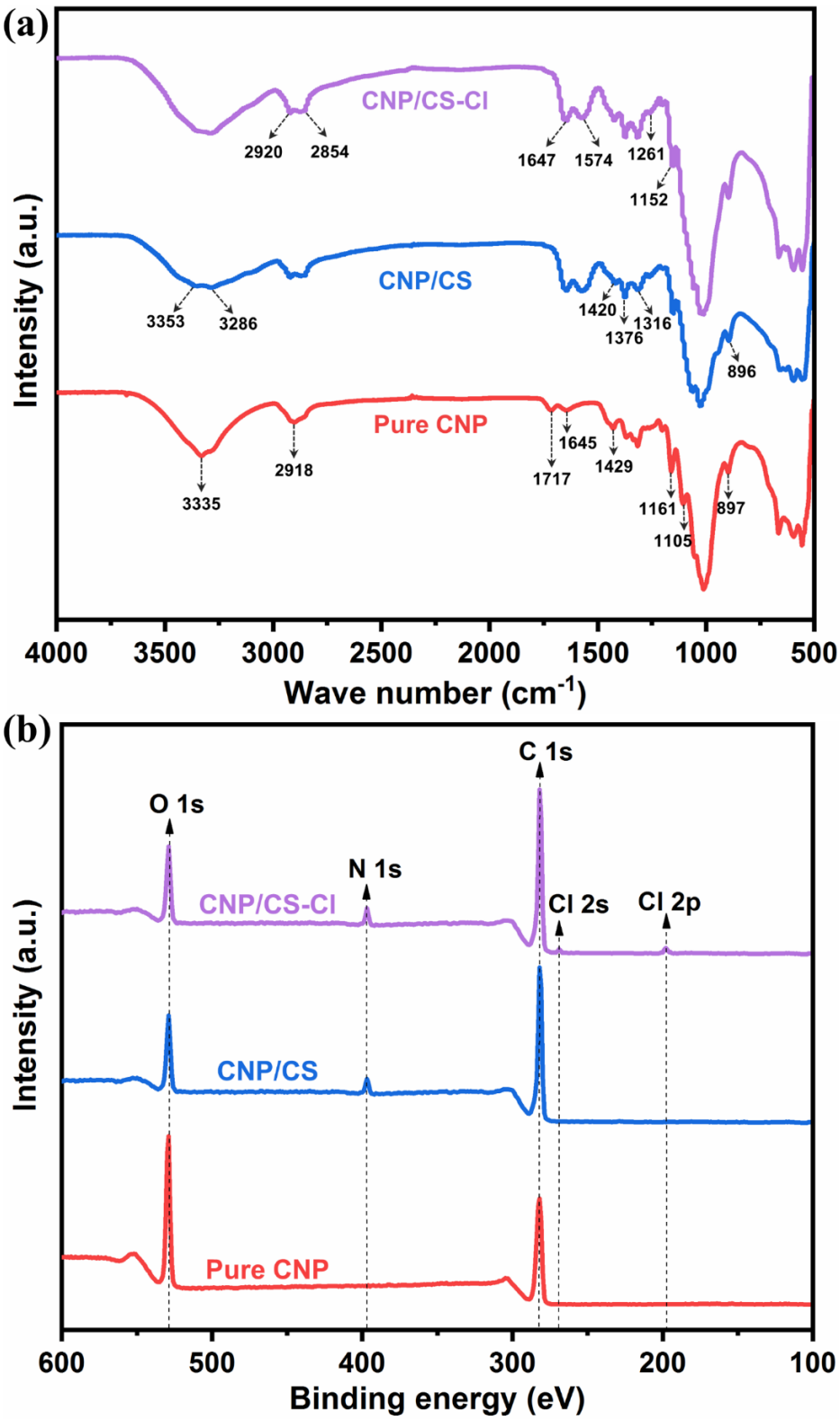

Figure 3-6. FTIR spectra (a) and XPS spectra (b) of pure CNP and functionalized CNP samples.

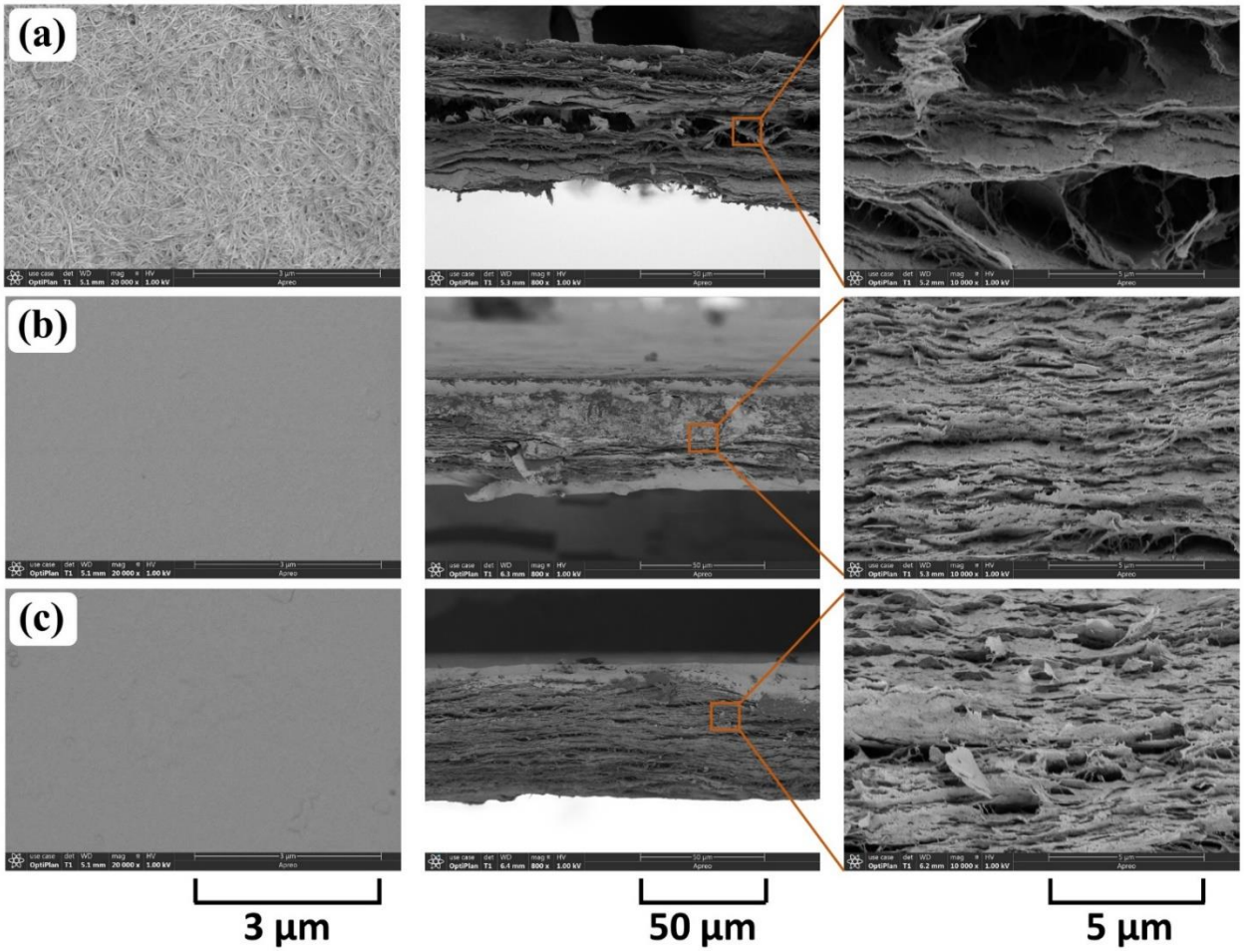

Figure 3-7. SEM surface and cross-section images of pure CNP (a), CNP/CS (b), and CNP/CS-Cl (c).

SEM analysis was further performed to examine the surface and cross-section morphology of CNP before and after impregnation. As shown in **Fig. 3-7a**, the pure CNP sample shows randomly entangled CNFs on the surface and a lamellar cross-section structure with notable gaps between layers. As indicated in **Fig. 3-7b**, the CNP/CS exhibits a much smoother surface and a much denser interlayer structure, since most of the voids between CNFs are filled with CS. When compared to the interior structure of CNF/CS film fabricated by LbL assembly,[256] the current one is slightly looser. However, the LbL assembly process is kind of complicated, since 150 bi-layer repetitive

units formed only a 1.5 μm thick film. Notably, the CNP/CS with a thickness of 55 μm can be easily prepared through two repeating impregnation processes. In addition, the current impregnation process can be potentially extended to the roll-to-roll coating process, which is more efficient and has greater potential to be scaled up than the conventional LbL assembly and blending plus casting methods. After further chlorination treatment, the obtained CNP/CS-Cl displays similar surface morphology to the CNP/CS with slightly expanded interior lamellar structure (**Fig. 3-7c**). This phenomenon is probably caused by the swelling of the CNP/CS structure during chlorination treatment. As indicted in the EDS spectrum of CNP/CS-Cl interior lamellar structure (**Fig. 3-8**), the Cl element is present in the lamellar structure of the CNP/CS-Cl. This result further indicates that the CS can not only retain on the surface of pure CNP, but also penetrate into the interior lamellar structure of the pure CNP throughout in the thickness direction.

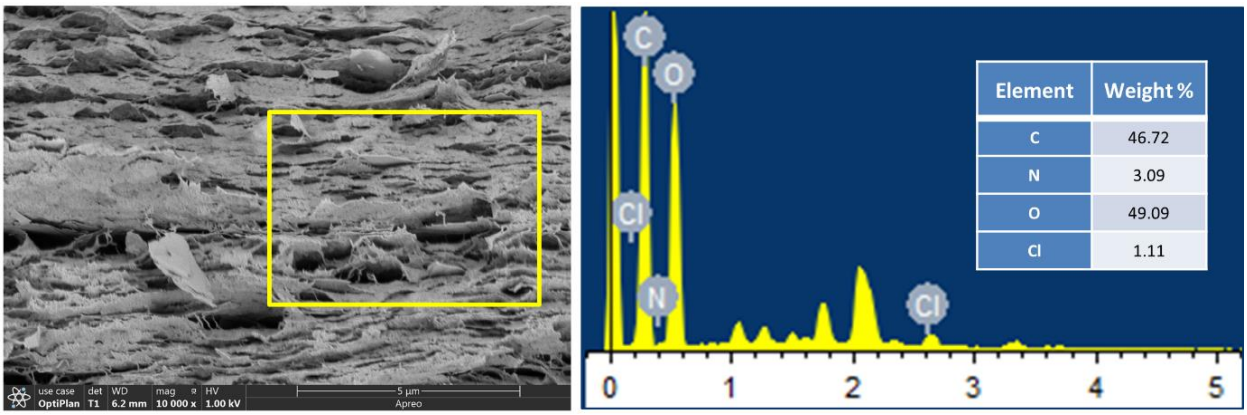

Figure 3-8. EDS spectra of CNP/CS-Cl interior lamellar structure.

3.3.4 Mechanical properties and surface wettability

As indicated in **Fig. 3-9a** and mentioned earlier, the impregnation of CS significantly improved the mechanical propeties of pure CNP in the dry state. Moreover, **Fig. 3-9b** displays the strain-

stress curves of pure CNP and functionalized CNP under the wet state. It can be clearly seen that the tensile strength of pure CNP remarkably decreased from 106 MPa (dry state) to around 7 MPa (wet state), whereas the tensile strength of CNP/CS sample maintained a relatively high wet tensile strength over 40 MPa which meets the required mechanical strength of a variety of packaging materials. The poor wet strength of pure CNP is mainly due to the hydrophilic surface of CNFs and the presence of numerous small voids within the self-assembled structure. The water molecule can severely interrupt the interfibrillar hydrogen bond among CNFs, leading to the swelling of CNP and a significant drop in mechanical strength.[145]

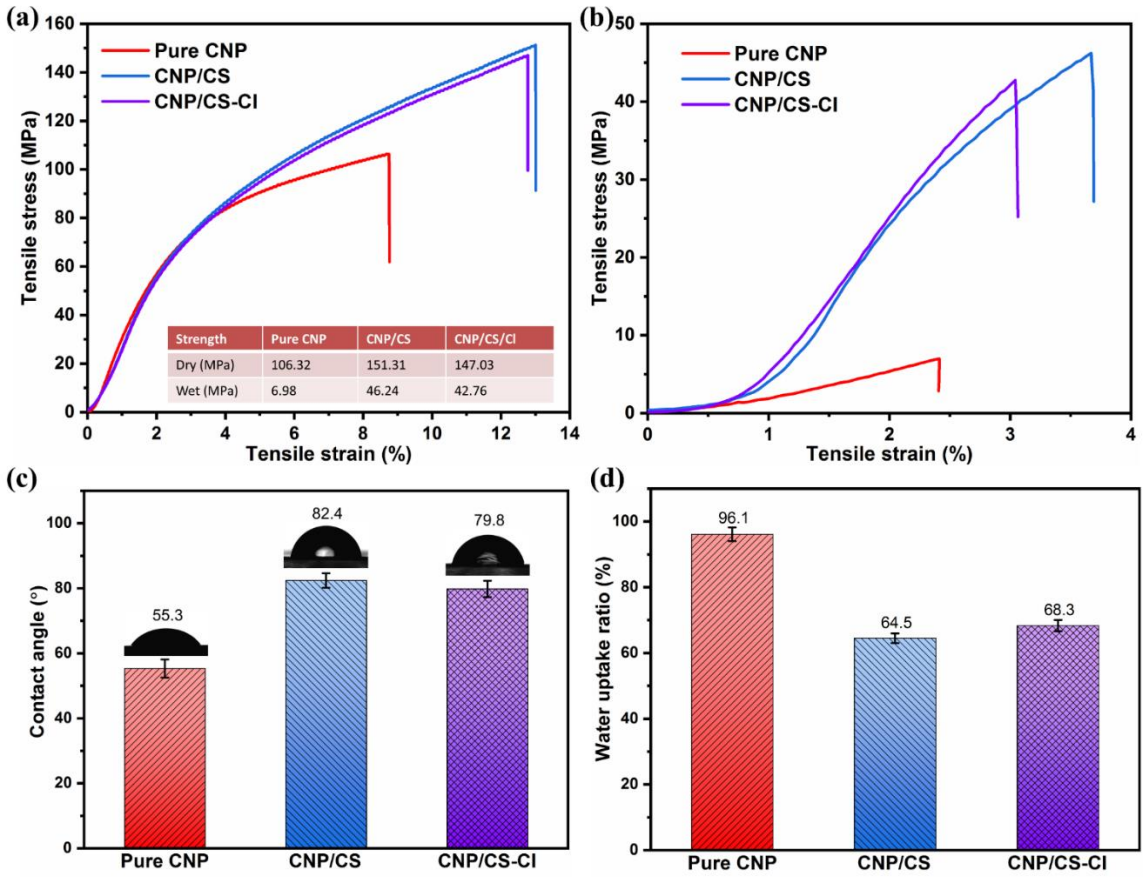

Figure 3-9. Strain-stress curves of pure CNP and functionalized CNP samples at dry state (a) and wet state (b). Water contact angles (c) and water uptake ratio (d) of pure CNP and functionalized CNP samples.

In contrast, the enhanced wet mechanical strength after introducing CS is mainly attributed to the synergetic action of the chemical and physical interactions between CNFs and CS, and the mending effect on the interstitial defects of pure CNP, as mentioned earlier. After halogenation, both the dry and wet strength slightly decreased, which is probably due to the bleaching agent would destroy some of the chemical bonds between CNFs and CS.[257]

Furthermore, water contact angle and water uptake ratio measurements were carried out to investigate the surface wettability of pure CNP and functionalized CNP samples, the results are shown in **Fig. 3-9c** and **Fig. 3-9d**, respectively. As we can see, the pure CNP has a relatively low contact angle of 55.3° due to the hydrophilic nature of CNF, which results in the highest water uptake ratio of 96.1%. After impregnating with CS, the contact angle of CNP/CS dramatically increased to 82.4° and the water uptake ratio reduced to 64.5%. This result is mainly due to the higher surface hydrophobicity and more compact structure of CS coating. After chlorination, the contact angle of CNP/CS-Cl slightly reduced to 79.8°, and the water uptake ratio increased from 64.5% to 68.3%, which are probably due to the introduction of hydrophilic –Cl groups on the CS molecule. As shown in **Fig. 3-10**, after probe ultrasonication in water at a high-power input (500 watts) for 10 min, both the CNP/CS and CNP/CS-Cl strips kept their original shape while the pure CNP strips almost completely disintegrated into many fragments. This phenomenon further proves that the water resistance of CNP can be significantly improved after impregnating with CS.

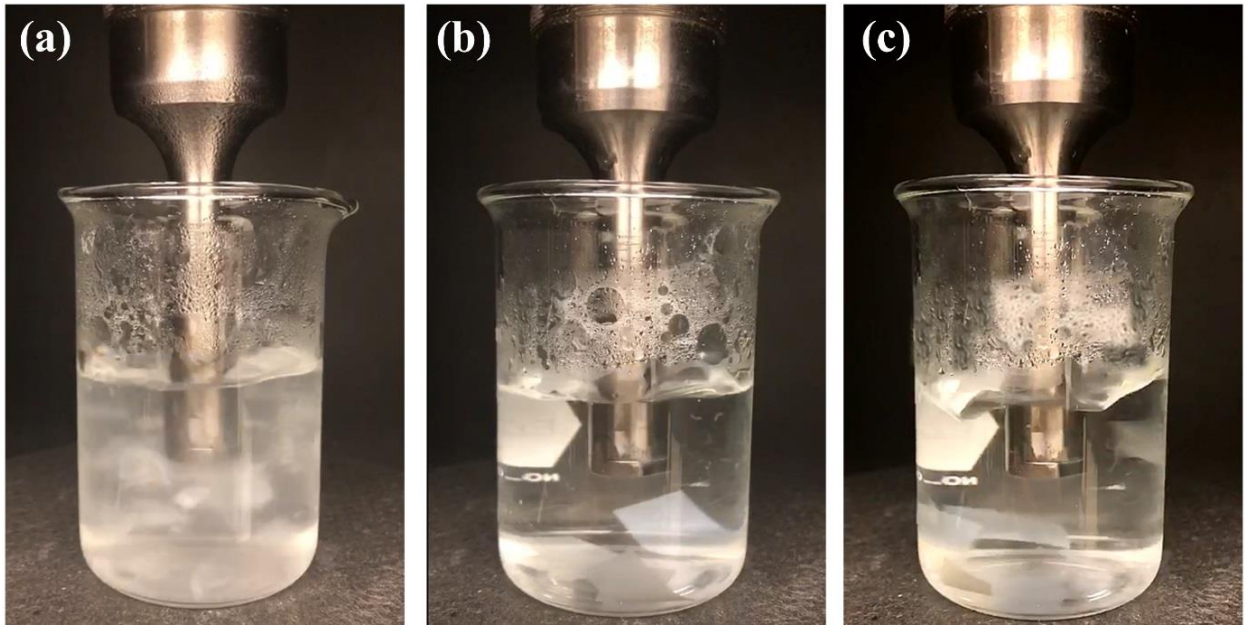

Figure 3-10. Photograph showing the stability of pure CNP (a), CNP/CS (b), and CNP/CS-Cl (c) in water after probe ultrasonication at a high-power input (500 watts) for 10 min.

3.3.4 Antibacterial efficacy

The antibacterial performance of pure CNP and functionalized CNP samples were evaluated against *S. aureus* and *E. coli*. As shown in **Fig. 3-11**, the pure CNP sample shows 66.50% and 56.44% bacterial reductions towards *S. aureus* and *E. coli*, respectively, within 30 min of contact. The bacterial reduction is mainly due to the fact that part of bacteria could adhere onto the porous fragments of CNP, since the pure CNP with poor water resistance were easily swelled and disintegrated into fragments during the vortexing process. Similar phenomenon was observed in the previous study.[244] For the CNP/CS sample, the biocidal activity against *S. aureus* and *E. coli* was significantly enhanced with the bacterial reduction of 97.32% (1.572 log) and 78.22% (0.662 log), respectively, within 30 min of contact. This result is mainly attributed to the modest antibacterial activity of CS, which is well documented in the literature.[242] Notably, after

halogenation of CS, the CNP/CS-Cl sample showed remarkably superior biocidal efficacy against both gram-positive and gram-negative bacteria, i.e., 7.114 log bacterial reduction for *S. aureus* and 7.386 log bacterial reduction for *E. coli* within a relatively short contact time of 10 min, which can be considered as 100% killing of bacteria. Even within 5 min of contact, the CNP/CS-Cl still caused 100% killing of *S. aureus* and 99.997% (4.481 log) reduction of *E. coli*. The rapid biocidal activity is mainly due to the introduction of oxidative Cl^{+} on the chlorinated CS, which can be easily transferred into the cell walls of bacteria upon contact.[244]

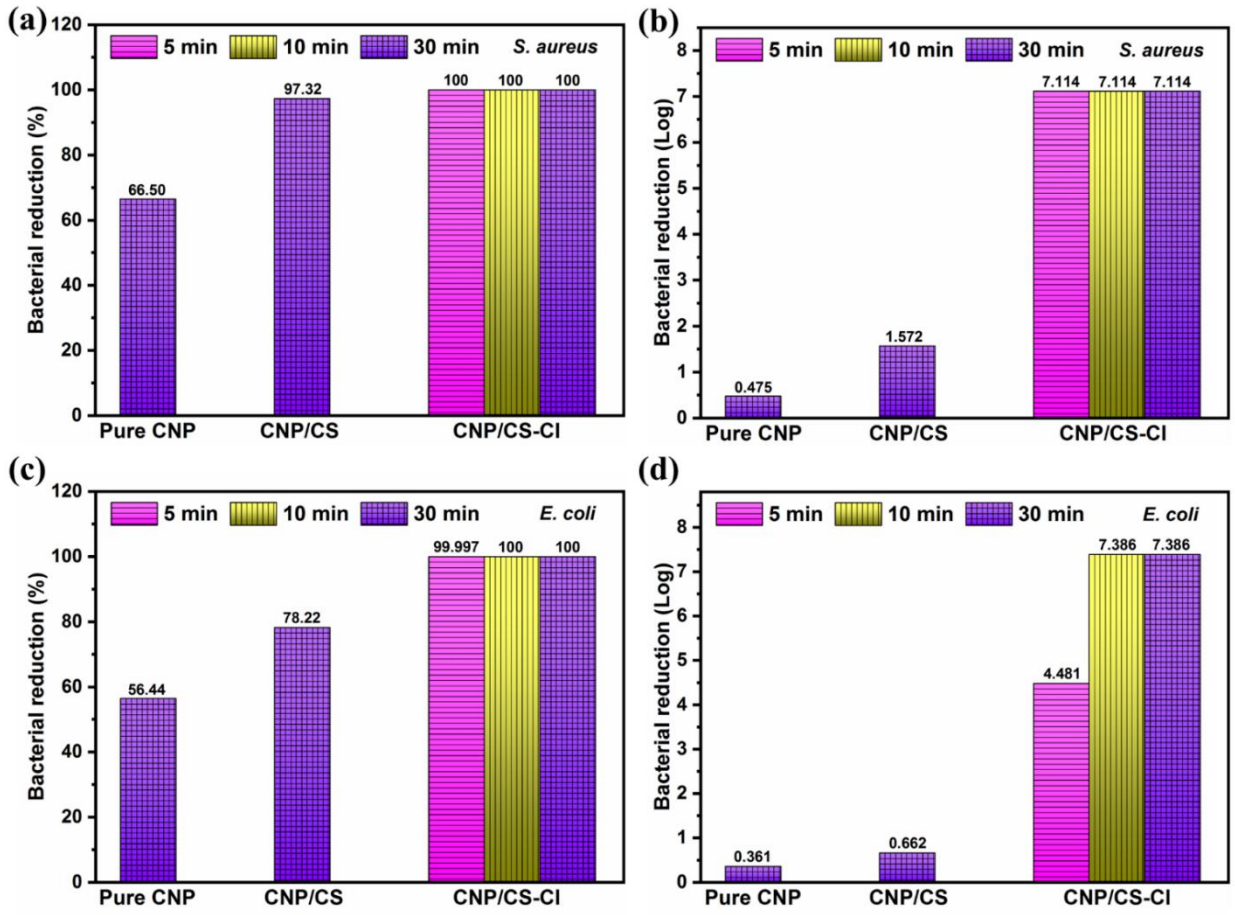

Figure 3-11. Biocidal results of pure CNP and functionalized CNP samples against *S. aureus* (a, b) and *E. coli* (c, d) with different contact time. Inoculum: 7.114 log CFU/sample of *S. aureus*, 7.386 log CFU/sample of *E. coli*.

Fig. 3-12a displays the visibility of bacterial colonies on the plate for comparing the antibacterial activity of CNP/CS and CNP/CS-Cl samples, which vividly demonstrates the significantly enhanced biocidal activity of CNP/CS-Cl after halogenation. In addition, the shelf life stability of the CNP/CS-Cl was examined by tracking the remaining chlorine content over storage time under dark condition. As shown in **Fig. 3-12b**, the chlorine content gradually decreased with the increasing storage time. After 4 weeks storage, the chlorine content decreased from the initial 0.45% to 0.05%, which is mainly due to the hydrophilic nature of CS-Cl. It is reported that the chlorinated CS could absorb moisture from the air, which would dissociate the N–Cl bonds.[244] Nevertheless, all the lost chlorine could be easily recharged by another bleach treatment, similar result was observed in the previous study.[242]

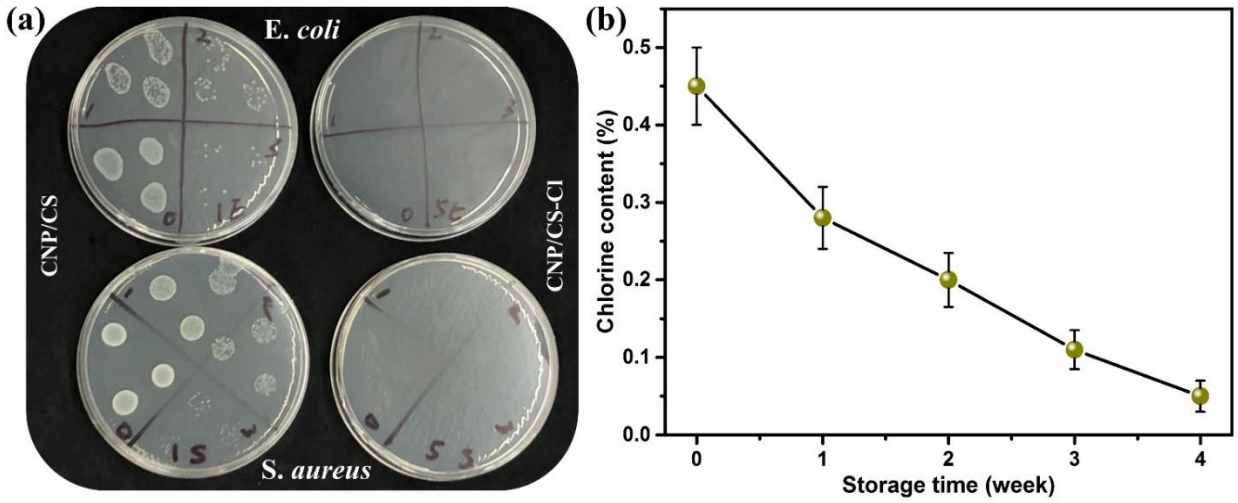

Figure 3-12. (a) Photograph of the plate showing the antibacterial activity of CNP/CS and CNP/CS-Cl towards *S. aureus* and *E. coli*. (b) Storage stability of CNP/CS-Cl in the dark at room temperature.

3.5 Barrier properties

The barrier properties towards water vapor and oxygen of pure CNP and the functionalized CNP samples were further evaluated, and the obtained results are summarized in **Table 3-2**. The pure CNP exhibits a relatively high WVP of 3982 ± 48 g·μm/m^2·day·kPa due to the hydrophilic nature of cellulose. Similar results of the CNP fabricated from other types of CNFs or cellulose nanocrystals (CNCs) were reported in the literature, such as TEMPO-mediated oxidized CNFs (2882-4220 g·μm/m^2·day·kPa),[258] *tert*-Butylamino CNCs (3300 g·μm/m^2·day·kPa).[259] Also, the pure CNP shows a quite good oxygen barrier property with the OP of 0.60 ± 0.15 cm^3·μm/m^2·day·kPa, which is similar to the reported value of CNP made from carboxymethylated CNFs (0.52-0.58 cm^3·μm/m^2·day·kPa).[138, 260] Notably, both the WVP and OP significantly decreased after introducing CS. This result is mainly due to the more compact structure of CNP/CS, as most of the small voids within the pure CNP were filled up with CS during the impregnating process. Compared to CNP/CS, the CNP/CS-Cl sample exhibits slightly higher WVP and OP. As mentioned earlier, the reason for this phenomennon could be the introduction of hydrophilic groups and minor negative effect on the structure of CNP/CS happened during the halogenation process. Based on the above discussion, the functionalized CNP samples exhibit obviously enhanced barrier properties than the pure CNP. As shown in **Fig. 3-13**, the functionalized CNP samples present much superior oxygen barrier propertis (several orders of magnitude lower OTR) than the traditional petroleum-based packaging materials such as PE, PP, PS, and PET. Although the functionalized CNP samples show inferior water vaper barrier properties when compared to conventional non-biodegradable polymers, the WVTR is still much lower than the commercially available biopolymers such as PLA and PCL. In recent years, many countries and regions around the world have enacted regulations to limit the use of non-

biodegradable plastics.[261] Considering the advantages of biodegradability, excellent barrier properties, water resistance, and antibacterial ability, the functionalized CNP presented in the current work could be considered as promising substitutes for non-biodegradable plastics.

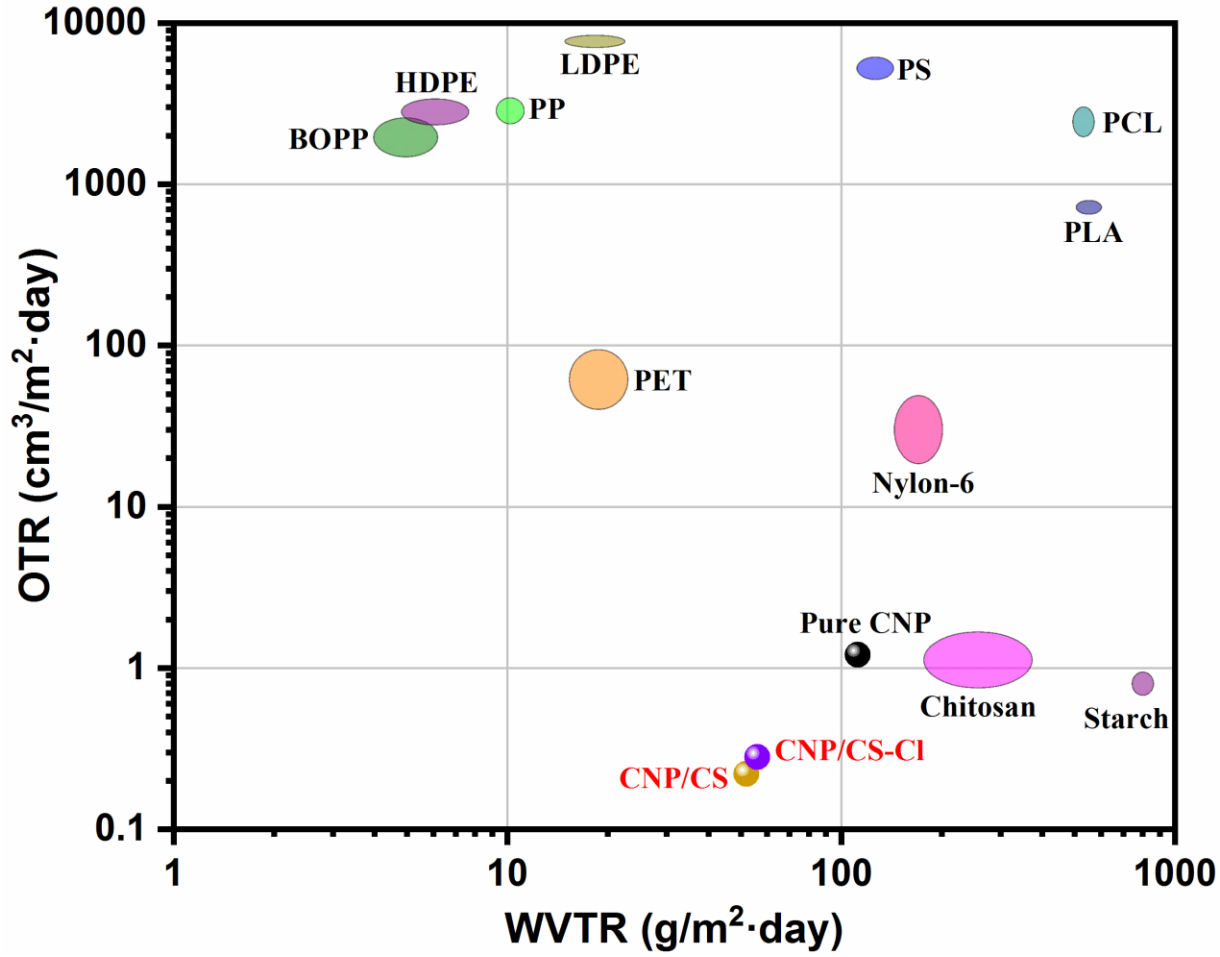

Figure 3-13. Barrier properties comparison for the pure CNP and functionalized CNP with the traditional packaging materials including BOPP (Biaxially oriented polypropylene),[262] HDPE (High-density polyethylene),[262] PP (Polypropylene),[262] LDPE (Low-density polyethylene),[262] PET (Polyethylene terephthalate),[262] PS (Polystyrene),[262] Nylon-6,[262] PCL (Poly-ε-caprolactone),[263] PLA (Polylactic acid),[264] chitosan,[265] and starch.[266]

Table 3-2. Summary of the barrier properties including water vapor transmission rate (WVTR) and water vapor permeability (WVP), oxygen transmission rate (OTR) and oxygen permeability (OP) of pure CNP and functionalized CNP samples.

Samples	**WVTR** $(g/m^2 \cdot day)$	**WVP** $(g \cdot \mu m/m^2 \cdot day \cdot kPa)$	**OTR** $(cm^3/m^2 \cdot day)$	**OP** $(cm^3 \cdot \mu m/m^2 \cdot day \cdot kPa)$
Pure CNP	112 ± 11	3982 ± 48	1.21 ± 0.18	0.60 ± 0.15
CNP/CS	52 ± 6	2034 ± 27	0.22 ± 0.05	0.12 ± 0.04
CNP/CS-Cl	56 ± 5	2190 ± 21	0.25 ± 0.03	0.14 ± 0.02

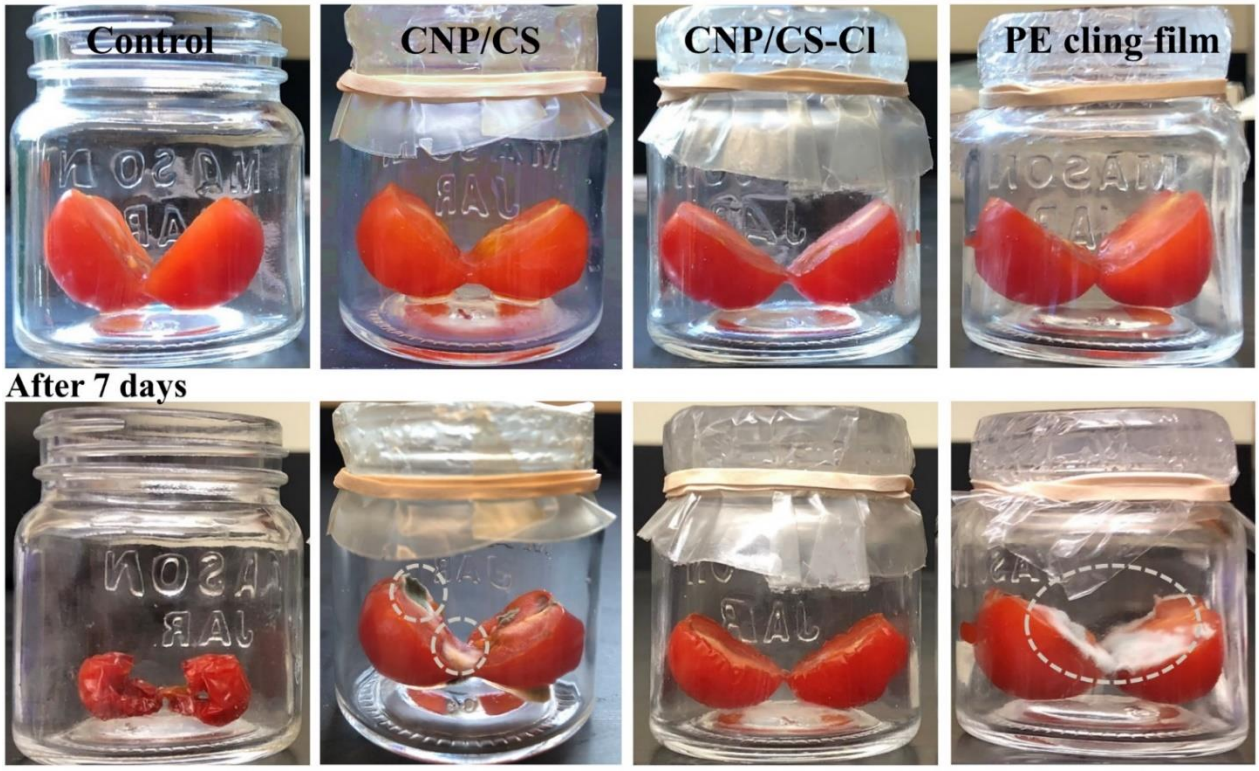

Figure 3-14. Optical images of fresh-cut tomatoes in the jars covered with CNP/CS, CNP/CS-Cl, PE cling film, and without cover (Control). Note: the tomatoes were stored at room temperature for 7 days.

Furthermore, tomatoes preservation experiments were carried out to evaluate the barrier properties of the functionalized CNP samples in comparation with the commercially available PE cling film. As shown in **Fig. 3-14**, after 7 days storage, the fresh-cut tomato was almost completely dried in the control group (without any cover), while the tomato covered by PE cling film still appears fresh with less than 10% weight loss ratio. The tomatoes covered by CNP/CS and CNP/CS-Cl are relatively fresh with the weight loss ratios of 23% and 27%, respectively. Notably, a lot of molds can be observed on the tomato covered by PE cling film, while less molds appeared on the tomato covered by CNP/CS. This observation can be explained from the aspect of the suitable environment for mold growth. It is well known that adequate moisture and sufficient oxygen are two of the most important factors for mold growth. The condition inside the jar covered by PE cling film perfectly meets the requirements for mold growth, since the PE cling film with a low WVTR and a very high OTR can hold most of the moisture and allow the oxygen to easily diffuse into the jar from outside atmosphere. By contrast, the CNP/CS shows a relatively high WVTR and a very low OTR, as indicated in **Fig. 3-13**. Thus, less moisture and oxygen are present in the jar covered by CNP/CS, which inhibit the growth of molds. Interestingly, no mold can be found on the tomato covered by the CNP/CS-Cl. This phenomenon is probably due to that fact that chlorine could be dissociated from the N–Cl bonds in the chlorinated CS, which together with the low moisture and oxygen condition could completely inhibit the growth of molds. Therefore, the CNP/CS-Cl with great barrier properties and excellent antibacterial performance may be a promising packaging material for a variety of potential applications.

3.4 Conclusion

In summary, the current study demonstrated a facile and sustainable approach to functionalize CNP with multifunctional properties including water resistance, antibacterial ability, and improved transparency and barrier performance. After impregnating with CS, the optimized CNP/CS exhibits significantly enhanced mechanical strength with 42% and 557% increment at dry and wet conditions, respectively, and the barrier properties towards both water vapor and oxygen were prominently improved as well. In addition, the light transmittance of the CNP/CS was increased from 75% of pure CNP to 83%, with a remarkably decrease in optical haze from 78% to 42%. More importantly, the CS in the CNP/CS could be converted to CS based N-halamine by a facile halogenation process, and the obtained CNP/CS-Cl exhibited superior biocidal efficacy against both gram-positive and gram-negative bacteria, which could kill 100% of *S. aureus* and *E. coli* within 10 min of contact. Moreover, negligible effects on the mechanical, optical and barrier properties were observed after bleaching treatment of the CNP/CS. In light of the above multifunctional properties, the obtained CNP/CS-Cl may find application in the fields of advanced packaging materials, substrates of flexible electronics, etc. All in all, this work provides a simple and versatile strategy to functionalize CNP, which holds great promise for large-scale production of high-performance CNP from renewable and sustainable bioresources.

Chapter 4 Multifunctional Cellulose Nanopaper with Superior Water Resistant, Conductive, and Antibacterial Properties Functionalized with Chitosan and Polypyrrole

4.1 Introduction

With increasing concern about the depletion of nonrenewable resources and environmental issues, lignocellulosic biomass has been recognized as a promising alternative to petroleum resources,[49] which have been utilized to produce biofuels, chemicals, and biomaterials.[5, 267, 268] Cellulose nanofibrils (CNFs), mainly extracted from lignocellulosic biomass, have received a great deal of attention due to their excellent physical, mechanical and chemical properties such as high elastic modulus (29-36 GPa) and tensile strength (2-6 GPa), large specific surface area (up to 600 m^2/g), high aspect ratio (larger than 100), low density (1.32-1.58 g/cm^3), and reactive surfaces along with biodegradability and renewability.[80, 112, 226] Due to the high aspect ratio and semi-crystalline structure, CNFs exhibit remarkable tendency to form three-dimensionally entangled networks suitable to fabricate cellulose nanopaper (CNP) by a self-assembly process such as vacuum filtration or casting.[228, 269] CNP has been a hot topic which has attracted extensive interest from both academia and industries.[229] Recent studies have shown that CNP is a promising material for use in many interdisciplinary fields such as electronic and photonic devices,[81, 270] energy storage electrodes and separators,[185, 271] EMI shielding materials,[231, 272] sensors,[148, 273] etc., in light of its good thermal stability, low thermal expansion coefficient (< 10 ppm/K), tunable optical properties and superior mechanical properties.[129]

It should be noted that the mechanical performance of CNP made by self-assembled CNFs is rather sensitive to moisture due to the hydrophilic nature of cellulose or introduction of hydrophilic

groups during preparation process, which significantly limits the usability of CNP in high-moisture environments. In order to address this problem, researchers have proposed several hydrophobic modification methods such as esterification, silylation, polymer grafting, etc.[234] However, these modification processes are usually time-consuming and involve in hazardous chemicals, which impede their commercial application.[145] Thus, it is of critical importance to develop facile, sustainable and environmentally friendly approach to impart water resistance to CNP. Meanwhile, introducing other functionalities such as antibacterial property and conductivity will be greatly desired to broaden the potential applications of CNP.

As a renewable and sustainable polysaccharide derived from chitin shells of crustaceans such as shrimps and crabs, chitosan (CS) has been widely used in diverse fields such as food packaging, biomedicine, waste treatment, healthcare due to its nontoxicity, antibacterial property, biocompatibility, film-forming and gelling properties.[235] It is reported that CS could form strong hydrogen bonding with cellulose because of the presence of abundant surface hydroxyl and amino groups.[200, 247, 274] Also, chitosan films exhibited good water resistance in neutral and alkaline environments.[236] Thus, several studies have proved that the wet tensile strength of cellulose paper or CNP can be improved by introducing CS as coatings or additives.[200, 238] In addition, it is well documented that CS shows some antimicrobial activity due to the presence of positively charged amino groups in the polymer backbone.[241]

Polypyrrole (PPy) has been considered as a promising conducting polymer with numerous potential applications including biomedical implants, EMI shielding, corrosion protection,[243] energy storage devices,[173] flexible electronics,[275] etc., in light of its advantages such as low cost, ease of synthesis, biocompatibility, environmental stability, and high electrical conductivity.[276, 277]

However, processing PPy based structural materials for practical applications is still challenging because of its poor solubility in solvents and inability to direct melt processing.[173] Recent studies suggested that CS and PPy composite structures (e.g. films, coatings, hydrogels) can be prepared for various applications such as anti-corrosion coating and biosensor due to the interaction and synergistic effect of CS and PPy.[278-280] Considering the easy polymerization, hydrophobic and conductive nature of PPy, as well as the interaction between CS and PPy, it is anticipated that CNP can be endowed with enhanced water resistance and electrical conductivity by introducing CS and PPy at the same time.

In Chapter 2, we demonstrated the low-cost preparation of CNFs from an industrial waste material, paper mill sludge, through a sustainable and efficient approach involving formic acid hydrolysis pretreatment and the followed microfluidization.[252] The as-prepared CNFs could be used to fabricate strong and transparent CNP *via* a simple vacuum filtration method. However, the obtained CNP shows inferior mechanical strength in high-humidity environment. In order to address this weakness and endow it with other functionalities, this project is aimed to provide a versatile and sustainable methodology to functionalize CNP with CS and PPy. As illustrated in **Fig. 4-1**, CNP is firstly immersed in CS solution and the CS functionalized CNP (CNP/CS) can be obtained after drying. Afterwards, CNP/CS/PPy is prepared by *in situ* polymerization of PPy within the CNP/CS. Compared with the original CNP, CNP/CS/PPy exhibits significant improvement on water resistance and new features of conductivity and antibacterial activity. This work will provide a facile and sustainable strategy to functionalize CNP and widen its potential applications.

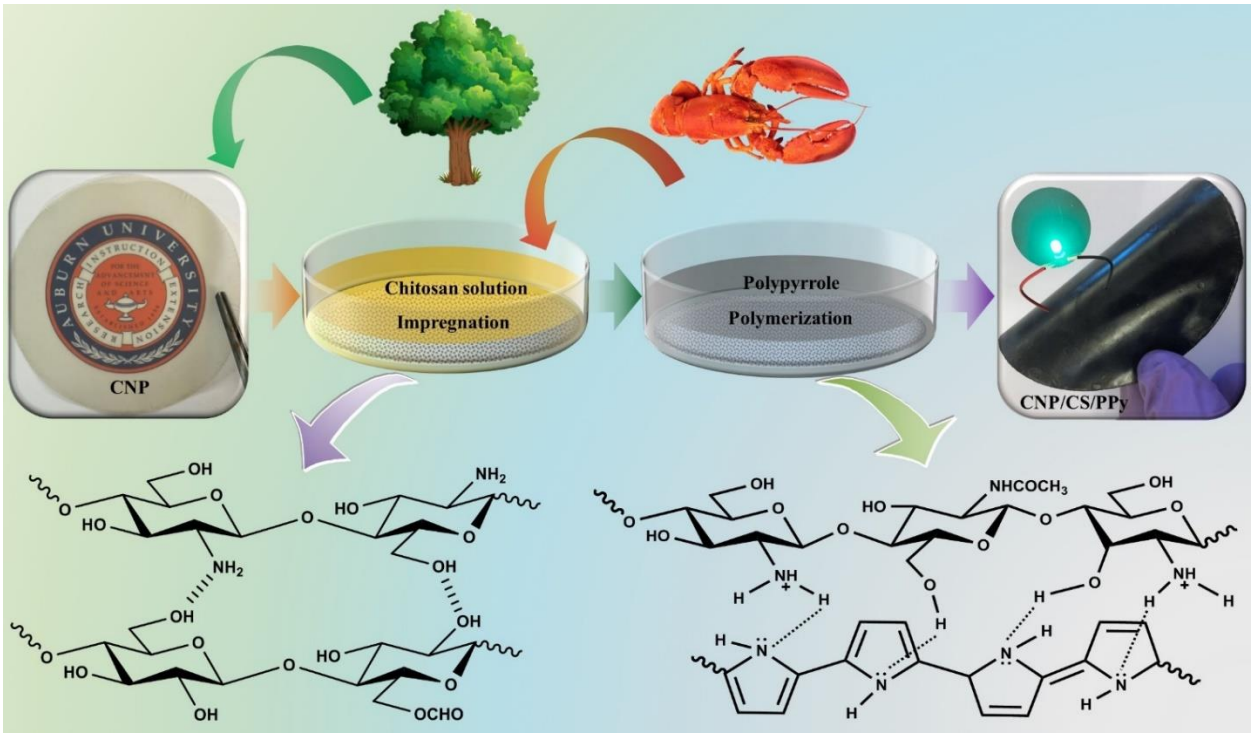

Figure 4-1. Schematic process flow diagram for the functionalization of CNP including the CS impregnation, and polymerization of PPy. The corresponding reaction schemes show the hydrogen bonding between CNFs and CS, and interaction between CS and PPy, respectively.

4.2 Experimental section

4.2.1 Materials

CNFs aqueous suspension with a concentration of 1.0 wt.% was prepared from paper mill sludge according to our previous work.[252] Chitosan with deacetylation degree of 85% and molecular weight of 310-375 kDa was purchased from Sigma-Aldrich, USA. Pyrrole monomer was purchased from Tokyo Chemical Industry. Ammonium persulfate (APS) was purchased from Alfa Aesar, USA. Acetate acid and sodium hydroxide were purchased from VWR, USA. *Staphylococcus aureus* (*S. aureus* ATCC 6538, gram-positive) and *Escherichia coli* (*E. coli*

O157:H7 ATCC 43895, gram-negative) were provided by American Type Culture Collection, Rockville, MD. All the reagents were used as received.

4.2.2 Preparation of CNP

CNP samples were prepared following the procedure reported in our previous work.[202] Briefly, 40 mL of the CNFs suspension (1.0 wt.%) were diluted with 160 mL deionized (DI) water. The diluted CNFs suspension was further mixed uniformly using magnetic stirring for 2 hours. Afterwards, the mixed CNFs suspension was poured into a filtration setup with a polypropylene (PP) filter membrane (diameter = 100 mm, pore size = 0.45 μm). After filtration, the obtained wet CNP was covered with another PP filter membrane and dried at 105 ºC for 2 h using a hot plate.

4.2.3 Impregnation of CS into CNP

Firstly, 1.5 wt.% CS solution was prepared by dissolving CS powder in 2 % (v/v) acetic acid aqueous solution. Then, CNP was soaked in the as-prepared CS solution at room temperature for 1 h. Afterwards, the CS impregnated CNP (CNP/CS) was dried on a glass plate under ambient condition for 12 h. The dried CNP/CS samples were further immersed in 0.1 mol/L NaOH aqueous solution at room temperature for 1 h to neutralize the residual acetic acid. Finally, the CNP/CS samples were thoroughly washed with DI water and air dried. The impregnation process was repeated twice, and the CS weight gain was 18.75 ± 1.47%.

4.2.4 Polymerization of PPy

Firstly, 0.5 mL of pyrrole monomer were added into 25 mL of DI water and mixed by magnetic stirring at room temperature for 30 min. Then, the CNP/CS sample was immersed into this mixture

under ambient condition for 1 h to swell the CNP/CS and absorb pyrrole monomer. During this process, the container was tightly covered with plastic film to avoid evaporation loss of pyrrole. Afterwards, 10 mL of 5.8 wt.% APS aqueous solution was directly added into the mixture to initiate the polymerization. The polymerization of PPy was carried out at room temperature for 1 h. Finally, the CNP/CS/PPy samples were rinsed with copious amount of DI water and air dried. For comparison, CNP/PPy was prepared from pure CNP following the same polymerization process.

4.2.5 Characterizations

4.2.5.1 Fourier transform infrared spectroscopy (FTIR)

FTIR spectra of samples were collected on a Thermo Nicolet 6700 FTIR spectrometer equipped with diamond ATR accessory and OMNIC 7.3 software. The spectra were recorded in the wavenumber range from 4000 to 500 cm^{-1} at a resolution of 4 cm^{-1}.

4.2.5.2 X-ray photoelectron spectroscopy (XPS)

XPS spectra of samples were collected on a photoelectron spectrometer (EscaLab Xi+, Thermo Fisher Scientific) using non-monochromatized Al Kα radiation (1486.6 eV) under the vacuum pressure of 8×10^{-10} Pa. The C1s spectrum (284.8 eV) was used to calibrate the binding energy scale for all the samples.

4.2.5.3 Scanning electron microscopy (SEM) and energy dispersive X-ray spectroscopy (EDS)

The surface and cross-section morphology and elemental compositions of samples were examined by using a field emission scanning electron microscope (FESEM, Apreo FE) at 1.0 kV.

4.2.5.4 Water contact angle

Static water contact angle of samples was measured on a contact angle goniometer (Rame-Hart model 200) at room temperature. The contact angle was determined immediately after the water droplets placed on the film surface. Three measurements were performed for each sample and the averaged value was reported.

4.2.5.5 Water uptake ratio

Water uptake ratio was measured by calculating the weight change of samples before and after immersion in DI water at room temperature. Briefly, the samples were cut into strips and the strips were transferred to a vacuum oven at 60 ºC for 24 h to eliminate any moisture. Afterwards, the strips were immediately weighted separately, and the weight of each of strips was noted as M_0. Then, the strips were immersed in DI water for 30 min. After that, the strips were weighted after removing any free water by using a blotting paper, and the weight of each of strips was noted as M_1. Finally, the water uptake ratio was calculated by the Equation (3), as follows:

$$Water\ uptake\ ratio = \frac{M_1 - M_0}{M_0} \times 100\% \qquad (3)$$

4.2.5.6 Tensile test

Dry and wet mechanical properties of the samples was evaluated by an Instron 4465 universal testing machine following the TAPPI standard method (TAPPI T497 and TAPPI T456). The samples were cut into 1 cm × 5 cm strips and placed at the conditions of 50% RH and 23 °C for at least 24 h before testing. Crosshead speed was set at 5 mm/min and the initial distance between

the two clamps was set to 20 mm. The results were reported as a mean value averaged from five measurements for each sample.

4.2.5.7 Antimicrobial efficacy test

The antimicrobial efficacy of pure CNP and functionalized CNP samples against gram-positive *S. aureus* ATCC 6538 and gram-negative *E. coli* O157:H7 ATCC 43895 strains was evaluated following the AATCC Test Method100-2400 with a slight modification. A single colony of each bacterium was transferred into 15 mL of Trypticase soy broth and incubated at 37 °C for 16 h. The culture was washed twice with Butterfield's phosphate buffer by centrifugation and was re-suspended in the same buffer. Bacterial population was estimated by the absorbance at O.D. $_{640\ nm}$ and the inoculum with the designated population was prepared. Prior to the antibacterial test, the samples were cut into 1 inch × 1 inch specimens. Firstly, a pair of the specimens were placed on a sterile plate. Then, an aliquot of 25 µL of the inoculum was added onto the center of one of the specimens, and the other specimen was overlaid on the previous specimen to ensure complete contact with the inoculated bacteria. After contacting for 5, 10, and 30 min, the specimens were immediately immersed in 5 mL of sterile 0.01 N sodium thiosulfate solution to quench the residual chlorine. Afterwards, the mixture was vortexed vigorously for 2 min to detach survived bacteria from the specimens. After vortexing, the liquid part for each sample was tenfold serial diluted and each dilution was plated on a Trypticase soy agar plate, respectively. Finally, all the plates were incubated at 37 ºC for 48 h and bacterial colonies were enumerated and recorded for antimicrobial efficacy analysis.

4.2.5.8 Sheet resistance and conductivity measurement

The sheet resistance of the CNP/PPy and CNP/CS/PPy was examined according to the van der Pauw four-point probe technique using a digital multimeter (RIGOL DM3068). The sample was cut into square specimens (1.3 × 1.3 cm^2). The four corners of each of specimens were coated with silver paint to ensure good electrical contacts. Afterwards, the four probes were contacted on the four corners of the specimen and the resistance (R) was recorded. The sheet resistance (R_s) was calculated based on the Equation (2),[281] as follows:

$$R_s = \frac{\pi R}{ln2} \approx 4.53R \qquad (2)$$

Further, the conductivity (ρ) can be calculated from Equation (3), as follows:

$$\rho = \frac{1}{R_s \times t} \qquad (3)$$

where t is the thickness of the specimen. Three independent determinations were carried out and the averaged value was reported.

4.2.5.9 Electromagnetic interference shielding measurement

The electromagnetic interference (EMI) shielding performance of the CNP/CS, CNP/PPy, and CNP/CS/PPy was evaluated by a vector network analyzer (N5244A, Agilent, USA) using the waveguide method in the frequency range of 8-12 GHz (X bands). The total EMI shielding effectiveness (SE_T), microwave reflection (SE_R), microwave absorption (SE_A) were calculated from the following equations:

$$SE_T = SE_R + SE_A + SE_M \qquad (4)$$

$$SE_T = -10\log(|S_{21}|^2) \qquad (5)$$

$$SE_R = -10\log(1 - |S_{11}|^2) \quad (6)$$

$$SE_A = -10\log\left(\frac{|S_{21}|^2}{1-|S_{11}|^2}\right) \quad (7)$$

where S_{11} and S_{21} are scattering parameters, SE_M is the microwave multiple internal reflection, which can be negligible when SE_T >10 dB.[282]

4.3 Results and discussion

4.3.1 Chemical and structural characterization

The chemical structure of pure CNP and functionalized CNP samples was investigated by FTIR and XPS. As shown in **Fig. 4-2a**, the peaks at 3335, 2918, 1645, 1429, 1161, 1105, and 897 cm^{-1} in the spectrum of pure CNP are assigned to the characteristic peaks of cellulose Iβ,[112, 251] and the band at 1717 cm^{-1} is attributed to the C=O stretching from ester groups, which are consistent with the results reported in our previous study.[252] After introducing CS, the typical bands of CS appear in the FTIR spectrum of CNP/CS. Among them, the strong band in the range of 3286 and 3353 cm^{-1} corresponds to the N-H and O-H stretching, and the peaks at 2920 and 2854 cm^{-1} are attributed to the C-H symmetric and asymmetric stretching, respectively.[253] The band at 1647 cm^{-1} corresponds to the C=O stretching of amide I, and the band at 1316 cm^{-1} is assigned to C-N stretching of amide III, both of which confirm the presence of residual N-acetyl groups. The peak at 1574 cm^{-1} is caused by the N-H bending of the primary amine. The peaks at 1420 and 1376 cm^{-1} are attributed to CH2 bending and CH3 symmetrical deformations, respectively. The band at 1152 cm^{-1} corresponds to the asymmetric stretching of C-O-C bridge.[254, 255] In addition, compared to the XPS spectrum of pure CNP, a stronger C 1s peak and a new N 1s peak appear in the XPS

spectrum of CNP/CS, indicating the introduction of CS coating on the CNP surface. For the CNP/PPy sample, the characteristic peaks of PPy can be observed in the FTIR spectrum. The peaks at 1540 cm^{-1} and 1461 cm^{-1} are attributed to the C=C and C-N stretching vibrations of pyrrole ring, respectively.[173] The bands at 1286 cm^{-1}, 1162 cm^{-1}, and 1030 cm^{-1} correspond to the C-H in-plane vibrations of pyrrole ring.[283]

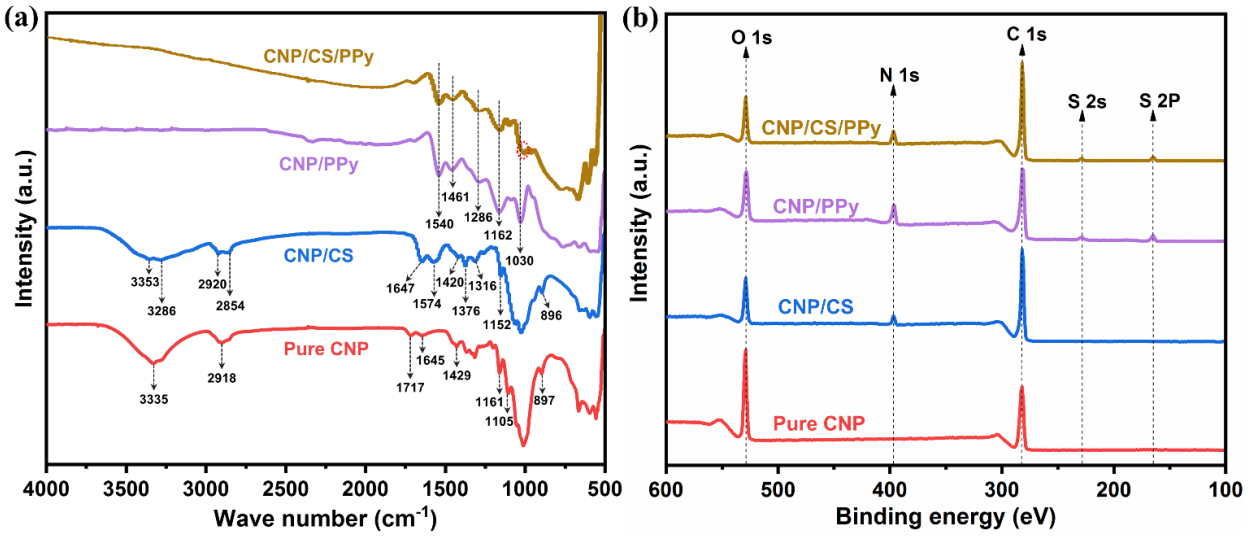

Figure 4-2. FTIR spectra (a) and XPS spectra (b) of pure CNP and functionalized CNP samples.

As indicated in **Fig. 4-2b**, a new N 1s peak and two new S 2s and S 2p core level peaks can be observed in the XPS spectrum of CNP/PPy, suggesting the presence of PPy on the surface of pure CNP. It should be noted that the S element comes from the SO_4^{2-} counterions on the PPy backbone, which are generated from APS during the oxidation process.[284] From **Fig. 4-2a**, it can be seen that the bands in the spectrum of CNP/CS/PPy are nearly parallel with the bands in the spectrum of CNP/PPy, indicating the formation of PPy within the CS coating. It should be noted that the peak at 1030 cm^{-1} for CNP/PPy was shifted to a lower wavenumber for the CNP/CS/PPy, suggesting the existence of interaction between PPy and CS, as illustrated in **Fig. 4-1**.[279, 280] Moreover,

compared with the XPS spectrum of CNP/CS, a stronger N 1s peak and two new S 2s and S 2p core level peaks can be observed in the XPS spectrum of CNP/CS/PPy, which further confirms the introduction of PPy in the CS coating.

The surface and cross-section morphology of pure CNP and functionalized CNP samples were further examined by SEM. As shown in **Fig. 4-3a**, the randomly entangled CNFs can be clearly observed on the surface of pure CNP. The cross-section of pure CNP displays a lamellar structure with notable gaps between layers. After introducing CS, the surface of CNP/CS becomes much smoother due to the compact structure of CS coating (**Fig. 4-3b**). Intriguingly, the cross-section of CNP/CS exhibits a much denser interlayer structure, since most of the voids between CNFs are filled with CS. This result indicates that the CS can not only retain on the surface of pure CNP, but also penetrate into the interior lamellar structure of the pure CNP. As shown in **Fig. 4-3c**, numerous PPy granular aggregates can be observed on the surface of CNP/PPy, which completely covered the network structure of pure CNP. Moreover, the CNP/PPy displays similar cross-section morphology to the pure CNP with slightly expanded interior lamellar structure. This phenomenon is probably caused by the swelling of the CNP structure during polymerization process and the generated PPy enlarged the distance among CNFs. As displayed in **Fig. 4-3d**, the surface of CNP/CS/PPy becomes rougher than that of CNP/CS after introducing PPy, and the PPy granules can be clearly seen on the surface. Moreover, the interlayer structure of CNP/CS/PPy is obviously expanded when compared to that of the CNP/CS. By comparing **Fig. 4-3c** and **Fig. 4-3d**, it can be clearly seen that the PPy granules on the surface of CNP/CS/PPy are more uniform than that on the CNP/CS surface. Also, the CNP/CS/PPy shows smoother surface morphology and denser interlayer structure than CNP/PPy. It is expected that the CNP/CS/PPy will offer a higher electrical conductivity and better mechanical properties. Finally, we performed EDS characterization on the

CNP/CS/PPy sample. As shown in **Fig. 4-4**, the EDS result indicates the presence of S element in the interlayer structure of CNP/CS/PPy, indicating that PPy could be introduced not only within the CS coating, but also within the interlayers of the CNP/CS.

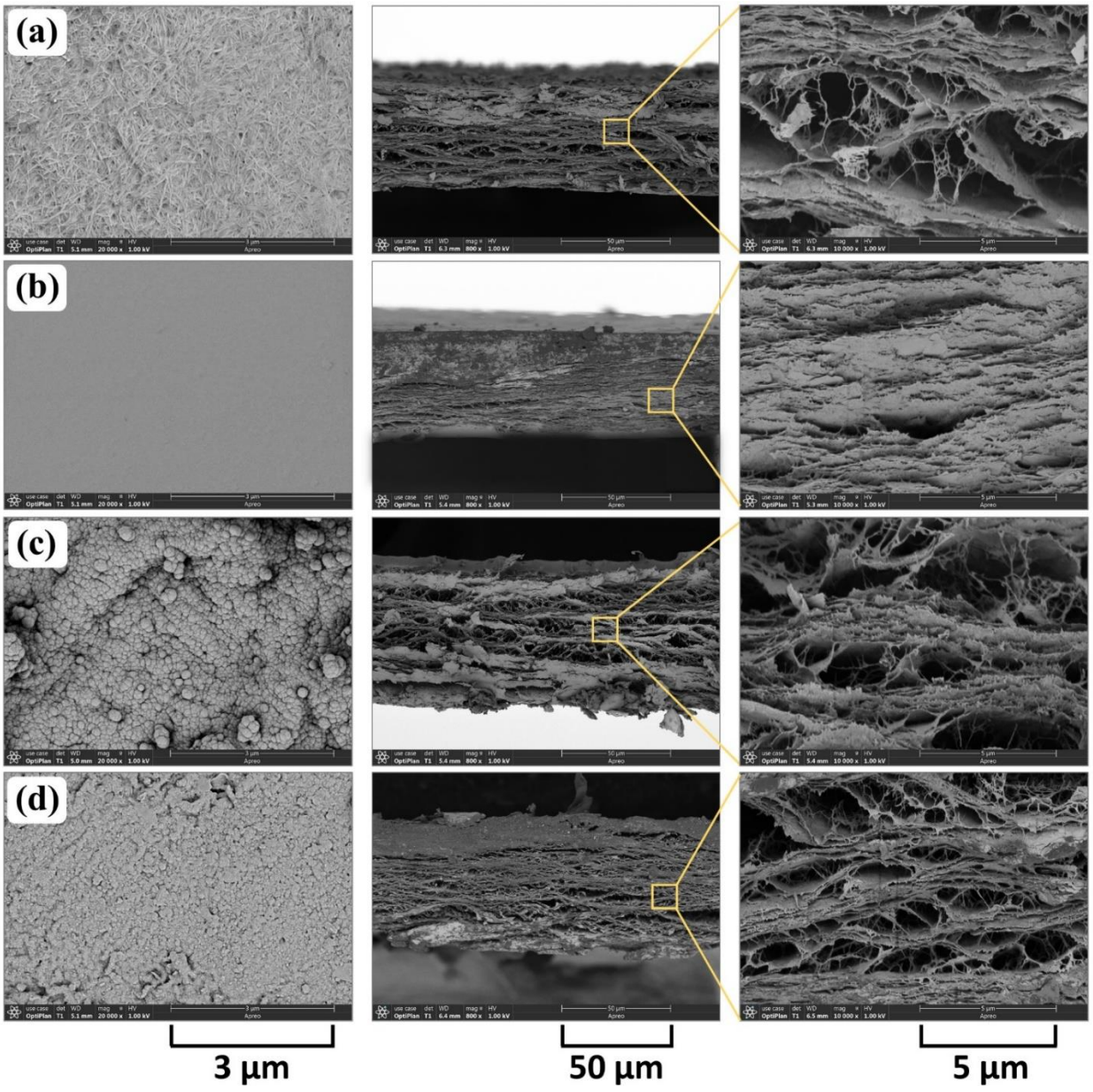

Figure 4-3. SEM surface and cross-section images of pure CNP (a), CNP/CS (b), CNP/PPy (c), and CNP/CS/PPy (d).

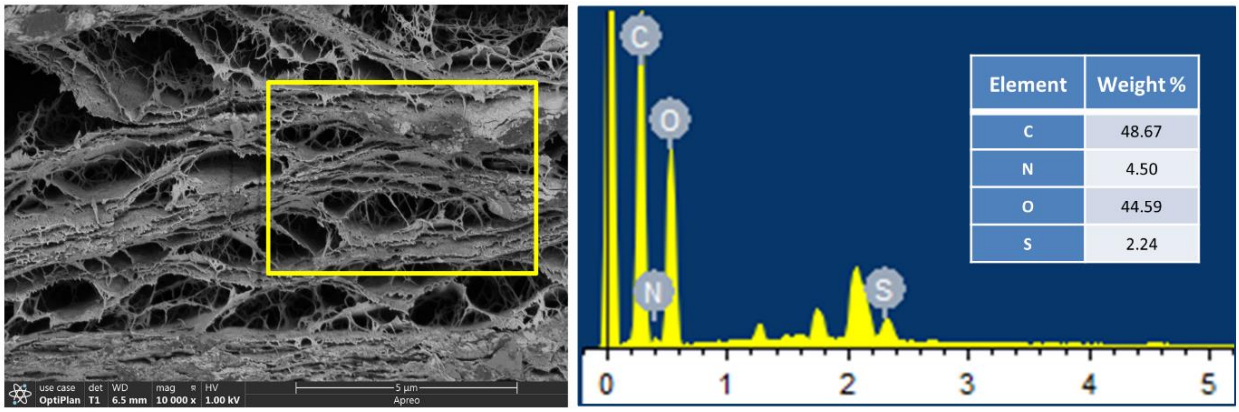

Figure 4-4. EDS spectrum of CNP/CS/PPy cross section.

4.3.2. Mechanical properties and water resistance

As indicated in **Fig. 4-5a**, the introduction of CS significantly improved the mechanical properties of pure CNP in the dry state. This result can be explained by the following two reasons: 1) the CNP got swelled in the CS solution during the impregnation process, which allowed the CS to penetrate into the small voids among CNFs. As verified in the SEM images, these small voids were filled up upon drying, which could fix the interstitial defects of CNP; 2) As shown in the reaction scheme of CNFs and CS in **Fig. 4-1**, the introduction of CS within the CNP could interact with CNFs through hydrogen bonding, covalent bonding, and electrostatic interaction.[200] These extra and abundant bonds or interactions are beneficial to more mechanically stable structure of the obtained CNP/CS under tension. By contrast, the CNP/PPy sample shows a decreased mechanical strength, which is mainly due to that fact that the PPy could disrupt part of the hydrogen bonds among CNFs.[285] The slightly expanded interlayer structure of CNP/PPy in **Fig. 4-3** supports this speculation. Compared with the CNP/CS, an obvious decrease in dry tensile strength of CNP/CS/PPy was observed in **Fig. 4-5a**. This phenomenon is probably due to the introduction of PPy could interrupt the strong hydrogen bonds between CS and CNFs. Also, as

indicated in the SEM images, the introduction of PPy could destroy the compact structure of CNP/CS to some extent, resulting in a slightly loose structure.

Fig. 4-5b displays the strain-stress curves of pure CNP and functionalized CNP under the wet state. It can be clearly seen that the tensile strength of pure CNP remarkably decreased from 106.32 MPa (dry state) to around 7 MPa (wet state). The poor wet strength of pure CNP is mainly due to the hydrophilic surface of CNFs and the presence of numerous small voids within the self-assembled structure. The water molecule can severely interrupt the interfibrillar hydrogen bond among CNFs, leading to the swelling of CNP and a significant drop in mechanical strength.[145] In contrast, the CNP/CS shows more than 6-fold higher wet mechanical strength than the pure CNP, which is mainly attributed to the synergetic action of the chemical and physical interactions between CNFs and CS, and the mending effect on the interstitial defects of pure CNP.[200] Interestingly, although the CNP/PPy shows inferior dry mechanical strength when compared to the pure CNP, obvious enhancement in wet strength can be observed in **Fig. 4-5b**. This phenomenon is probably due to the introduction of water-resistant PPy, which could reduce the possibility of CNP interior structure being wetted by water molecules.[230] Notably, the CNP/CS/PPy exhibits the highest wet mechanical strength (80.13 MPa) among all the samples. The enhanced wet strength is mainly attributed to the compact structure and surface hydrophobicity derived from the synergy between CS and PPy, which could alleviate the penetration of water into the structure and protect most of the chemical bonds from the interruption by water molecules.[230] Intriguingly, the inset photograph in **Fig. 4-5b** demonstrates that a CNP/CS/PPy strip with the thickness of 63 μm and width of 1 cm could lift up a 500 g weight in water, indicating excellent water resistance and high wet tensile strength.

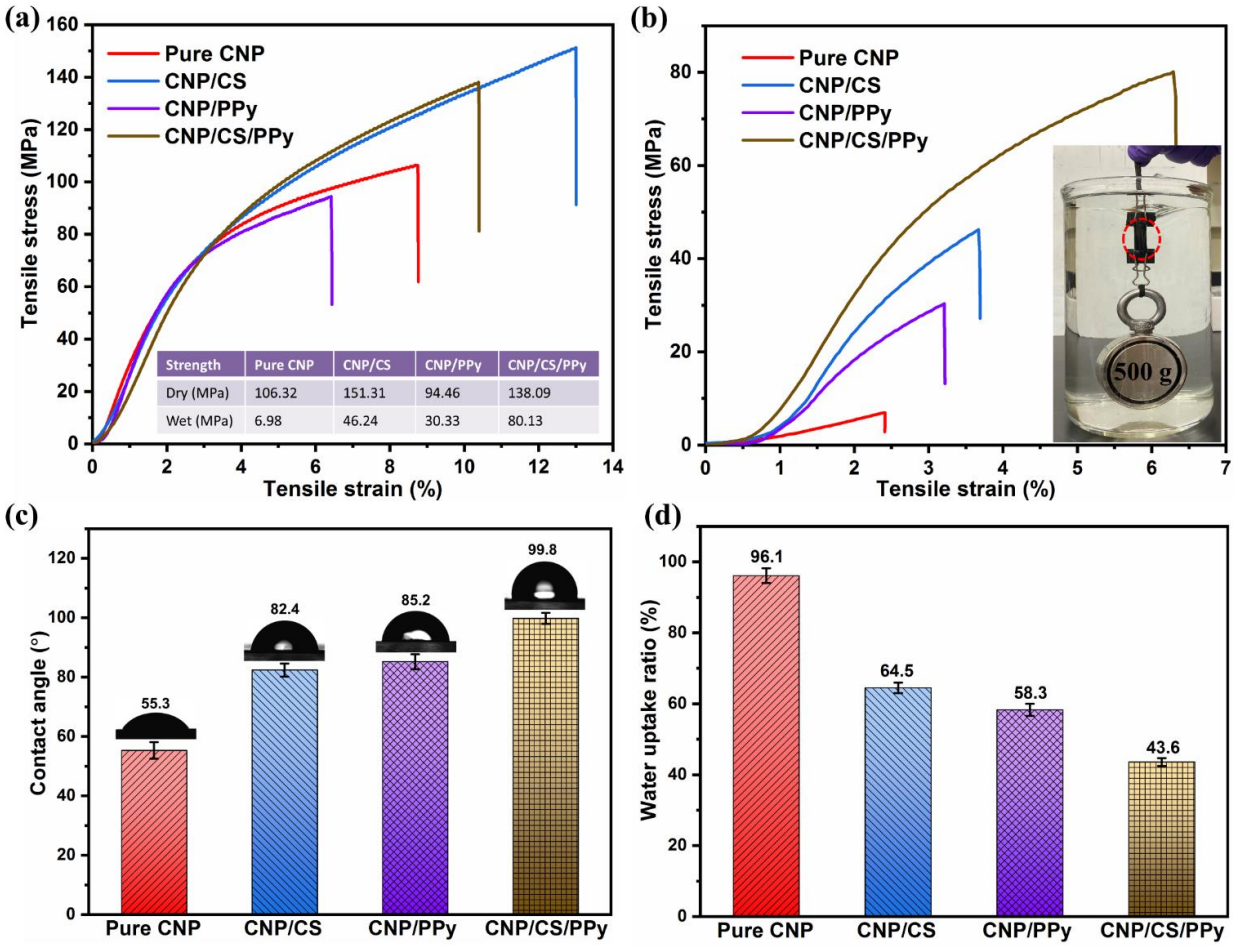

Figure 4-5. Strain-stress curves of pure CNP and functionalized CNP samples at dry state (a) and wet state (b), the inset photograph showing that the CNP/CS/PPy strip (63 μm thick and 1 cm wide) could lift up a 500 g weight in water. (c) Water contact angles of pure CNP and functionalized CNP samples. (d) Water uptake ratio of pure CNP and functionalized CNP samples.

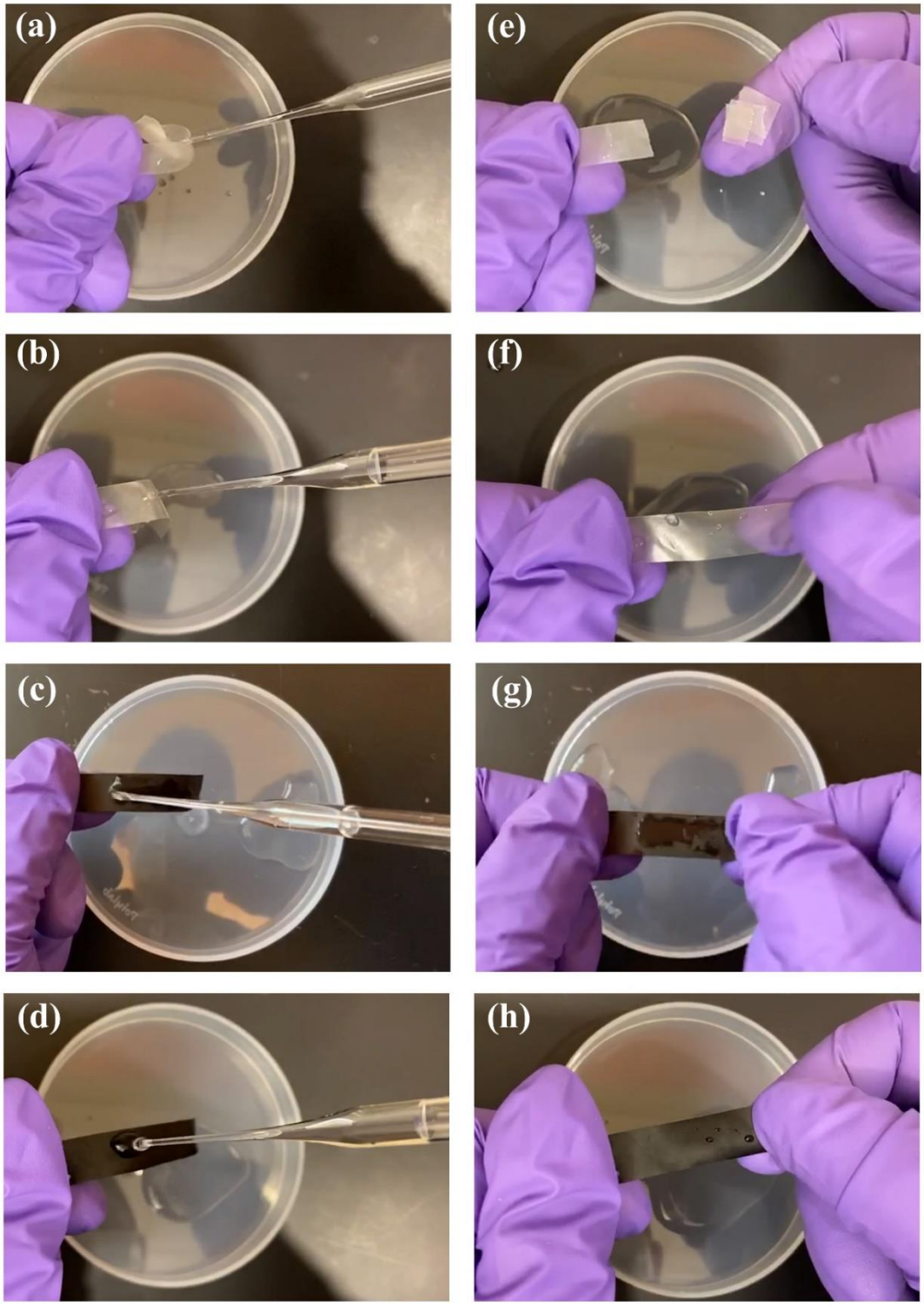

Figure 4-6. Photographs showing the surface wettability of pure CNP (a), CNP/CS (b), CNP/ PPy (c), CNP/CS/PPy (d), and the corresponding images of the samples under small tension after wetting (e-h).

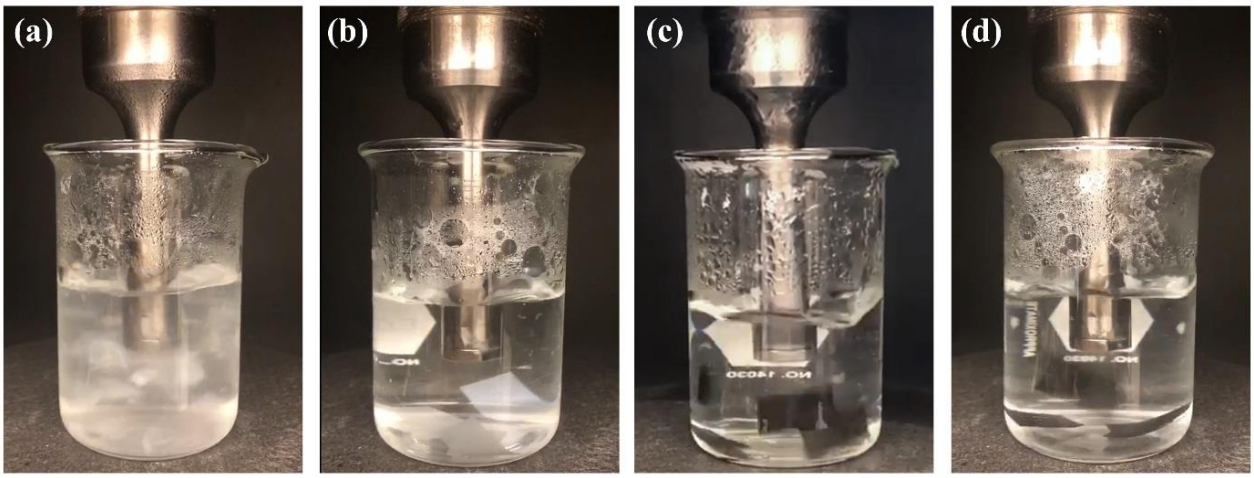

Figure 4-7. Photograph showing the stability of pure CNP (a), CNP/CS (b), CNP/PPy (c), and CNP/CS/PPy (d) in the water after probe ultrasonication at a high-power input (500 watts) for 10 min.

In order to understand the mechanism of the enhanced water resistance and wet tensile strength, water contact angle measurements were carried out to investigate the surface wettability of pure CNP and functionalized CNP samples, water uptake ratio was examined as well. As shown in **Fig. 4-5c**, the pure CNP has a relatively low contact angle of 55.3° due to the hydrophilic nature of CNFs, which results in the highest water uptake ratio of 96.1%. Correspondingly, **Figs. 4-6 (a, e)** vividly display that the pure CNP rapidly absorbed the water and crimped, and it got broken very easily under a small tension. After impregnating with CS, the contact angle of CNP/CS dramatically increased to 82.4°, and the water uptake ratio decreased to 64.5%, which is mainly due to the increased surface hydrophobicity and the more compact structure. As shown in **Figs. 4-6 (b, f)**, although the CNP/CS strip got bended after absorbing water, the wetted CNP/CS strip could still withstand certain tension. Moreover, the CNP/PPy sample exhibits a slightly higher contact angle and a lower water uptake ratio than CNP/CS because of the good water resistance of PPy.[230] **Figs. 4-6 (c, g)** demonstrate that the PPy layer allows less water to penetrate into the strip,

and the strip keeps its original shape under a small tension. Remarkably, the CNP/CS/PPy shows the highest contact angle of 99.8° and the lowest water uptake ratio (43.6%), suggesting a hydrophobic surface (> 90°) and excellent water resistance. As indicated in **Figs. 4-6 (d, h)**, water drops can be hardly retained on the CNP/CS/PPy surface when rinsing with water. This phenomenon is mainly attributed to the hydrophobic surface of CNP/CS/PPy. Moreover, **Fig. 4-7** displays the stability of pure CNP and functionalized CNP samples in water after probe ultrasonication at a high-power input (500 watts) for 10 min. It can be clear seen that the CNP/CS, CNP/PPy, and CNP/CS/PPy strips could retain their original shape without dissociation of any CS or PPy, while the pure CNP almost completely disintegrated into many fragments. This phenomenon again proves that the water resistance of CNP can be significantly improved by introducing CS/PPy.

4.3.3 Antibacterial efficacy

The antibacterial performance of pure CNP and functionalized CNP samples were evaluated against *S. aureus* and *E. coli*, and the results are summarized in **Fig. 4-8**. For the pure CNP sample, within 30 min of contact around 66.50% and 56.44% bacterial reductions were observed towards *S. aureus* and *E. coli*, respectively. The bacterial reduction is mainly due to the fact that pure CNP easily swelled and disintegrated into fragments during the vortexing process because of its poor water resistance, and part of bacterial could adhere onto these porous fragments. Similar result was reported in our previous study.[244] After introducing CS, the biocidal activity against *S. aureus* and *E. coli* was significantly enhanced with the bacterial reduction of 97.32% and 78.22%, respectively. This result is mainly attributed to the modest antibacterial activity of CS, which is well documented in the literature.[242] Moreover, the CNP/PPy shows quite good antibacterial

property towards *S. aureus* and *E. coli*, with the bacterial reductions of 95.74% and 92.34%, respectively. The biocidal action is mainly attributed to the positive charges on the PPy backbone, which has been proved in the previous work.[277, 286] Interestingly, due to the synergy of CS and PPy, the CNP/CS/PPy exhibited enhanced antibacterial activity with the bacterial reductions of 99.28% and 95.59% towards *S. aureus* and *E. coli*, respectively. This result is comparable with or even better than some previous results reported in the literatures.[247, 277] Considering its excellent mechanical strength, water resistance, and good antibacterial property, the CNP/CS/PPy can be potentially used in the biomedical filed for practical purposes.

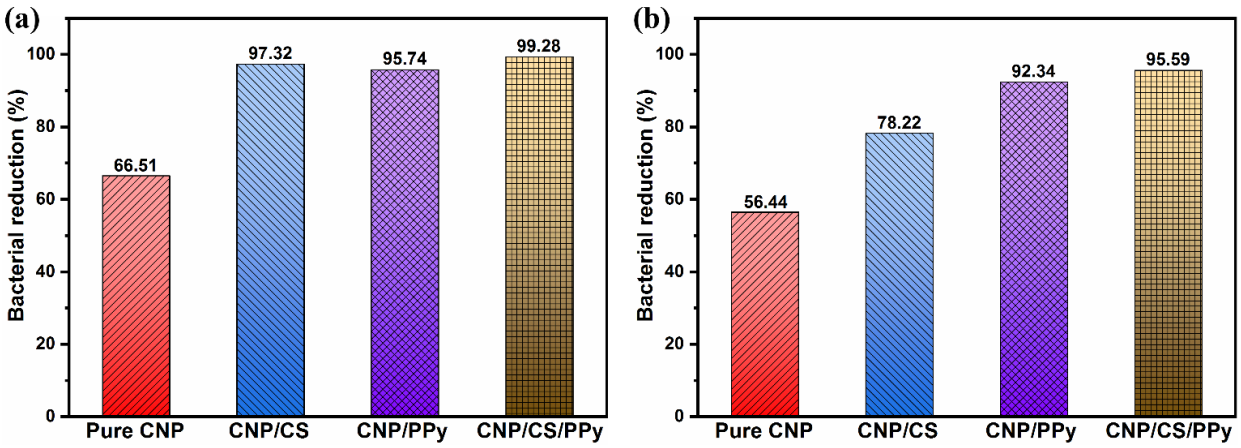

Figure 4-8. Biocidal results of pure CNP and functionalized CNP samples against *S. aureus* (a) and *E. coli* (b) with the contact time of 30 min.

4.3.4 Conductivity and EMI shielding performance

The conductivity of the CNP/PPy and CNP/CS/PPy was examined through the four-point probe measurement. Results indicate the CNP/CS/PPy shows a higher electrical conductivity of 6.5 S cm^{-1} than that (1.8 S cm^{-1}) of the CNP/PPy. This result is probably due to the fact that the CS coating could provide a smooth surface for interaction with pyrrole monomers and oligomers

through hydrogen bonding (see the reaction scheme in **Fig. 4-1**), thus resulting in a smoother and more uniform PPy coating, as indicated in the SEM images (**Fig. 4-3d**). Similar results were observed for PPy/PVA-CNP in the previous study.[230] As shown in **Fig. 4-9**, when a CNP/CS/PPy strip was connected into a circuit, the LED could be lighted on even at the bent and twisting states of the strip, indicating excellent conductivity and flexibility. **Fig. 4-10a** presents the comparison of the CNP/CS/PPy with other conducting polymer and cellulose based composite films in terms of conductivity and tensile strength. It can be clearly seen that the CNP/CS/PPy fabricated in this work shows both superior conductivity and mechanical strength than most of the reported values in the literature. In light of the high conductivity, good flexibility, high mechanical strength, water resistance and antibacterial ability, the as-prepared CNP/CS/PPy may find applications in a variety of high-tech fields such as medical packaging, electronic packaging, EMI shielding, etc.

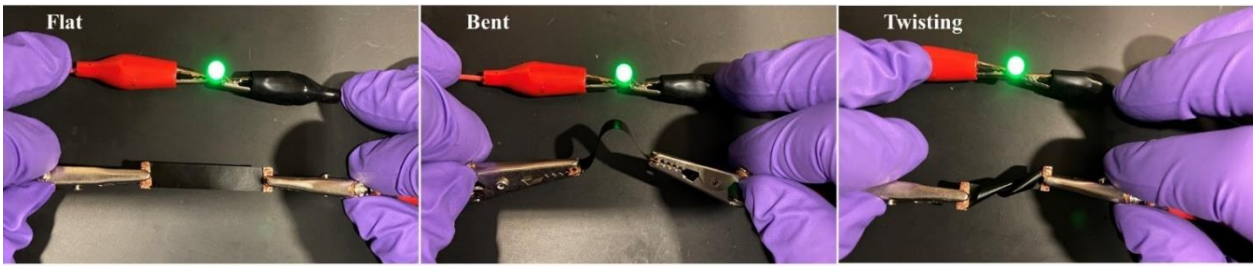

Figure 4-9. Photographs showing the good electrical conductivity of the CNP/CS/PPy at flat, bent, and twisting states.

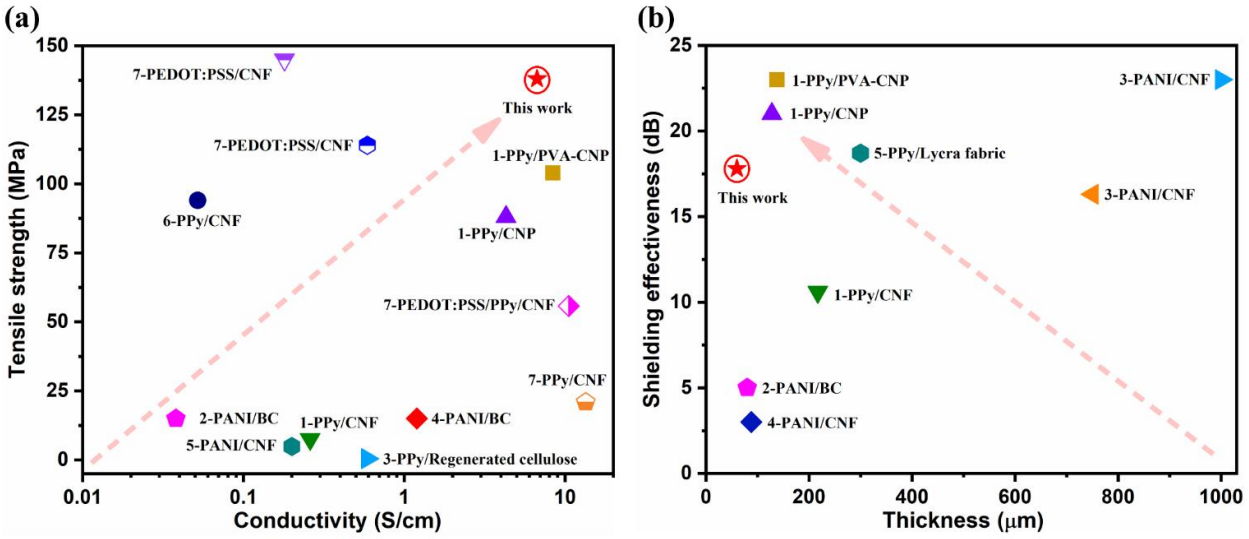

Figure 4-10. (a) Comparison of conductivity vs. tensile strength for the cellulose and conducting polymer based composite films. 1-PPy/PVA-CNP, 1-PPy/CNP, and 1-PPy/CNF,[230] 2-PANI/BC,[287] 3-PPy/Regenerated cellulose,[288] 4-PANI/BC,[289] 5-PANI/CNF,[290] 6-PPy/CNF,[291] 7-PEDOT:PSS/CNF, 7-PEDOT:PSS/PPy/CNF, and 7-PPy/CNF.[292] (b) Comparison of EMI shielding performance for cellulose and conducting polymer based composite films. 1-PPy/PVA-CNP, 1-PPy/CNP, and 1-PPy/CNF,[230] 2-PANI/BC,[287] 3-PANI/CNF,[293] 4-PANI/CNF,[290] 5-PPy/Lycra fabric.[294]

Finally, the application of the CNP/CS/PPy for EMI shielding was demonstrated in the current work. As shown in **Fig. 4-11a**, the control sample of CNP/CS shows nearly zero shielding effectiveness due to the non-conductive feature, leading to easy and fast transmission of the electromagnetic energy through the structure. The CNP/PPy sample exhibits a moderate shielding effectiveness of approximately 10 dB in the X band. Notably, the CNP/CS/PPy exhibits a high SE_T around 18 dB in the X band even with a low thickness of 63 μm. This result is mainly attributed to the high conductivity and the unique heterostructure of the CNP/CS/PPy. In order to explore the shielding mechanisms of the CNP/CS/PPy, SE_T, SE_A, and SE_R of the CNP/CS/PPy at 10 GHz were calculated. As shown in **Fig. 4-11b**, the contribution of SE_A to the SE_T is significantly higher than SE_R. This observation can be explained by the heterostructure of the CNP/CS/PPy.

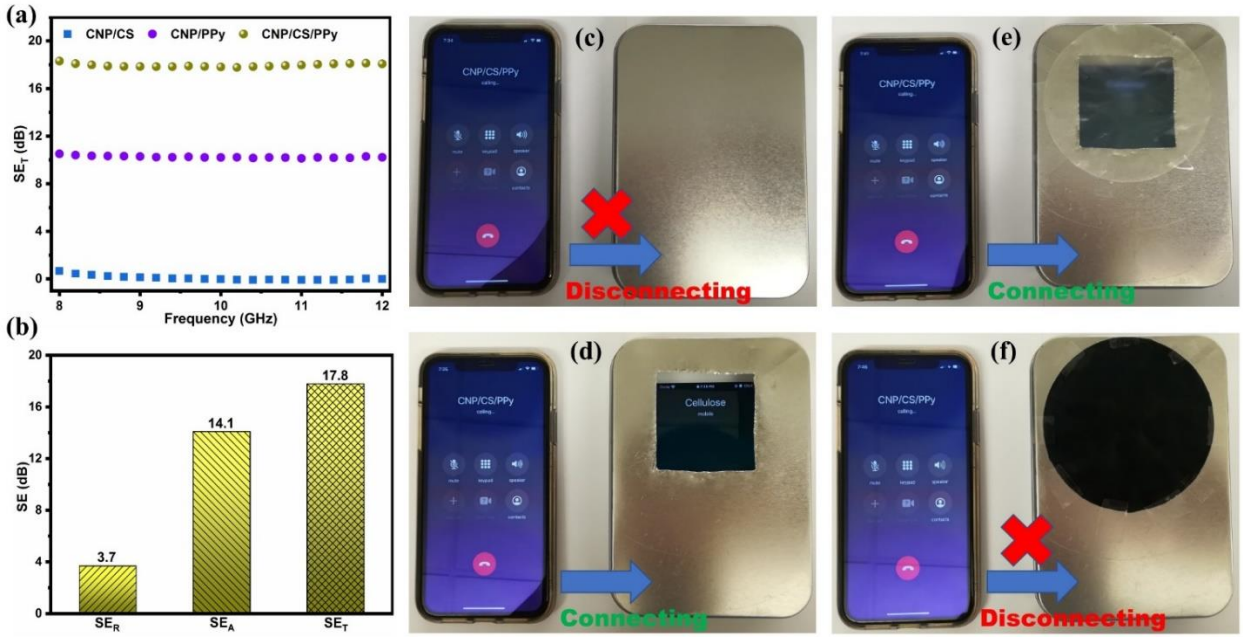

Figure 4- 11. (a) EMI shielding performances of CNP/CS, CNP/PPy, and CNP/CS/PPy samples. (b) The comparison of SE_T, SE_A, and SE_R of the CNP/CS/PPy at 10 GHz. (c-f) Photographs demonstrating the realistic application of the CNP/CS/PPy: disconnecting when the phone was placed in an iron box (c), connecting when the iron cover with a square hole (d), connecting when the hole was covered with CNP/CS (e), and disconnecting when the hole was covered with CNP/CS/PPy (f).

As illustrated in **Fig. 4-12**, the CS/PPy serves as the continuously conductive matrix while the CNFs act as insulating nanofillers, eventually constructing a unique heterostructure. It is well documented that the construction of heterostructure could facilitate microwave absorption due to the multiple reflections within the heterostructure.[295, 296] Specifically, when the incident microwaves strike the CNP/CS/PPy heterostructure, a small part of the microwaves could be immediately reflected by the external highly conductive and compact CS/PPy layer. The remaining microwaves would reflect at the interface between CNFs and CS/PPy due to the big difference in conductivity and dielectric constant of CNFs and CS/PPy, and these multiple reflections impart the heterostructure with superior absorption capability.[297] As a consequence, the incident

electromagnetic power can be effectively dissipated and attenuated. Moreover, a communication shielding demonstration was performed to illustrate the EMI shielding performance of the CNP/CS/PPy.

As shown in **Figs. 4-11c** and **4-11d**, when a mobile phone was placed into an iron box completely covered with an iron cover, it cannot be connected with another one. While the phone can be smoothly connected by another one when the iron cover with a square hole, since the electromagnetic waves was able to leak through the hole. As indicated in **Fig. 4-11e**, when the hole was tightly covered with the control sample (CNP/CS), the connection was still observed due to the poor shielding effectiveness of CNP/CS. As expected, the connection was totally blocked when the hole was covered by the CNP/CS/PPy (**Fig. 4-11f**). Lastly, a comparison of EMI shielding performance for cellulose and conducting polymer based composite films was conducted, and the results are summarized in **Fig. 4-10b**. It can be clearly seen that the CNP/CS/PPy prepared in this work exhibits high shielding performance, which is better than most previous work. Considering the advantages of high shielding performance, high mechanical strength, light weight, excellent flexibility, as well as the facile and cost-effective preparation strategy, the obtained CNP/CS/PPy can be potentially used as sustainable EMI shielding materials for commercial applications, especially for wearable electronics, aviation and mobile devices.

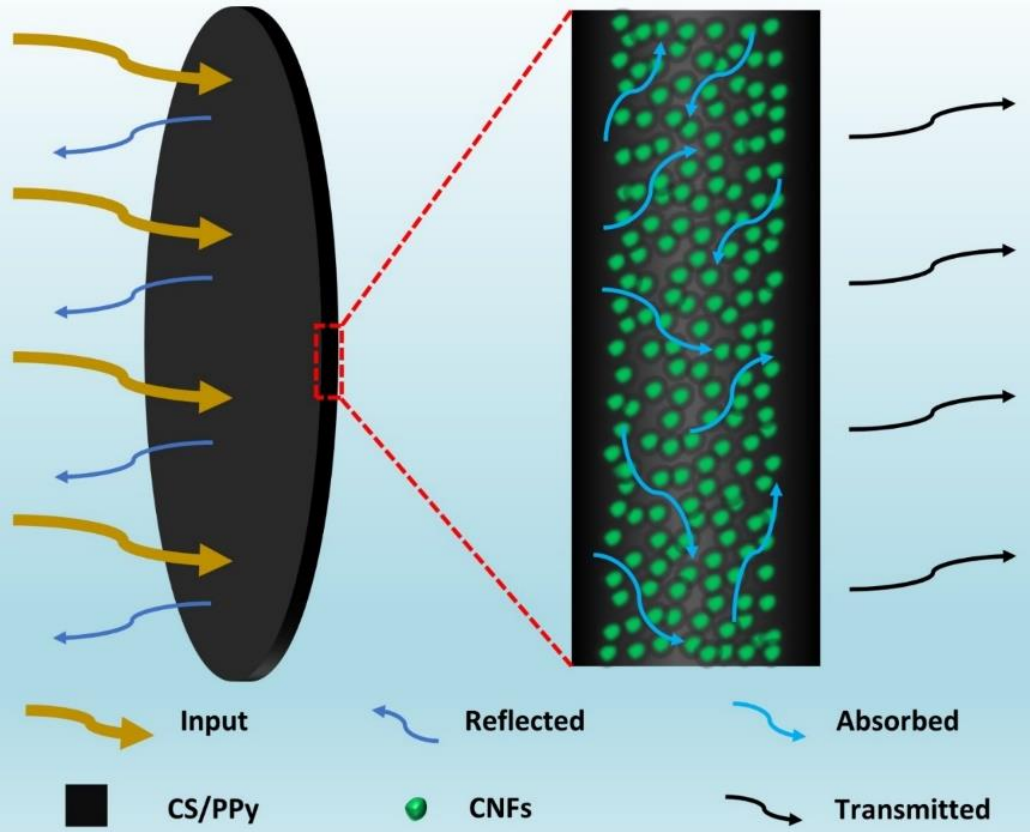

Figure 4-12. Schematic illustration of the EMI shielding mechanism of the CNP/CS/PPy.

4.4 Conclusion

In conclusion, we prepared CNP from a waste material (paper mill sludge) through a sustainable process and demonstrated a facile and versatile approach to functionalize the CNP for achieving multifunctional properties including superior water resistance, electrical conductivity, and antibacterial ability. In the first step, CNP/CS was obtained by a simple impregnation process. Then, PPy was introduced into the CNP/CS through an *in-situ* polymerization route, resulting in the multifunctional CNP/CS/PPy. It was found that the obtained CNP/CS/PPy with a hydrophobic surface (water contact angle > 99°) exhibited excellent water resistance. Compared with the pure CNP, the CNP/CS/PPy exhibits significantly enhanced mechanical strength with 30% and 1048%

increment at dry and wet conditions, respectively. Due to the synergy of CS and PPy, the CNP/CS/PPy shows good antibacterial property towards both gram-positive and gram-negative bacteria, i.e., 99.28% bacterial reduction for *S. aureus* and 95.59% bacterial reduction for *E. coli*. Intriguingly, the CNP/CS/PPy exhibits high electrical conductivity (6.5 S cm^{-1}), which can be used as sustainable EMI shielding materials with a high shielding performance (around 18 dB at a thickness of 63 μm). As a whole, this work provides a facile and sustainable strategy for the functionalization of CNP, which holds great promise for large-scale production of multifunctional CNP from renewable sources. The functionalized CNP may find applications in a variety of high-tech fields.

Chapter 5 Highly flexible, mechanically strong, and conductive PEDOT:PSS/cellulose nanofibrils nanopaper electrodes for flexible supercapacitors

5.1 Introduction

For the past few years, portable and wearable electronic devices have witnessed remarkable growth with the rapid development of artificial intelligence and flexible electronic technologies.[298] Flexible supercapacitors have emerged as promising power supply for various wearable devices, in light of their advantages of wearable characteristics, reliable safety, high power density, long cycling life, etc.[299, 300] To date, a variety of active materials including carbon nanomaterials (e.g., graphene, carbon nanotubes), transition metal oxides (e.g., MnO_2, MoO_3), and conducting polymers (e.g., polyaniline, polypyrrole) have been used for the design and fabrication of flexible supercapacitor electrodes.[301-304] However, most of these active materials lack of the ability to form mechanically stable freestanding films. Thus, many efforts have been made to develop substrate-supported flexible electrodes, in which paper, textile, yarn, and various polymeric films have been used as the flexible substrates.[299] Nevertheless, these substrates account for a large portion of weight of the device yet without contributing to the capacitance, leading to a low specific capacitance based on the weight of the whole device. Therefore, it is of critical importance to develop freestanding electrodes with robust mechanical flexibility, high specific capacitance, excellent cycling stability for the fabrication of high-performance flexible supercapacitors.

As a polythiophene derivative, poly (3,4-ethylenedioxythiphoenes) (PEDOT) has attracted a great deal of attention in both academic research and industrial applications due to its higher conductivity, better stability in ambient conditions, and easier processability than other conducting

polymers such as polyaniline and polypyrrole.[305] Nevertheless, PEDOT is insoluble in water and most of organic solvents, which limits its practical application. Thanks to the efforts of researchers, an important breakthrough was realized by introducing a water-soluble polymeric counter-ions namely polystyrene sulfonate (PSS) onto PEDOT backbone.[306] The resultant PEDOT:PSS could be well dispersed in aqueous and some organic media, which enabled good solution processability. In light of the high conductivity, excellent optical/electrical properties, and easy processability, PEDOT:PSS has been widely used in the fields of flexible displays, organic light emitting diodes, solar cells and energy storage devices etc.[305, 307] Several studies have demonstrated the fabrication of flexible supercapacitors by using PEDOT:PSS coatings or thin films as electrodes.[308, 309] Although PEDOT:PSS thin film exhibits good flexibility, the self-standing film with a large thickness (e.g., > 30 μm) is prone to crack and shows inferior mechanical strength, due to the lack of ability to form stable chemical bonds and its inability to form entangled networks. In order to realize its practical application, developing suitable processing strategies for the formation of mechanically robust and flexible PEDOT:PSS bulk film is highly desired.

Cellulose nanofibrils (CNFs) have emerged as promising nanomaterials with great application potential in diverse fields, in light of their outstanding physiochemical properties such as superior mechanical strength, large specific surface area, high aspect ratio, tunable surface chemistry, along with renewability and biodegradability.[80, 269] Due to the presence of abundant hydroxyl groups on the surface and the semi-crystalline structure, CNF exhibit remarkable tendency to form mechanically stable nanostructures (e.g., films, foams) by self-assembly processes such as filtration, casting, and freeze-drying.[228] Thus, CNFs have been widely used as building blocks to be compounded with various active materials for the preparation of flexible electrodes for supercapacitors. Recently, several attempts have been made to fabricate PEDOT-based flexible

electrodes by using CNFs as building blocks. For example, Wang et al.[310] reported the fabrication of PEDOT/CNF nanopaper using solution-based reactions. The obtained PEDOT/CNF nanopaper can be directly used as the electrodes for symmetric supercapacitors, which exhibited a high specific capacitance (e.g., 920 mF/cm^2) and excellent cycling stability. However, the PEDOT/CNF nanopaper showed inferior mechanical strength (only 2.0 MPa). Ko et al.[311] demonstrated the preparation of highly conductive PEDOT:PSS/CNF nanopaper by vacuum filtration of commercial PEDOT:PSS and CNF dispersion mixtures and post-treatment with organic solvents. Although the obtained PEDOT:PSS/CNF nanopaper showed excellent flexibility and high conductivity, it exhibited quite low specific capacitance, i.e., only 25 F/g at 0.1 A/g. In addition, the high cost of commercial PEDOT:PSS may be the major barrier for its practical application for supercapacitors. Therefore, it is still challenging to inexpensively manufacture mechanically strong and highly conductive PEDOT:PSS/CNF nanopaper electrodes for high-performance supercapacitors.

In Chapter 2, we developed a sustainable and economically feasible approach for the preparation of CNF from paper mill sludge (PMS), which is around 100 times cheaper than the CNF produced by commonly used TEMPO oxidation pretreatment plus mechanical fibrillation.[252] This project is aimed to investigate the feasibility of using the PMS-derived CNF as building blocks for the fabrication of PEDOT:PSS based flexible electrodes. Instead of using commercial PEDOT:PSS, we implement a facile and low-cost strategy for the fabrication of mechanically strong and conductive PEDOT:PSS/CNF nanopaper (denoted as PEDOT:PSS/CNP) by an in situ polymerization process. As shown in **Fig. 5-1**, PEDOT:PSS was firstly polymerized from EDOT monomers with the presence of CNF as building blocks, resulting in the well-dispersed PEDOT:PSS/CNF aqueous suspension. Afterwards, strong and flexible PEDOT:PSS/CNP was produced from the PEDOT:PSS/CNF suspension by a simple vacuum filtration process. It is well

documented that the presence of extra PSS in the PEDOT polymer backbone is detrimental to the electrical conductivity and electrochemical performance of the PEDOT.[312] In order to remove excess PSS, the PEDOT:PSS/CNP was further treated with DMSO. Finally, the as-prepared PEDOT:PSS/CNP was used as the flexible electrodes for supercapacitors, and the electrochemical properties of the assembled supercapacitors were systematically studied.

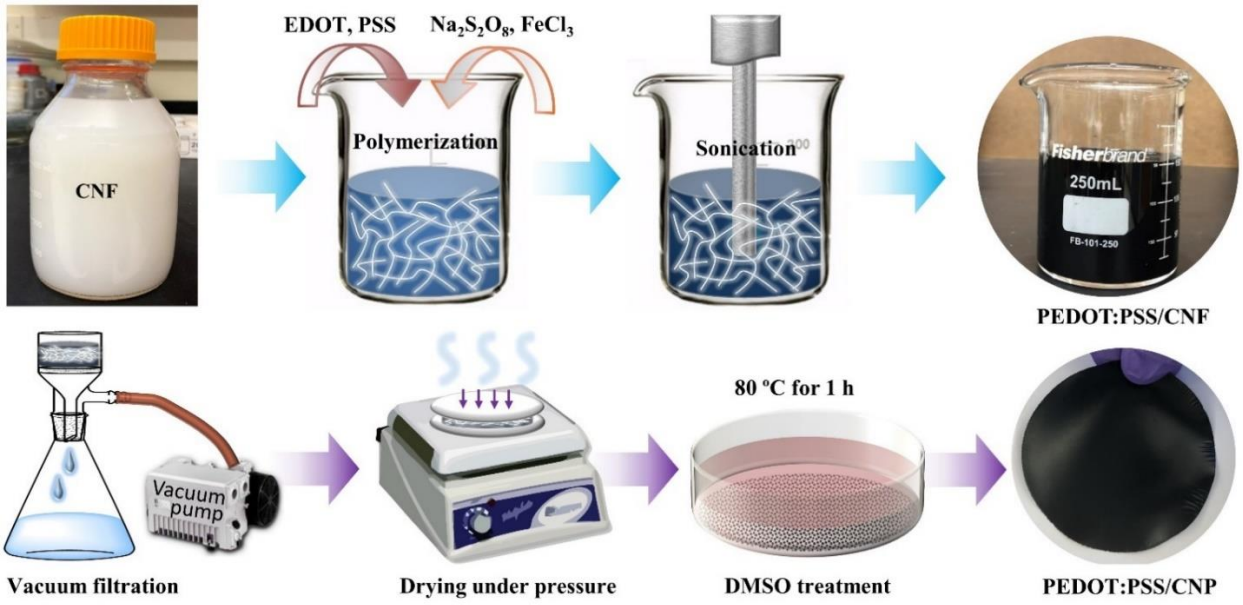

Figure 5-1. Schematic illustration of the preparation of PEDOT:PSS/CNF and the fabrication of PEDOT:PSS/CNP.

5.2 Experimental section

5.2.1 Materials

CNF aqueous suspension with a concentration of 1.0 wt.% was produced from paper mill sludge following the procedure reported in our previous work.[252] EDOT monomer and PSS (18 wt.%) were purchased from Sigma-Aldrich, USA. Sodium persulfate ($Na_2S_2O_8$) was purchased from Alfa Aesar, USA. Sulfuric acid, anhydrous ferric chloride ($FeCl_3$), and dimethylsulfoxide (DMSO)

were purchased from VWR, USA.

5.2.2 Preparation of PEDOT:PSS/CNF

PEDOT:PSS/CNF samples with different loading of PEDOT:PSS were prepared following the procedure reported in the previous work with a slight modification. Firstly, 30 mL of CNF suspension (1.0 wt.%) was diluted to a total volume of 60 mL with DI water. Then, EDOT monomer, PSS with specified amounts (**Table 5-1**) were added in the CNF suspension. The mixture was mixed by magnetic stirring (300 rpm) for 10 min. Afterwards, desired amount of $Na_2S_2O_8$ and $FeCl_3$ were added into the mixture to initiate the polymerization. The reaction was carried out at room temperature for 16 h with magnetic stirring at 300 rpm. Upon completion, the mixture was centrifuged at 6000 rpm for 3 min to seperate the solid part (PEDOT:PSS/CNF) and reaction media. Then, the PEDOT:PSS/CNF was washed with water/methanol (1:1 v/v) twice to remove the unreacted EDOT. The PEDOT:PSS/CNF was further washed with DI water for several times. Finally, the PEDOT:PSS/CNF was diluted with DI water to a total volume of 200 mL.

Table 5-1. Reactant composition in the preparation of PEDOT:PSS/CNF.

Samples	**CNF (g)**	**EDOT (mL)**	**PSS (g)**	**$Na_2S_2O_8$ (g)**	**$FeCl_3$ (mg)**	**Weight ratio of PEDOT:PSS (%)**
PEDOT:PSS/CNF-1	0.3	0.05	0.0612	0.136	0.34	8.5 ± 0.6
PEDOT:PSS/CNF-2	0.3	0.10	0.1224	0.272	0.68	19.4 ± 1.7
PEDOT:PSS/CNF-3	0.3	0.15	0.1836	0.408	1.02	38.6 ± 2.1
PEDOT:PSS/CNF-4	0.3	0.20	0.2448	0.544	1.36	53.5 ± 2.3
PEDOT:PSS/CNF-5	0.3	0.25	0.3060	0.680	1.70	62.5 ± 3.6

Note: the density of EDOT is around 1.36 g/cm^3.

5.2.3 Preparation of PEDOT:PSS/CNP

The diluted PEDOT:PSS/CNF suspension was sonicated with a probe ultrasonicator at a power input of 500 watts for 5 min. After sonication, the PEDOT:PSS/CNF suspension was used to fabricate PEDOT:PSS/CNP by vacuum filtration using a polypropylene filter membrane (diameter of 10 cm, pore size of 0.45 μm). Then, the obtained wet PEDOT:PSS/CNP was placed between two filter membranes and dried at 105 °C for 2 h to remove the moisture.

5.2.4 DMSO treatment of PEDOT:PSS/CNP

In order to remove the excess PSS, the PEDOT:PSS/CNP was further treated by DMSO following a previously reported procedure with a slight modification.[313] Briefly, the PEDOT:PSS/CNP was immersed in DMSO at 80 °C for 1 h. Then, the PEDOT:PSS/CNP was carefully picked up, and excess DMSO was absorbed by using a blotting paper. Finally, the PEDOT:PSS/CNP was placed between two filter membranes and dried at 160 °C for 30 min to remove residual DMSO.

5.2.5 Tensile test

The mechanical properties of PEDOT:PSS/CNP samples were evaluated by an Instron 4465 universal testing machine following the TAPPI standard method (TAPPI T497). The samples were cut into 1 cm × 5 cm strips for all the measurements. The gauge length was adjusted to 20 mm, and the crosshead speed was set at 5 mm/min. Three measurements were carried out for each sample and the averaged value was reported.

5.2.6 Sheet resistance and conductivity measurement

The sheet resistance of the PEDOT:PSS/CNP samples were examined according to the van der Pauw four-point probe technique using a digital multimeter (RIGOL DM3068). Before test, the sample was cut into square specimens (1.5 × 1.5 cm^2), and four corners of the specimen were coated with silver paint to ensure good electrical contacts. Then, the four probes were contacted on the four corners of the specimen and the resistance (R) was recorded. The sheet resistance (R_s) was calculated based on the Equation (1),[281] as follows:

$$R_s = \frac{\pi R}{ln2} \approx 4.53R \qquad (1)$$

Further, the conductivity (ρ) can be calculated from Equation (2), as follows:

$$\rho = \frac{1}{R_s \times t} \qquad (2)$$

where t is the thickness of the specimen. Three independent determinations were carried out and the averaged value was reported.

5.2.7 Materials characterization

Fourier transform infrared spectroscopy (FTIR) spectra of samples were recorded on a Thermo Nicolet 6700 FTIR spectrometer from 4000 to 500 cm^{-1} at a resolution of 4 cm^{-1}. XPS spectra of PEDOT:PSS/CNP samples before and after DMSO treatment were collected on a photoelectron spectrometer (EscaLab Xi+, Thermo Fisher Scientific) with a non-monochromatized Al Kα radiation (1486.6 eV) under the vacuum pressure of 8 × 10^{-10} Pa. A field emission scanning electron microscope (FESEM, Apreo FE) coupled with an energy dispersive X-ray spectroscope

(EDS) was used to examine the surface and cross-section morphology and elemental compositions of samples. The morphology of CNF and PEDOT:PSS/CNF samples was observed on a high-resolution transmission electron microscopy (HRTEM, JEM-2100) operated at an acceleration voltage of 200 kV. The elemental mappings of PEDOT:PSS/CNF were obtained using a scanning transmission electron microscope with a high-angle annular darkfield (HAADF) detector (HITACHI S-5500).

5.2.8 Electrochemical measurements

The electrochemical measurements were conducted on a CHI 660E electrochemical workstation (CHI, USA) using 1.0 M H_2SO_4 as the electrolyte. As shown in **Fig. 5-2**, two configurations were used to evaluate the electrochemical performance of the as prepared PEDOT:PSS/CNP. The electrochemical properties of the PEDOT:PSS/CNP before and after DMSO treatment was firstly examined in a three-electrode system, the specimen with a dimension of 1 cm × 1 cm × 70 μm was directly used as working electrode with the platinum (Pt) mesh as current collector. Pt mesh and Ag/AgCl with 3 M KCl were used as the counter electrode and reference electrode, respectively. Cyclic voltammetry (CV) measurements were performed within a potential range of 0 V-0.8 V at the scan rate of 50 mV s^{-1}. Electrochemical impedance spectroscopy (EIS) measurements were recorded within the frequency range from 100 kHz to 0.01 Hz by applying an amplitude AC voltage of 5 mV.

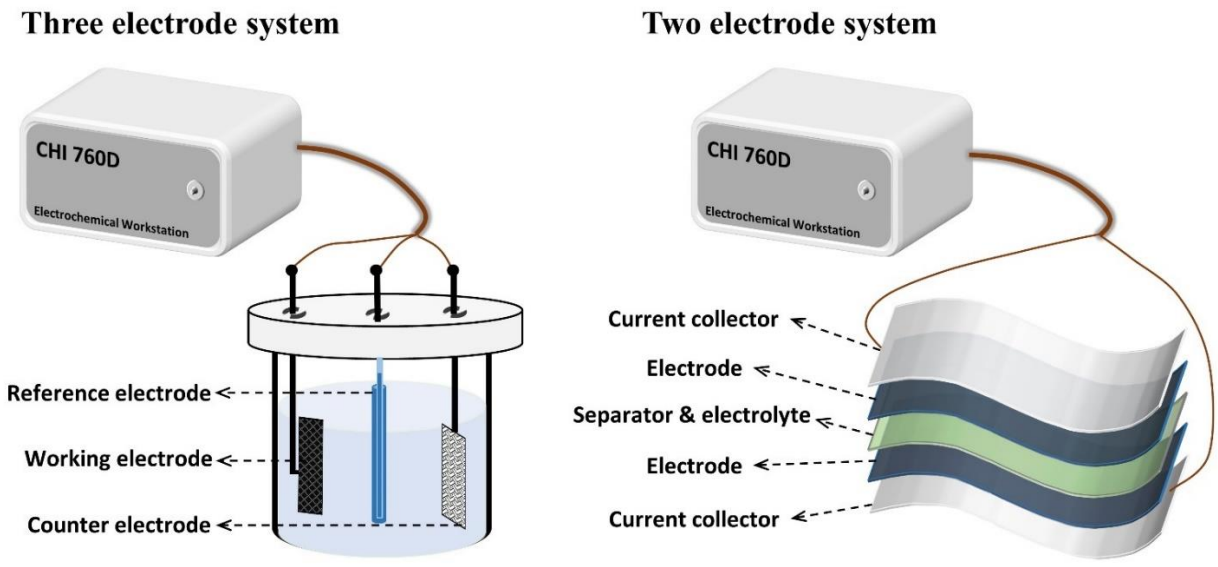

Figure 5-2. Two different configurations of the electrochemical measurement.

Furthermore, a symmetrical supercapacitor device was assembled by using two piece of DMSO-treated PEDOT:PSS/CNP (dimension of each electrode: 1 cm × 1 cm × 70 μm) as both positive and negative electrodes with polypropylene membrane (absorbed with 1.0 M H_2SO_4) as separator. The electrochemical performance of the assembled device was evaluated in a two-electrode mode. CV measurements were performed within a potential range of 0 V to 1.0 V with varying scan rate ranges from 2 to 500 mV s^{-1}. Galvanostatic charge-discharge (GCD) measurements were conducted within a potential window of 0 to 1.0 V with different current density. Moreover, EIS measurements were performed using the same parameters as mentioned in the three-electrode system.

The cell capacitance (C_{cell}) of the symmetric device was determined from the CV curves in the two-electrode configuration by using the following equation:

$$C_{cell} = \frac{\int \mathrm{I} dV}{vA\Delta \mathrm{V}} \qquad (3)$$

Where I is the voltammetric discharge current (mA), υ is the scan rate (mV s^{-1}), A is the total aera of the two electrodes of the device (2 cm^2), ΔV is the potential window (1 V).

The specific capacitance (C_{sp}) of a single electrode can be derived from the cell capacitance, as follows [314]:

$$C_{sp} = 4C_{cell} \quad (4)$$

The energy density (E) and power density (P) can be calculated by the following equations [315]:

$$E = \frac{C_{cell} \times \Delta V^2}{2 \times 3600} \ (Wh\ cm^{-2}) \quad (5)$$

$$P = \frac{3.6 \times E \times v}{\Delta V} \ (W\ cm^{-2}) \quad (6)$$

Where C_{cell} (F cm^{-2}), ΔV (1 V), and υ (mV s^{-1}) are as described above.

5.3 Results and discussion

5.3.1 Mechanical property

Fig. 5-3 shows the strain-stress curves of PEDOT:PSS/CNP samples with different PEDOT:PSS loading and the control sample (pure CNP). It can be clearly seen that the mechanical strength decreased with the increasing ratio of PEDOT:PSS, since the strength is mainly attributed to the hydrogen bonding among the CNF. The more PEDOT:PSS coated on the surface of CNF, the more severely hinder the formation of hydrogen bonding. Nevertheless, the PEDOT:PSS-/CNP (53.5%) still exhibited relatively high tensile strength over 70 MPa. As demonstrated in the photograph, a PEDOT:PSS/CNP (53.5%) strip with a width of around 8 mm and a thickness of 70 μm is able to

lift up an autoclave with a weight about 2 kg. This excellent mechanical strength will promote its potential for the practical applications.

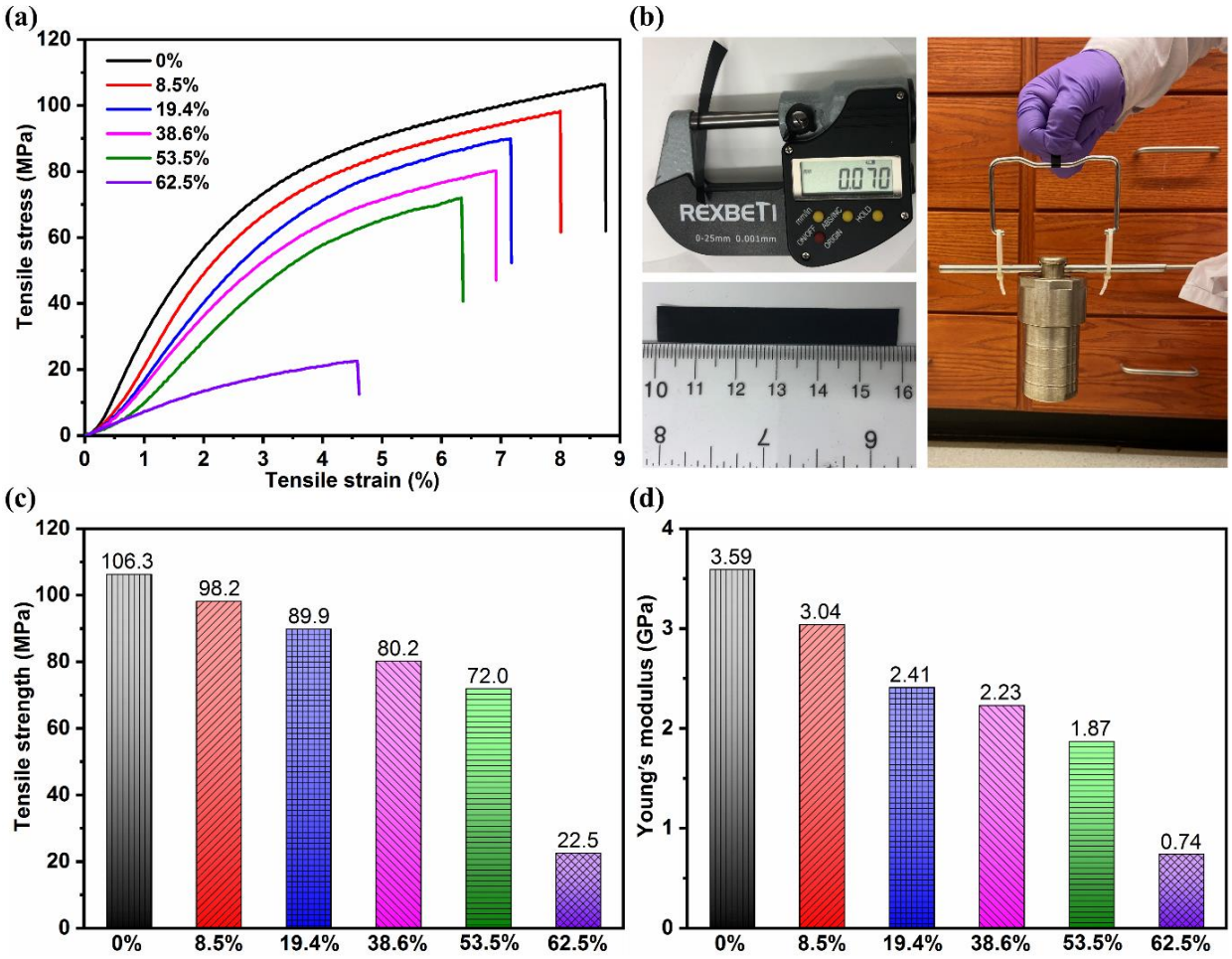

Figure 5-3. (a) Strain-stress curves of the pure CNP (0%) and PEDOT:PSS/CNP with different PEDOT:PSS loading (8.5%-62.5%). (b) Photograph showing the dimension of the PEDOT:PSS/CNP (53.5%) strip, which could lift up an autoclave with a weight of 2 kg. The tensile strength (c) and Young's modulus (d) of pure CNP and PEDOT:PSS/CNP samples.

5.3.2 Conductivity

As shown in **Fig. 5-4a**, with the increasing loading of PEDOT:PSS, the conductivity of the PEDOT:PSS/CNP remarkably increased by several orders of magnitude. More importantly,

significant enhancement in the conductivity was observed after DMSO treatment. The maximum conductivity of 126.21 S/cm was achieved for the PEDOT:PSS/CNP (62.5%). However, as indicated in **Fig. 5-3**, the PEDOT:PSS/CNP (62.5%) shows inferior mechanical strength, which may limit its practical application. Notably, the PEDOT:PSS/CNP (53.5%) still exhibits relatively superior conductivity of 66.67 S/cm. This value is higher than most of the results of conducting polymer and CNF based nanocomposite films reported in the literature, such as PEDOT:PSS/CNF (2.58 S/cm),[292] PEDOT:PSS/PPy/CNF (10.55 S/cm),[292] PPy/CNF (0.26 S/cm),[230] PEDOT:PSS/CNF (45 S/cm).[316] Considering the superior conductivity and high mechanical strength, the DMSO treated PEDOT:PSS/CNP (53.5%) sample is considered as the optimal sample in this work. Without further specification, PEDOT:PSS/CNF and PEDOT:PSS/CNP will be directly used in the following sections, in which the weight ratio of PEDOT:PSS is 53.5%.

It should be noted that the conductivity of the PEDOT:PSS/CNP sample was increased from 4.02 S/cm to 66.67 S/cm after DMSO treatment, indicating more than 16-fold increment. This enhancement can be explained by the fact that DMSO can dissolve part of the excess PSS shell to release the conductive PEDOT.[317] As illustrated in **Fig. 5-4d**, the PEDOT:PSS appears like a core-shell structure before DMSO treatment, including PEDOT-rich core and PSS-rich shell. There are weak hydrogen bonding reactions among the PSS shells, which limit the charge transfer. Upon DMSO treatment, the excess PSS shells can be removed because the strong hydrogen bonding between PSS and DMSO which facilitates the removal of PSS from the PEDOT:PSS complex. Eventually, continuous PEDOT-rich chains can be formed to provide continuous pathways for the charge carriers.[318] Furthermore, **Figs. 5-4b** and **5-4c** demonstrates that a LED can be lighted when the PEDOT:PSS/CNP strip was connected into a circuit even at the twisting state, suggesting its excellent conductivity and flexibility.

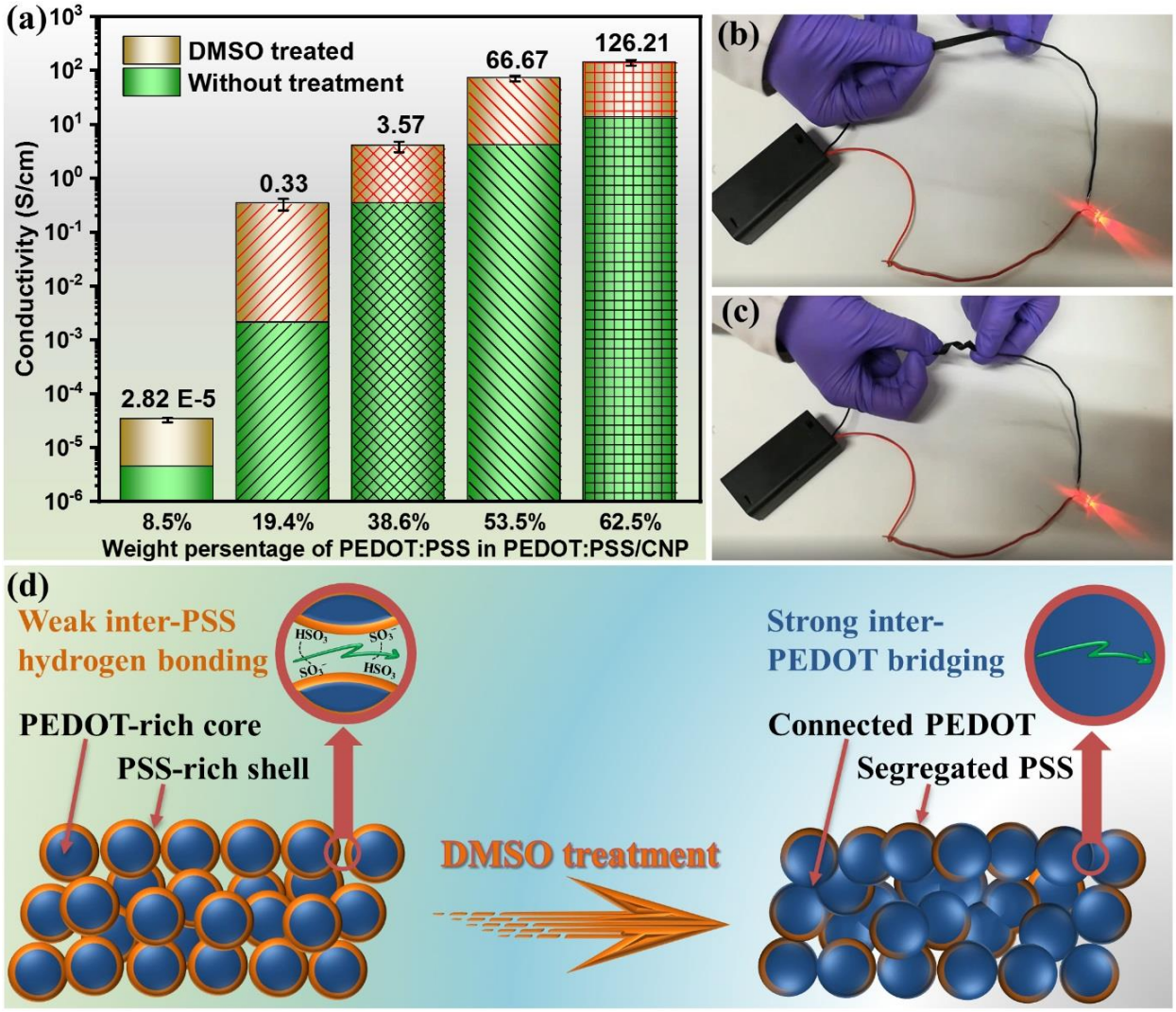

Figure 5-4. (a) Comparison of conductivity of PEDOT:PSS/CNP samples without and with DMSO treatment. Photographs showing the good electrical conductivity of the DMSO treated PEDOT:PSS/CNP at flat (b) and twisting (c) states. (d) Schematic illustration of the PEDOT:PSS before and after DMSO treatment.

5.3.3 Materials characterization

The chemical structure of the obtained PEDOT:PSS/CNF and PEDOT:PSS/CNP samples was firstly investigated by FTIR. As shown in **Fig. 5-5a**, the bands at 3335, 2918, 1645, 1429, 1161, 1105, and 897 cm^{-1} in the spectrum of pure CNF are the characteristic peaks of cellulose Iβ, and

the peak at 1717 cm^{-1} is attributed to the C=O stretching from ester groups on the CNF.[252] In the spectrum of pure PEDOT:PSS, the typical bands of PEDOT:PSS can be observed. Among them, the strong band at 3353 cm^{-1} corresponds to the O-H stretching, and the peaks at 2920 and 2854 cm^{-1} are attributed to the C-H symmetric and asymmetric stretching, respectively.[319] The band at 1645 cm^{-1} corresponds to the C=C bonds of the thiophene ring, and the band at 1120 is assigned to the SO_3H group of PSS.[320] The bands near 1514 and 1321 cm^{-1} are assigned to the C=C asymmetric stretching and C–C inter-ring stretching, respectively.[321] The bands at 1182 and 1086 cm^{-1} correspond to the C–O–C bending vibrations in the ethylenedioxy group, while the peaks at 980, 828, and 674 cm^{-1} are assigned to the C–S–C stretching vibrations in the thiophene ring.[321-323] As shown in the spectrum of PEDOT:PSS/CNF, mixed peaks either from CNF or PEDOT:PSS can be observed. For example, the peak at 980 cm^{-1} comes from the PEDOT:PSS, while the peak at 1062 cm^{-1} contributed by CNF. This result indicates the formation of a composite between CNF and PEDOT:PSS after in situ polymerization. After DMSO treatment, the peaks in the spectrum of DMSO-treated PEDOT:PSS/CNF are nearly parallel with the bands in the spectrum of PEDOT:PSS/CNF. However, it is difficult to examine the chemical structure change of PEDOT:PSS/CNF before and after DMSO treatment. Only a notable difference in the peak intensity at 2920 cm^{-1} can be observed, which is probably due to the removal of extra PSS after DMSO treatment.

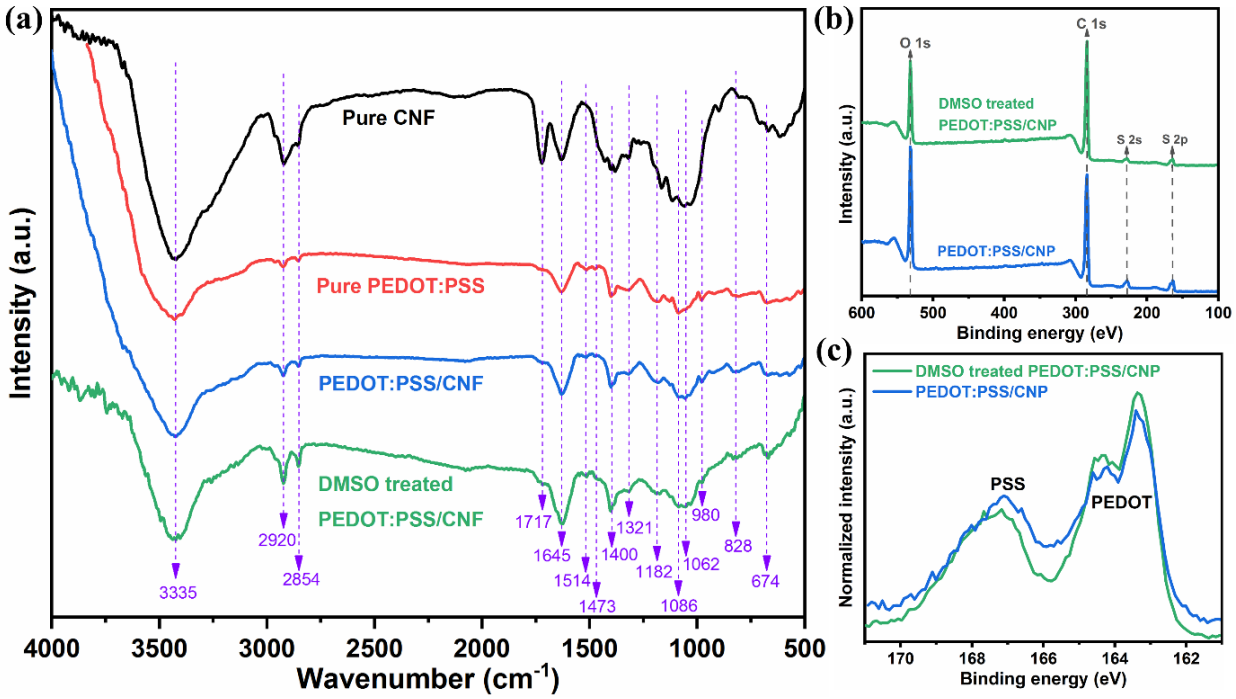

Figure 5-5. (a) FTIR spectra of pure CNF, pure PEDOT:PSS, PEDOT:PSS/CNF, and DMSO treated PEDOT:PSS/CNF. (b) XPS survey spectra of PEDOT:PSS/CNP samples with and without DMSO treatment. (c) XPS (S 2p) spectra of PEDOT:PSS/CNP samples with and without DMSO treatment.

In order to further elucidate the mechanism of DMSO treatment, XPS analysis of the PEDOT:PSS/CNP with and without DMSO treatment was carried out. **Fig. 5-5b** displays the XPS survey spectra of PEDOT:PSS/CNP before and after DMSO treatment. It can be clearly seen that both the S 2p and S 2s core level peaks become smaller after DMSO treatment. By integrating the XPS peaks, elemental composition was further calculated. Results indicated that the S element in the PEDOT:PSS/CNP reduced from 9.5% to 5.4% after DMSO treatment, indicating the extra PSS was removed during the DMSO treatment process. Moreover, two peaks at around 167.2 eV and 163.2 eV in the XPS (S 2p) spectra of PEDOT:PSS/CNP samples before and after DMSO treatment (**Fig. 5-5c**) can be observed, which correspond to the sulfur signals from PSS and

PEDOT, respectively.[324] By comparing the normalized peak intensity, it can be concluded that the excess PSS was successfully removed after DMSO treatment.

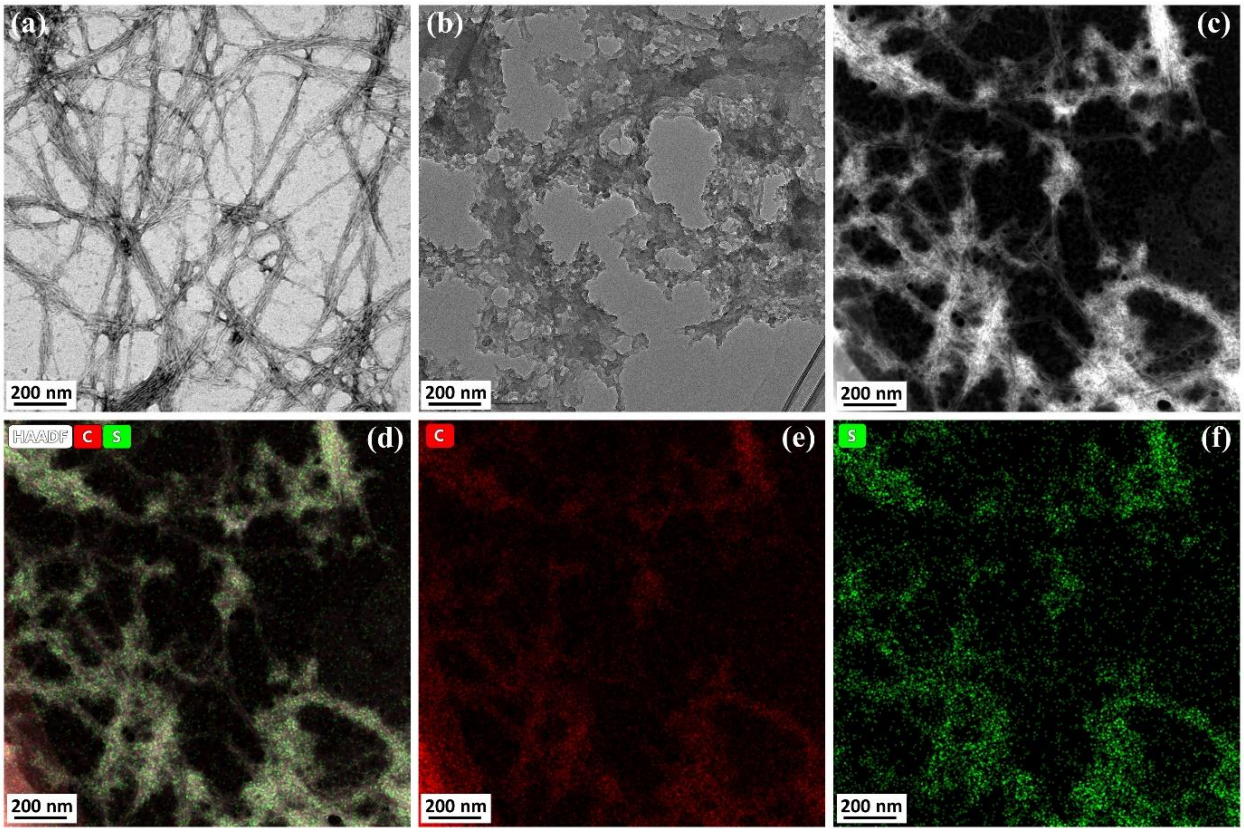

Figure 5-6. TEM images of CNF (a), PEDOT:PSS (b), and PEDOT:PSS/CNF (c). HAADF-STEM image of PEDOT:PSS/CNF and the corresponding elemental mappings of C and S (d-f).

The morphology of CNF, PEDOT:PSS, and the PEDOT:PSS/CNF was examined by TEM analysis. As shown in **Fig. 5-6a**, the CNF shows fiber structure with the average diameter of around 24 nm, and the length more than 1 μm. From **Fig. 5-6b**, it can be seen that the PEDOT:PSS exhibits aggregate particle morphology. **Fig. 5-6c** displays a mixture of CNF and PEDOT:PSS, in which the PEDOT:PSS aggregate particles coated on the CNF. Moreover, **Figs. 5-6 (d-f)** show the HAADF-STEM image of the PEDOT:PSS/CNF and the corresponding elemental mappings of C and S. It can be clearly seen that the CNF has been uniformly coated with PEDOT:PSS.

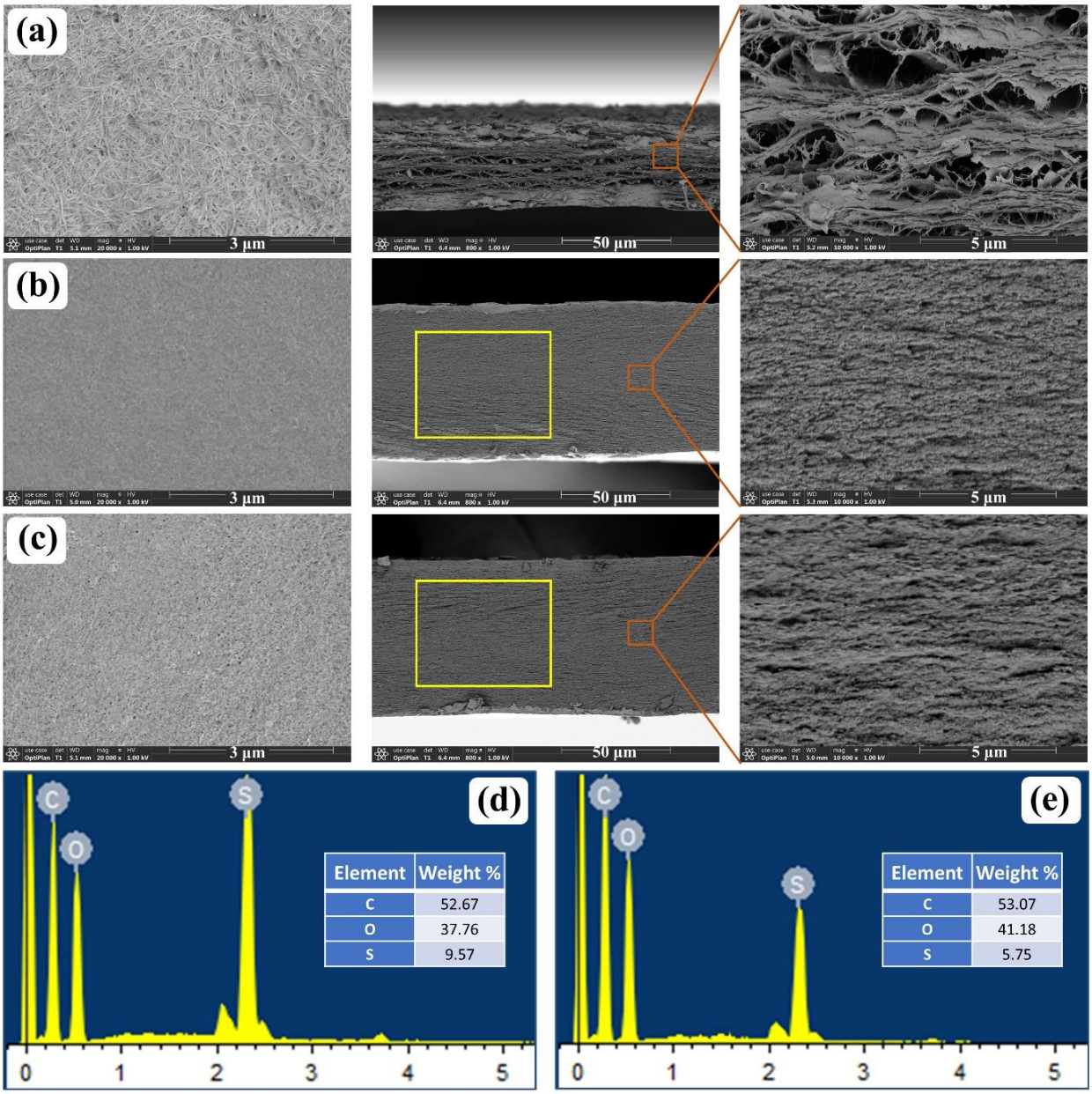

Figure 5-7. SEM surface and cross-section images of pure CNP (a), PEDOT:PSS/CNP (b), and DMSO-treated PEDOT:PSS/CNP (c); EDS spectra of PEDOT:PSS/CNP (d) and DMSO-treated PEDOT:PSS/CNP (e).

The surface and cross-section morphology of the pure CNP and PEDOT:PSS/CNP with and without DMSO treatment was further characterized by SEM. As shown in **Fig. 6a**, randomly entangled CNFs can be observed on the surface of pure CNP. Also, the pure CNP exhibits a

lamellar cross-section structure with notable gaps between layers, which is mainly due to the rigid structure and the broad diameter distribution of the CNF. Interestingly, the PEDOT:PSS/CNP shows smoother surface and denser interlayer structure, which is probably due to the voids between CNFs are filled with PEDOT:PSS. As indicated in **Fig. 6c**, a lot of small holes appeared on the surface of the PEDOT:PSS/CNP after DMSO treatment, and the interior lamellar structure become slightly rough. This phenomenon is probably due to removal of extra PSS upon DMSO treatment, and similar results have been reported in the previous study.[311]

5.3.4 Electrochemical characterization

The electrochemical performance of PEDOT:PSS/CNP with and without DMSO treatment was firstly examined in a three-electrode system. As indicted in **Fig. 5-8a**, the DMSO treated sample shows a quasi-rectangular shape, while the distorted leaf-shaped CV curve can be observed for the untreated sample. It is well-known that the more likely rectangular shape of the CV curve, the better supercapacitive performance of the electrode materials. Also, the area enclosed within the CV curves is proportional to the capacitance. Obviously, the DMSO treated PEDOT:PSS/CNP sample shows better electrochemical performance and higher specific capacitance than the untreated counterpart.

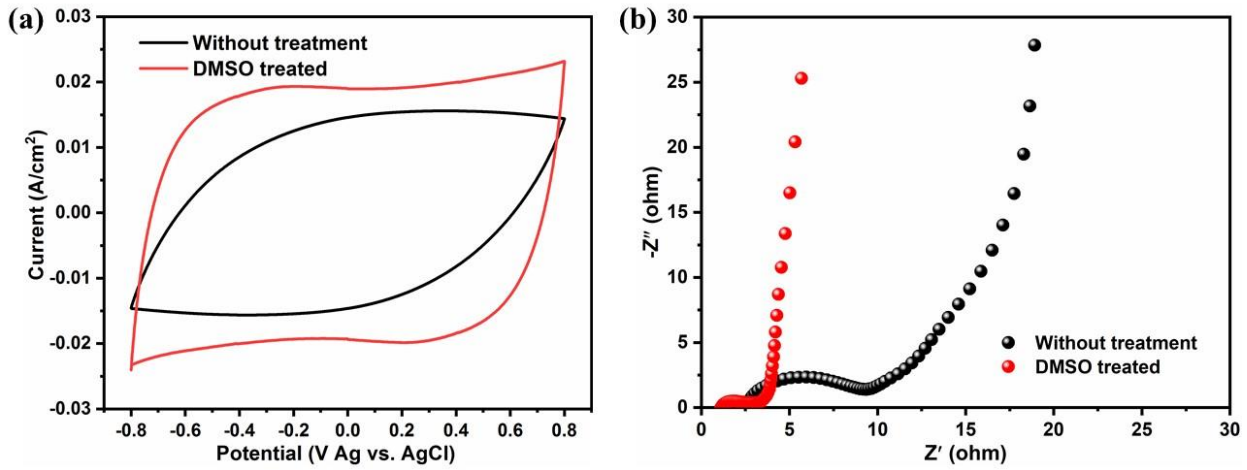

Figure 5-8. Comparison of CV curves (a) and Nyquist impedance plots (b) of the PEDOT:PSS/CNP with and without DMSO treatment.

Moreover, EIS was further performed to investigate the electrochemical behavior of the electrodes, and the Nyquist plots are shown in **Fig. 5-8b**. Both the Nyquist plots show similar shape with quasi-semicircular parts at high frequency region and near-vertical linear parts at low frequency region. The intercept of the semicircle on the x-axis represents equivalent series resistance (ESR) that originates from the total internal resistance of the cell, and the semicircle diameter reflects the charge-transfer resistance (R_{ct}). As indicated in **Fig. 5-8b**, the DMSO treated sample shows a smaller ESR (1.02 Ω) than that (2.55 Ω) of the untreated sample, which is in line with the conductivity results (**Fig. 5-4a**). Moreover, the DMSO treated sample exhibits a low R_{ct} of around 2.5 Ω, which is much lower than that (7.2 Ω) of the untreated sample. This result indicates the DMSO treatment enables the fast faradaic charge transfer process of the electrode, which accounts for the enhanced electrochemical performance of the DMSO treated PEDOT:PSS/CNP sample.

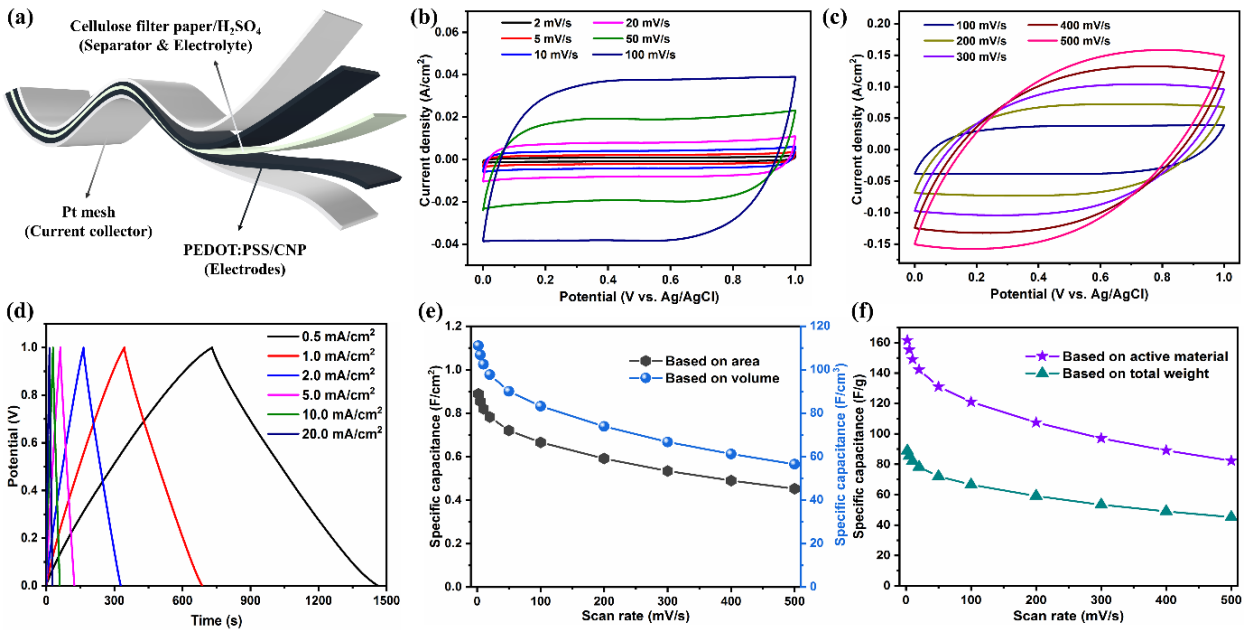

Figure 5-9. Schematic illustration of the PEDOT:PSS/CNP supercapacitor device (a). CV curves at different scan rate (b, c), GCD curves at different current density (d), and specific capacitance based on area and volume (e), and mass (f) of the assembled supercapacitor.

Based on the results obtained in the three-electrode system, it can be concluded that the DMSO treated PEDOT:PSS/CNP sample exhibits significantly enhanced electrochemical performance than its untreated counterpart. As illustrated in **Fig. 5-9a**, the DMSO treated PEDOT:PSS/CNP (simplified as PEDOT:PSS/CNP in the following sections) was directly used as both the positive and negative electrodes to assemble a real supercapacitor device, polypropylene membrane (absorbed with 1.0 M H_2SO_4) and Pt mesh served as separator and current collector, respectively. The electrochemical performance of the assembled PEDOT:PSS/CNP supercapacitor device was examined following the two-electrode configuration. **Figs. 5-9b** and **5-9c** show the CV curves of the assembled device at different scan rates from 2 to 500 mV/s with the potential range of 0-1.0 V. At lower scan rates than 100 mV/s, all of the CV curves show symmetrical quasi-rectangular shapes without obvious redox peaks, indicating that over the whole CV range, the charge and

discharge process of the electrodes are at a pseudo-constant rate.[325] As the scan rate increases from 100 mV/s to 500 mV/s, the CV curves deviated from quasi-rectangular like shapes to distorted leaf shapes. This phenomenon is mainly due to the polarization of the electrodes.[326] More specifically, at a very high scan rate, the diffusion rate of electrolyte from the solid/liquid interface to the active site of electrode material cannot match the rate of the electrochemical reaction of electrode materials which leads to the electrolyte enriched at the solid/liquid interface and the polarization occurred.[173]

As show in **Fig. 5-9d**, the GCD curves of the device at different current densities ranging from 0.5 mA/cm^2 to 20 mA/cm^2 were collected. It can be clear seen that all of the GCD curves exhibit symmetrical triangular shapes, which indicates the good charge-discharge reversibility of the electrodes. Moreover, negligible internal resistance drop can be observed for all the GCD curves, suggesting a low ESR of the assembled device. Finally, the specific capacitance based on mass, area, and volume of the electrode material was calculated, respectively, and the results are summarized in **Figs. 5-9e** and **5-9f**. Moreover, the areal specific capacitance and volumetric specific capacitance were calculated to be 888.7 mF/cm^2 and 111.1 F/cm^3 at 2 mV/s, respectively, which are higher than most of the previous reported values. As we can see from **Fig. 5-9f**, a high specific capacitance of 166.1 F/g can be obtained at a scan rate of 2 mV/s based on the active material (PEDOT:PSS). Even based on the total weight of the PEDOT:PSS/CNP, a relatively high specific capacitance of 88.9 F/g can be achieved. Notably, around 62% capacitance retention was observed when the scan rate increase from 2 mV/s to 500 mV/s, indicating that the device shows excellent rate performance.

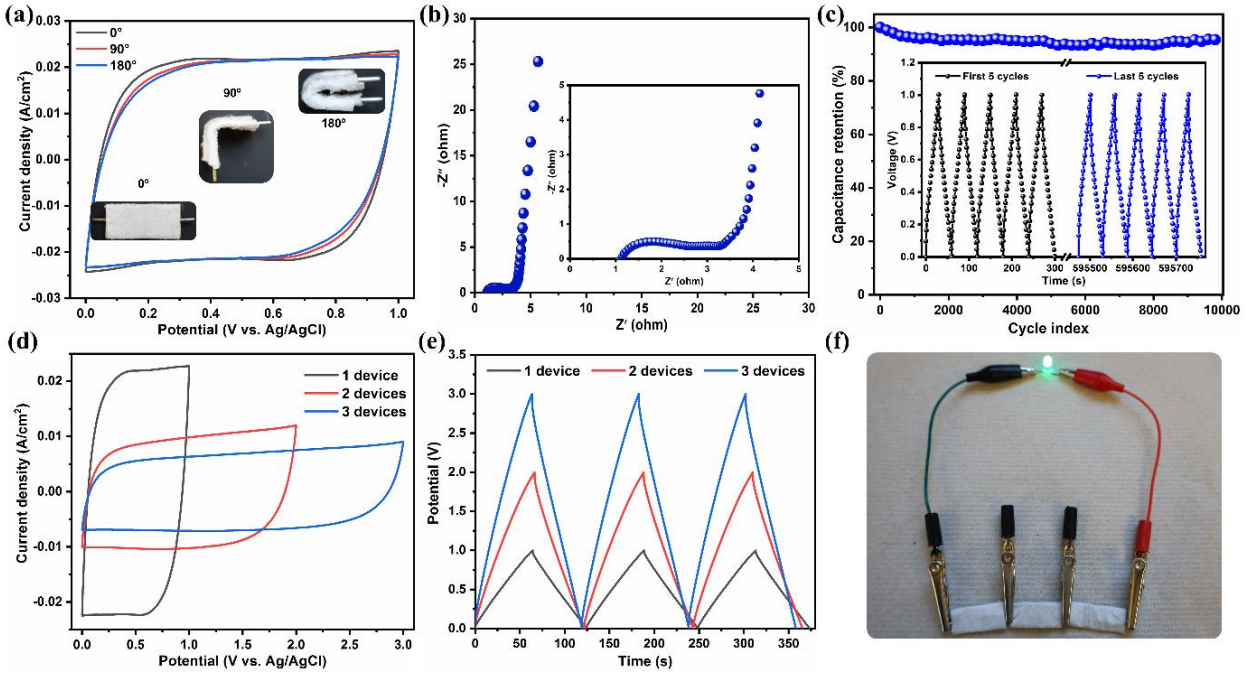

Figure 5-10. (a) CV curves (at 50 mV/s) of the device at different bending angle. (b) Nyquist plot of the device, the inset shows the magnified Nyquist plot at high frequency region. (c) Cycling stability of the device at a current density of 10 mA/cm^2, the inset displays the GCD curves of the initial 5 cycles and the last 5 cycles. (d) CV curves (at 50 mV/s) of 1 device, 2 devices in series connection, and 3 devices in series connection. (e) GCD curves (at 5 mA/cm^2) of 1 device, 2 devices in series connection, and 3 devices in series connection. (f) The photograph showing that 3 devices in series connection could light a LED lamp.

As indicate in **Fig. 5-10a**, the assembled supercapacitor showed good flexibility, which was able to work under deformation, even up to 180, with negligible change of the CV curve. **Fig. 5-10b** shows the Nyquist plot of the device, which is similar to that obtained in the three-electrode system. This result indicates that the assembled device also exhibited low ESR and charge-transfer resistance. Moreover, the near-vertical line at the low frequency region suggests excellent capacitive behavior of the device.[327] As indicated in **Fig. 5-10c**, the device exhibited remarkable cycling stability with the capacitance retention of 95.8% after 10,000 charge/discharge cycles at a current density of 10 mA/cm^2. In order to demonstrate the practical application potential of the PEDOT:PSS/CNP supercapacitor device, the energy storage performance was further investigated

by connecting multiple devices in series. As shown in **Fig. 5-10d**, the tandem devices exhibited stepwise increasing operating voltage from 1.0 V for a single device, 2.0 V for two, and 3.0 V for three without changing the quasi-rectangular shape of the CV curves. Similarly, the galvanostatic voltages linearly increased with the increasing number of devices being connected in series (**Fig. 5-10e**). Also, the GCD curves retained their original symmetrical triangular shapes perfectly with negligible internal resistance drop, even at a high voltage of 3.0 V. **Fig. 5-10f** demonstrates that 3 devices connected in series were able to provide enough charge to light a LED lamp, suggesting its attractive practical application.

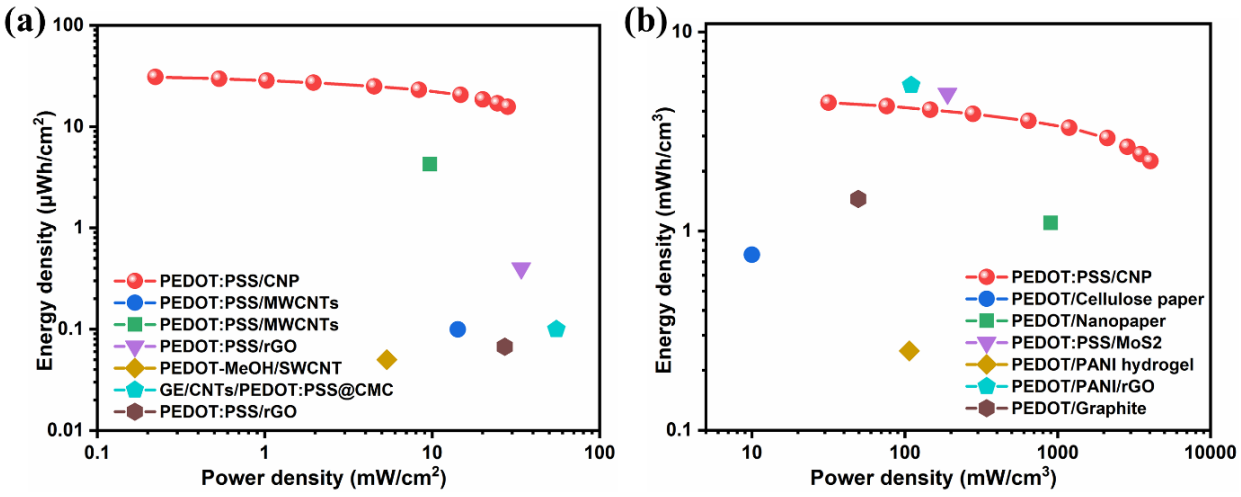

Figure 5-11. Ragone plots the symmetrical PEDOT:PSS/CNP supercapacitor device based on area (a) and volume (b) in comparison with other reported results.

Finally, the Ragone plots (energy density vs. power density) of the device based on area and volume are shown in **Figs. 10a** and **10b**, respectively. The supercapacitor can deliver an energy density of 30.86 μWh/cm^2 at a power density of 0.22 mW/cm^2 and it still maintains an energy density of 15.71 μWh/cm^2 at a power density of 28.27 mW/cm^2, which are among the highest values reported for PEDOT:PSS based supercapacitors. Also, it can offer the highest volumetric

energy density of 4.41 mWh/cm^3 at a power density of 31.74 mW/cm^3, which is comparable with or even higher than the previously reported results for PEDOT:PSS based supercapacitors.

5.4 Conclusion

In summary, we demonstrated a facile and low-cost strategy for the fabrication of mechanically strong and conductive PEDOT:PSS/CNP by using PMS-derived CNF as building blocks. The optimized PEDOT:PSS/CNP exhibited excellent flexibility, high mechanical strength (70 MPa) and high electrical conductivity (66.67 S/cm), which can be directly used as flexible electrodes for supercapacitors. It was found that the assembled PEDOT:PSS/CNP supercapacitor device exhibited a high areal specific capacitance (888.7 mF cm^{-2} at 2 mV/s) and excellent rate property (around 62% capacitance retention as the scan rate increased from 2 mV/s to 500 mV/s). Notably, the device showed high energy density and power density, i.e., the highest energy density of 30.86 μWh/cm^2 (corresponding to 4.41 mWh/cm^3) at a power density of 0.22 mW/cm^2 (corresponding to 31.74 mW/cm^3), which surpass most of pure PEDOT based supercapacitors and are even comparable with some PEDOT based composite supercapacitors. More importantly, the PEDOT:PSS/CNP device exhibited excellent cycling stability with 95.8% capacitance retention after 10,000 cycles. Thus, the PEDOT:PSS/CNP could be promising electrode materials for flexible supercapacitors. This work may open up new opportunities for large-scale production of flexible energy storage devices from renewable and sustainable bioresources.

Chapter 6 Conclusions and future work

In summary, this dissertation established the valorization of PMS into CNFs and their multifunctional nanocomposites. Firstly, a facile and sustainable approach by FA hydrolysis pretreatment and the followed microfluidization was established in the first project to efficiently convert PMS into surface functionalized CNFs. Mechanically strong CNP can be further fabricated from the PMS-derived CNFs through a simple vacuum filtration approach. It should be noted that the CNP exhibits inferior mechanical strength at high-humidity environment due to the hydrophilic nature of cellulose, which significantly impedes its practical application. Therefore, we developed two facile and versatile approaches to functionalize CNP for achieving multifunctional properties including water resistance, antibacterial ability, improved barrier performance, and electric conductivity in the second and third projects. In the last project, the feasibility of using the PMS-derived CNF as building blocks for the fabrication of mechanically strong and conductive PEDOT:PSS based flexible electrodes was investigated. In the following sections, the main findings and the future work of each project will be summarized separately.

In the first project, we demonstrated a sustainable approach to efficiently convert PMS to CNFs by FA hydrolysis pretreatment and the followed microfluidization. It is found that FA hydrolysis (4-6 h) could swell and shorten PMS fibers, and only two-pass microfluidization is sufficient to get uniform CNFs from the collected cellulose residual. Results indicate that the obtained CNFs show high thermal stability and crystallinity index, surface functionality (ester groups), as well as a high yield of over 75 wt.%. Notably, more than 90% FA can be recovered through distillation, and the hydrolyzed sugars could be potentially used to produce platform chemicals (e.g., lactic acid, furfural). More importantly, the chemical cost for FA hydrolysis is only 2.6 USD/kg CNFs,

about 86 times lower than that for TEMPO oxidation. Finally, transparent CNP was prepared from the CNFs suspension via a simple vacuum filtration technique. The resultant CNP showed good mechanical properties with the maximum tensile strength and toughness of 106.4 MPa and 6.62 MJ/m3, respectively. Therefore, the first project provides a green and sustainable method to valorize PMS for the production of valuable CNFs and CNP.

Future study can focus on establishing optimized process conditions of FA hydrolysis pretreatment to produce CNF with optimized yield and tunable physiochemical properties (e.g., aspect ratio, degree of substitution of ester groups, degree of polymerization, crystallinity, thermal stability). Regarding the presence of ester groups on the CNFs surface, it would be interesting to the feasibility of the surface functionalized CNFs as nanofillers for polymeric matrices (e.g., PLA). During the FA hydrolysis pretreatment process, most of the hemicellulose and the disordered regions of cellulose can be hydrolyzed to carbohydrates (e.g., glucose, xylose), the purification of these sugars or further conversion of these carbohydrates into platform chemicals (e.g., lactic acid) is worth to be investigated. Last but not least, this strategy would be applicable to other agro-industrial wastes. For example, the FA hydrolysis could be directly applied to pretreat wood sawdust to produce lignin-containing CNFs.

In the second project, a facile and sustainable approach was established to functionalize the PMS-derived CNP by impregnation of CS and the followed halogenation. It was found that the tensile strength of the functionalized CNP (CNP/CS-Cl) was enhanced by 38.3% and 512.6% at dry and wet conditions, respectively. Meanwhile, the total transmittance (at 550 nm) of CNP/CS-Cl was increased from 75% of pure CNP to 85%, with 35% decrease in optical haze. Moreover, the CNP/CS-Cl exhibited significant enhancement in barrier properties. Importantly, part of the amino

groups on CS were transformed into N-halamines during the halogenation process, which endowed the CNP/CS-Cl with excellent antibacterial performance against both *S. aureus* and *E. coli* with 100% bacterial reduction after 10 min of contact. Thus, this project provides a simple and efficient approach to functionalize CNP with water resistance, high transparency, excellent antibacterial and barrier properties, which will expand the potential applications of CNP, for example as advanced packaging materials.

For the future study, the interaction mechanism between CNFs and CS can be further elucidated by using advanced characterization techniques and molecular dynamics simulations. The processing approaches and parameters significantly affect the structure and mechanical properties of the produced CNP and CNP/CS. The CNP quality (e.g., surface smoothness, wrinkles, transparency) can be further controlled and optimized by studying different processing approaches and parameters. Moreover, the current impregnation process can be potentially extended to the roll-to-roll coating process, which will be more efficient towards large-scale production of CS functionalized CNP.

In the third project, we further introduced hydrophobic and electrically conductive PPy into the CNP/CS through a facile in situ polymerization approach. Results indicate that the obtained CNP/CS/PPy showed excellent water resistance with the wet tensile strength up to 80 MPa, which was more than 10 times higher than that of the pure CNP. Intriguingly, new features (e.g., electrical conductivity, antibacterial ability) can be achieved at the same time. The functionalized CNP/CS/PPy exhibited a high conductivity of 6.5 S cm^{-1}, which can be used for EMI shielding application with a high shielding performance around 18 dB. In addition, the CNP/CS/PPy exhibited good antibacterial activity towards *S. aureus* and *E. coli*, with the bacterial reductions of

99.28% and 95.59%, respectively. Thus, this project provides a simple and versatile approach to functionalize CNP for achieving multifunctional properties.

In the future work, the EMI shielding performance of the composite films can be further enhanced by introducing other active materials. For example, highly conductive nanomaterials such as graphene, carbon nanotubes, and silver nanowires can be introduced either in the CNP preparation process or the CS impregnation process. In addition to the EMI shielding application, the CNP/CS/PPy used for some other applications such as supercapacitors and sensors can be explored.

In the fourth project, the feasibility of using the PMS-derived CNFs as building blocks for the fabrication of PEDOT:PSS based flexible electrodes was investigated. PEDOT:PSS/CNF suspension was firstly prepared via a simple in situ polymerization process. Afterwards, flexible and conductive PEDOT:PSS/CNF nanopaper (PEDOT:PSS/CNP) were prepared from the PEDOT:PSS/CNF suspension by vacuum filtration and DMSO post-treatment. Results showed that the optimized PEDOT:PSS/CNP exhibited excellent flexibility, high tensile strength (70 MPa), and high electrical conductivity (66.67 S/cm). Finally, a symmetric supercapacitor was assembled using the PEDOT:PSS/CNP as electrodes. The assembled supercapacitor could deliver the maximum areal specific capacitance of 888.7 mF cm^{-2} (corresponding to 111.1 F cm^{-3}) and offer the highest areal energy density of 30.86 μWh cm^{-2} (corresponding to 4.41 mWh cm^{-3}), which are among the highest values reported for PEDOT:PSS based supercapacitors. More importantly, the assembled supercapacitor showed remarkable cycling stability with the capacitance retention of 95.8% after 10,000 charge/discharge cycles. Considering the facile preparation process and excellent electrochemical performance, the PEDOT:PSS/CNP could be a promising electrode

material for flexible supercapacitors.

For the future work of this project, the electrical conductivity and electrochemical properties of the PEDOT:PSS/CNP can be further improved by introducing highly conductive carbon nanomaterials such as graphene and carbon nanotubes. More insights on the molecular interaction between active components and CNFs in the electrode/electrolyte interface should be fundamentally understood in the future study. In addition, it would be interesting to make all-solid-state supercapacitor devices by using gel or solid flexible electrolytes.

References

1. Yang, X.; Choi, H. S.; Park, C.; Kim, S. W., Current states and prospects of organic waste utilization for biorefineries. *Renew. Sustain. Energy Rev.* **2015,** *49*, 335-349.

2. Saini, J. K.; Saini, R.; Tewari, L., Lignocellulosic agriculture wastes as biomass feedstocks for second-generation bioethanol production: concepts and recent developments. *3 Biotech* **2015,** *5* (4), 337-353.

3. Zhu, H.; Luo, W.; Ciesielski, P. N.; Fang, Z.; Zhu, J. Y.; Henriksson, G.; Himmel, M. E.; Hu, L., Wood-Derived Materials for Green Electronics, Biological Devices, and Energy Applications. *Chem. Rev.* **2016,** *116* (16), 9305-74.

4. Dufresne, A., Nanocellulose Processing Properties and Potential Applications. *Curr. For. Rep.* **2019,** *5* (2), 76-89.

5. Xu, H.; Li, B.; Mu, X., Review of Alkali-Based Pretreatment To Enhance Enzymatic Saccharification for Lignocellulosic Biomass Conversion. *Ind. Eng. Chem. Res.* **2016,** *55* (32), 8691-8705.

6. Klemm, D.; Heublein, B.; Fink, H. P.; Bohn, A., Cellulose: Fascinating biopolymer and sustainable raw material. *Angew. Chem. Int. Ed.* **2005,** *44* (22), 3358-3393.

7. Kim, J.-H.; Shim, B. S.; Kim, H. S.; Lee, Y.-J.; Min, S.-K.; Jang, D.; Abas, Z.; Kim, J., Review of nanocellulose for sustainable future materials. *Int. J. Precis. Eng. Manuf. - Green Technol.* **2015,** *2* (2), 197-213.

8. Klemm, D.; Kramer, F.; Moritz, S.; Lindstrom, T.; Ankerfors, M.; Gray, D.; Dorris, A., Nanocelluloses: a new family of nature-based materials. *Angew. Chem. Int. Ed.* **2011,** *50* (24), 5438-66.

9. Chen, H., Chemical Composition and Structure of Natural Lignocellulose. In *Biotechnology of Lignocellulose: Theory and Practice*, Springer Netherlands: Dordrecht, 2014; pp 25-71.

10. Naik, S. N.; Goud, V. V.; Rout, P. K.; Dalai, A. K., Production of first and second generation biofuels: A comprehensive review. *Renew. Sustain. Energy Rev.* **2010,** *14* (2), 578-597.

11. Chandel, A. K.; Singh, O. V.; Venkateswar Rao, L., Biotechnological Applications of Hemicellulosic Derived Sugars: State-of-the-Art. In *Sustainable Biotechnology: Sources of Renewable Energy*, Singh, O. V.; Harvey, S. P., Eds. Springer Netherlands: Dordrecht, 2010; pp 63-81.

12. Yang, S.-T., Chapter 1 - Bioprocessing – from Biotechnology to Biorefinery. In *Bioprocessing for Value-Added Products from Renewable Resources*, Yang, S.-T., Ed. Elsevier: Amsterdam, 2007; pp 1-24.

13. Silveira, M. H.; Morais, A. R.; da Costa Lopes, A. M.; Olekszyszen, D. N.; Bogel-Lukasik, R.; Andreaus, J.; Pereira Ramos, L., Current Pretreatment Technologies for the Development of Cellulosic Ethanol and Biorefineries. *ChemSusChem* **2015,** *8* (20), 3366-90.

14. Brunner, G., Chapter 8 - Processing of Biomass with Hydrothermal and Supercritical Water. In *Supercritical Fluid Science and Technology*, Brunner, G., Ed. Elsevier: 2014; Vol. 5, pp 395-509.

15. Maki-Arvela, P.; Salmi, T.; Holmbom, B.; Willfor, S.; Murzin, D. Y., Synthesis of sugars by hydrolysis of hemicelluloses--a review. *Chem. Rev.* **2011,** *111* (9), 5638-66.

16. Peng, F.; Ren, J. L.; Xu, F.; Sun, R.-C., Chemicals from Hemicelluloses: A Review. In *Sustainable Production of Fuels, Chemicals, and Fibers from Forest Biomass*, American Chemical Society: 2011; Vol. 1067, pp 219-259.

17. Nhuchhen, D. R.; Basu, P.; Acharya, B., A comprehensive review on biomass torrefaction. *International Journal of Renewable Energy & Biofuels* **2014,** *2014*, 1-56.

18. Hatfield, R.; Vermerris, W., Lignin Formation in Plants. The Dilemma of Linkage Specificity. *Plant Physiol.* **2001,** *126* (4), 1351-1357.

19. Boerjan, W.; Ralph, J.; Baucher, M., Lignin Biosynthesis. *Annu. Rev. Plant Biol.* **2003,** *54* (1), 519-546.

20. Koch, G.; Schmitt, U., Topochemical and electron microscopic analyses on the lignification of individual cell wall layers during wood formation and secondary changes. In *Cellular aspects of wood formation*, Springer: 2013; pp 41-69.

21. Novaes, E.; Kirst, M.; Chiang, V.; Winter-Sederoff, H.; Sederoff, R., Lignin and biomass: a negative correlation for wood formation and lignin content in trees. *Plant Physiol.* **2010,** *154* (2), 555-61.

22. Koch, G. W.; Sillett, S. C.; Jennings, G. M.; Davis, S. D., The limits to tree height. *Nature* **2004,** *428* (6985), 851-854.

23. Liu, Q.; Luo, L.; Zheng, L., Lignins: Biosynthesis and Biological Functions in Plants. *Int. J. Mol. Sci.* **2018,** *19* (2).

24. Bhuiyan, N. H.; Selvaraj, G.; Wei, Y.; King, J., Role of lignification in plant defense. *Plant Signaling Behav.* **2009,** *4* (2), 158-159.

25. Chen, F.; Dixon, R. A., Lignin modification improves fermentable sugar yields for biofuel production. *Nat. Biotechnol.* **2007,** *25* (7), 759-761.

26. Bajwa, D. S.; Pourhashem, G.; Ullah, A. H.; Bajwa, S. G., A concise review of current lignin production, applications, products and their environmental impact. *Ind. Crops Prod.* **2019,** *139*, 111526.

27. Linger, J. G.; Vardon, D. R.; Guarnieri, M. T.; Karp, E. M.; Hunsinger, G. B.; Franden, M. A.; Johnson, C. W.; Chupka, G.; Strathmann, T. J.; Pienkos, P. T.; Beckham, G. T., Lignin valorization through integrated biological funneling and chemical catalysis. *Proc. Natl. Acad. Sci. U.S.A.* **2014,** *111* (33), 12013-8.

28. Ragauskas, A. J.; Beckham, G. T.; Biddy, M. J.; Chandra, R.; Chen, F.; Davis, M. F.; Davison, B. H.; Dixon, R. A.; Gilna, P.; Keller, M.; Langan, P.; Naskar, A. K.; Saddler, J. N.; Tschaplinski, T. J.; Tuskan, G. A.; Wyman, C. E., Lignin valorization: improving lignin processing in the biorefinery. *Science* **2014,** *344* (6185), 1246843.

29. Kai, D.; Tan, M. J.; Chee, P. L.; Chua, Y. K.; Yap, Y. L.; Loh, X. J., Towards lignin-based functional materials in a sustainable world. *Green Chem.* **2016,** *18* (5), 1175-1200.

30. Sun, Z.; Fridrich, B.; de Santi, A.; Elangovan, S.; Barta, K., Bright Side of Lignin Depolymerization: Toward New Platform Chemicals. *Chem. Rev.* **2018,** *118* (2), 614-678.

31. Pattiya, A., 1 - Fast pyrolysis. In *Direct Thermochemical Liquefaction for Energy Applications*, Rosendahl, L., Ed. Woodhead Publishing: 2018; pp 3-28.

32. Pecha, B.; Garcia-Perez, M., Chapter 26 - Pyrolysis of Lignocellulosic Biomass: Oil, Char, and Gas. In *Bioenergy*, Dahiya, A., Ed. Academic Press: Boston, 2015; pp 413-442.

33. Sudiyani, Y.; Sembiring, K. C.; Adilina, I. B., Bioethanol G2: Production process and recent studies. In *Biomass Bioenergy*, Springer: 2014; pp 345-364.

34. Yadav, M.; Paritosh, K.; Chawade, A.; Pareek, N.; Vivekanand, V., Genetic Engineering of Energy Crops to Reduce Recalcitrance and Enhance Biomass Digestibility. *Agriculture* **2018,** *8* (6), 76.

35. van Dam, J. E. G.; Gorshkova, T. A., CELL WALLS AND FIBERS | Fiber Formation. In *Encyclopedia of Applied Plant Sciences*, Thomas, B., Ed. Elsevier: Oxford, 2003; pp 87-96.

36. Jia, C.; Li, Y.; Yang, Z.; Chen, G.; Yao, Y.; Jiang, F.; Kuang, Y.; Pastel, G.; Xie, H.; Yang, B.; Das, S.; Hu, L., Rich Mesostructures Derived from Natural Woods for Solar Steam Generation. *Joule* **2017,** *1* (3), 588-599.

37. Ramage, M. H.; Burridge, H.; Busse-Wicher, M.; Fereday, G.; Reynolds, T.; Shah, D. U.; Wu, G.; Yu, L.; Fleming, P.; Densley-Tingley, D.; Allwood, J.; Dupree, P.; Linden, P. F.; Scherman, O., The wood from the trees: The use of timber in construction. *Renew. Sustain. Energy Rev.* **2017,** *68*, 333-359.

38. Zobel, B. J.; van Buijtenen, J. P., Wood Variation and Wood Properties. In *Wood Variation: Its Causes and Control*, Springer Berlin Heidelberg: Berlin, Heidelberg, 1989; pp 1-32.

39. Gibson, L. J., The hierarchical structure and mechanics of plant materials. *J. R. Soc. Interface* **2012,** *9* (76), 2749-66.

40. Bajpai, P., Chapter 8 - Energy Conservation Measures for Mechanical Pulping. In *Pulp and Paper Industry*, Bajpai, P., Ed. Elsevier: Amsterdam, 2016; pp 125-144.

41. Viikari, L.; Suurnäkki, A.; Grönqvist, S.; Raaska, L.; Ragauskas, A., Forest Products: Biotechnology in Pulp and Paper Processing. In *Encyclopedia of Microbiology (Third Edition)*, Schaechter, M., Ed. Academic Press: Oxford, 2009; pp 80-94.

42. Xu, E.; Wang, D.; Lin, L., Chemical Structure and Mechanical Properties of Wood Cell Walls Treated with Acid and Alkali Solution. *Forests* **2020,** *11* (1), 87.

43. Bajpai, P., Chapter 12 - Pulping Fundamentals. In *Biermann's Handbook of Pulp and Paper (Third Edition)*, Bajpai, P., Ed. Elsevier: 2018; pp 295-351.

44. Chen, C.; Hu, L., Nanocellulose toward Advanced Energy Storage Devices: Structure and Electrochemistry. *Acc. Chem. Res.* **2018,** *51* (12), 3154-3165.

45. Conners, T. E., Wood: Ultrastructure. In *Encyclopedia of Materials: Science and Technology*, Buschow, K. H. J.; Cahn, R. W.; Flemings, M. C.; Ilschner, B.; Kramer, E. J.; Mahajan, S.; Veyssière, P., Eds. Elsevier: Oxford, 2001; pp 9751-9759.

46. Rubin, E. M., Genomics of cellulosic biofuels. *Nature* **2008,** *454* (7206), 841-5.

47. Plomion, C.; Leprovost, G.; Stokes, A., Wood Formation in Trees. *Plant Physiol.* **2001,** *127* (4), 1513-1523.

48. Zhang, N.; Li, S.; Xiong, L.; Hong, Y.; Chen, Y., Cellulose-hemicellulose interaction in wood secondary cell-wall. *Modell. Simul. Mater. Sci. Eng.* **2015,** *23* (8), 085010.

49. Isikgor, F. H.; Becer, C. R., Lignocellulosic biomass: a sustainable platform for the production of bio-based chemicals and polymers. *Polym. Chem.* **2015,** *6* (25), 4497-4559.

50. Brandt, A.; Gräsvik, J.; Hallett, J. P.; Welton, T., Deconstruction of lignocellulosic biomass with ionic liquids. *Green Chem.* **2013,** *15* (3), 550.

51. Terashima, N.; Yoshida, M.; Hafrén, J.; Fukushima, K.; Westermark, U., Proposed supramolecular structure of lignin in softwood tracheid compound middle lamella regions. *Holzforschung*, **2012**, 66, 907.

52. Kang, X.; Kirui, A.; Dickwella Widanage, M. C.; Mentink-Vigier, F.; Cosgrove, D. J.; Wang, T., Lignin-polysaccharide interactions in plant secondary cell walls revealed by solid-state NMR. *Nat. Commun.* **2019,** *10* (1), 347.

53. Penttilä, P., Structural characterization of cellulosic materials using x-ray and neutron scattering. Doktorarbeit, University of Helsinki: 2013.

54. Widsten, P., *Oxidative activation of wood fibers for the manufacture of medium-density fiberboard (MDF)*. Helsinki University of Technology: 2002.

55. Doherty, W. O. S.; Mousavioun, P.; Fellows, C. M., Value-adding to cellulosic ethanol: Lignin polymers. *Ind. Crops Prod.* **2011,** *33* (2), 259-276.

56. Zhu, H.; Jia, Z.; Chen, Y.; Weadock, N.; Wan, J.; Vaaland, O.; Han, X.; Li, T.; Hu, L., Tin anode for sodium-ion batteries using natural wood fiber as a mechanical buffer and electrolyte reservoir. *Nano Lett.* **2013,** *13* (7), 3093-100.

57. Moon, R. J.; Martini, A.; Nairn, J.; Simonsen, J.; Youngblood, J., Cellulose nanomaterials review: structure, properties and nanocomposites. *Chem. Soc. Rev.* **2011,** *40* (7), 3941-94.

58. Dornath, P.; Cho, H. J.; Paulsen, A.; Dauenhauer, P.; Fan, W., Efficient mechano-catalytic depolymerization of crystalline cellulose by formation of branched glucan chains. *Green Chem.* **2015,** *17* (2), 769-775.

59. Poletto, M.; Pistor, V.; Zattera, A. J., Structural characteristics and thermal properties of native cellulose. *Cellulose-fundamental aspects* **2013,** *2*, 45-68.

60. Fernandes, A. N.; Thomas, L. H.; Altaner, C. M.; Callow, P.; Forsyth, V. T.; Apperley, D. C.; Kennedy, C. J.; Jarvis, M. C., Nanostructure of cellulose microfibrils in spruce wood. *Proc. Natl. Acad. Sci. U.S.A.* **2011,** *108* (47), E1195-203.

61. Bregado, J. L.; Secchi, A. R.; Tavares, F. W.; de Sousa Rodrigues, D.; Gambetta, R., Amorphous paracrystalline structures from native crystalline cellulose: A molecular dynamics protocol. *Fluid Phase Equilib.* **2019,** *491*, 56-76.

62. Nishiyama, Y.; Johnson, G. P.; French, A. D.; Forsyth, V. T.; Langan, P., Neutron Crystallography, Molecular Dynamics, and Quantum Mechanics Studies of the Nature of Hydrogen Bonding in Cellulose Iβ. *Biomacromolecules* **2008,** *9* (11), 3133-3140.

63. Matthews, J. F.; Himmel, M. E.; Crowley, M. F., Conversion of cellulose Iα to Iβ via a high temperature intermediate (I-HT) and other cellulose phase transformations. *Cellulose* **2011,** *19* (1), 297-306.

64. Nishiyama, Y.; Sugiyama, J.; Chanzy, H.; Langan, P., Crystal Structure and Hydrogen Bonding System in Cellulose Iα from Synchrotron X-ray and Neutron Fiber Diffraction. *J. Am. Chem. Soc.* **2003,** *125* (47), 14300-14306.

65. Li, Q.; Renneckar, S., Supramolecular structure characterization of molecularly thin cellulose I nanoparticles. *Biomacromolecules* **2011,** *12* (3), 650-9.

66. Gross, A. S.; Chu, J.-W., On the Molecular Origins of Biomass Recalcitrance: The Interaction Network and Solvation Structures of Cellulose Microfibrils. *J. Phys. Chem. B* **2010,** *114* (42), 13333-13341.

67. Wang, C.; Zhao, M.; Huang, P.; Rao, X.; Wu, M.; Huang, Y., Influence of medium polarity and mechanical force on morphology and structure of nanocellulose. *Acta Polym. Sin.* **2017,** (9), 1415-1425.

68. Mazeau, K.; Rivet, A., Wetting the (110) and (100) surfaces of Iβ cellulose studied by molecular dynamics. *Biomacromolecules* **2008,** *9* (4), 1352-1354.

69. Zhao, Z.; Crespi, V. H.; Kubicki, J. D.; Cosgrove, D. J.; Zhong, L., Molecular dynamics simulation study of xyloglucan adsorption on cellulose surfaces: effects of surface hydrophobicity and side-chain variation. *Cellulose* **2013,** *21* (2), 1025-1039.

70. Zhao, M.; Kuga, S.; Jiang, S.; Wu, M.; Huang, Y., Cellulose nanosheets induced by mechanical impacts under hydrophobic environment. *Cellulose* **2016,** *23* (5), 2809-2818.

71. Kang, X.; Sun, P.; Kuga, S.; Wang, C.; Zhao, Y.; Wu, M.; Huang, Y., Thin Cellulose Nanofiber from Corncob Cellulose and Its Performance in Transparent Nanopaper. *ACS Sustainable Chem. Eng.* **2017,** *5* (3), 2529-2534.

72. Malaspina, D. C.; Faraudo, J., Molecular insight into the wetting behavior and amphiphilic character of cellulose nanocrystals. *Adv. Colloid Interface Sci.* **2019,** *267*, 15-25.

73. Rao, X.; Kuga, S.; Wu, M.; Huang, Y., Influence of solvent polarity on surface-fluorination of cellulose nanofiber by ball milling. *Cellulose* **2015,** *22* (4), 2341-2348.

74. Huang, P.; Zhao, Y.; Kuga, S.; Wu, M.; Huang, Y., A versatile method for producing functionalized cellulose nanofibers and their application. *Nanoscale* **2016,** *8* (6), 3753-9.

75. Huang, P.; Wu, M.; Kuga, S.; Wang, D.; Wu, D.; Huang, Y., One-step dispersion of cellulose nanofibers by mechanochemical esterification in an organic solvent. *ChemSusChem* **2012,** *5* (12), 2319-22.

76. Wang, C.; Li, L.; Zhao, M.; Huang, P.; Kuga, S.; Wu, M.; Huang, Y., Co-effect of Mechanical Ball-milling and Microenvironmental Polarity on Morphology and Properties of Nanocellulose. *Paper Biomater.* **2017,** *2* (4), 8-18.

77. Trache, D.; Hussin, M. H.; Haafiz, M. K.; Thakur, V. K., Recent progress in cellulose nanocrystals: sources and production. *Nanoscale* **2017,** *9* (5), 1763-1786.

78. Rajinipriya, M.; Nagalakshmaiah, M.; Robert, M.; Elkoun, S., Importance of Agricultural and Industrial Waste in the Field of Nanocellulose and Recent Industrial Developments of Wood Based Nanocellulose: A Review. *ACS Sustainable Chem. Eng.* **2018,** *6* (3), 2807-2828.

79. Xie, H.; Du, H.; Yang, X.; Si, C., Recent Strategies in Preparation of Cellulose Nanocrystals and Cellulose Nanofibrils Derived from Raw Cellulose Materials. *Int. J. Polym. Sci.* **2018,** *2018*, 1-25.

80. Du, H.; Liu, W.; Zhang, M.; Si, C.; Zhang, X.; Li, B., Cellulose nanocrystals and cellulose nanofibrils based hydrogels for biomedical applications. *Carbohydr. Polym.* **2019,** *209,* 130-144.

81. Zhao, D.; Zhu, Y.; Cheng, W.; Chen, W.; Wu, Y.; Yu, H., Cellulose-Based Flexible Functional Materials for Emerging Intelligent Electronics. *Adv. Mater.* **2020**, e2000619.

82. Salas, C.; Nypeloe, T.; Rodriguez-Abreu, C.; Carrillo, C.; Rojas, O. J., Nanocellulose properties and applications in colloids and interfaces. *Curr. Opin. Colloid Interface Sci.* **2014,** *19* (5), 383-396.

83. Domingues, R. M. A.; Gomes, M. E.; Reis, R. L., The Potential of Cellulose Nanocrystals in Tissue Engineering Strategies. *Biomacromolecules* **2014,** *15* (7), 2327-2346.

84. Du, H. S.; Liu, C.; Zhang, M. M.; Kong, Q. S.; Li, B.; Xian, M., Preparation and Industrialization Status of Nanocellulose. *Progress in Chemistry* **2018,** *30* (4), 448-462.

85. Du, H. S.; Liu, C.; Mu, X. D.; Gong, W. B.; Lv, D.; Hong, Y. M.; Si, C. L.; Li, B., Preparation and characterization of thermally stable cellulose nanocrystals via a sustainable approach of FeCl3-catalyzed formic acid hydrolysis. *Cellulose* **2016,** *23* (4), 2389-2407.

86. Kargarzadeh, H.; Ahmad, I.; Abdullah, I.; Dufresne, A.; Zainudin, S. Y.; Sheltami, R. M., Effects of hydrolysis conditions on the morphology, crystallinity, and thermal stability of cellulose nanocrystals extracted from kenaf bast fibers. *Cellulose* **2012,** *19* (3), 855-866.

87. Yu, H.; Qin, Z.; Liang, B.; Liu, N.; Zhou, Z.; Chen, L., Facile extraction of thermally stable cellulose nanocrystals with a high yield of 93% through hydrochloric acid hydrolysis under hydrothermal conditions. *J. Mater. Chem. A* **2013,** *1* (12), 3938-3944.

88. Kontturi, E.; Meriluoto, A.; Penttila, P. A.; Baccile, N.; Malho, J. M.; Potthast, A.; Rosenau, T.; Ruokolainen, J.; Serimaa, R.; Laine, J.; Sixta, H., Degradation and Crystallization

of Cellulose in Hydrogen Chloride Vapor for High-Yield Isolation of Cellulose Nanocrystals. *Angew. Chem. Int. Ed.* **2016,** *55* (46), 14455-14458.

89. Camarero Espinosa, S.; Kuhnt, T.; Foster, E. J.; Weder, C., Isolation of thermally stable cellulose nanocrystals by phosphoric acid hydrolysis. *Biomacromolecules* **2013,** *14* (4), 1223-30.

90. Ding, M.; Li, C.; Chen, F., Isolation and characterization of cellulose nanocrystals from cloth hairs and evaluation of their compatibility with PLLA. *Cellulose* **2017,** *24*(11), 4785-4792.

91. Sadeghifar, H.; Filpponen, I.; Clarke, S. P.; Brougham, D. F.; Argyropoulos, D. S., Production of cellulose nanocrystals using hydrobromic acid and click reactions on their surface. *J. Mater. Sci.* **2011,** *46* (22), 7344-7355.

92. Cao, Y.; Jiang, Y.; Song, Y.; Cao, S.; Miao, M.; Feng, X.; Fang, J.; Shi, L., Combined bleaching and hydrolysis for isolation of cellulose nanofibrils from waste sackcloth. *Carbohydr. Polym.* **2015,** *131*, 152-158.

93. Cheng, M.; Qin, Z. Y.; Chen, Y. Y.; Liu, J. M.; Ren, Z. C., Facile one-step extraction and oxidative carboxylation of cellulose nanocrystals through hydrothermal reaction by using mixed inorganic acids. *Cellulose* **2017,** *24* (8), 3243-3254.

94. Ureña-Benavides, E. E.; Ao, G.; Davis, V. A.; Kitchens, C. L., Rheology and Phase Behavior of Lyotropic Cellulose Nanocrystal Suspensions. *Macromolecules* **2011,** *44* (22), 8990-8998.

95. Liu, Y.; Wang, H.; Yu, G.; Yu, Q.; Li, B.; Mu, X., A novel approach for the preparation of nanocrystalline cellulose by using phosphotungstic acid. *Carbohydr. Polym.* **2014,** *110*, 415-422.

96. Torlopov, M. A.; Udoratina, E. V.; Martakov, I. S.; Sitnikov, P. A., Cellulose nanocrystals prepared in H3PW12O40-acetic acid system. *Cellulose* **2017,** *24* (5), 2153-2162.

97. Du, H. S.; Liu, C.; Wang, D.; Zhang, Y. D.; Yu, G.; Si, C. L.; Li, B.; Mu, X. D.; Peng, H., Sustainable preparation and characterization of thermally stable and functional cellulose nanocrystals and nanofibrils via formic acid hydrolysis. *J Bioresour. Bioprod.* **2017,** *2* (1), 10-15.

98. Chen, L. H.; Zhu, J. Y.; Baez, C.; Kitin, P.; Elder, T., Highly thermal-stable and functional cellulose nanocrystals and nanofibrils produced using fully recyclable organic acids. *Green Chem.* **2016,** *18* (13), 3835-3843.

99. Xu, W.; Grénman, H.; Liu, J.; Kronlund, D.; Li, B.; Backman, P.; Peltonen, J.; Willför, S.; Sundberg, A.; Xu, C., Mild Oxalic-Acid-Catalyzed Hydrolysis as a Novel Approach to Prepare Cellulose Nanocrystals. *ChemNanoMat* **2017,** *3* (2), 109-119.

100. Miao, J. J.; Yu, Y. Q.; Jiang, Z. M.; Zhang, L. P., One-pot preparation of hydrophobic cellulose nanocrystals in an ionic liquid. *Cellulose* **2016,** *23* (2), 1209-1219.

101. Abushammala, H.; Krossing, I.; Laborie, M. P., Ionic liquid-mediated technology to produce cellulose nanocrystals directly from wood. *Carbohydr. Polym.* **2015,** *134*, 609-16.

102. Sirvio, J. A.; Visanko, M.; Liimatainen, H., Acidic Deep Eutectic Solvents As Hydrolytic Media for Cellulose Nanocrystal Production. *Biomacromolecules* **2016,** *17* (9), 3025-32.

103. Liu, Y. Z.; Guo, B. T.; Xia, Q. Q.; Meng, J.; Chen, W. S.; Liu, S. X.; Wang, Q. W.; Liu, Y. X.; Li, J.; Yu, H. P., Efficient Cleavage of Strong Hydrogen Bonds in Cotton by Deep Eutectic Solvents and Facile Fabrication of Cellulose Nanocrystals in High Yields. *ACS Sustainable Chem. Eng.* **2017,** *5* (9), 7623-7631.

104. Nechyporchuk, O.; Belgacem, M. N.; Bras, J., Production of cellulose nanofibrils: A review of recent advances. *Ind. Crops Prod.* **2016,** *93*, 2-25.

105. Hammud, H. H.; Chahine, M. M.; El-Hamaoui, B.; Hanifehpour, Y., Lead uptake by new silica-carbon nanoparticles. *Eur. J. Chem.* **2013,** *4* (4), 425-433.

106. Lin, C.; Wang, Q.; Deng, Q.; Huang, H.; Huang, F.; Huang, L.; Ni, Y.; Chen, L.; Cao, S.; Ma, X., Preparation of highly hazy transparent cellulose film from dissolving pulp. *Cellulose* **2019,** *26* (6), 4061-4069.

107. Chirayil, C. J.; Mathew, L.; Thomas, S., Review of recent research in nano cellulose preparation from different lignocellulosic fibers. *Rev. Adv. Mater. Sci.* **2014,** *37*, 20-28.

108. Chaker, A.; Boufi, S., Cationic nanofibrillar cellulose with high antibacterial properties. *Carbohydr. Polym.* **2015,** *131*, 224-32.

109. Liu, C.; Li, B.; Du, H.; Lv, D.; Zhang, Y.; Yu, G.; Mu, X.; Peng, H., Properties of nanocellulose isolated from corncob residue using sulfuric acid, formic acid, oxidative and mechanical methods. *Carbohydr. Polym.* **2016,** *151*, 716-724.

110. Abdul Khalil, H. P.; Davoudpour, Y.; Islam, M. N.; Mustapha, A.; Sudesh, K.; Dungani, R.; Jawaid, M., Production and modification of nanofibrillated cellulose using various mechanical processes: a review. *Carbohydr. Polym.* **2014,** *99*, 649-665.

111. Jonoobi, M.; Oladi, R.; Davoudpour, Y.; Oksman, K.; Dufresne, A.; Hamzeh, Y.; Davoodi, R., Different preparation methods and properties of nanostructured cellulose from various natural resources and residues: a review. *Cellulose* **2015,** *22* (2), 935-969.

112. Du, H. S.; Liu, C.; Zhang, Y. D.; Yu, G.; Si, C. L.; Li, B., Preparation and characterization of functional cellulose nanofibrils via formic acid hydrolysis pretreatment and the followed high-pressure homogenization. *Ind. Crops Prod.* **2016,** *94*, 736-745.

113. Saelee, K.; Yingkamhaeng, N.; Nimchua, T.; Sukyai, P., An environmentally friendly xylanase-assisted pretreatment for cellulose nanofibrils isolation from sugarcane bagasse by high-pressure homogenization. *Ind. Crops Prod.* **2016,** *82*, 149-160.

114. Eriksen, Ø.; Syverud, K.; Gregersen, Ø., The use of microfibrillated cellulose produced from kraft pulp as strength enhancer in TMP paper. *Nord. Pulp Paper Res. J.*, **2008,** *23*, 299.

115. Paakko, M.; Ankerfors, M.; Kosonen, H.; Nykanen, A.; Ahola, S.; Osterberg, M.; Ruokolainen, J.; Laine, J.; Larsson, P. T.; Ikkala, O.; Lindstrom, T., Enzymatic hydrolysis combined with mechanical shearing and high-pressure homogenization for nanoscale cellulose fibrils and strong gels. *Biomacromolecules* **2007,** *8* (6), 1934-1941.

116. Chen, Y.; Fan, D.; Han, Y.; Li, G.; Wang, S., Length-controlled cellulose nanofibrils produced using enzyme pretreatment and grinding. *Cellulose* **2017,** *24*(12), 5431-5442.

117. Liu, X.; Jiang, Y.; Qin, C.; Yang, S.; Song, X.; Wang, S.; Li, K., Enzyme-assisted mechanical grinding for cellulose nanofibers from bagasse: energy consumption and nanofiber characteristics. *Cellulose* **2018,** *25*(12), 7065-7078.

118. Tian, C.; Yi, J.; Wu, Y.; Wu, Q.; Qing, Y.; Wang, L., Preparation of highly charged cellulose nanofibrils using high-pressure homogenization coupled with strong acid hydrolysis pretreatments. *Carbohydr. Polym.* **2016,** *136*, 485-492.

119. Davoudpour, Y.; Hossain, S.; Khalil, H. P. S. A.; Haafiz, M. K. M.; Ishak, Z. A. M.; Hassan, A.; Sarker, Z. I., Optimization of high pressure homogenization parameters for the isolation of cellulosic nanofibers using response surface methodology. *Ind. Crops Prod.* **2015,** *74*, 381-387.

120. Saito, T.; Nishiyama, Y.; Putaux, J. L.; Vignon, M.; Isogai, A., Homogeneous suspensions of individualized microfibrils from TEMPO-catalyzed oxidation of native cellulose. *Biomacromolecules* **2006,** *7* (6), 1687-1691.

121. Isogai, A.; Saito, T.; Fukuzumi, H., TEMPO-oxidized cellulose nanofibers. *Nanoscale* **2011,** *3* (1), 71-85.

122. Naderi, A.; Lindström, T.; Sundström, J., Repeated homogenization, a route for decreasing the energy consumption in the manufacturing process of carboxymethylated nanofibrillated cellulose? *Cellulose* **2015,** *22* (2), 1147-1157.

123. Im, W.; Lee, S.; Rajabi Abhari, A.; Youn, H. J.; Lee, H. L., Optimization of carboxymethylation reaction as a pretreatment for production of cellulose nanofibrils. *Cellulose* **2018,** *25*(7), 3873-3883.

124. Zhang, H.; Zeng, X.; Xie, J.; Li, Z.; Li, H., Study on the sorption process of triclosan on cationic microfibrillated cellulose and its antibacterial activity. *Carbohydr. Polym.* **2016,** *136*, 493-498.

125. Saini, S.; Yücel Falco, Ç.; Belgacem, M. N.; Bras, J., Surface cationized cellulose nanofibrils for the production of contact active antimicrobial surfaces. *Carbohydr. Polym.* **2016,** *135*, 239-247.

126. Saito, T.; Isogai, A., Introduction of aldehyde groups on surfaces of native cellulose fibers by TEMPO-mediated oxidation. *Colloids Surf., A* **2006,** *289* (1-3), 219-225.

127. Saito, T.; Shibata, I.; Isogai, A.; Suguri, N.; Sumikawa, N., Distribution of carboxylate groups introduced into cotton linters by the TEMPO-mediated oxidation. *Carbohydr. Polym.* **2005,** *61* (4), 414-419.

128. Fukuzumi, H.; Saito, T.; Wata, T.; Kumamoto, Y.; Isogai, A., Transparent and High Gas Barrier Films of Cellulose Nanofibers Prepared by TEMPO-Mediated Oxidation. *Biomacromolecules* **2009,** *10* (1), 162-165.

129. Benítez, A. J.; Walther, A., Cellulose nanofibril nanopapers and bioinspired nanocomposites: a review to understand the mechanical property space. *J. Mater. Chem. A* **2017,** *5* (31), 16003-16024.

130. Yu, H. Y.; Abdalkarim, S. Y. H.; Zhang, H.; Wang, C.; Tam, K. C., Simple Process To Produce High-Yield Cellulose Nanocrystals Using Recyclable Citric/Hydrochloric Acids. *ACS Sustainable Chem. Eng.* **2019,** *7* (5), 4912-4923.

131. Saito, T.; Kuramae, R.; Wohlert, J.; Berglund, L. A.; Isogai, A., An ultrastrong nanofibrillar biomaterial: the strength of single cellulose nanofibrils revealed via sonication-induced fragmentation. *Biomacromolecules* **2013,** *14* (1), 248-253.

132. Nogi, M.; Iwamoto, S.; Nakagaito, A. N.; Yano, H., Optically Transparent Nanofiber Paper. *Adv. Mater.* **2009,** *21* (16), 1595-1598.

133. Nogi, M.; Karakawa, M.; Komoda, N.; Yagyu, H.; Nge, T. T., Transparent Conductive Nanofiber Paper for Foldable Solar Cells. *Sci. Rep.* **2015,** *5*, 17254.

134. Markstedt, K.; Mantas, A.; Tournier, I.; Martinez Avila, H.; Hagg, D.; Gatenholm, P., 3D Bioprinting Human Chondrocytes with Nanocellulose-Alginate Bioink for Cartilage Tissue Engineering Applications. *Biomacromolecules* **2015,** *16* (5), 1489-1496.

135. Zanini, M.; Lavoratti, A.; Zimmermann, M. V.; Galiotto, D.; Matana, F.; Baldasso, C.; Zattera, A. J., Aerogel preparation from short cellulose nanofiber of the Eucalyptus species. *J. Cell. Plast.* **2017,** *53* (5), 503-512.

136. Zhang, Z.; Sèbe, G.; Rentsch, D.; Zimmermann, T.; Tingaut, P., Ultralightweight and Flexible Silylated Nanocellulose Sponges for the Selective Removal of Oil from Water. *Chem. Mater.* **2014,** *26* (8), 2659-2668.

137. Qing, Y.; Sabo, R.; Wu, Y.; Zhu, J. Y.; Cai, Z., Self-assembled optically transparent cellulose nanofibril films: effect of nanofibril morphology and drying procedure. *Cellulose* **2015,** *22* (2), 1091-1102.

138. Aulin, C.; Gällstedt, M.; Lindström, T., Oxygen and oil barrier properties of microfibrillated cellulose films and coatings. *Cellulose* **2010,** *17* (3), 559-574.

139. Parit, M.; Aksoy, B.; Jiang, Z., Towards standardization of laboratory preparation procedure for uniform cellulose nanopapers. *Cellulose* **2018,** *25* (5), 2915-2924.

140. Sehaqui, H.; Liu, A.; Zhou, Q.; Berglund, L. A., Fast preparation procedure for large, flat cellulose and cellulose/inorganic nanopaper structures. *Biomacromolecules* **2010,** *11* (9), 2195-2198.

141. Mautner, A.; Lee, K.-Y.; Tammelin, T.; Mathew, A. P.; Nedoma, A. J.; Li, K.; Bismarck, A., Cellulose nanopapers as tight aqueous ultra-filtration membranes. *React. Funct. Polym.* **2015,** *86*, 209-214.

142. Hu, L.; Zheng, G.; Yao, J.; Liu, N.; Weil, B.; Eskilsson, M.; Karabulut, E.; Ruan, Z.; Fan, S.; Bloking, J. T.; McGehee, M. D.; Wågberg, L.; Cui, Y., Transparent and conductive paper from nanocellulose fibers. *Energy Environ. Sci.* **2013,** *6* (2), 513-518.

143. Xu, X.; Zhou, J.; Jiang, L.; Lubineau, G.; Ng, T.; Ooi, B. S.; Liao, H. Y.; Shen, C.; Chen, L.; Zhu, J. Y., Highly transparent, low-haze, hybrid cellulose nanopaper as electrodes for flexible electronics. *Nanoscale* **2016,** *8* (24), 12294-12306.

144. Wang, Z. H.; Carlsson, D. O.; Tammela, P.; Hua, K.; Zhang, P.; Nyholm, L.; Stromme, M., Surface Modified Nanocellulose Fibers Yield Conducting Polymer-Based Flexible Supercapacitors with Enhanced Capacitances. *ACS Nano* **2015,** *9* (7), 7563-7571.

145. Wang, Q.; Du, H.; Zhang, F.; Zhang, Y.; Wu, M.; Yu, G.; Liu, C.; Li, B.; Peng, H., Flexible cellulose nanopaper with high wet tensile strength, high toughness and tunable ultraviolet blocking ability fabricated from tobacco stalk via a sustainable method. *J. Mater. Chem. A* **2018,** *6* (27), 13021-13030.

146. Barhoum, A.; Samyn, P.; Öhlund, T.; Dufresne, A., Review of recent research on flexible multifunctional nanopapers: Nanocellulose, electrospun nanofiber, and carbon-based nanopapers. *Nanoscale* **2017,** *9*(40), 15181-15205.

147. Dong, H.; Snyder, J. F.; Williams, K. S.; Andzelm, J. W., Cation-induced hydrogels of cellulose nanofibrils with tunable moduli. *Biomacromolecules* **2013,** *14* (9), 3338-3345.

148. Dai, L.; Wang, Y.; Zou, X.; Chen, Z.; Liu, H.; Ni, Y., Ultrasensitive Physical, Bio, and Chemical Sensors Derived from 1-, 2-, and 3-D Nanocellulosic Materials. *Small* **2020,** *16* (13), e1906567.

149. De France, K. J.; Hoare, T.; Cranston, E. D., Review of Hydrogels and Aerogels Containing Nanocellulose. *Chem. Mater.* **2017,** *29* (11), 4609-4631.

150. Liu, C.; Du, H. S.; Dong, L.; Wang, X.; Zhang, Y. D.; Yu, G.; Li, B.; Mu, X. D.; Peng, H.; Liu, H. Z., Properties of Nanocelluloses and Their Application as Rheology Modifier in Paper Coating. *Ind. Eng. Chem. Res.* **2017,** *56* (29), 8264-8273.

151. Kargarzadeh, H.; Huang, J.; Lin, N.; Ahmad, I.; Mariano, M.; Dufresne, A.; Thomas, S.; Galeski, A., Recent developments in nanocellulose-based biodegradable polymers, thermoplastic polymers, and porous nanocomposites. *Prog. Polym. Sci.* **2018,** *87*, 197-227.

152. Ansari, F.; Berglund, L. A., Toward Semistructural Cellulose Nanocomposites: The Need for Scalable Processing and Interface Tailoring. *Biomacromolecules* **2018,** *19* (7), 2341-2350.

153. Rol, F.; Belgacem, M. N.; Gandini, A.; Bras, J., Recent advances in surface-modified cellulose nanofibrils. *Prog. Polym. Sci.* **2019,** *88*, 241-264.

154. Rasmussen, S. C., The path to conductive polyacetylene. *Bull. Hist. Chem* **2014,** *39* (1), 64-72.

155. Chiang, C. K.; Fincher Jr, C.; Park, Y. W.; Heeger, A. J.; Shirakawa, H.; Louis, E. J.; Gau, S. C.; MacDiarmid, A. G., Electrical conductivity in doped polyacetylene. *Phys. Rev. Lett.* **1977,** *39* (17), 1098.

156. Shirakawa, H.; Louis, E. J.; MacDiarmid, A. G.; Chiang, C. K.; Heeger, A. J., Synthesis of electrically conducting organic polymers: halogen derivatives of polyacetylene,(CH) x. *J. Chem. Soc., Chem. Commun.* **1977,** (16), 578-580.

157. Ibanez, J. G.; Rincon, M. E.; Gutierrez-Granados, S.; Chahma, M.; Jaramillo-Quintero, O. A.; Frontana-Uribe, B. A., Conducting Polymers in the Fields of Energy, Environmental Remediation, and Chemical-Chiral Sensors. *Chem. Rev.* **2018,** *118* (9), 4731-4816.

158. Alemour, B.; Yaacob, M.; Lim, H.; Hassan, M. R., Review of Electrical Properties of Graphene Conductive Composites. *Int. J. Nanoelectron. Mater.* **2018,** *11* (4), 371-398.

159. Bauhofer, W.; Kovacs, J. Z., A review and analysis of electrical percolation in carbon nanotube polymer composites. *Compos. Sci. Technol.* **2009,** *69* (10), 1486-1498.

160. Dias, A. M. A.; Marceneiro, S.; Johansen, H. D.; Barsan, M. M.; Brett, C. M. A.; de Sousa, H. C., Phosphonium ionic liquids as greener electrolytes for poly(vinyl chloride)-based ionic conducting polymers. *RSC Adv.* **2016,** *6* (92), 88979-88990.

161. Wang, Y.; Chen, K. S.; Mishler, J.; Cho, S. C.; Adroher, X. C., A review of polymer electrolyte membrane fuel cells: Technology, applications, and needs on fundamental research. *Appl. Energy* **2011,** *88* (4), 981-1007.

162. Langenhorst, F.; Campione, M., Ideal and real structures of different forms of carbon, with some remarks on their geological significance. J. Geol. Soc. **2019,** *176* (2), 337-347.

163. Peschel, G., Carbon-carbon bonds: hybridization. *Obtained online from: http://www. physik. fu-berlin. de/einrichtungen/ag/ag-reich/lehre/Archiv/ss2011/docs/Gina_Peschel-Handout. pdf, published on* **2011,** *5* (5), 1-6.

164. Moiz, S. A.; Khan, I. A.; Younis, W. A.; Karimov, K. S., Space Charge–Limited Current Model for Polymers. *Conducting Polymers* **2016**, 5, 91.

165. Alcácer, L., Orbitals and bands in organic semiconductors. In *Electronic Structure of Organic Semiconductors*, Morgan & Claypool Publishers: 2018; pp 5-1-5-14.

166. Vollhardt, K. P. C.; Schore, N. E., *Organic Chemistry; Palgrave Version: Structure and Function*. Macmillan International Higher Education: 2014.

167. Le, T. H.; Kim, Y.; Yoon, H., Electrical and Electrochemical Properties of Conducting Polymers. *Polymers (Basel)* **2017,** *9* (4), 150.

168. Schirripa Spagnolo, G.; Leccese, F.; Leccisi, M., LED as Transmitter and Receiver of Light: A Simple Tool to Demonstration Photoelectric Effect. *Crystals* **2019,** *9* (10), 531.

169. Borchert, H., Physics and Chemistry of Conductive Polymers. In *Solar Cells Based on Colloidal Nanocrystals*, Springer International Publishing: Cham, 2014; pp 39-60.

170. Swamy, N. K.; Sandeep, S.; Santhosh, A., Conductive polymers and their nanohybrid transducers for electrochemical biosensors applications: A brief review. *Indian J. Adv. Chem. Sci.* **2017,** *6*, 9.

171. Bredas, J. L.; Street, G. B., Polarons, bipolarons, and solitons in conducting polymers. *Acc. Chem. Res.* **1985,** *18* (10), 309-315.

172. Lüssem, B.; Riede, M.; Leo, K., Doping of organic semiconductors. *Phys. Status Solidi A* **2013,** *210* (1), 9-43.

173. Zhang, M.; Nautiyal, A.; Du, H.; Li, J.; Liu, Z.; Zhang, X.; Wang, R., Polypyrrole film based flexible supercapacitor: mechanistic insight into influence of acid dopants on electrochemical performance. *Electrochim. Acta* **2020,** *357*, 136877.

174. Mishra, A. K., Conducting Polymers: Concepts and Applications. *Journal of Atomic, Molecular, Condensate and Nano Physics* **2018,** *5* (2), 159-193.

175. Zhang, L.; Du, W.; Nautiyal, A.; Liu, Z.; Zhang, X., Recent progress on nanostructured conducting polymers and composites: synthesis, application and future aspects. *Sci. China Mater.* **2018,** *61*(3), 303-352.

176. Keplinger, T.; Wang, X.; Burgert, I., Nanofibrillated cellulose composites and wood derived scaffolds for functional materials. *J. Mater. Chem. A* **2019,** *7* (7), 2981-2992.

177. Mokhena, T. C.; John, M. J., Cellulose nanomaterials: new generation materials for solving global issues. *Cellulose* **2019,** *27*(3), 1149-1194.

178. Bian, H.; Wei, L.; Lin, C.; Ma, Q.; Dai, H.; Zhu, J. Y., Lignin-Containing Cellulose Nanofibril-Reinforced Polyvinyl Alcohol Hydrogels. *ACS Sustainable Chem. Eng.* **2018,** *6* (4), 4821-4828.

179. Luo, H.; Cha, R.; Li, J.; Hao, W.; Zhang, Y.; Zhou, F., Advances in tissue engineering of nanocellulose-based scaffolds: A review. *Carbohydr. Polym.* **2019,** *224*, 115144.

180. Hoeng, F.; Denneulin, A.; Bras, J., Use of nanocellulose in printed electronics: a review. *Nanoscale* **2016,** *27* (8), 13131-13154.

181. Golmohammadi, H.; Morales-Narváez, E.; Naghdi, T.; Merkoçi, A., Nanocellulose in Sensing and Biosensing. *Chem. Mater.* **2017,** *29* (13), 5426-5446.

182. Thomas, B.; Raj, M. C.; B, A. K.; H, R. M.; Joy, J.; Moores, A.; Drisko, G. L.; Sanchez, C., Nanocellulose, a Versatile Green Platform: From Biosources to Materials and Their Applications. *Chem. Rev.* **2018,** *118* (24), 11575-11625.

183. Xing, J.; Tao, P.; Wu, Z.; Xing, C.; Liao, X.; Nie, S., Nanocellulose-graphene composites: A promising nanomaterial for flexible supercapacitors. *Carbohydr. Polym.* **2019,** *207*, 447-459.

184. Zhang, Y.; Hao, N.; Lin, X.; Nie, S., Emerging challenges in the thermal management of cellulose nanofibril-based supercapacitors, lithium-ion batteries and solar cells: A review. *Carbohydr. Polym.* **2020,** *234*, 115888.

185. Chen, W.; Yu, H.; Lee, S. Y.; Wei, T.; Li, J.; Fan, Z., Nanocellulose: a promising nanomaterial for advanced electrochemical energy storage. *Chem. Soc. Rev.* **2018,** *47* (8), 2837-2872.

186. Osong, S. H.; Norgren, S.; Engstrand, P., Processing of wood-based microfibrillated cellulose and nanofibrillated cellulose, and applications relating to papermaking: a review. *Cellulose* **2016,** *23* (1), 93-123.

187. Huang, P.; Wang, C.; Huang, Y.; Wu, M., Structure and Properties of Cellulose Nanofibrils. In *Nanocellulose: From Fundamentals to Advanced Materials*, Huang, J.; Dufresne, A.; Lin, N., Eds. John Wiley & Sons, Inc.: 2019; pp 53-80.

188. Nie, S.; Zhang, K.; Lin, X.; Zhang, C.; Yan, D.; Liang, H.; Wang, S., Enzymatic pretreatment for the improvement of dispersion and film properties of cellulose nanofibrils. *Carbohydr. Polym.* **2018,** *181*, 1136-1142.

189. Bian, H.; Dong, M.; Chen, L.; Zhou, X.; Ni, S.; Fang, G.; Dai, H., Comparison of mixed enzymatic pretreatment and post-treatment for enhancing the cellulose nanofibrillation efficiency. *Bioresour. Technol.* **2019,** *293*, 122171.

190. Chen, Y.; Zhou, L.; Chen, L.; Duan, G.; Mei, C.; Huang, C.; Han, J.; Jiang, S., Anisotropic nanocellulose aerogels with ordered structures fabricated by directional freeze-drying for fast liquid transport. *Cellulose* **2019,** *26* (11), 6653-6667.

191. Tejado, A.; Alam, M. N.; Antal, M.; Yang, H.; van de Ven, T. G. M., Energy requirements for the disintegration of cellulose fibers into cellulose nanofibers. *Cellulose* **2012,** *19* (3), 831-842.

192. Arvidsson, R.; Nguyen, D.; Svanstrom, M., Life cycle assessment of cellulose nanofibrils production by mechanical treatment and two different pretreatment processes. *Environ. Sci. Technol.* **2015,** *49* (11), 6881-90.

193. Bian, H.; Chen, L.; Dai, H.; Zhu, J. Y., Integrated production of lignin containing cellulose nanocrystals (LCNC) and nanofibrils (LCNF) using an easily recyclable di-carboxylic acid. *Carbohydr. Polym.* **2017,** *167*, 167-176.

194. Bian, H.; Chen, L.; Wang, R.; Zhu, J., Green and Low-cost Production of Thermally Stable and Carboxylated Cellulose Nanocrystals and Nanofibrils Using Highly Recyclable Dicarboxylic Acids. *JoVE* **2017,** (119), e55079.

195. Bian, H. Y.; Chen, L. H.; Gleisner, R.; Dai, H. Q.; Zhu, J. Y., Producing wood-based nanomaterials by rapid fractionation of wood at 80 degrees C using a recyclable acid hydrotrope. *Green Chem.* **2017,** *19* (14), 3370-3379.

196. Bian, H. Y.; Chen, L. H.; Dai, H. Q.; Zhu, J. Y., Effect of fiber drying on properties of lignin containing cellulose nanocrystals and nanofibrils produced through maleic acid hydrolysis. *Cellulose* **2017,** *24* (10), 4205-4216.

197. Jia, C.; Chen, L.; Shao, Z.; Agarwal, U. P.; Hu, L.; Zhu, J. Y., Using a fully recyclable dicarboxylic acid for producing dispersible and thermally stable cellulose nanomaterials from different cellulosic sources. *Cellulose* **2017,** *24* (6), 2483-2498.

198. Bian, H. Y.; Luo, J.; Wang, R. B.; Zhou, X. L.; Ni, S. Z.; Shi, R.; Fang, G. G.; Dai, H. Q., Recyclable and Reusable Maleic Acid for Efficient Production of Cellulose Nanofibrils with Stable Performance. *ACS Sustainable Chem. Eng.* **2019,** *7* (24), 20022-20031.

199. Li, B.; Xu, W.; Kronlund, D.; Maattanen, A.; Liu, J.; Smatt, J. H.; Peltonen, J.; Willfor, S.; Mu, X.; Xu, C., Cellulose nanocrystals prepared via formic acid hydrolysis followed by TEMPO-mediated oxidation. *Carbohydr. Polym.* **2015,** *133*, 605-612.

200. Wu, M.; Sukyai, P.; Lv, D.; Zhang, F.; Wang, P.; Liu, C.; Li, B., Water and humidity-induced shape memory cellulose nanopaper with quick response, excellent wet strength and folding resistance. *Chem. Eng. J.* **2020,** *392*, 123673.

201. Lv, D.; Du, H.; Che, X.; Wu, M.; Zhang, Y.; Liu, C.; Nie, S.; Zhang, X.; Li, B., Tailored and Integrated Production of Functional Cellulose Nanocrystals and Cellulose Nanofibrils via Sustainable Formic Acid Hydrolysis: Kinetic Study and Characterization. *ACS Sustainable Chem. Eng.* **2019,** *7* (10), 9449-9463.

202. Hu, L.; Du, H.; Liu, C.; Zhang, Y.; Yu, G.; Zhang, X.; Si, C.; Li, B.; Peng, H., Comparative Evaluation of the Efficient Conversion of Corn Husk Filament and Corn Husk Powder to Valuable Materials via a Sustainable and Clean Biorefinery Process. *ACS Sustainable Chem. Eng.* **2018,** *7* (1), 1327-1336.

203. Nie, S.; Zhang, C.; Zhang, Q.; Zhang, K.; Zhang, Y.; Tao, P.; Wang, S., Enzymatic and cold alkaline pretreatments of sugarcane bagasse pulp to produce cellulose nanofibrils using a mechanical method. *Ind. Crops Prod.* **2018,** *124*, 435-441.

204. Wu, J.; Du, X.; Yin, Z.; Xu, S.; Xu, S.; Zhang, Y., Preparation and characterization of cellulose nanofibrils from coconut coir fibers and their reinforcements in biodegradable composite films. *Carbohydr. Polym.* **2019,** *211*, 49-56.

205. Kang, L.; Wang, W.; Lee, Y. Y., Bioconversion of kraft paper mill sludges to ethanol by SSF and SSCF. *Appl. Biochem. Biotechnol.* **2010,** *161* (1-8), 53-66.

206. Karthikeyan, K.; Balasubramanian, S., Studies on the characterization and possibilities of reutilization of solid wastes from a waste paper based paper industry. *Glob. Environ. Res.* **2010,** *4* (1), 18-22.

207. Guan, W.; Shi, S.; Tu, M.; Lee, Y. Y., Acetone-butanol-ethanol production from Kraft paper mill sludge by simultaneous saccharification and fermentation. *Bioresour. Technol.* **2016,** *200*, 713-721.

208. Naderi, A.; Lindstrom, T.; Erlandsson, J.; Sundstrom, J.; Flodberg, G., A comparative study of the properties of three nanofibrillated cellulose systems that have been produced at about the same energy consumption levels in the mechanical delamination step. *Nord. Pulp Paper Res. J.* **2016,** *31* (3), 364-371.

209. Ioelovich, M., Chapter 9 - Nanocellulose-fabrication, structure, properties, and application in the area of care and cure. In *Fabrication and Self-Assembly of Nanobiomaterials*, Grumezescu, A. M., Ed. William Andrew Publishing: 2016; pp 243-288.

210. Serra, A.; Gonzalez, I.; Oliver-Ortega, H.; Tarres, Q.; Delgado-Aguilar, M.; Mutje, P., Reducing the Amount of Catalyst in TEMPO-Oxidized Cellulose Nanofibers: Effect on Properties and Cost. *Polymers (Basel)* **2017,** *9* (11), 557.

211. Delgado-Aguilar, M.; Gonzalez, I.; Tarres, Q.; Alcala, M.; Angels Pelach, M.; Mutje, P., Approaching a Low-Cost Production of Cellulose Nanofibers for Papermaking Applications. *Bioresources* **2015,** *10* (3), 5345-5355.

212. Novo, L. P.; Bras, J.; Garcia, A.; Belgacem, N.; Curvelo, A. A. S., Subcritical Water: A Method for Green Production of Cellulose Nanocrystals. *ACS Sustainable Chem. Eng.* **2015,** *3* (11), 2839-2846.

213. Qua, E. H.; Hornsby, P. R.; Sharma, H. S. S.; Lyons, G., Preparation and characterisation of cellulose nanofibres. *J. Mater. Sci.* **2011,** *46* (18), 6029-6045.

214. Claverie, M.; Dumas, A.; Careme, C.; Poirier, M.; Le Roux, C.; Micoud, P.; Martin, F.; Aymonier, C., Synthetic Talc and Talc-Like Structures: Preparation, Features and Applications. *Chem. Eur. J.* **2018,** *24* (3), 519-542.

215. Adu, C.; Berglund, L.; Oksman, K.; Eichhorn, S. J.; Jolly, M.; Zhu, C., Properties of cellulose nanofibre networks prepared from never-dried and dried paper mill sludge. *J. Cleaner Prod.* **2018,** *197*, 765-771.

216. Zhao, J.; Zhang, W.; Zhang, X.; Zhang, X.; Lu, C.; Deng, Y., Extraction of cellulose nanofibrils from dry softwood pulp using high shear homogenization. *Carbohydr. Polym.* **2013,** *97* (2), 695-702.

217. Yu, H. Y.; Zhang, H.; Song, M. L.; Zhou, Y.; Yao, J.; Ni, Q. Q., From Cellulose Nanospheres, Nanorods to Nanofibers: Various Aspect Ratio Induced Nucleation/Reinforcing Effects on Polylactic Acid for Robust-Barrier Food Packaging. *ACS Appl. Mater. Interfaces* **2017,** *9* (50), 43920-43938.

218. Liu, Y.; Liu, L.; Wang, K.; Zhang, H.; Yuan, Y.; Wei, H.; Wang, X.; Duan, Y.; Zhou, L.; Zhang, J., Modified ammonium persulfate oxidations for efficient preparation of carboxylated cellulose nanocrystals. *Carbohydr. Polym.* **2020,** *229*, 115572.

219. Lavoine, N.; Bras, J.; Saito, T.; Isogai, A., Improvement of the Thermal Stability of TEMPO-Oxidized Cellulose Nanofibrils by Heat-Induced Conversion of Ionic Bonds to Amide Bonds. *Macromol. Rapid Commun.* **2016,** *37* (13), 1033-9.

220. Hu, Z.; Zhai, R.; Li, J.; Zhang, Y.; Lin, J., Preparation and Characterization of Nanofibrillated Cellulose from Bamboo Fiber via Ultrasonication Assisted by Repulsive Effect. *Int. J. Polym. Sci.* **2017,** *2017*, 1-9.

221. Xie, H.; Zou, Z.; Du, H.; Zhang, X.; Wang, X.; Yang, X.; Wang, H.; Li, G.; Li, L.; Si, C., Preparation of thermally stable and surface-functionalized cellulose nanocrystals via mixed H2SO4/Oxalic acid hydrolysis. *Carbohydr. Polym.* **2019,** *223*, 115116.

222. Yousefi, H.; Faezipour, M.; Hedjazi, S.; Mousavi, M. M.; Azusa, Y.; Heidari, A. H., Comparative study of paper and nanopaper properties prepared from bacterial cellulose nanofibers and fibers/ground cellulose nanofibers of canola straw. *Ind. Crops Prod.* **2013,** *43*, 732-737.

223. Du, H., Parit, M., Liu, K., Zhang, M., Jiang, Z., Huang, T.S., Zhang, X. and Si, C., Engineering cellulose nanopaper with water resistant, antibacterial, and improved barrier properties by impregnation of chitosan and the followed halogenation. *Carbohydr. Polym.* **2021,** *270*, 118372.

224. Meng, Q.; Wang, T. J., Mechanics of Strong and Tough Cellulose Nanopaper. *Appl. Mech. Rev.* **2019,** *71* (4), 040801.

225. Li, M. C.; Wu, Q.; Moon, R. J.; Hubbe, M. A.; Bortner, M. J., Rheological Aspects of Cellulose Nanomaterials: Governing Factors and Emerging Applications. *Adv. Mater.* **2021**, e2006052.

226. Liu, W.; Du, H. S.; Zhang, M. M.; Liu, K.; Liu, H. Y.; Xie, H. X.; Zhang, X. Y.; Si, C. L., Bacterial Cellulose-Based Composite Scaffolds for Biomedical Applications: A Review. *ACS Sustainable Chem. Eng.* **2020,** *8* (20), 7536-7562.

227. Fu, Q.; Cui, C.; Meng, L.; Hao, S.; Dai, R.; Yang, J., Emerging cellulose-derived materials: a promising platform for the design of flexible wearable sensors toward health and environment monitoring. *Mater. Chem. Front.* **2021,** *5* (5), 2051-2091.

228. Miao, C.; Du, H.; Parit, M.; Jiang, Z.; Tippur, H. V.; Zhang, X.; Liu, Z.; Li, J.; Wang, R., Superior crack initiation and growth characteristics of cellulose nanopapers. *Cellulose* **2020,** *27* (6), 3181-3195.

229. Fang, Z.; Hou, G.; Chen, C.; Hu, L., Nanocellulose-based films and their emerging applications. *Curr. Opin. Solid State Mater. Sci.* **2019,** *23* (4), 100764.

230. Parit, M.; Du, H.; Zhang, X.; Prather, C.; Adams, M.; Jiang, Z., Polypyrrole and cellulose nanofiber based composite films with improved physical and electrical properties for electromagnetic shielding applications. *Carbohydr. Polym.* **2020,** *240*, 116304.

231. Cao, W. T.; Chen, F. F.; Zhu, Y. J.; Zhang, Y. G.; Jiang, Y. Y.; Ma, M. G.; Chen, F., Binary Strengthening and Toughening of MXene/Cellulose Nanofiber Composite Paper with Nacre-Inspired Structure and Superior Electromagnetic Interference Shielding Properties. *ACS Nano* **2018,** *12* (5), 4583-4593.

232. Dias, O. A. T.; Konar, S.; Leao, A. L.; Yang, W.; Tjong, J.; Sain, M., Current State of Applications of Nanocellulose in Flexible Energy and Electronic Devices. *Front. Chem.* **2020,** *8*, 420.

233. Yang, X.; Biswas, S. K.; Han, J.; Tanpichai, S.; Li, M. C.; Chen, C.; Zhu, S.; Das, A. K.; Yano, H., Surface and Interface Engineering for Nanocellulosic Advanced Materials. *Adv. Mater.* **2020**, e2002264.

234. Sun, L.; Zhang, X.; Liu, H.; Liu, K.; Du, H.; Kumar, A.; Sharma, G.; Si, C., Recent Advance in Hydrophobic Modification of Nanocellulose. *Curr. Org. Chem.* **2021,** *25* (3), 417-436.

235. Bakshi, P. S.; Selvakumar, D.; Kadirvelu, K.; Kumar, N. S., Chitosan as an environment friendly biomaterial - a review on recent modifications and applications. *Int. J. Biol. Macromol.* **2020,** *150*, 1072-1083.

236. Mao, H.; Wei, C.; Gong, Y.; Wang, S.; Ding, W., Mechanical and Water-Resistant Properties of Eco-Friendly Chitosan Membrane Reinforced with Cellulose Nanocrystals. *Polymers (Basel)* **2019,** *11* (1), 166.

237. H.P.S, A. K.; Saurabh, C. K.; A.S, A.; Nurul Fazita, M. R.; Syakir, M. I.; Davoudpour, Y.; Rafatullah, M.; Abdullah, C. K.; M. Haafiz, M. K.; Dungani, R., A review on chitosan-cellulose blends and nanocellulose reinforced chitosan biocomposites: Properties and their applications. *Carbohydr. Polym.* **2016,** *150*, 216-226.

238. Toivonen, M. S.; Kurki-Suonio, S.; Schacher, F. H.; Hietala, S.; Rojas, O. J.; Ikkala, O., Water-resistant, transparent hybrid nanopaper by physical cross-linking with chitosan. *Biomacromolecules* **2015,** *16* (3), 1062-1071.

239. Zhao, K.; Wang, W.; Teng, A.; Zhang, K.; Ma, Y.; Duan, S.; Li, S.; Guo, Y., Using cellulose nanofibers to reinforce polysaccharide films: Blending vs layer-by-layer casting. *Carbohydr. Polym.* **2020,** *227*, 115264.

240. Wagberg, L.; Erlandsson, J., The Use of Layer-by-Layer Self-Assembly and Nanocellulose to Prepare Advanced Functional Materials. *Adv. Mater.* **2020**, e2001474.

241. Wang, W.; Meng, Q.; Li, Q.; Liu, J.; Zhou, M.; Jin, Z.; Zhao, K., Chitosan Derivatives and Their Application in Biomedicine. *Int. J. Mol. Sci.* **2020,** *21* (2), 487.

242. Cao, Z.; Sun, Y., N-halamine-based chitosan: preparation, characterization, and antimicrobial function. *J. Biomed. Mater. Res. A* **2008,** *85* (1), 99-107.

243. Nautiyal, A.; Qiao, M.; Ren, T.; Huang, T.-S.; Zhang, X.; Cook, J.; Bozack, M. J.; Farag, R., High-performance Engineered Conducting Polymer Film towards Antimicrobial/Anticorrosion Applications. *Eng. Sci.* **2018,** *4*, 70-78.

244. Ma, W.; Li, L.; Xiao, X.; Du, H.; Ren, X.; Zhang, X.; Huang, T. S., Construction of Chlorine Labeled ZnO–Chitosan Loaded Cellulose Nanofibrils Film with Quick Antibacterial Performance and Prominent UV Stability. *Macromol. Mater. Eng.* **2020,** *305* (8), 2000228.

245. Li, Y.; Vasileva, E.; Sychugov, I.; Popov, S.; Berglund, L., Optically Transparent Wood: Recent Progress, Opportunities, and Challenges. *Adv. Opt. Mater.* **2018**, 1800059.

246. Zhang, H.; Shi, L.; Feng, X., Use of chitosan to reinforce transparent conductive cellulose nanopaper. *J. Mater. Chem. C* **2018,** *6* (2), 242-248.

247. Gao, Q.; Lei, M.; Zhou, K.; Liu, X.; Wang, S.; Li, H., Preparation of a microfibrillated cellulose/chitosan/polypyrrole film for Active Food Packaging. *Prog. Org. Coat.* **2020,** *149*, 105907.

248. Yang, W.; Jiao, L.; Min, D.; Liu, Z.; Dai, H., Effects of preparation approaches on optical properties of self-assembled cellulose nanopapers. *RSC Adv.* **2017,** *7* (17), 10463-10468.

249. Cranston, E. D.; Gray, D. G., Birefringence in spin-coated films containing cellulose nanocrystals. *Colloids Surf., A* **2008,** *325* (1-2), 44-51.

250. Azofeifa, D. E.; Arguedas, H. J.; Vargas, W. E., Optical properties of chitin and chitosan biopolymers with application to structural color analysis. *Opt. Mater.* **2012,** *35* (2), 175-183.

251. Liu, K.; Du, H.; Zheng, T.; Liu, H.; Zhang, M.; Zhang, R.; Li, H.; Xie, H.; Zhang, X.; Ma, M.; Si, C., Recent advances in cellulose and its derivatives for oilfield applications. *Carbohydr. Polym.* **2021,** *259*, 117740.

252. Du, H.; Parit, M.; Wu, M.; Che, X.; Wang, Y.; Zhang, M.; Wang, R.; Zhang, X.; Jiang, Z.; Li, B., Sustainable valorization of paper mill sludge into cellulose nanofibrils and cellulose nanopaper. *J. Hazard. Mater.* **2020,** *400*, 123106.

253. Branca, C.; D'Angelo, G.; Crupi, C.; Khouzami, K.; Rifici, S.; Ruello, G.; Wanderlingh, U., Role of the OH and NH vibrational groups in polysaccharide-nanocomposite interactions: A FTIR-ATR study on chitosan and chitosan/clay films. *Polymer* **2016,** *99*, 614-622.

254. Fernandes Queiroz, M.; Melo, K. R.; Sabry, D. A.; Sassaki, G. L.; Rocha, H. A., Does the use of chitosan contribute to oxalate kidney stone formation? *Mar. Drugs* **2014,** *13* (1), 141-58.

255. Yasmeen, S.; Kabiraz, M. K.; Saha, B.; Qadir, M. R.; Gafur, M. A.; Masum, S. M., Chromium (VI) ions removal from tannery effluent using chitosan-microcrystalline cellulose composite as adsorbent. *Int. Res. J. Pure Appl. Chem.* **2016**, 1-14.

256. Carosio, F.; Ghanadpour, M.; Alongi, J.; Wagberg, L., Layer-by-layer-assembled chitosan/phosphorylated cellulose nanofibrils as a bio-based and flame protecting nano-exoskeleton on PU foams. *Carbohydr. Polym.* **2018,** *202*, 479-487.

257. Cheng, X.; Ma, K.; Li, R.; Ren, X.; Huang, T. S., Antimicrobial coating of modified chitosan onto cotton fabrics. *Appl. Surf. Sci.* **2014,** *309*, 138-143.

258. Kumar, V.; Bollström, R.; Yang, A.; Chen, Q.; Chen, G.; Salminen, P.; Bousfield, D.; Toivakka, M., Comparison of nano- and microfibrillated cellulose films. *Cellulose* **2014,** *21* (5), 3443-3456.

259. Visanko, M.; Liimatainen, H.; Sirvio, J. A.; Mikkonen, K. S.; Tenkanen, M.; Sliz, R.; Hormi, O.; Niinimaki, J., Butylamino-functionalized cellulose nanocrystal films: barrier properties and mechanical strength. *RSC Adv.* **2015,** *5* (20), 15140-15146.

260. Aulin, C.; Salazar-Alvarez, G.; Lindstrom, T., High strength, flexible and transparent nanofibrillated cellulose-nanoclay biohybrid films with tunable oxygen and water vapor permeability. *Nanoscale* **2012,** *4* (20), 6622-6628.

261. Liu, W.; Liu, H.; Liu, K.; Du, H.; Liu, Y.; Si, C., Paper-based Products as Promising Substitutes for Plastics in the Context of Bans on Non-biodegradables. *BioResources* **2020,** *15* (4), 7309-7312.

262. Khalifa, Y., Effect of the printing remedies and lamination techniques on barrier properties "WVTR and OTR Value" for Polypropylene Film. *EC Nutrition* **2016,** *5* (2), 1089-1099.

263. Jost, V., Packaging related properties of commercially available biopolymers-An overview of the status quo. *eXPRESS Polym. Lett.* **2018,** *12* (5), 429-435.

264. Carosio, F.; Colonna, S.; Fina, A.; Rydzek, G.; Hemmerlé, J.; Jierry, L.; Schaaf, P.; Boulmedais, F., Efficient Gas and Water Vapor Barrier Properties of Thin Poly(lactic acid)

Packaging Films: Functionalization with Moisture Resistant Nafion and Clay Multilayers. *Chem. Mater.* **2014,** *26* (19), 5459-5466.

265. Caner, C.; Vergano, P.; Wiles, J., Chitosan film mechanical and permeation properties as affected by acid, plasticizer, and storage. *J. Food Sci.* **1998,** *63* (6), 1049-1053.

266. Shit, S. C.; Shah, P. M., Edible Polymers: Challenges and Opportunities. *J. Polym.* **2014,** *2014*, 1-13.

267. Xu, R.; Liu, K.; Du, H.; Liu, H.; Cao, X.; Zhao, X.; Qu, G.; Li, X.; Li, B.; Si, C., Falling Leaves Return to Their Roots: A Review on the Preparation of gamma-Valerolactone from Lignocellulose and Its Application in the Conversion of Lignocellulose. *ChemSusChem* **2020,** *13* (24), 6461-6476.

268. Liu, H.; Xu, T.; Liu, K.; Zhang, M.; Liu, W.; Li, H.; Du, H.; Si, C., Lignin-based electrodes for energy storage application. *Ind. Crops Prod.* **2021,** *165*, 113425.

269. Liu, W.; Du, H.; Liu, K.; Liu, H.; Xie, H.; Si, C.; Pang, B.; Zhang, X., Sustainable preparation of cellulose nanofibrils via choline chloride-citric acid deep eutectic solvent pretreatment combined with high-pressure homogenization. *Carbohydr. Polym.* **2021,** *267*, 118220.

270. Wu, J.; Che, X.; Hu, H.-C.; Xu, H.; Li, B.; Liu, Y.; Li, J.; Ni, Y.; Zhang, X.; Ouyang, X., Organic solar cells based on cellulose nanopaper from agroforestry residues with an efficiency of over 16% and effectively wide-angle light capturing. *J. Mater. Chem. A* **2020,** *8* (11), 5442-5448.

271. Pang, B.; Jiang, G.; Zhou, J.; Zhu, Y.; Cheng, W.; Zhao, D.; Wang, K.; Xu, G.; Yu, H., Molecular‐Scale Design of Cellulose‐Based Functional Materials for Flexible Electronic Devices. *Adv. Electron. Mater.* **2020,** *7* (2), 2000944.

272. Cao, W.; Ma, C.; Tan, S.; Ma, M.; Wan, P.; Chen, F., Ultrathin and Flexible CNTs/MXene/Cellulose Nanofibrils Composite Paper for Electromagnetic Interference Shielding. *Nano-Micro Lett.* **2019,** *11* (1), 72.

273. Song, M.; Yu, H.; Zhu, J.; Ouyang, Z.; Abdalkarim, S. Y. H.; Tam, K. C.; Li, Y., Constructing stimuli-free self-healing, robust and ultrasensitive biocompatible hydrogel sensors with conductive cellulose nanocrystals. *Chem. Eng. J.* **2020,** *398*, 125547.

274. Wang, Y.; Uetani, K.; Liu, S.; Zhang, X.; Wang, Y.; Lu, P.; Wei, T.; Fan, Z.; Shen, J.; Yu, H.; Li, S.; Zhang, Q.; Li, Q.; Fan, J.; Yang, N.; Wang, Q.; Liu, Y.; Cao, J.; Li, J.; Chen, W., Multifunctional Bionanocomposite Foams with a Chitosan Matrix Reinforced by Nanofibrillated Cellulose. *ChemNanoMat* **2017,** *3* (2), 98-108.

275. Chen, Y.; Zhu, J.; Yu, H.-Y.; Li, Y., Fabricating robust soft-hard network of self-healable polyvinyl alcohol composite films with functionalized cellulose nanocrystals. *Compos. Sci. Technol.* **2020,** *194*, 108165.

276. Huang, Y.; Li, H.; Wang, Z.; Zhu, M.; Pei, Z.; Xue, Q.; Huang, Y.; Zhi, C., Nanostructured Polypyrrole as a flexible electrode material of supercapacitor. *Nano Energy* **2016,** *22*, 422-438.

277. Nautiyal, A.; Qiao, M.; Cook, J. E.; Zhang, X.; Huang, T.-S., High performance polypyrrole coating for corrosion protection and biocidal applications. *Appl. Surf. Sci.* **2018,** *427*, 922-930.

278. Huang, H.; Wu, J.; Lin, X.; Li, L.; Shang, S.; Yuen, M. C.; Yan, G., Self-assembly of polypyrrole/chitosan composite hydrogels. *Carbohydr. Polym.* **2013,** *95* (1), 72-76.

279. Yalçınkaya, S.; Demetgül, C.; Timur, M.; Çolak, N., Electrochemical synthesis and characterization of polypyrrole/chitosan composite on platinum electrode: Its electrochemical and thermal behaviors. *Carbohydr. Polym.* **2010,** *79* (4), 908-913.

280. Ruhi, G.; Modi, O. P.; Dhawan, S. K., Chitosan-polypyrrole-SiO2 composite coatings with advanced anticorrosive properties. *Synth. Met.* **2015,** *200*, 24-39.

281. Zhu, M.; Wu, J.; Du, Z.; Tay, R. Y.; Li, H.; Özyilmaz, B.; Teo, E. H. T., A wafer-scale graphene and ferroelectric multilayer for flexible and fast-switched modulation applications. *Nanoscale* **2015,** *7* (35), 14730-14737.

282. Chen, Y.; Pang, L.; Li, Y.; Luo, H.; Duan, G.; Mei, C.; Xu, W.; Zhou, W.; Liu, K.; Jiang, S., Ultra-thin and highly flexible cellulose nanofiber/silver nanowire conductive paper for effective electromagnetic interference shielding. *Compos. Part A Appl. Sci. Manuf.* **2020,** *135*, 105960.

283. Zhang, X.; Wu, X.; Lu, C.; Zhou, Z., Dialysis-Free and in Situ Doping Synthesis of Polypyrrole@Cellulose Nanowhiskers Nanohybrid for Preparation of Conductive Nanocomposites with Enhanced Properties. *ACS Sustainable Chem. Eng.* **2015,** *3* (4), 675-682.

284. Blinova, N. V.; Stejskal, J.; Trchová, M.; Prokeš, J.; Omastová, M., Polyaniline and polypyrrole: A comparative study of the preparation. *Eur. Polym. J.* **2007,** *43* (6), 2331-2341.

285. Lizundia, E.; Nguyen, T.-D.; Vilas, Jose L.; Hamad, W. Y.; MacLachlan, M. J., Chiroptical, morphological and conducting properties of chiral nematic mesoporous cellulose/polypyrrole composite films. *J. Mater. Chem.* **2017,** *5* (36), 19184-19194.

286. Sanchez Ramirez, D. O.; Varesano, A.; Carletto, R. A.; Vineis, C.; Perelshtein, I.; Natan, M.; Perkas, N.; Banin, E.; Gedanken, A., Antibacterial properties of polypyrrole-treated fabrics by ultrasound deposition. *Mater. Sci. Eng. C Mater. Biol. Appl.* **2019,** *102*, 164-170.

287. Marins, J. A.; Soares, B. G.; Fraga, M.; Müller, D.; Barra, G. M. O., Self-supported bacterial cellulose polyaniline conducting membrane as electromagnetic interference shielding material: effect of the oxidizing agent. *Cellulose* **2014,** *21* (3), 1409-1418.

288. Liu, S.; He, K.; Wu, X.; Luo, X.; Li, B., Surface modification of cellulose scaffold with polypyrrole for the fabrication of flexible supercapacitor electrode with enhanced capacitance. *RSC Adv.* **2015,** *5* (106), 87266-87276.

289. Fei, G.; Wang, Y.; Wang, H.; Ma, Y.; Guo, Q.; Huang, W.; Yang, D.; Shao, Y.; Ni, Y., Fabrication of Bacterial Cellulose/Polyaniline Nanocomposite Paper with Excellent Conductivity, Strength, and Flexibility. *ACS Sustainable Chem. Eng.* **2019,** *7* (9), 8215-8225.

290. Omura, T.; Chan, C. H.; Wakisaka, M.; Nishida, H., Organic Thin Paper of Cellulose Nanofiber/Polyaniline Doped with (+/-)-10-Camphorsulfonic Acid Nanohybrid and Its Application to Electromagnetic Shielding. *ACS Omega* **2019,** *4* (5), 9446-9452.

291. Lay, M.; Mendez, J. A.; Delgado-Aguilar, M.; Bun, K. N.; Vilaseca, F., Strong and electrically conductive nanopaper from cellulose nanofibers and polypyrrole. *Carbohydr. Polym.* **2016,** *152*, 361-369.

292. Lay, M.; Pelach, M. A.; Pellicer, N.; Tarres, J. A.; Bun, K. N.; Vilaseca, F., Smart nanopaper based on cellulose nanofibers with hybrid PEDOT:PSS/polypyrrole for energy storage devices. *Carbohydr. Polym.* **2017,** *165*, 86-95.

293. Gopakumar, D. A.; Pai, A. R.; Pottathara, Y. B.; Pasquini, D.; Carlos de Morais, L.; Luke, M.; Kalarikkal, N.; Grohens, Y.; Thomas, S., Cellulose Nanofiber-Based Polyaniline Flexible Papers as Sustainable Microwave Absorbers in the X-Band. *ACS Appl. Mater. Interfaces* **2018,** *10* (23), 20032-20043.

294. Gahlout, P.; Choudhary, V., Microwave shielding behaviour of polypyrrole impregnated fabrics. *Compos. B. Eng.* **2019,** *175*, 107093.

295. Zhang, Y.; Qiu, M.; Yu, Y.; Wen, B.; Cheng, L., A Novel Polyaniline-Coated Bagasse Fiber Composite with Core-Shell Heterostructure Provides Effective Electromagnetic Shielding Performance. *ACS Appl. Mater. Interfaces* **2017,** *9* (1), 809-818.

296. Lee, T. W.; Lee, S. E.; Jeong, Y. G., Highly Effective Electromagnetic Interference Shielding Materials based on Silver Nanowire/Cellulose Papers. *ACS Appl. Mater. Interfaces* **2016,** *8* (20), 13123-13132.

297. Zhang, Y.; Yang, Z.; Pan, T.; Gao, H.; Guan, H.; Xu, J.; Zhang, Z., Construction of natural fiber/polyaniline core-shell heterostructures with tunable and excellent electromagnetic shielding capability via a facile secondary doping strategy. *Compos. Part A Appl. Sci. Manuf.* **2020,** *137*, 105994.

298. Xu, C.; Song, Y.; Han, M.; Zhang, H., Portable and wearable self-powered systems based on emerging energy harvesting technology. *Microsyst. Nanoeng.* **2021,** *7* (1), 1-14.

299. Dubal, D. P.; Chodankar, N. R.; Kim, D. H.; Gomez-Romero, P., Towards flexible solid-state supercapacitors for smart and wearable electronics. *Chem. Soc. Rev.* **2018,** *47* (6), 2065-2129.

300. Palchoudhury, S.; Ramasamy, K.; Gupta, R. K.; Gupta, A., Flexible Supercapacitors: A Materials Perspective. *Front. Mater.* **2019,** *5*, 83.

301. Zheng, Q.; Kvit, A.; Cai, Z.; Ma, Z.; Gong, S., A freestanding cellulose nanofibril–reduced graphene oxide–molybdenum oxynitride aerogel film electrode for all-solid-state supercapacitors with ultrahigh energy density. *J. Mater. Chem. A* **2017,** *5* (24), 12528-12541.

302. Zheng, Q. F.; Xie, R. S.; Fang, L. M.; Cai, Z. Y.; Ma, Z. Q.; Gong, S. Q., Oxygen-deficient and nitrogen- doped MnO2 nanowire- reduced graphene oxide- cellulose nanofibril

aerogel electrodes for high- performance asymmetric supercapacitors. *J. Mater. Chem. A* **2018,** *6* (47), 24407-24417.

303. Sheng, N.; Chen, S.; Yao, J.; Guan, F.; Zhang, M.; Wang, B.; Wu, Z.; Ji, P.; Wang, H., Polypyrrole@TEMPO-oxidized bacterial cellulose/reduced graphene oxide macrofibers for flexible all-solid-state supercapacitors. *Chem. Eng. J.*. **2019,** *368*, 1022-1032.

304. Wang, D. C.; Yu, H. Y.; Qi, D.; Ramasamy, M.; Yao, J.; Tang, F.; Tam, K. M. C.; Ni, Q., Supramolecular Self-Assembly of 3D Conductive Cellulose Nanofiber Aerogels for Flexible Supercapacitors and Ultrasensitive Sensors. *ACS Appl. Mater. Interfaces* **2019,** *11* (27), 24435-24446.

305. Gueye, M. N.; Carella, A.; Faure-Vincent, J.; Demadrille, R.; Simonato, J.-P., Progress in understanding structure and transport properties of PEDOT-based materials: A critical review. *Prog. Mater Sci.* **2020,** *108*, 100616.

306. Wen, Y.; Xu, J., Scientific Importance of Water-Processable PEDOT-PSS and Preparation, Challenge and New Application in Sensors of Its Film Electrode: A Review. *J. Polym. Sci., Part A: Polym. Chem.* **2017,** *55* (7), 1121-1150.

307. Sun, K.; Zhang, S.; Li, P.; Xia, Y.; Zhang, X.; Du, D.; Isikgor, F. H.; Ouyang, J., Review on application of PEDOTs and PEDOT:PSS in energy conversion and storage devices. *J. Mater. Sci.: Mater. Electron.* **2015,** *26* (7), 4438-4462.

308. Kumar, N.; Ginting, R. T.; Kang, J.-W., Flexible, large-area, all-solid-state supercapacitors using spray deposited PEDOT:PSS/reduced-graphene oxide. *Electrochim. Acta* **2018,** *270*, 37-47.

309. Liu, Y.; Weng, B.; Razal, J. M.; Xu, Q.; Zhao, C.; Hou, Y.; Seyedin, S.; Jalili, R.; Wallace, G. G.; Chen, J., High-Performance Flexible All-Solid-State Supercapacitor from Large Free-Standing Graphene-PEDOT/PSS Films. *Sci. Rep.* **2015,** *5*, 17045.

310. Wang, Z.; Tammela, P.; Huo, J.; Zhang, P.; Strømme, M.; Nyholm, L., Solution-processed poly(3,4-ethylenedioxythiophene) nanocomposite paper electrodes for high-capacitance flexible supercapacitors. *J. Mater. Chem. A* **2016,** *4* (5), 1714-1722.

311. Ko, Y.; Kim, J.; Kim, D.; Kwon, G.; Yamauchi, Y.; You, J., Fabrication of Highly Conductive Porous Cellulose/PEDOT:PSS Nanocomposite Paper via Post-Treatment. *Nanomaterials (Basel)* **2019,** *9* (4), 612.

312. Kayser, L. V.; Lipomi, D. J., Stretchable Conductive Polymers and Composites Based on PEDOT and PEDOT:PSS. *Adv. Mater.* **2019,** *31* (10), e1806133.

313. Li, Y.; Ren, G.; Zhang, Z.; Teng, C.; Wu, Y.; Lu, X.; Zhu, Y.; Jiang, L., A strong and highly flexible aramid nanofibers/PEDOT:PSS film for all-solid-state supercapacitors with superior cycling stability. *J. Mater. Chem. A* **2016,** *4* (44), 17324-17332.

314. Chen, L.; Chen, L.; Ai, Q.; Li, D.; Si, P.; Feng, J.; Zhang, L.; Li, Y.; Lou, J.; Ci, L., Flexible all-solid-state supercapacitors based on freestanding, binder-free carbon nanofibers@polypyrrole@graphene film. *Chem. Eng. J.* **2018,** *334*, 184-190.

315. Orangi, J.; Hamade, F.; Davis, V. A.; Beidaghi, M., 3D Printing of Additive-Free 2D Ti3C2Tx (MXene) Ink for Fabrication of Micro-Supercapacitors with Ultra-High Energy Densities. *ACS Nano* **2020,** *14* (1), 640-650.

316. Unuma, T.; Kobayashi, O.; Hamdany, I. F. A.; Kumar, V.; Saarinen, J. J., Terahertz complex conductivity of nanofibrillar cellulose-PEDOT:PSS composite films. *Cellulose* **2019,** *26* (5), 3247-3253.

317. Yildirim, E.; Wu, G.; Yong, X.; Tan, T. L.; Zhu, Q.; Xu, J.; Ouyang, J.; Wang, J.-S.; Yang, S.-W., A theoretical mechanistic study on electrical conductivity enhancement of DMSO treated PEDOT:PSS. *J. Mater. Chem. C* **2018,** *6* (19), 5122-5131.

318. Lee, I.; Kim, G. W.; Yang, M.; Kim, T.-S., Simultaneously Enhancing the Cohesion and Electrical Conductivity of PEDOT:PSS Conductive Polymer Films using DMSO Additives. *ACS Appl. Mater. Interfaces* **2015,** *8* (1), 302-310.

319. Ly, C. T.; Phan, C. T.; Vu, C. N.; Le, H. S.; Nguyen, T. T.; Tran, D. L.; Le, L. A.; Vu, T. T., Electrodeposition of PEDOT-rGO film in aqueous solution for detection of acetaminophen in traditional medicaments. *Adv. Nat. Sci.: Nanosci. Nanotechnol.* **2019,** *10* (1), 015013.

320. Khasim, S.; Pasha, A.; Badi, N.; Lakshmi, M.; Mishra, Y. K., High performance flexible supercapacitors based on secondary doped PEDOT–PSS–graphene nanocomposite films for large area solid state devices. *RSC Adv.* **2020,** *10* (18), 10526-10539.

321. Olivares, A. J.; Cosme, I.; Sanchez-Vergara, M. E.; Mansurova, S.; Carrillo, J. C.; Martinez, H. E.; Itzmoyotl, A., Nanostructural Modification of PEDOT:PSS for High Charge Carrier Collection in Hybrid Frontal Interface of Solar Cells. *Polymers (Basel)* **2019,** *11* (6), 1034.

322. Xie, Y.; Shi-Hao, Z.; Hai-Yun, J.; Zeng, H.; Wu, R.-M.; Chen, H.; Ya-Fang, G.; Yi-Yang, H.; Hai-Long, B., Properties of carbon black-PEDOT composite prepared via in-situ chemical oxidative polymerization. *e-Polymers* **2019,** *19* (1), 61-69.

323. Yeon, C.; Kim, G.; Lim, J. W.; Yun, S. J., Highly conductive PEDOT:PSS treated by sodium dodecyl sulfate for stretchable fabric heaters. *RSC Adv.* **2017,** *7* (10), 5888-5897.

324. Kim, Y. H.; Sachse, C.; Machala, M. L.; May, C.; Müller-Meskamp, L.; Leo, K., Highly Conductive PEDOT:PSS Electrode with Optimized Solvent and Thermal Post-Treatment for ITO-Free Organic Solar Cells. *Adv. Funct. Mater.* **2011,** *21* (6), 1076-1081.

325. Peng, S.; Fan, L.; Wei, C.; Liu, X.; Zhang, H.; Xu, W.; Xu, J., Flexible polypyrrole/copper sulfide/bacterial cellulose nanofibrous composite membranes as supercapacitor electrodes. *Carbohydr. Polym.* **2017,** *157*, 344-352.

326. Xu, C.; Sun, J.; Gao, L., Synthesis of novel hierarchical graphene/polypyrrole nanosheet composites and their superior electrochemical performance. *J. Mater. Chem.* **2011,** *21* (30), 11253.

327. Zhang, M.; Nautiyal, A.; Du, H.; Wei, Z.; Zhang, X.; Wang, R., Electropolymerization of polyaniline as high-performance binder free electrodes for flexible supercapacitor. *Electrochim. Acta* **2021,** *376*, 138037.